Molecular Gas in Early-type Galaxies

by

Katherine Anne Alatalo

A dissertation submitted in partial satisfaction of the
requirements for the degree of
Doctor of Philosophy

in

Astrophysics

in the

Graduate Division
of the
University of California, Berkeley

Committee in charge:
Professor Carl Heiles, Chair
Professor Jonathan Arons
Professor Adrian Lee
Professor Christopher McKee

Fall 2012

Molecular Gas in Early-type Galaxies

Abstract

Molecular Gas in Early-type Galaxies

by

Katherine Anne Alatalo
Doctor of Philosophy in Astrophysics

University of California, Berkeley

Professor Carl Heiles, Chair

This thesis explores the relationship between molecular gas and early-type galaxies (ETGs). Specifically, I explore how molecular gas behaves and is configured in a complete sample of morphologically selected elliptical and lenticular galaxies. I also highlight a case study where molecular gas is being expelled and its host is rapidly transitioning from starforming to quiescent.

I first present the Combined Array for Research for Millimeter Astronomy (CARMA) ATLAS^{3D} CO imaging survey of 30 nearby CO-rich ETGs which, when combined with archival data, creates a catalog of 40 ETGs with available CO imaging within the context of the ATLAS^{3D} survey. I examine the distribution of the morphologies of the molecular gas within these systems, and correlate them with other properties of the host galaxy, such as color and environment membership.

Following the molecular gas observations from both CARMA and the Submillimeter Array, I present molecular gas data for nearby field galaxy NGC 1266, which hosts a massive molecular outflow that is being driven by a central AGN. I present the properties and energetics associated with the system, and hypothesize about the driving mechanism. I compare the outflow in NGC 1266 to other known outflowing molecular systems and argue why NGC 1266 is unique.

From photometric observations from the Hubble Space Telescope as well as radio continuum observations from the Very Long Baseline Array, I present evidence that NGC 1266 is in a special phase of evolution, likely in a key part of the transition from being a blue starforming galaxy to a quiescent, red sequence galaxy. I argue that NGC 1266 should be considered a poststarburst galaxy, and explain why it is essential that searches for such transition objects find NGC 1266 analogs.

I dedicate this dissertation to my parents, Bruce and Anne Alatalo, who have supported and guided my enthusiasm for science throughout my life.

Contents

List of Figures

List of Tables

Acknowledgments

I'd like to first thank my supervisor, Carl Heiles, for his encouragement throughout the duration of this thesis. Without his guidance and ever present support, I would not have been able to find my science path and follow my instincts. A very special thanks also goes to Lisa Young for her constant support and spot on advice. Without her mastery of molecular gas in early-type galaxies and many insightful discussions, I would have found myself lost. I'd also like to thank Philip Chang, who helped me hone my scientific intuition and mentor me from being a student to truly "getting" science. Without the support of these three, I would not have been able to make this thesis what it is.

I would also like to thank my thesis committee. Jon Arons: even through the teasing about my love of the University of Michigan, you were always there with great science advice and were my go-to "theoretical perspective." Chris McKee: your insights and thoughtful comments throughout my thesis have only made it, and my own viewpoint on science better. Adrian Lee: from meeting you before I became a student until now, it has been a pleasure talking science with you.

Within the Berkeley community, I would first like to thank Dick Plambeck for teaching me the many nuances of the CARMA telescope, from the `MIRIAD` reduction system, to how to reset a correlator. I'd also like to thank Leo Blitz for helping to create a collaboration between Berkeley and the ATLAS^{3D} team, making my thesis possible. Genevieve Graves: for the many conversations we have had about science, as they frequently led to very interesting new ideas. Colette Patt: for being willing to sit with me and help me strategize for the future, keeping me on the path to becoming a scientist.

I also have to thank the many students that I have had the pleasure of knowing throughout the years: Andrew Wetzel and Jeff Silverman: we made it! Long live JAK! Graduating radio students: Amber Bauermeister, Statia Cook, Peter Williams, Andrew Siemion: thanks for making our sub-specialty here at Berkeley especially fun. Upcoming radio students: Chat Hull (my mentee!), Karto Keating (ATA whizkid), James McBride (my research brother), Jonnie Pober and Dyas Utomo: you are a great group, and make the old radio fogies like myself proud. To the graduates from Berkeley: Kristen Shapiro, Daniel Perley, Charles Hansen, Linda Strubbe and Ruth Murray Clay. Kristen: your spot-on advice always made my path more clear. Thanks for emulating the kind of scientist that I strove to become. Carlos: you will always be my arch nemesis, thanks for lightening the mood in our rooftop office. Ruth: thanks for being an amazing mentor

to me! Your advice, especially in the more challenging graduate student times really put things in perspective and kept me seeing the light at the end of the tunnel. Linda: thank you for your kindness and caring. I always enjoyed having coffee with you out on the Mining Circle. And finally Dan - my night owl Campbell Hall buddy. How many times did we have dinner on North side talking about sciencey things? Thanks for being such an amazing friend.

To the many non-Berkeley friends I have gotten to know along the way. Kristina Nyland: not only did you fully welcome me into your NRAO Socorro family, but always vastly improve those things you get your hands on. Laura Lopez: you helped me bring my first *Chandra* proposal to fruition! Thanks for being so willing to lend your expertise in both X-rays and life. Lisa Wei: Our collaboration goes so much further than NGC 5173! Thanks for the many science, CO, star formation and miscellaneous conversations. Joan Schmelz : thank you for your expertise and advice in how to blaze your own science trail. Daniela Calzetti: thank you for the many words of advice and guidance for my path forward. My time at U-Mass was refreshing and reminded me why I do astronomy. Tim McKay: you started me down this path when I was a young undergrad still getting my scientific feet underneath me. Thanks for being patient and cultivating my enthusiasm for astronomy. Heather Flewelling: my Hawaii postdoc and friend since undergrad. Thanks for always having an encouraging word. Pierre-Yves Lablanche: you had exactly the right thing to say as I worked on this thesis, as you were going through the same things at the same time! Richard McDermid: for being my window into the ATLAS^{3D} team, and always having time to talk science. Jesus Falcón-Barroso: for the wonderful conversations about star formation, and the future. Susana Deustua: planning and working with you on HST observations has been a pleasure. John Carpenter: the true CARMA guru. You were always there to answer questions when CARMA operations became tricky and did so with patience and support. Fred Adams: from the first time I walked into your office as an enthusiastic undergrad to the conversations we get to have on my brief trips back home. Thanks for always having spot on science and life advice for me.

To my CARMA family. Thanks to the entire staff of the Owens Valley Radio Observatory and the many many students and postdocs that I have had the pleasure of getting to know over the course of my many years of observing at CARMA. Century club members unite!

Thanks goes to the CO ATLAS^{3D} team! First off, Tim Davis my ATLAS^{3D} compatriot. Thank you for the many chats and arguments about science. I always felt like we both came out of those discussions smarter and with a new intuition about what we were doing. Alison Crocker: the one who blazed the path of creating a sample like this one. Thank you for the many times that you were able to lend your experience to us. Martin Bureau: without that conversation with Leo, this thesis would not be possible. Thank you for your meticulous planning and detailed look at the world. You helped me see the details.

Thanks finally to the entire ATLAS^{3D} team, who I have been lucky enough to be

a part of. Maxime Bois, Frédéric Bournaud, Michele Cappellari, Roger Davies, P. Tim de Zeeuw, Pierre-Alain Duc, Eric Emsellem, Sadegh Khochfar, Davor Krajnović, Harald Kuntschner, Raffaella Morganti, Thorsten Naab, Tom Oosterloo, Marc Sarzi, Nic Scott, Paolo Serra and Anne-Marie Weijmans. Working with you all has enriched my own science, and I am so glad to have been able to work on such an exciting project with you all!

Finally I would like to thank my parents: Anne and Bruce Alatalo for always encouraging their budding scientist through frequent library trips and conversations with teachers, to proofreading this thesis. There were a million places that I could have diverted from this path. Thanks for helping me stay on it. To my boyfriend Glenn: you have been there for me through my entire tenure as a grad student despite studying 2500 miles away at Stony Brook. Thanks for being my ever-present rock.

My degree has been funded by the Berkeley Astronomy Department, the National Science Foundation (NSF) Graduate Fellowship, and through the NSF grant AST-0838258. My research was also supported in part by the National Aeronautics Space Administration (NASA) through *Chandra* Award Number 11700538 issued by the Chandra X-ray Observatory Center, which is operated by the Smithsonian Astrophysical Observatory for and on behalf of NASA under contract NAS8-03060. Research was finally also provided by NASA through grant number HST-GO-12526.01-A from the Space Telescope Science Institute, which is operated by AURA, Inc., under NASA contract NAS 5-26555.

Support for CARMA construction was derived from the Gordon and Betty Moore Foundation, the Kenneth T. and Eileen L. Norris Foundation, the James S. McDonnell Foundation, the Associates of the California Institute of Technology, the University of Chicago, the states of California, Illinois, and Maryland, and the National Science Foundation. Ongoing CARMA development and operations are supported by the National Science Foundation under a cooperative agreement, and by the CARMA partner universities. Based on observations carried out with the IRAM 30m Telescope. IRAM is supported by INSU/CNRS (France), MPG (Germany) and IGN (Spain). The Submillimeter Array is a joint project between the Smithsonian Astrophysical Observatory and the Academia Sinica Institute of Astronomy and Astrophysics and is funded by the Smithsonian Institution and the Academia Sinica. The National Radio Astronomy Observatory is a facility of the National Science Foundation operated under cooperative agreement by Associated Universities, Inc. Based on observations made with the NASA/ESA Hubble Space Telescope, which is operated by the Association of Universities for Research in Astronomy, Inc., under NASA contract NAS 5-26555. These observations are associated with program # 12526. This research has made use of data obtained from the Chandra Data Archive and the Chandra Source Catalog, and software provided by the Chandra X-ray Center (CXC) in the application packages CIAO, ChIPS, and Sherpa.

I acknowledge use of NASA/IPAC Extragalactic Database (NED), and the HyperLeda database (http://leda.univ-lyon1.fr).

Chapter 1

Introduction

1.1 Early-type galaxies and red-sequence galaxies

The bimodal morphological classification of galaxies has long been known (Fig. 1.1; Hubble 1926). Typical galaxies are either classified as "late-type" galaxies (LTGs), which are very thin disks, exhibit spiral structure, and exhibit blue colors or "early-type" galaxies (ETGs) tend to be more ellipsoidal, contain smoother isophotes, and red colors. The galaxy bimodality can be explained simply: a merger between two LTGs creates an ETG in simulation (Toomre & Toomre 1972; Springel, Di Matteo & Hernquist 2005). Faber et al. (2007) used the DEEP survey to show that galaxies also break into a bimodal distribution when plotted on a color-magnitude diagram. This bimodality is based primarily on the star formation properties of the individual galaxies. Star-forming galaxies (SFGs) are blue in color and span a large range of magnitudes, which is known as the "blue cloud". Red sequence galaxies (RSGs), on the other hand, inhabit a well defined region, with much smaller variations in color. (Figure 1.2). The "green valley" sits between the blue cloud and red sequence, and hosts transition objects. There is a dearth of green valley objects, which suggests the transition between being a SFG and a RSG is rapid. Just as in the case of morphological classification of galaxies, the color bimodality seen in galaxies can be explained simply, by quenching star formation. Once a SFG has had its star formation quenched, it quickly migrates from the blue cloud and becomes a RSG (Harker et al. 2006). The morphological and color properties of individual galaxies are mostly well-matched, with ETGs also being RSGs, and LTGs also being SFGs. This means that the processes of merging and quenching star formation are well-connected.

Figure 1.3 represents the separate RSG/ETG classifications for galaxies in the form of a Venn diagram. Despite the overwhelming overlap between RSGs and ETGs, outliers do exist. On one side, there are passive disk galaxies, explained in detail by both Bundy et al. (2010) and Masters et al. (2010) as objects that have ceased star formation. On the other side, there are blue, starforming ETGs, which are the focus of this thesis, and detailed below.

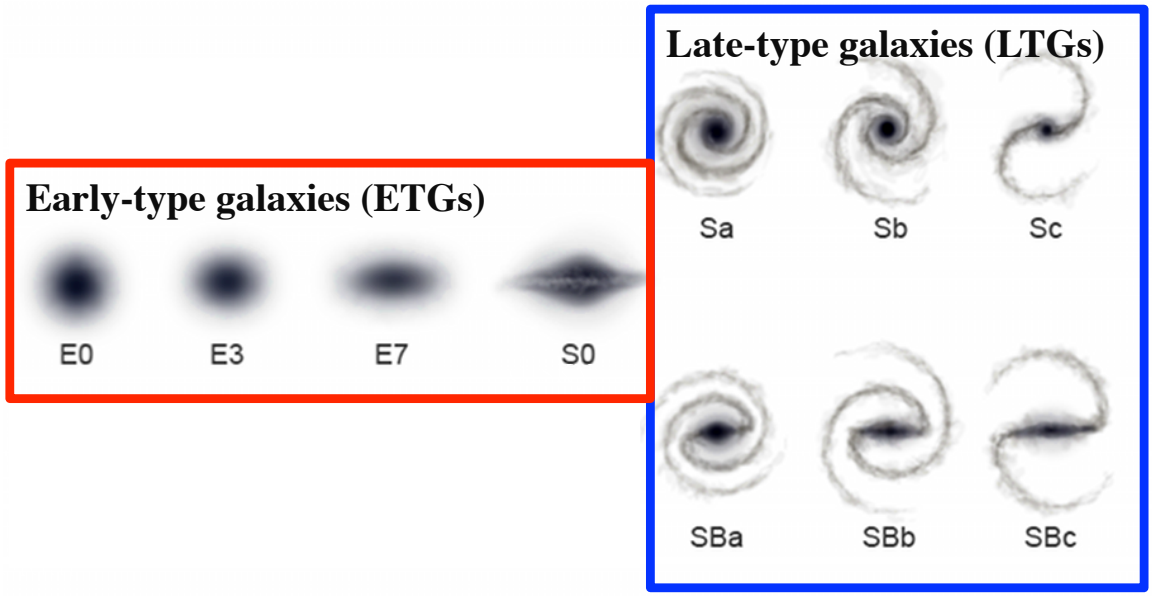

Figure 1.1 The well known Hubble sequence of galaxies is shown, overlaid with their morphological classification. The tuning fork sequence includes early-type (ETG) and late-type galaxies (LTGs). "Typical" LTGs are disky, contain spiral structure, and are blue in color and starforming. "Typical" ETGs have smooth light profiles, are red in color and quiescent. ETGs also come in two types: lenticular (or S0) galaxies, which are disky but lack spiral structure, and elliptical, which have ellipsoidal light profiles. Image Credit: Ville Koistinen

1.2 A census of molecular gas in early-type galaxies

The origin of early-type galaxies is a major area of study in galaxy evolution. Stellar populations in these galaxies are generally termed "red and dead," and the primordial gas is severely depleted. Recent observations have shown that many of the original SAURON galaxies (about 20%) show evidence of recent star formation as well as gas reservoirs (Combes, Young & Bureau 2007; Shapiro et al. 2010). The SAURON project studied 48 nearby early-type galaxies with a wide field spectrograph placed on the William Herschel telescope (WHT). SAURON found evidence for a vast variety of structures occurring in early type galaxies, including many that hinted at complicated merger histories (Emsellem et al. 2004). The ATLAS^{3D} collaboration is an extension of the original SAURON survey, which increases the sample from 48 to 260 galaxies, and provides multiwavelength information.

ATLAS^{3D} is a complete volume-limited survey of 260 ellipticals and lenticulars within 42 Mpc that provides the best constraints on dynamics and stellar populations, and thus the formation and evolution of early-type galaxies at $z = 0$ through multi-wavelength studies (see Cappellari et al. 2011a). The survey provides optical integral-field spec-

troscopy over the central $41'' \times 33''$ region of each galaxy, giving maps of the density and kinematics of the ionized gas and stars, as well as stellar ages, metallicities and α-element

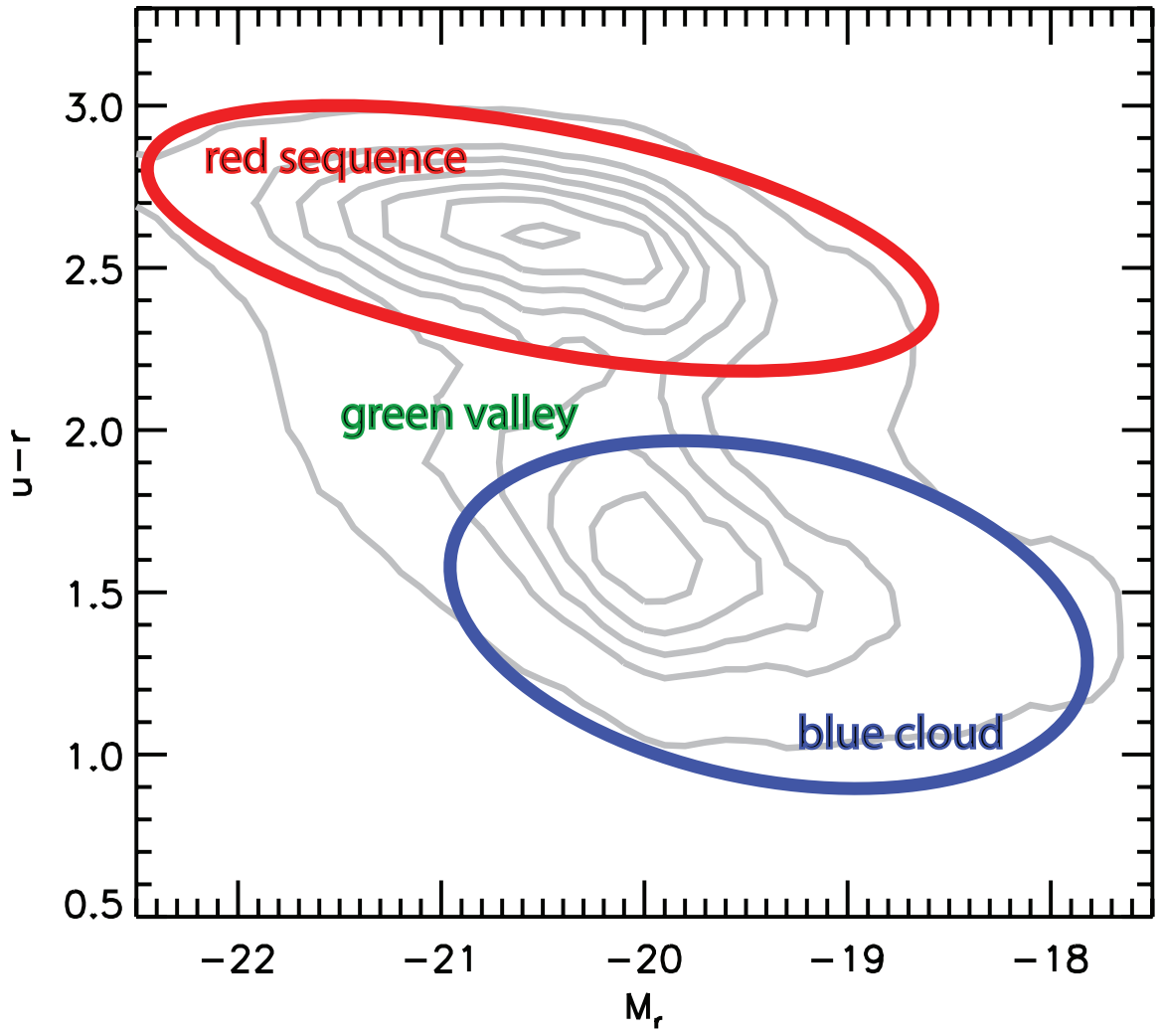

Figure 1.2 The color-magnitude diagram of all SDSS galaxies below $z \approx 0.1$. The three main galaxy evolutionary phases are labeled. The "red sequence" located at the top of the distribution, includes a narrow range of colors, has higher average mass than the rest of the distribution, and tends to represent quiescent galaxies. The "blue cloud," located in the lower right-hand corner in the distribution, represents lower masses and bluer colors. The blue cloud has more scatter in color than the red sequence, and tends to represent blue, starforming galaxies. The "green valley" sits between the red sequence and the blue cloud, and is underpopulated with galaxies. Its galaxies are thought to be the transition between the two phases seen in the distribution. The dearth of green valley galaxies is thought to be due to the rapidity of the transition from one phase to another.

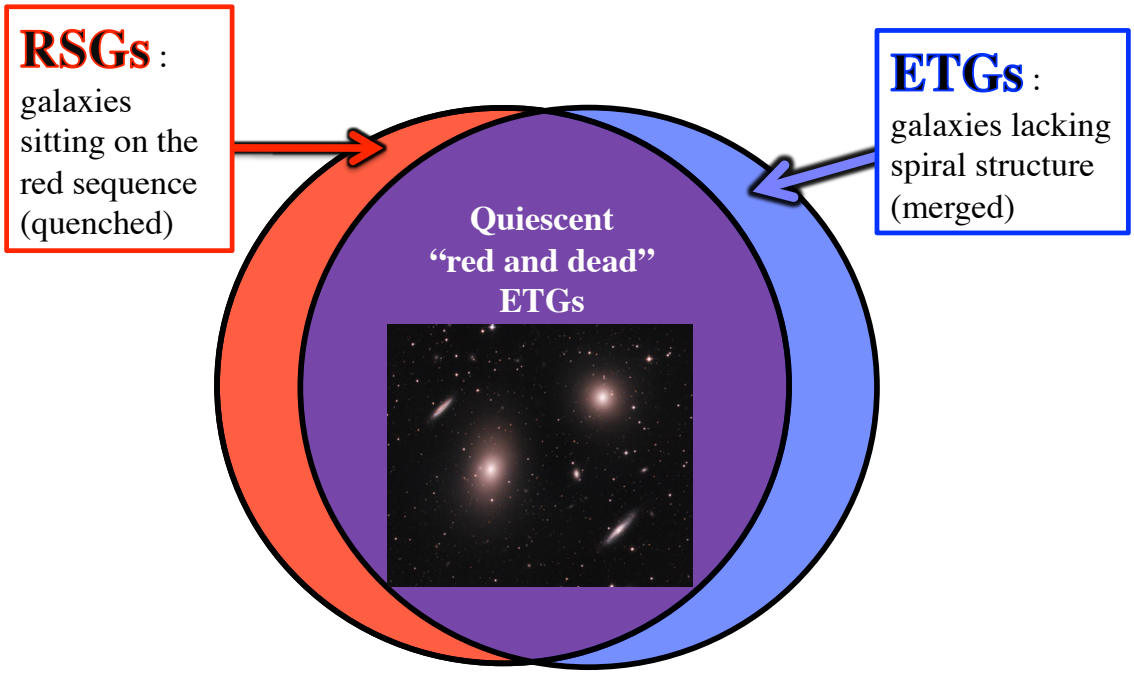

Figure 1.3 The Venn diagram shows the significant overlap that exists between ETGs and RSGs. The vast majority of ETGs are also RSGs. In order to understand this population, understanding the outliers is also important: passive spiral galaxies as well as the blue ETGs. Blue ETGs are discussed in a lot more detail in this thesis.

abundances. This is ideal for identifying kinematic subcomponents (e.g. cold inner disks and kinematically decoupled cores, KDCs; Krajnović et al. 2011), and recent star formation (Kuntschner et al. 2006; Sarzi et al. 2006). These properties can then be compared with the atomic and molecular gas content of the galaxies through our H I from the Westerbork Synthesis Radio Telescope (WSRT) (Serra et al. 2012) and CO observations (Young et al. 2011). The galaxies' formation histories are imprinted in their structures, and with the existing ATLAS^{3D} N-body, hydro, and semi-analytic simulations of galaxy formation (Bois et al. 2011; Khochfar et al. 2011; Lablanche et al. 2012), we are using these datasets to infer the detailed formation histories of a complete sample of early-type galaxies.

All ATLAS^{3D} galaxies were observed for CO with the IRAM 30m at Pico Veleta and 60/260 (23%) were detected at a 3σ flux limit of 3 mK T_a^*, reliably showing that even normal E/S0s can have substantial molecular gas. This single-dish work constitutes by far the best survey of molecular gas in early-type galaxies to date, with new results such as the detection rate being independent of galaxy mass and Virgo Cluster membership (environment), but dependent on stellar kinematics (Young et al. 2011).

The true power of the integral-field/CO synergy however lies with having optical and CO maps of comparable spatial resolution. Interferometric work from the Berkeley-

Illinois-Maryland Array (BIMA) and the Plateau de Bure Interferometer (PdBI) of 10 galaxies (e.g. Young, Bureau & Cappellari 2008; Crocker et al. 2008, 2009, 2011) shows that CO traces nascent decoupled stellar disks, indicating a direct connection between young stars and cold gas. The molecular gas often exhibits kinematic misalignments with respect to the stars, implying complex SF and mass assembly histories and tightly constraining the origin of the cold gas. However, in order to unravel the formation histories of early-type galaxies and gain a proper quantitative understanding of the role of cold gas in their evolution, we need a complete statistical sample to combat small number statistics.

Firstly, CO maps provide a statistically robust census of the molecular gas content and distribution in ETGs. They will reveal how often the gas is relaxed or disturbed (with direct consequences for the mass assembly history), how prevalent molecular spiral arms/rings/bars/disks are, and whether specific structures correlate with environment, the presence of an AGN, or H I gas.

Secondly, by simply comparing the angular momenta of the molecular gas and stars, stringent constraints on the origin of the gas can be placed, bearing directly on the importance of dissipation, and thus on the migration of ETGs to/from the red sequence. Combining CO data with the ionized gas and H I data probes the relationships between these three phases, answering questions such as whether they share the same origin, whether the gas cycles between them, how much of the Balmer emission is SF-driven, etc.

Thirdly, by comparing CO with SAURON stellar/ionized-gas maps, we are able to literally map the relationship of the cold gas to different stellar populations and gas ionization processes. Our census reveals where, when, how, and why the molecular gas turns into stars, and on what timescale it gets depleted and replenished. Using the gas surface densities and the galaxies' rotation curves (from ionized gas and/or stellar kinematics), we can test the standard spiral galaxy SF laws in a new regime (Toomre's instability criterion, Schmidt-Kennicutt relations, etc). Multiple spatially-resolved tests are necessary before we can fully understand the molecular gas evolution and regulation of SF.

Finally, a large volume-limited survey is able to shed light on the unexpected, evidenced by the detection of an AGN-driven massive molecular outflow in a seemingly quiescent early-type galaxy, NGC 1266.

1.3 NGC 1266: a massive AGN-driven molecular outflow

The present-day galaxy population has a bimodal color distribution, with a genuine decrement of green valley galaxies (e.g., Fig. 1.2; Strateva et al. 2001; Baldry et al. 2004). This dearth of green valley galaxies, coupled with the increase in quiescent red galaxies since $z \sim 1$, implies that galaxies quench star formation (SF) and transition rapidly from blue to red optical colors (e.g., Bell et al. 2004; Faber et al. 2007). However,

it is unclear to what degree AGN feedback (e.g., Springel, Di Matteo & Hernquist 2005; Hopkins et al. 2005; Croton et al. 2006) is responsible. There is circumstantial evidence to support AGN-driven SF quenching—e.g., Schawinski et al. (2007) have found that AGN are predominantly found in green valley galaxies—but direct evidence (e.g. a galaxy where the AGN is clearly responsible for the rapid expulsion of all starforming material) is lacking. There are some promising candidates for powerful AGN feedback at $z \sim 2$ (e.g., Nesvadba et al. 2008), but only limited information can be obtained for such distant objects. Markarian 231 has also recently been shown to host high velocity outflows in molecular gas (Feruglio et al. 2010; Fischer et al. 2010), and evidence is mounting that quasars might commonly host these phenomena (Nesvadba et al. 2011), but quasars are rare occurrences and tend to be far away, limiting the total information we are able to obtain. It is therefore highly desirable to identify and study local examples of AGN feedback in action. Recent millimeter observations of the nearby field lenticular galaxy NGC 1266 show that it harbors a massive, AGN-driven molecular outflow, providing an excellent local laboratory for studying AGN-driven SF quenching.

Although NGC 1266 is an ordinary-looking lenticular galaxy in the local Universe ($D = 29.9$ Mpc), it harbors a surprisingly large amount of CO emission (Young et al. 2011; Alatalo et al. 2011). CARMA and SMA measurements suggest that $\sim 10^9$ $M_\odot$ of molecular gas is contained within the central 100 pc of this galaxy and that a non-negligible amount of this gas is involved in a massive outflow ($M_{\rm out} \sim 10^7 - 10^8\,M_\odot$), with maximum velocities in excess of the escape velocity of the galaxy, and 2.5% of the outflowing molecular gas already exceeding the central escape velocity of the galaxy, $v_{\rm esc}$.

The case for a central AGN in the heart of NGC 1266 is supported in multiple observing regimes. The 5 GHz Very Large Array (VLA) radio continuum data reveal a compact, unresolved ($\lesssim 60$ pc) core, which alone is a good AGN indicator (Ho 2008). Since compact nuclear starbursts are limited to $T_{\rm b} \lesssim 10^5$ K (Condon et al. 1991), the detection of a high brightness temperature radio core beyond this limit is generally considered strong evidence for accretion onto a black hole. Very Long Baseline Array (VLBA) observations presented in this thesis of NGC 1266 have revealed compact emission with a brightness temperature $T_{\rm b} > 6.7 \times 10^6$ K, confirming the presence of an AGN. The *Chandra* data reveal a hard X-ray core ($L_{\rm X}$=10^{39} ergs s^{-1}), approximately coincident with the 5 GHz radio core. In the mid-IR, NGC 1266 has the hottest dust temperature ($f_{70}/f_{160} = 1.1$; Dale et al. 2007) and highest $L_{\rm TIR}/L_{\rm UV}$ ratio of any galaxy in the Spitzer Infrared Nearby Galaxy Survey (SINGS) sample (Dale et al. 2007). Such high-temperature dust is usually attributed to AGN heating, since photons from a starforming region are not sufficiently energetic. Optically, NGC 1266 is classified as a low-ionization nuclear emission region (LINER) (Moustakas & Kennicutt 2006) with a black hole of mass $M_{\rm bh} \approx 2.8 \times 10^6\ M_\odot$ according to the $M_{\rm bh}$–σ_c relation (Gebhardt et al. 2000).

The velocity structure of the molecular gas emission breaks into three separate components: a compact circumnuclear core at the systemic velocity ($v_{\rm sys}$) of the galaxy, plus two high velocity lobes redshifted and blueshifted by ~ 400 km s^{-1} from $v_{\rm sys}$. SAURON

and Gemini GMOS integral field spectra further detected ionized gas in Hα, Hβ, [OIII], [SII], [NII] and [NI] with similar velocity profiles and a conical spatial structure with the observed outflowing molecular gas at its base. Recent VLA observations have shown the presence of H I absorption with the same spectral shape as the blueshifted CO emission (Alatalo et al. 2011). Furthermore, the radio continuum and X-ray data show evidence of bow shocks where the outflow is encountering the ISM. Finally, optical imaging shows an obscuration cone matching the shape and structure of the outflow and originating at the location of the AGN. The cone structure is potentially a result of dust entrained with the outflowing material, similar to what is seen in NGC 3079 (Cecil et al. 2001).

NGC 1266 is the only early-type, non-interacting galaxy found to host a molecular outflow. Other local galaxies with molecular outflows (e.g., M51, M82, Arp 220 and Mrk 231) have mass loss rates comparable to their SF rates (Matsushita, Muller & Lim 2007; Walter, Weiss & Scoville 2002; Sakamoto et al. 2009; Feruglio et al. 2010). Models of SF-driven feedback from momentum coupling (Murray et al. 2005) naturally produce such a relationship between the SF rate (SFR) and the outflow rate. However, the SFR in NGC 1266 falls short. The SFR of NGC 1266 is at least a factor of four less than the lower limit of the molecular gas outflow rate, and could be as much as two orders of magnitude too small, depending on the $L_{\rm CO} - {\rm H_2}$ conversion factor that applies. In NGC 1266, the momentum of the outflow is much larger than what can be produced by radiation pressure and stellar winds. The outflow must be powered by a different energy source and driven by a different physical mechanism. The mechanical energy available in the emerging radio bubble in NGC 1266 (Bîrzan et al. 2008) is sufficient to drive the outflow, meaning that the AGN is the likely culprit.

Poststarburst galaxies (i.e., K+A and E+A galaxies, Dressler & Gunn 1986; Quintero et al. 2004) contain evidence of having undergone rapid cessation of star formation, with young stellar populations indicated in their absorption features, but a lack of current star formation, usually through the lack of ionized gas emission (Hα or [O II]; Yan et al. 2006). Poststarburst galaxies are more likely to be found within the green valley of the color-magnitude diagram, and are therefore considered to be a key to how the cessation of star formation is able to transition galaxies from star forming to quiescent. Poststarburst quasars are found to have two morphological classes: merger remnants and undisturbed. The poststarburst galaxies with merger remnant morphologies have a clear triggering mechanism: the merger itself. The second group of undisturbed galaxies is harder to explain, but some of the most common explanations are strangulation (in which a galaxy falls into a cluster environment; Evrard 1991; Fujita 1998; Bekki et al. 2002; Boselli & Gavazzi 2006), harassment (where companions gravitationally interact with the galaxy without a complete merger; Icke 1985; Mihos 1995; Bekki 1998; Moore et al. 1996) and morphological quenching (in which the gravitational potential within a bulge-dominated system allows its molecular gas to be more stable against gravitational collapse; Martig et al. 2009.) The first two suggestions require a cluster environment. Understanding the mechanism most responsible for the undisturbed population of poststarburst galaxies will

bolster our understanding of the ways in which galaxies transition to quiescent galaxies.

NGC 1266 seems to have been caught in a remarkable time in its evolution, having been observed in the period where it was actively expelling its molecular gas, and therefore actively transitioning to a poststarburst system, and finally to an ETG, without the telltale signs of having undergone a significant merger in the recent past. Understanding the triggering mechanism responsible for NGC 1266 will likely provide a wealth of information on the undisturbed poststarburst population, allowing us to identify processes other than mergers that allow galaxies to transition to the red sequence.

This thesis is primarily concerned with investigating the relationship between molecular gas and the evolution of galaxies, studying both how molecular gas sustains itself in a population of early-type galaxies as well as studying the remarkable case study of NGC 1266, a galaxy that has been caught in a violent snapshot of its evolution from a blue starforming galaxy to a red quiescent galaxy.

In Chapter 2, I detail the CARMA ATLAS^{3D} survey, a CO imaging survey of 30 ETGs, originally detected in CO with the IRAM 30m (Young et al. 2011), and identifying their morphologies and how that relates to their environments and stellar photometric properties. In Chapter 3, I focus on the discovery of an AGN-driven molecular outflow in the quiescent galaxy, NGC 1266, detected serendipitously within the ATLAS^{3D} survey, and shown through CARMA and SMA observations to host a large amount of molecular gas, that will be exhausted from the system in $\lesssim 100$ Myr. In Chapter 4, I further detail NGC 1266, confirming the presence of an AGN via a radio continuum detection from the VLBA, as well as use photometry from the HST to put the galaxy into the context of galaxy evolution. In Chapter 5, I present my conclusions and lay out directions for future work.

Chapter 2

The CARMA ATLAS^{3D} Survey

Abstract

We present the Combined Array for Research in Millimeter Astronomy ATLAS^{3D} molecular gas imaging survey, a systematic study of the distribution and kinematics of molecular gas in CO-rich early-type galaxies. Our Combined Array for Research in Millimeter Astronomy sample of early-type galaxies consists of 30 ATLAS^{3D} galaxies previously detected in ^{12}CO(1–0) by the Institut de Radioastronomie Millimétrique 30m telescope. We combine these interferometric data with those of 10 additional ATLAS^{3D} galaxies from the literature. Our full sample of 40 CO-rich early-type galaxies is complete to a ^{12}CO(1–0) integrated flux of 18.5 Jy km s^{-1} and represents the largest, best-studied sample of molecular gas in early-type galaxies to date. A comparison of the CO distribution of each galaxy to an unsharp-masked g-band dust image shows that the molecular gas and dust distributions are in good agreement and trace the same underlying interstellar medium. The Combined Array for Research in Millimeter Astronomy ATLAS^{3D} galaxies exhibit a variety of CO morphologies, including discs (50%), rings (15%), bars+rings (10%), spiral arms (5%), and mildly (12.5%) and strongly (7.5%) disrupted morphologies. There appear to be weak trends between galaxy mass and CO morphology, whereby the most massive galaxies in the sample tend to have molecular gas in a disc configuration. We derive a lower limit to the total accreted molecular gas mass across the Combined Array for Research in Millimeter Astronomy ATLAS^{3D} sample of 2.48×10^{10} $M_{\odot}$, or approximately 8.3×10^{8} $M_{\odot}$ per minor merger within the sample.

2.1 Introduction

The bimodality in the morphological classification of galaxies has long been known (Hubble 1926). Late-type galaxies (LTGs) typically have exponential discs, spiral structure and blue colours. Early-type galaxies (ETGs) are more ellipsoidal, with smoother

isophotes and red colours. One scenario for producing this galaxy bimodality is via mergers. Simulations have shown that a merger between two LTGs often can create an ETG (Toomre & Toomre 1972; Springel, Di Matteo & Hernquist 2005). ETGs are also much more likely to be found on the "red sequence" portion of the color-magnitude diagram (CMD; Baldry et al. 2004; Faber et al. 2007), presumably due to the loss of most of their star-forming material.

ETGs have been shown to be deficient in star formation relative to LTGs (Visvanathan & Sandage 1977; Bower et al. 1992), and therefore should be molecular and atomic gas-poor (Lees et al. 1991). Recently, it has however become clear that they are not devoid of cold gas, containing reservoirs of dust (e.g. Hawarden et al. 1981; Jura 1986; Knapp et al. 1989), neutral atomic gas (e.g. Knapp et al. 1985; Sage & Welch 2006; Oosterloo et al. 2010) and molecular gas (e.g. Sage & Wrobel 1989; Welch & Sage 2003; Combes, Young & Bureau 2007).

The ATLAS^{3D} sample is a complete, volume-limited survey of 260 local ETGs brighter than $M_K = -21.5$, covering distances to 42 Mpc with some restrictions on declination and Galactic latitude (Cappellari et al. 2011a). The survey was designed to help us understand ETG formation and evolution. Optical integral-field spectroscopy with `SAURON` on the William Herschel Telescope (WHT) has been obtained over the central $41'' \times 33''$ region of all ATLAS^{3D} galaxies, revealing their internal stellar kinematics, stellar population properties and ionized gas distributions and kinematics. The ATLAS^{3D} sample has also been completely observed in CO J=1–0 and J=2–1 with the Institut de Radioastronomie Millimétrique (IRAM) 30m telescope (Young et al. 2011), and 65% of the sample has been observed in H I with the Westerbork Synthesis Radio Telescope (WSRT; Morganti et al. 2006; Oosterloo et al. 2010; Serra et al. 2012). For studies of the cold and warm interstellar medium (ISM), the ATLAS^{3D} sample is thus one of the largest and best-observed samples of local ETGs available.

Of the 260 ETGs in the ATLAS^{3D} sample, 56 were detected in CO (22% detection rate; Young et al. 2011). However, despite emerging evidence that a non-negligible fraction of ETGs contain molecular gas, little is known about its origin and evolution, although various scenarios have been put forth (see e.g. Davis et al. 2011b). The three most prominent scenarios are outlined here. First, it is possible that the gas survived the galaxy's transformation into an ETG and was not completely consumed subsequently through secular evolution. Second, the molecular gas may have accumulated internally through stellar mass loss (Faber & Gallagher 1976). In the ATLAS^{3D} sample, it is expected that each galaxy produces on average 0.1 $M_\odot$ yr^{-1} of ISM through mass loss from the old stellar population alone (Ciotti et al. 1991). Third, it is possible that the molecular gas was accreted from an external source, through tidal stripping events, cold accretion and/or minor mergers with gas-rich companions. The minor merger (1:4–1:10 mass ratios) rate calculated by Lotz et al. (2008, 2011) suggests that there are approximately 0.12 minor mergers per galaxy per Gyr, so the ETGs of the ATLAS^{3D} sample as a whole should have undergone a total of ≈ 30 minor mergers in the last Gyr. It is also possible that this

molecular gas is leftover from major mergers that have taken place, but minor mergers dominate in number. Determining the origin of the molecular gas therefore requires a detailed analysis of its distribution and kinematics (e.g. angular momentum), only available from interferometric maps, and a comparison to the stellar kinematics (as done in Davis et al. 2011b).

How the properties of the molecular gas depend on the environment of the host galaxy is an open question. For instance, galaxies in clusters may well be unable to acquire cold external gas, specifically atomic hydrogen (H I), due to the presence of the hot intracluster medium (ICM) and associated ram pressure stripping (Cayatte et al. 1990; Böhringer et al. 1994; Davis et al. 2011b). A first effort towards studying the molecular gas properties of ETGs with multiple molecular transitions (including ^{13}CO, HCN and HCO$^+$, in addition to ^{12}CO, Crocker et al. 2012) shows that the molecular gas properties widely vary amoung ETGs, probably due to optical thickness variations within ^{12}CO linked to the dynamical state of the gas.

It is also not well determined whether the properties of individual galaxies are the determining factors in the behavior of the molecular gas, or whether the molecular gas in ETGs follows the same star-formation relations as in spirals (e.g. Kennicutt 1998; Bigiel et al. 2008; Shapiro et al. 2010; Wei et al. 2010a; Crocker et al. 2011). Recent studies of star formation in ETGs appear to indicate that it does, but these were done using small carefully selected samples, rather than large unbiased samples. To completely understand star formation in ETGs, it is vital to study an unbiased sample of resolved molecular gas within them. Therefore, as part of the ATLAS^{3D} project we performed the present imaging survey with the Combined Array for Research in Millimeter Astronomy (CARMA), which is the first of its kind, capable of providing significant conclusions about the state of molecular gas in ordinary ETGs from interferometric imaging.

In §2.2, we describe the selection criteria used to define the CARMA sample. In §2.3, we describe the observational strategy, the data calibration and reduction, and the analysis techniques. In §2.4, we investigate the properties of the molecular gas in the sample, including the range of morphologies represented, and their relationships to other properties of the host galaxies. We conclude briefly in §2.5. Appendix A.1 describes the CO data of individual galaxies in the CARMA ATLAS^{3D} sample. Appendix A.2 presents literature data of ATLAS^{3D} galaxies which will be included in the official data release in a uniform manner.

2.2 The CARMA sample

The sample of ETGs chosen for the CARMA survey was extracted from from the ATLAS^{3D} survey. All ATLAS^{3D} galaxies were observed with the IRAM 30m telescope in CO(1–0) and CO(2–1), mostly by Combes, Young & Bureau (2007) and Young et al. (2011), though a few were observed by Welch & Sage (2003). The CARMA sample consists of 30 of the CO-detected ATLAS^{3D} galaxies. NGC 2697 and NGC 4292, removed from

the ATLAS^{3D} sample because of evidence of spiral structure in the stellar isophotes and of a lack of SAURON data, respectively, were also already imaged with CARMA. We present their maps in Appendix A.3, but will not use them in any statistical work discussed in §2.4.

Including 10 CO-detected sample galaxies that have already been interferometrically-mapped (see §2.3.5), the sample of imaged CO-detected ATLAS^{3D} galaxies is complete for the 34 brightest objects, down to an integrated CO(1–0) flux limit of 18.5 Jy km s^{-1}(corresponding to the flux of NGC 3182). Two galaxies with fluxes below this threshold also have CARMA CO images, UGC 05408 and NGC 5173. Five other CO-faint galaxies have CO maps in the literature (i.e. NGC 4550 by Crocker et al. 2009; NGC 2768, NGC 4477 and NGC 3489 by Crocker et al. 2011; NGC 2685 by Schinnerer & Scoville 2002). Including the literature galaxies, the total number of ATLAS^{3D} galaxies discussed in this paper is 40. The faintest detections from Young et al. (2011) were not observed due to observing time restrictions.

Objects in the CARMA ATLAS^{3D} sample have total absolute K-band magnitudes ranging from $M_K = -21.57$ to -25.09, and distances from 13.4 Mpc to 45.8 Mpc[1]. Six of the 30 galaxies belong to the Virgo cluster. All galaxies but three (IC 719, NGC 1222 and NGC 7465) are regular rotators, according to their stellar kinematics (Krajnović et al. 2011, hereafter Paper II). NGC 1222, classified as a non-regular rotator, is known to be undergoing a strong interaction with a neighbor. NGC 7465 is undergoing an interaction with NGC 7464 and NGC 7463, and has a kinematically decoupled core. IC 719 does show ordered rotation in its stellar component, but is recognized as a 2σ (double-peaked) galaxy, indicating two counter-rotating stellar discs, when the velocity dispersion map is considered. Further properties of the sample galaxies are listed in Table 2.1.

2.3 Observations, Calibration and Data Reduction

2.3.1 CARMA observations

Observations for this survey were taken in the ^{12}CO(1–0) line at CARMA over the course of five semesters, beginning in Autumn 2008 and finishing in November 2010. Galaxies were always first observed with the CARMA D–array, with 11–150m baselines, corresponding to observable angular scales of 3.5″– 48″ at CO(1–0). NGC 2697 and NGC 7465, that appeared to have significant flux resolved out, were then followed up with the lower resolution E–array (8–66m baselines). NGC 1266 was spatially unresolved in D-array, and was followed up with the CARMA B and A arrays (a detailed discussion of NGC 1266 can be found in Alatalo et al. 2011). The CARMA ATLAS^{3D} survey had surface brightness sensitivity (in 100 km s^{-1} linewidth) ranging between 1.2 and 99

[1]UGC 05408 was kept in the ATLAS^{3D} survey because its estimated distance is still within 42 Mpc, when errors in the distance estimate are taken into account (Cappellari et al. 2011a)

Table 2.1 CARMA ATLAS^{3D} galaxy sample.

Name	α (J2000)	δ (J2000)	v_{sys} (km s^{-1})	i (deg)	ϕ_{mol} (deg)	d (Mpc)	Virgo Membership
IC 676	11 12 39.84	+09 03 20.7	1429	69	16.5	24.6	0
IC 719	11 40 18.52	+09 00 35.6	1833	74	229.0	29.4	0
IC 1024	14 31 27.07	+03 00 30.0	1479	72	24.5	24.2	0
NGC 1222	03 08 56.76	−02 57 19.3	2422	41	33.0[c]	33.3	0
NGC 1266	03 16 00.79	−02 25 38.6	2170	26	270	29.9	0
NGC 2764	09 08 17.44	+21 26 35.8	2706	65	202.5	39.6	0
NGC 2824	09 19 02.22	+26 16 12.3	2758	61	161.5	40.7	0
NGC 3182	10 19 33.02	+58 12 21.0	2118	35	331.5	34.0	0
NGC 3607	11 16 54.54	+18 03 07.1	942	34	302.5	22.2	0
NGC 3619	11 19 21.60	+57 45 28.3	1560	48	74.5	26.8	0
NGC 3626	11 20 03.78	+18 21 25.6	1486	67	169.5	19.5	0
NGC 3665	11 24 43.64	+38 45 46.2	2069	64	219.5	33.1	0
NGC 4119	12 08 09.60	+10 22 44.7	1656	69	296.0	16.5	1
NGC 4150	12 10 33.65	+30 24 05.5	208	54	146.0	13.4	0
NGC 4324	12 23 06.17	+05 15 02.8	1665	62	232.0	16.5	1
NGC 4429	12 27 26.56	+11 06 27.3	1104	68	82.0	16.5	1
NGC 4435	12 27 40.49	+13 04 44.3	791	52	201.0	16.7	1
NGC 4694	12 48 15.10	+10 59 01.3	1171	69	155.5	16.5	1
NGC 4710	12 49 39.36	+15 10 11.7	1102	86	207.0	16.5	1
NGC 4753	12 52 22.07	−01 11 57.9	1163	75	93.0	22.9	0
NGC 5173	13 28 25.29	+46 35 29.9	2424	24	100[c]	38.4	0
NGC 5379	13 55 34.35	+59 44 34.3	1774	64	66	30.0	0
NGC 5866	15 06 29.60	+55 45 48.0	755	89	127	14.9	0
NGC 6014	15 55 57.39	+05 55 54.7	2381	22	139.5	35.8	0
NGC 7465	23 02 00.96	+15 57 53.3	1960	70	106.0	29.3	0
PGC 029321	10 05 51.18	+12 57 40.7	2816	38	76	40.9	0
PGC 058114	16 26 04.29	+02 54 23.6	1507	71	94.5	23.8	0
UGC 05408	10 03 51.86	+59 26 10.2	2998	31	315[c]	45.8	0
UGC 06176	11 07 24.68	+21 39 25.6	2677	68	201.0	40.1	0
UGC 09519	14 46 21.12	+34 22 14.2	1631	41	177.5	27.6	0
NGC 2697[a]	08 54 59.40	−02 59 15.2	1814[b]	30	301.5	22.0	0
NGC 4292[a]	12 21 16.49	+04 35 44.3	2258[b]	50	230	29.8	0

[a] Removed from the ATLAS^{3D} sample, but the CO data are presented in Appendix A.3.
[b] From the `HYPERLEDA` catalog, due to the absence of `SAURON` data.
[c] Not originally in citetdavis+11a.

Notes:
Column (1): The name is the principle designation from LEDA, which is used as the standard designation.
Column (2): The right ascension (J2000) of each galaxy from LEDA.
Column (3): The declination (J2000) of each galaxy from LEDA.
Column (4): Optical stellar heliocentric velocity, from Cappellari et al. (2011a).
Column (5): Best-determined CO inclination angle, from Davis et al. (2011a).
Column (6): Kinematic position angle of the molecular gas, from Davis et al. (2011b).
Column (7): Average distance to each galaxy, from Cappellari et al. (2011a), originally from Tonry et al. (2001) and Mei et al. (2007).
Column (8): Virgo membership of each galaxy, from Cappellari et al. (2011a).

$M_\odot$ pc^{-2}, with median sensitivity of 16 $M_\odot$ pc^{-2}. On average, ≈100 hours of observations were obtained each semester. Observational parameters are listed in Table 2.2.

Upgrades to the CARMA correlator and receivers were taking place while the ATLAS^{3D} survey was ongoing, so data taken later in the programme have larger bandwidths and simultaneous observations of ^{12}CO(1–0) and ^{13}CO(1–0). A handful of ATLAS^{3D} galaxies thus also have ^{13}CO detections, which will be presented in an upcoming paper. The galaxies with large line widths were observed only after the CARMA correlator was upgraded, providing sufficient bandwidth and channel resolution to properly cover and sample the line. We were able to reliably image 3mm continuum in three sources (NGC 1266, NGC 3665 and NGC 5866), and Table 2.2 lists those fluxes as well as upper limits for the other galaxies.

2.3.2 Calibration and imaging

Raw CARMA visibility data were reduced in the usual way, using the Multichannel Image Reconstruction Image Analysis and Display (`MIRIAD`) package (Sault et al. 1995). For each source and track, raw data were first Hanning-smoothed in velocity. Then the phase vs. time behaviour of the calibrator was checked to search for decorrelations over baselines, which were flagged out. Next, the data were corrected for differences in the lengths of the fiber optic lines between the antennas and the correlator. The bandpass was then determined using a high signal-to-noise ratio (S/N) observation of a bright calibrator, and used to correct for instrumental spectral fluctuations. The atmospheric phase offsets present in the data were determined using a phase calibrator, usually a quasar within 20° of the source. Amplitude calibration was performed using the phase calibrator. A catalog of the most up-to-date fluxes of each calibrator is maintained at CARMA both through monitoring of calibrator fluxes in science tracks as well as dedicated flux calibration tracks taken on a weekly basis, updated weekly using all tracks that include a primary calibrator (e.g. a planet), which is used to infer the fluxes of the secondary calibrators present (Bauermeister et al., in prep). Flux calibration uncertainties are assumed to be 20%, which is standard for millimeter observations from planetary models (Petric et al., in prep). Any errant large fluctuations in phase of the phase calibrator were also flagged. After the data were satisfactorily processed, the gain solutions derived from the nearby calibrator were applied to the source. The calibrated source data of all observations of each source were then combined into one visibility file for imaging.

We then used `MIRIAD` to convert all visibility files to three-dimensional (3D) data cubes. When possible, a zeroth order continuum fit to the *uv*-data was made using channels uncontaminated by line emission, and subtracted from all channels. Only galaxies observed after the correlator was upgraded (bandwidth $>$ 420 km s^{-1}) had sufficient bandwidth for a reliable continuum fit. Galaxies with narrower bandwidths were not continuum-subtracted (continuum emission generally adds $<$ 10% extra flux to each galaxy, much less than the total flux calibration uncertainties). The continuum-subtracted

Table 2.2 Observational parameters of CARMA galaxies

Name		Semester	Gain Calibrator	Total Hours	$\theta_{\rm maj} \times \theta_{\rm min}$ (arcsec)	ΔV (km s^{-1})	BW (km s^{-1})
IC	676	2009B	1058+015	3.75	3.8×3.3	10	410
IC	719	2010A	3C273	13.17	3.9×2.8	20	580
IC	1024	2008B	3C279	4.68	3.9×3.0	10	420
NGC	1222	2008B	0339-017	5.20	3.6×3.2	5	420
NGC	1266	2008B	0339-017	5.43	4.2×3.3	10	410
NGC	2764	2009B	0854+201	4.43	3.5×2.9	10	410
NGC	2824	2008B	0956+252	8.79	4.3×4.0	25	400
NGC	3182	2009A	0927+390	7.42	5.2×4.1	30	390
NGC	3607	2010B	1058+015	9.30	5.6×5.0	20	900
NGC	3619	2010B	0958+655	24.44	4.4×3.9	40	880
NGC	3626	2009B	1159+292	7.50	3.9×3.7	25	400
NGC	3665	2010B	1159+292	16.59	4.3×4.2	10	910
NGC	4119	2008B	3C273	3.67	5.0×4.0	10	410
NGC	4150	2010A	1159+292	6.74	5.3×4.1	10	560
NGC	4324	2009A	3C273	20.18	4.7×3.9	20	400
NGC	4429	2010B	3C273	8.83	4.7×3.7	10	840
NGC	4435	2010B	3C273	8.48	3.9×3.4	10	920
NGC	4694	2010A	3C273	5.38	3.9×3.1	10	390
NGC	4710	2009A	3C273	5.10	3.9×3.2	10	410
NGC	4753	2010B	3C273	10.38	5.6×4.1	15	735
NGC	5173	2009B[a]	1310+323	7.06	3.9×3.5	20	240
NGC	5379	2010A	1642+689	5.33	5.2×3.6	10	410
NGC	5866	2010B	1419+543	3.52	3.6×3.1	10	920
NGC	6014	2008B	1751+096	3.85	4.2×3.9	10	350
NGC	7465	2008B 2009A[b]	3C454.3	15.02	6.6×5.6	10	410
PGC	029321	2009B	1058+015	4.52	3.8×3.7	10	410
PGC	058114	2009A	1549+026	3.62	4.4×3.8	10	410
UGC	05408	2009A	0927+390	2.00	4.6×3.5	25	196
UGC	06176	2009A	1159+292	4.08	3.5×2.8	15	735
UGC	09519	2008B	1310+323	3.75	3.4×2.9	10	410
NGC	2697	2008B 2009A[b]	0927+390	14.33	6.8×5.1	20	380
NGC	4292	2008B	3C273	19.86	4.1×3.3	10	410

[a] Observed both in C- and D-arrays

[b] Observed in D-array in 2008B and E-array in 2009A.

Notes:

Column (1): The name is the principle designation from LEDA, which is used as the standard designation.

Column (2): The semester in which the observations were taken at CARMA.

Column (3): The gain calibrator used for observing tracks.

Column (4): The total on-source observing hours.

Column (5): FWHM of the major and minor axes of the synthesized beam.

Column (6): Velocity channel width.

Column (7): Velocity bandwidth (BW) covering the line.

uv-datasets were then transformed into RA-Dec-velocity space (with velocities determined from the line being imaged, mainly ^{12}CO but also occasionally ^{13}CO). Channel widths were chosen to achieve at least a 3σ detection in each channel where flux was present, and were always larger (by at least a factor of 2) than the original spectral resolution of the *uv*-data. Pixels of $1''\times1''$ were chosen as a compromise between spatial sampling and resolution, typically giving approximately 4 pixels. A constant pixel size was chosen to maintain uniform spatial sampling across the sample. One arcsecond corresponds to a physical scale between 72 and 222 pc, depending on the distance of the source. The image areas were generally chosen to be within the primary beam of the 10m antennas ($\approx 54''$), but in the cases of sources that extend beyond this (NGC 4324, NGC 4710 and NGC 5866), the image area was taken to be closer to the primary beam of the 6m antennas ($\approx 90''$). In these cases, the `MIRIAD` imaging task `INVERT` was run with the mosaicking option, to properly scale the data and account for the different primary beam widths.

`Robust=0` weighting was used by default, but was changed if the size and make-up of the source dictated it, natural (`robust = 1`) weighting being used for sources where `robust = 0` weighting resolved out flux (NGC 3619, NGC 3626 and NGC 4324). The dirty cubes were cleaned in regions of source emission to a threshold equal to the rms of the dirty channels. The clean components were then added back and re-convolved using a Gaussian beam of full-width at half maximum (FWHM) equal to that of the dirty beam. This produced the final, reduced and fully calibrated data cube for each galaxy.

The 3D data cubes produced were then used to create moment maps of each galaxy: a zeroth moment (moment0) or integrated intensity map, and a first moment (moment1) or mean velocity map. The data cubes were first Hanning-smoothed in velocity and Gaussian-smoothed spatially (with a FWHM equal to that of the beam), and masks were created by selecting all pixels above fixed flux thresholds, adjusted to recover as much flux as possible in the moment maps while minimising the noise (generally about 2–3 times the rms noise in the smoothed channels). The moment maps were then created using the unsmoothed fully reduced cubes within the masked region only.

All data products were converted into FITS files using `MIRIAD`. Table 2.3 lists some datacube properties for each of the ATLAS^{3D} CARMA galaxies. Figure 2.1 shows the CO moment0 contours of each CARMA ATLAS^{3D} sample galaxy overlaid on an *r*-band image, either from the Sloan Digital Sky Survey (SDSS) or the Isaac Newton Telescope (INT) when SDSS imaging is unavailable (Scott et al., in prep). Figure 2.2 displays the moment1 maps of the 30 sample galaxies. Figure 2.4 displays position-velocity diagrams (PVDs) of galaxies whose kinematics are not well represented with moment1 maps, due to multiple velocity components along the line-of-sight (NGC 2764, NGC 4710 and NGC 5866). Figure 2.3 shows the CO moment0 contours overlaid on unsharp-masked optical images, to enhance dust features. Appendix A.1 contains multiple figures for each CARMA ATLAS^{3D} galaxy, including a *r*-band-moment0 overlay, moment0 map, moment1 map, a comparison of the CARMA and IRAM 30m spectra, a PVD along the position angle determined kinematically in Davis et al. (2011b), and individual channel maps. A

more detailed analysis of the PVD, as well as a comparison to the stellar potential is available in Davis et al. 2012, submitted.

The continuum measurement or upper limit for each galaxy depended on the correlator configuration. For narrow-band (BW $\approx$ 420 km s^{-1}) galaxies that did not include ^{13}CO in the lower sideband, the full lower sideband was used to calculate the continuum (BW $\approx$ 186 MHz). For narrow-band galaxies that included ^{13}CO observations, the edge of the bands in the lower sideband were used (BW $\approx$ 124 MHz). Galaxies that were observed with the upgraded correlator were treated individually, the continuum being modeled in line-free channels only, which varied from galaxy to galaxy. The continuum upper limit was taken to be the 3σ rms of the dirty map produced by inverting the line-free channels. Galaxies where a continuum source was detected (NGC 1266, NGC 3665 and NGC 5866), the flux was measured from the detected point source, and the rms noise was measured in the flux-free regions of the cleaned maps.

2.3.3 Analysis of the data

To calculate the noise level, $\sigma_{\rm rms}$ of each data cube, we selected all the pixels within each cube outside the region known to contain flux, and simply took the standard deviation. The total flux per channel was then calculated by creating a masked 2D image using the region of the moment0 map that did not contain flux, then summing over all unmasked pixels in each channel, using the 2D mask. The statistical noise per channel was then calculated by multiplying $\sigma_{\rm rms}$ by the square root of the total unmasked pixels, converted to beam area. The CARMA integrated spectra presented in Appendix A.1 have been constructed using this method. The integrated fluxes in the channel maps were converted from the native Jansky beam^{-1} units into Jansky by dividing out the total beam area in pixels.

PVDs were created by taking thin (5 pixel) slices through the data cubes, positioned to intersect the centre of the CO emission, and using the position angle determined in Davis et al. (2011b). Table 2.1 also lists the position angle of galaxies not originally listed in Davis et al. (2011b), but subsequently had kinematic position angles fitted using the same methods (detailed in Krajnović et al. 2011).

2.3.4 Comparison to the 30m data

The integrated spectra from CARMA and the IRAM 30m telescope are overlaid in Figs. A.1–A.30. Millimeter measurements are assumed to have 20% absolute flux uncertainties. This means that a flux ratio between 0.66 and 1.5 is considered to be in agreement. The spectra from the IRAM 30m agree with the CARMA ones for 19/30 galaxies. In all 11 cases where there is disagreement, CARMA recovers more than the 30m flux. Every discrepant galaxy either extends beyond, or fills the majority of the single dish beam. CARMA was able to observe flux beyond the extent of the single dish and

Table 2.3 Data parameters of CARMA galaxies

Name	$\sigma_{\rm rms}$ (mJy bm^{-1})	Continuum (mJy bm^{-1})	$F_{\rm CARMA}$ (Jy km s^{-1})	$\log(M)$ ($M_\odot$)	$\frac{F_{\rm CARMA}}{F_{\rm 30m}}$	Morph. Class.
IC 676	30.6	< 3.09	66.3 ± 2.5	8.71 (0.04)	1.2 ± 0.05	D
IC 719	6.63	< 0.351	20.4 ± 1.0	8.34 (0.05)	1.2 ± 0.12	D
IC 1024	19.4	< 3.06	94.6 ± 1.7	8.87 (0.02)	1.8 ± 0.04	D
NGC 1222	23.1	< 1.97	147.6 ± 1.6	9.33 (0.01)	1.8 ± 0.04	X
NGC 1266	22.8	$= 7.49 \pm 1.96$	162.9 ± 0.7	9.28 (0.01)	1.0 ± 0.03	D
NGC 2764	12.9	< 1.85	85.4 ± 1.5	9.23 (0.02)	1.1 ± 0.04	B+R
NGC 2824	10.2	< 2.21	37.8 ± 0.8	8.91 (0.02)	1.8 ± 0.08	D
NGC 3182	8.16	< 1.68	16.4 ± 0.7	8.41 (0.04)	1.2 ± 0.12	R
NGC 3607	7.50	< 0.830	58.0 ± 0.8	8.50 (0.01)	1.2 ± 0.04	D
NGC 3619	3.23	< 0.327	15.2 ± 0.4	8.28 (0.03)	0.7 ± 0.12	M
NGC 3626	5.34	< 1.48	43.2 ± 0.9	8.32 (0.02)	1.3 ± 0.10	D
NGC 3665	10.2	$= 8.98 \pm 0.42$	94.3 ± 1.2	9.11 (0.01)	1.6 ± 0.06	D
NGC 4119	20.2	< 2.64	39.3 ± 0.9	8.14 (0.02)	1.8 ± 0.07	R
NGC 4150	9.41	< 1.87	20.5 ± 0.4	7.82 (0.02)	0.7 ± 0.08	M
NGC 4324	4.30	< 0.974	27.2 ± 0.6	7.97 (0.02)	1.9 ± 0.12	R
NGC 4429	9.53	< 0.375	70.8 ± 0.9	8.39 (0.01)	2.2 ± 0.08	D
NGC 4435	11.5	< 0.375	31.6 ± 1.0	8.05 (0.03)	1.5 ± 0.10	R
NGC 4694	9.30	< 0.512	21.7 ± 0.6	8.01 (0.03)	0.7 ± 0.07	X
NGC 4710	14.0	< 5.20	351.2 ± 1.7	9.08 (0.01)	2.3 ± 0.03	B+R
NGC 4753	11.1	< 0.521	74.7 ± 1.1	8.70 (0.01)	1.4 ± 0.06	M
NGC 5173	8.16	< 1.46	12.5 ± 0.2	8.36 (0.02)	1.2 ± 0.14	X
NGC 5379	10.8	< 0.450	18.5 ± 0.8	8.53 (0.04)	1.6 ± 0.15	B+R
NGC 5866	17.6	$= 4.02 \pm 0.54$	258.2 ± 3.4	8.75 (0.01)	1.9 ± 0.02	B+R
NGC 6014	22.4	< 3.61	34.5 ± 1.0	8.77 (0.03)	1.0 ± 0.07	S
NGC 7465	9.71	< 1.39	93.6 ± 0.4	9.02 (0.01)	1.7 ± 0.04	M
PGC 029321	13.1	< 2.09	18.3 ± 0.7	8.61 (0.04)	1.2 ± 0.09	D
PGC 058114	15.7	< 2.21	73.7 ± 0.9	8.75 (0.01)	1.4 ± 0.04	D
UGC 05408	13.6	< 2.83	6.1 ± 0.5	8.32 (0.08)	0.8 ± 0.18	D
UGC 06176	10.8	< 0.524	28.5 ± 0.8	8.76 (0.03)	1.5 ± 0.10	D
UGC 09519	19.5	< 2.27	51.4 ± 1.4	8.77 (0.03)	0.9 ± 0.04	M
NGC 2697	9.89	< 1.36	48.2 ± 0.7	8.61 (0.01)	2.3 ± 0.11	R
NGC 4292	9.58	< 1.05	13.8 ± 0.5	7.74 (0.04)	1.2 ± 0.14	R

Notes:
Column (1): The name is the principle designation from LEDA, which is used as the standard designation.
Column (2): Root mean square noise level per channel, measured in regions devoid of line emission.
Column (3): Continuum emission or upper limits.
Column (4): Flux recovered by CARMA.
Column (5): Total molecular gas mass reported from the CARMA observations.
Column (6): Fraction of flux recovered by CARMA (with respect to the IRAM 30m telescope.)
Column (7): CO morphological classification of the molecular gas, based on the moment0 and moment1 maps:
D = disc, X = strongly disturbed, R = ring, M = mildly disrupted, B = bar/ring, S=spiral.

thus recovered extended emission beyond the spatial region covered by the single dish in a single pointing. In fact, only 7 of the galaxies within the CARMA ATLAS^{3D} sample are well contained within the 21.6″ IRAM beam. It is of note that because so many galaxies extend beyond the single dish beam, that it would be difficult to identify galaxies with flux recovered from the single dish but not by CARMA.

As discussed above, all galaxies detected with the IRAM 30m were also detected at CARMA. However, the IRAM 30m selection for the current CARMA survey does imply that galaxies with molecular gas exclusively beyond the 30m beam (e.g. rings, arms and tidal features beyond a radius of $\approx 12''$) would have been missed. It is impossible to estimate the incidence of these objects based on the CO data alone, but the Galaxy Evolution Explorer (*GALEX*) ultraviolet imaging survey of the SAURON sample (tracing the associated star formation) suggests that they are very rare (of 34 galaxies, only one, NGC 2974; Jeong et al. 2009). Lower density neutral hydrogen is however fairly common at large radii (Serra et al. 2012).

Because the molecular gas in many ($> 75\%$) galaxies extends beyond the single dish beam, it is likely that the flux CARMA has measured more accurately reflects the total molecular mass in each galaxy, and therefore we adopt CARMA derived molecular masses for the remainder of the paper.

2.3.5 Literature data

Twelve galaxies of the ATLAS^{3D} sample already have interferometric CO data available in the literature. Those galaxies are: NGC 4710 (Wrobel & Kenney 1992); NGC 2685 (Schinnerer & Scoville 2002), and the ten galaxies that will be a part of the ATLAS^{3D} data release: NGC 4476 (Young 2002); NGC 3032, NGC 4150, NGC 4459 and NGC 4526 (Young, Bureau & Cappellari 2008); NGC 2768 (Crocker et al. 2008); NGC 4550 (Crocker et al. 2009); NGC 524, NGC 3489 and NGC 4477 (Crocker et al. 2011). Names, distances, Virgo membership, CO morphological classes and references of these galaxies are listed in Table 2.4. when required, data for each of the galaxies were provided by the original authors for use in this work. Moment maps and dust comparisons appear in Figure A.32 for the galaxies whose data will be included in the data release. Both NGC 4710 and NGC 4150 were re-observed as part of the CARMA ATLAS^{3D} survey, and we only present these updated data in this paper.

2.3.6 A catalog of ATLAS^{3D} interferometric CO data

The archive will include CARMA data for all 30 galaxies, as well as data for the 10 previously published galaxies and the two non-ATLAS^{3D} sources. The data products provided will include data cubes, and moment0 and moment1 maps in Flexible Image Transport System (FITS) format. They will be hosted through the CARMA data archive[2]

[2]http //carma-server.ncsa.uiuc.edu 8181/

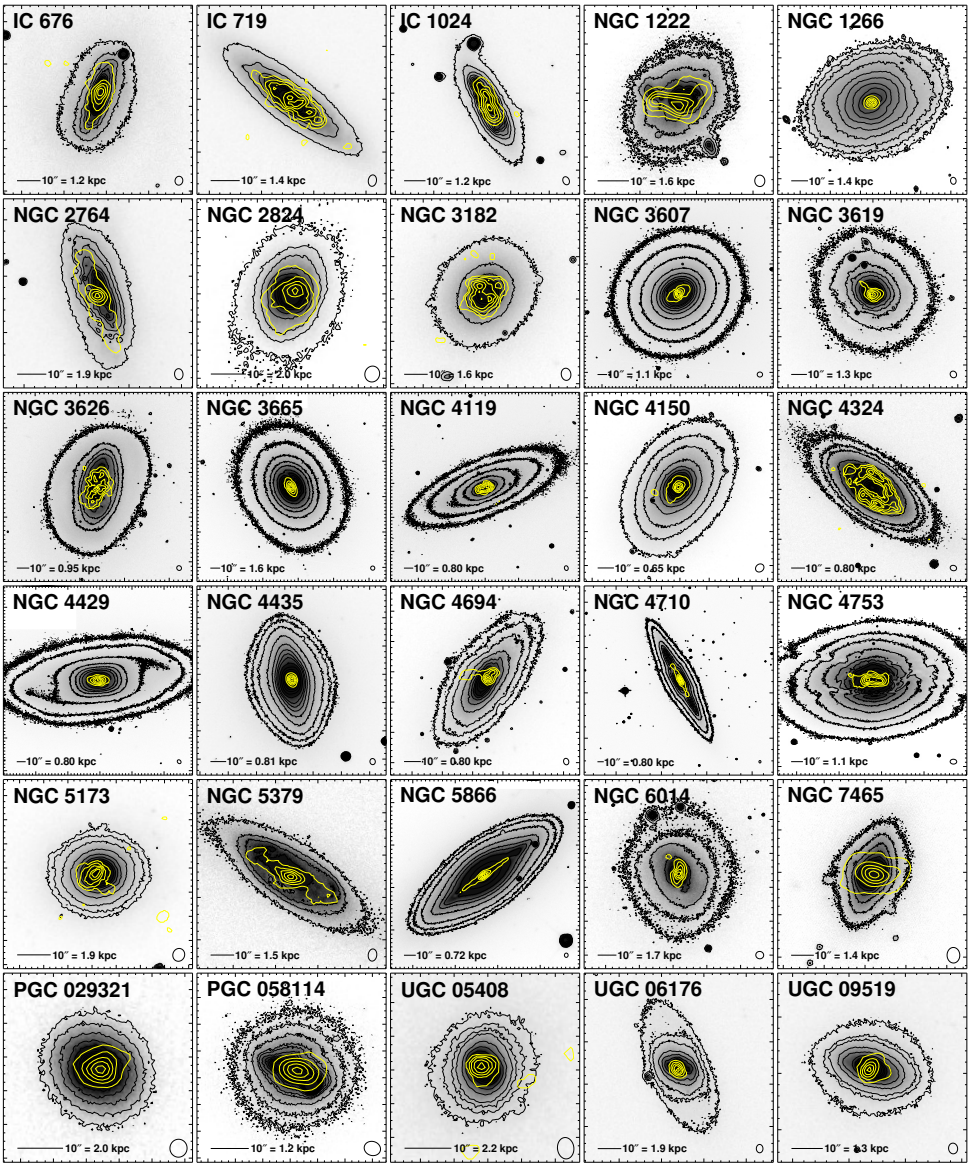

Figure 2.1 r-band images (and black contours) overlaid with integrated CO(1–0) contours (yellow) for the 30 galaxies in the ATLAS^{3D} CARMA sample. The r-band images were either taken from the SDSS or a dedicated program with the INT (Scott et al., 2011, in prep.) The CO synthesized beam is shown in the bottom-right corner of each panel. A bar indicates the scale of 10″ in the bottom left corner of each panel, as well as the equivalent physical scale at the distance of the galaxy.

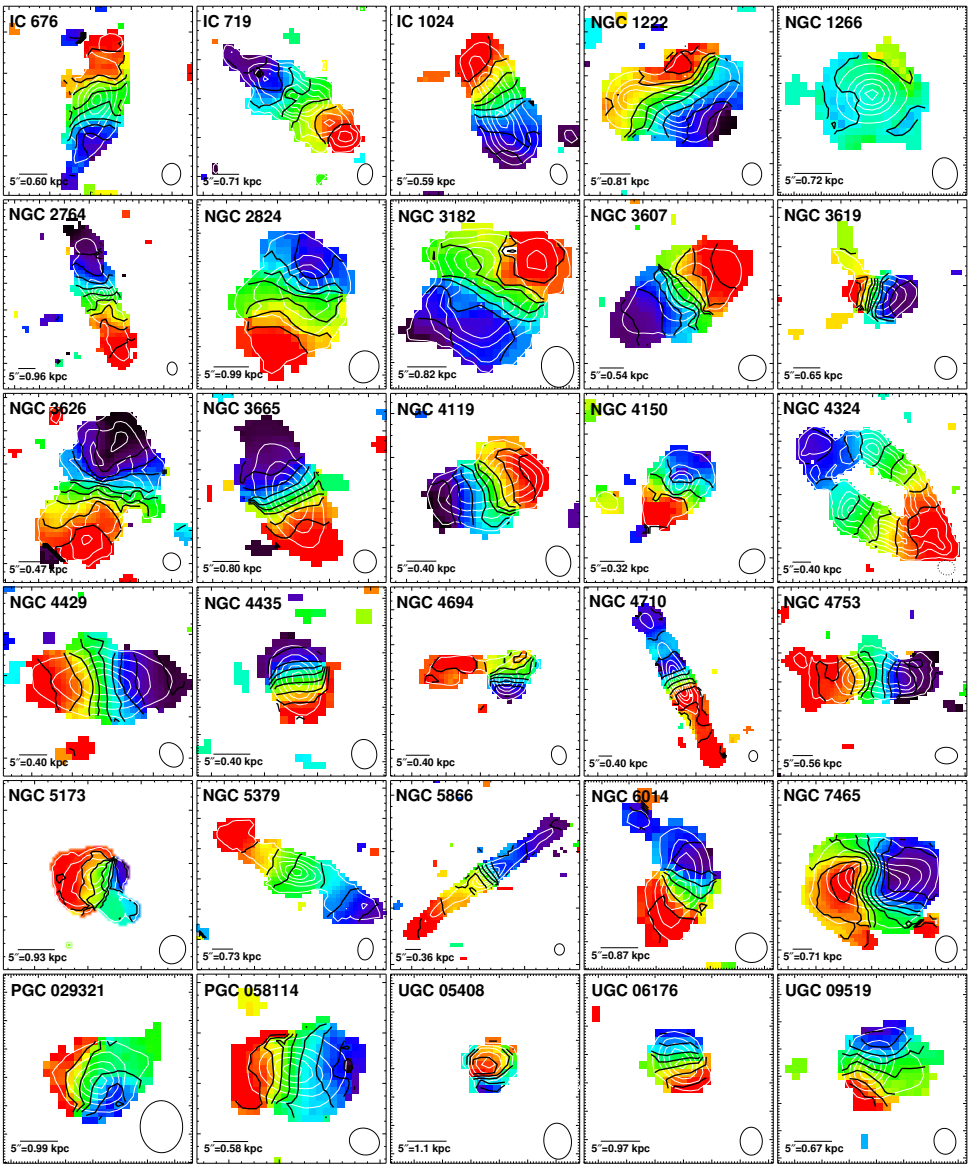

Figure 2.2 Mean CO(1–0) velocity maps of the 30 galaxies of the ATLAS^{3D} CARMA sample. Iso-velocity contours (solid black lines) are overlaid at 20 km s^{-1} intervals, as are contours from the moment0 map (dotted black lines). The CO synthesized beam is shown at the bottom-right corner of each panel. A bar indicates the scale of 5″ in the bottom left corner of each panel, as well as the equivalent physical scale at the distance of the galaxy.

and reachable from our project website[3].

2.4 Discussion

Figures 2.1 and 2.2 show the 30 ETGs imaged as part of the CARMA ATLAS^{3D} survey. Before the survey was complete (including the 10 literature galaxies mentioned in §2.3.5), 16 ETGs had CO maps (Wrobel & Kenney 1992; Schinnerer & Scoville 2002; Young 2002, 2005; Wei et al. 2010a), most obtained as part of individual or small-scale studies. The addition of the CARMA ATLAS^{3D} sources increases this amount to over 50 (including the 10 literature galaxies imaged by Young, Bureau & Cappellari 2008 and Crocker et al. 2011), and provides a largely unbiased sample. Combined with the maps from the SAURON integral-field spectrograph, the CARMA ATLAS^{3D} galaxies thus provide the most robust picture of molecular gas-rich ETGs.

We now focus our analysis on the CO-rich ATLAS^{3D} ETGs only, adding the eleven ATLAS^{3D} galaxies imaged in CO with the Berkeley-Illinois-Maryland Array (BIMA), the Owens Valley Radio Observatory (OVRO) and the Plateau de Bure Interferometer (PdBI), prior to the CARMA effort. Between the 30 CARMA galaxies and 11 previously published galaxies, we image 65% of the CO detections in Paper IV, more than 90% of the total molecular gas mass in those detections, and are complete down to a CO(1–0) integrated flux of 18.5 Jy km s^{-1}.

2.4.1 Comparison to the dust

Figure 2.3 shows the CO moment0 contours of each galaxy overlaid on a dust image. The dust images were produced by using an unsharp-mask filter with a Gaussian kernel on g-band SDSS images (and for NGC 1222, NGC 1266 and NGC 7465, where SDSS images are unavailable, on Isaac Newton Telescope images). PGC 058114 is not included because of contamination by a foreground bright star. The unsharp masking enhances the visibility of dust features and gives a qualitative view of the distribution of the filamentary dust in each galaxy of the ATLAS^{3D} CARMA sample. This dust, for the most part, is a good indicator of the distribution of the molecular gas. Indeed, the CO is nearly always (28/29 instances) associated with evidence of dust obscuration. It is evident that the converse is not true, as a Hubble Space Telescope (HST) survey of nearby ellipticals contained dust in nearly half the cases (Tran et al. 2001; Lauer et al. 2005), much higher than the CO detection rate of ATLAS^{3D}. Additional dust is seen beyond the limits of the detected CO emission in most galaxies, (but notably in NGC 3619, NGC 4753 and NGC 4694). However, there is no noticeable dust beyond the detected extent of the CO in others (notably NGC 4429 and NGC 4459). It thus appears that in most cases where the dust and CO are co-spatial, dust provides a good, high spatial resolution rendering of

[3]http://purl.org/atlas3d

Table 2.4 Morphologies of the ATLAS^{3D} literature galaxies

Name	Distance (Mpc)	Morph. Class.[a]	Virgo?	Reference
NGC 524	23.3	D	0	6
NGC 2685	16.7	R	0	1
NGC 2768	21.8	D	0	4
NGC 3032	21.4	D	0	3
NGC 3489	11.7	S	0	6
NGC 4459	16.1	D	1	3
NGC 4476	17.6	D	1	2
NGC 4477	16.5	R	1	6
NGC 4526	16.4	D	1	3
NGC 4550	15.5	D	1	5

References: (1) Schinnerer & Scoville (2002); (2) Young (2002); (3) Young, Bureau & Cappellari (2008); (4) Crocker et al. (2008); (5) Crocker et al. (2009); (6) Crocker et al. (2011)

[a]Morphological classification of the molecular gas based on the moment0 and moment1 maps.

D = disc, X = strongly disturbed, R = ring, M = mildly disrupted, B = bar/ring, S=spiral.

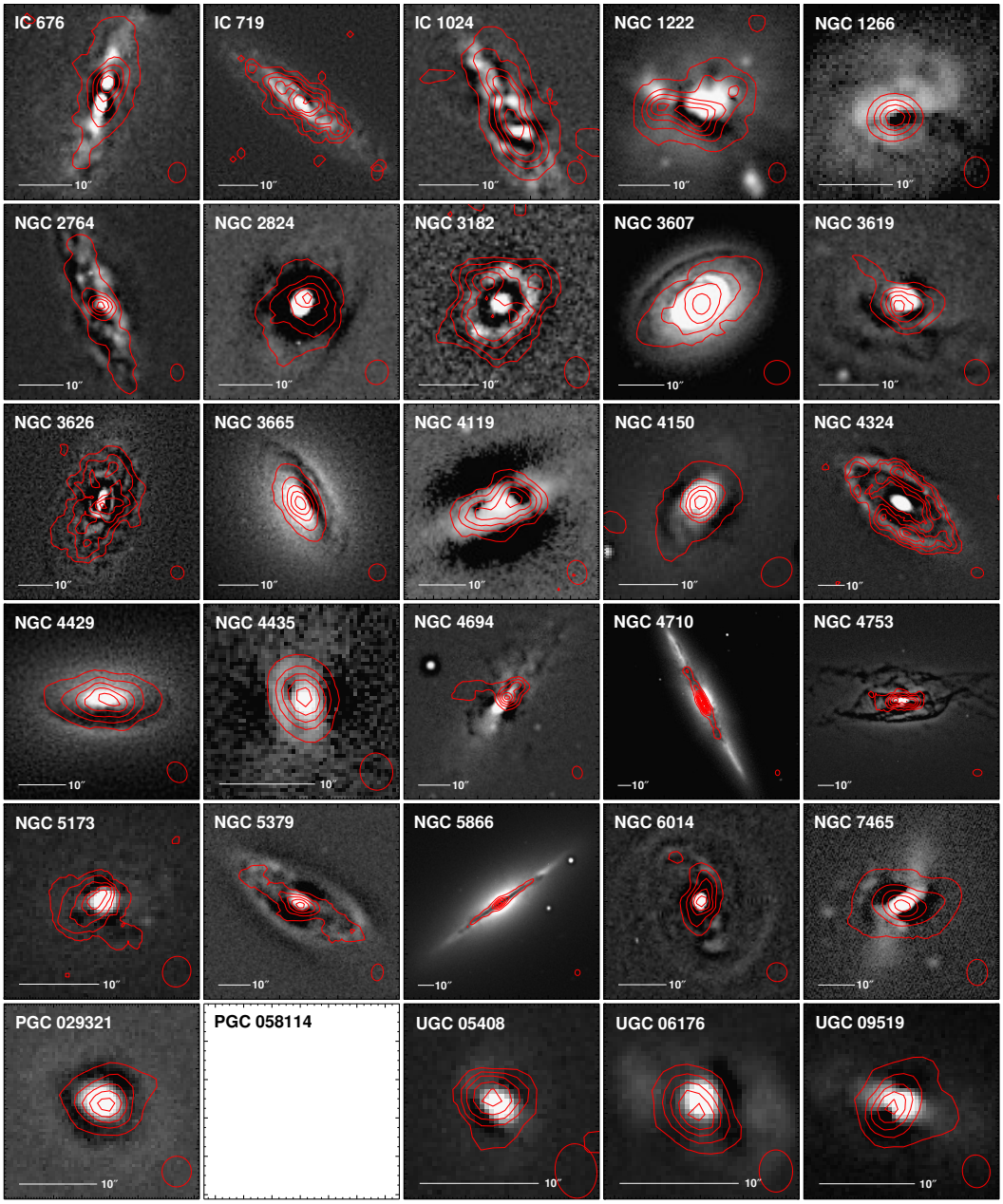

Figure 2.3 Comparison of the integrated CO(1–0) distribution (red contours) to dust (grayscale) for the 30 galaxies of the ATLAS^{3D} CARMA sample, using unsharp-masking of the g-band image of each galaxy. It appears that galaxies with disturbed CO morphologies also exhibit said disturbance in the dust distribution, and overall the molecular gas in the galaxies traces the filamentary dust. PGC 058114 is not displayed because of the presence of a bright star in the galaxy field.

the molecular gas structure. Where dust is more extended than the CO, it could simply be that the CO is below our detection threshold, or that the ISM is not molecular at all (for instance, it could be atomic or warm). With this caveat in mind, we use the dust as a useful guide to the morphological structures in which the cold ISM resides. We exploit this fact below when the CO morphological class is difficult to determine (e.g. IC 676 and NGC 4435).

2.4.2 Morphologies of the molecular gas

The CARMA ATLAS^{3D} survey illustrates that the molecular gas in ETGs comes in a large variety of configurations. We have identified six different configurations, including smooth discs (D), spirals (S), mildly disrupted objects (M), severely disrupted objects (X), rings (R) and bars+rings (B+R), as bars are always found with rings, never alone. These classifications are strictly for the molecular gas, as all galaxies are optically classified as ETGs. The CO morphological classification of each galaxy was based on an analysis of its moment0 and dust maps (Figure 2.3), moment1 map (Figure 2.2) and major-axis PVD (Figs. A.11-30). In many cases the moment0 and moment1 map allowed us to unambiguously classify a galaxy. For ambiguous cases, the PVD was used to search for distinct kinematic signatures, and finally the dust map was used as a higher spatial resolution proxy for the molecular gas.

The criteria for each CO morphological class are as follows. A galaxy is classified as strongly disrupted (X) for showing strong irregularities in the CO kinematics. Galaxies classified as discs (D) show regular rotation and a smooth elliptical shape. The PVD of D-classed objects also show smooth velocity variations with no discontinuity. Galaxies classed as mildly disrupted (M) have mainly regular disc configurations, but include small deviations in their moment0 and moment1 maps. Galaxies classified as spirals (S) show regular rotation, but the moment0 and/or dust maps exhibit discrete spiral arms. Galaxies classified as rings (R), like discs, exhibit regular rotation, but unlike discs, the PVD of R-classed objects include a solid-body component and/or a discontinuity in velocity. Well-resolved rings show a central hole in the moment0 map. In the most ambiguous cases, the dust map was consulted to search for a dust ring (e.g. NGC 4119 and NGC 4435). Finally, bar+ring systems (B+R) were identified either directly from the moment1 map, when the bar and ring are both distinctly visible, or using the PVD and searching for an X-shaped pattern (in the case of edge-on systems; see §2.4.2).

Strongly and mildly disrupted objects

The origin of the strongly disrupted (X) objects is the most easily explained. These galaxies show highly irregular CO distributions and kinematics, that are normally characteristic of interacting systems, a fact often confirmed by observations at other wavelengths. In the case of NGC 1222 and NGC 4694, it is clear that they acquired their gas via exter-

Table 2.5 CO morphologies of the ATLAS^{3D} interferometric sample.

Morphological Configuration	Symbol	Number (out of 40)	Fraction (%)
Disc	D	20	50
Spiral	S	2	5
Ring	R	6	15
Bar+Ring	B+R	4	10
Mild disruption	M	5	12.5
Strong disruption	X	3	7.5

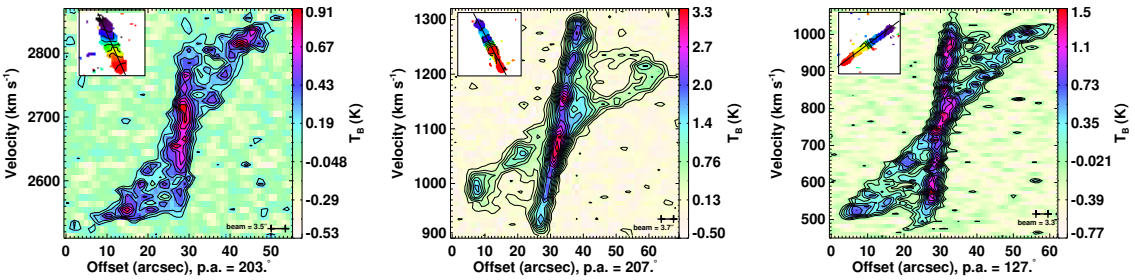

Figure 2.4 Position-velocity diagrams of the three CARMA ATLAS^{3D} ETGs with clear two-component velocity profiles, that are not properly represented by the moment1 maps. The galaxies are NGC 2764 (left), NGC 4710 (middle) and NGC 5866 (right). All 3 galaxies are edge-on or almost edge-on and show the characteristic X-shaped PVD signature of an edge-on bar (see §2.4.2)

nal accretion (see Beck, Turner & Kloosterman 2007 and Duc et al. 2007 for details on each galaxy). NGC 5173 is known to host a large misaligned H I disk (Serra et al. 2012).

Mildly disrupted CO distributions (M) also appear to be in less relaxed systems than the rest. In some cases, there is strong evidence that the gas is being acquired externally, such as in NGC 7465 (Li & Seaquist 1994), which is accreting from an external H I reservoir via a close interaction with other galaxies. NGC 3619 and UGC 09519, are known to host large misaligned H I discs (Serra et al. 2012) providing a likely source for the molecular gas. The irregular dust filaments in NGC 4753 are the main reason that the CO is classified as an M morphology. The NGC 4753 dust structure is well explained as twisted disk precession, after the accretion of a gas-rich dwarf companion (Steiman-Cameron, Kormendy & Durisen 1992). The original BIMA observations of NGC 4150 (Young, Bureau & Cappellari 2008) show a pronounced low surface density elongated tail that was not recovered by CARMA due both to a smaller field of view, and higher resolution observation than BIMA. A study of the gas-phase metallicity of NGC 4150 also show it to be sub-solar ($Z \sim 0.3 - 0.5\ Z_{\odot}$), and therefore is very likely due to an external accretion event (Crockett et al. 2011).

It appears that field galaxies are far more likely to exhibit disturbed morphologies than Virgo galaxies, with $24 \pm 8\%$ (7/29) of field galaxies classified as either M or X, as opposed to $9 \pm 9\%$ (1/11) for Virgo galaxies. This is unsurprising, given the results of Davis et al. (2011b), which suggested that galaxies virialized within the cluster are unable to replenish their stores of molecular gas via external accretion, and thus only long-lived phenomena survive. Overall, the M- and X-classed objects seem to come from an external origin, and are probably dynamically younger than the other objects, which explains the dearth of such objects within Virgo.

Molecular rings and bars

Rings (R) and bars+rings (B+R) also make up a non-negligible fraction of the ATLAS^{3D} molecular gas morphologies, representing about a quarter of the CO sample. It is of note that cold gas in barred galaxies accumulates in rings associated with the major resonances (e.g. Buta & Combes 1996), so it is possible that bar+ring systems are simply in an early stage of an evolutionary sequence, whereby the bar funnels gas into the centre (e.g. Bournaud & Combes 2002), evacuating the central (but not nuclear) regions of molecular gas, and later leaving the ring structure intact, without a molecular gas-rich bar. This scenario would explain why bars are only seen with rings, but not the converse.

Figure 2.4 shows the PVDs of three edge-on systems: NGC 2764, NGC 4710 and NGC 5866. In all three cases, the molecular gas kinematics clearly illustrate the presence of a bar. The two visible kinematic components seen in the PVDs are identifiable as the x_1 (parallel to the bar) and x_2 (perpendicular) orbital components. All three PVDs also exhibit a gap between the two orbital components (Athanassoula & Bureau 1999), a confirmation of the presence in these three systems of bars. Closer inspection of the x_2

component in these galaxies as well, shows that they are brightest at the outskirts, which is a signature of a ring, confirming that these edge-on systems have the morphological classification of B+R.

The fraction of molecular gas-rich ETGs that contain a ring structure is also a factor of ≈ 2 larger than that for spirals, based on the BIMA Survey of Nearby Galaxies (SONG) sample (Sheth et al. 2002; Helfer et al. 2003), modified to match the average noise and redshift of the ATLAS^{3D} sample (as in Davis et al. 2012, submitted and §2.4.2). Also, unlike for spiral galaxies, the molecular gas morphology does not necessarily follow the stellar morphology, most notably stellar bars. Galaxies with stellar bars identified in Krajnović et al. (2011) are as likely to have a disc-like (D) CO morphology as R and B+R morphologies.

It also appears that Virgo cluster galaxies are slightly more likely than field galaxies to have R and B+R structures, with $45 \pm 15\%$ (5/11) of Virgo galaxies classified as either R or B+R, as opposed to $17 \pm 7\%$ (5/29) for field galaxies. Davis et al. (2011b) has shown that the molecular gas in ETGs is preferentially kinematically-aligned with the stars in Virgo galaxies, so it is perhaps not surprising to find relatively more bars and rings there, where the gas has been under the influence of secular processes without external gas interference. This may also point to these morphologies being long lived, as opposed to the M and X morphologies, discussed above. It is also quite possible that the slightly higher detection rate of R and B+R in Virgo with respect to the field galaxies is due to a spatial resolution effect, as Virgo galaxies are closer on average ($D \approx 16.5$ Mpc; Mei et al. 2007) than the field galaxies in the sample ($D \approx 28$ Mpc). If we redshift the Virgo galaxies to the average distance of field galaxies, the detection of R and B+R drops from 5 to 2, and is statistically consistent with the field rate, with NGC 4119, NGC 4435 and NGC 4477 becoming unresolved. Higher resolution and deeper imaging is required to determine whether the higher rate in Virgo is a resolution effect or an intrinsic property.

Molecular discs and spirals

Smooth molecular discs make up the largest fraction of the CO morphologies that are seen in the ATLAS^{3D} CARMA galaxies, while spirals make up the smallest fraction. This relative dearth of discrete spirals as compared to smooth discs seems to indicate that there is something fundamentally different about the way in which molecular gas behaves within an ETG as opposed to a LTG. A caveat to this scenario is that galaxies with molecular gas spirals would likely be classified as LTGs, and precluded from the sample.

It is possible that molecular gas in ETGs remains in a smooth distribution and lacks distinct spiral arms for dynamical reasons. For example, the steep potential wells in the central parts of ETGs (where the molecular gas resides) yield high epicyclic frequencies, and may thus prevent gravitational instabilities linked to spiral arms from developing (Toomre Q parameter; e.g. Toomre 1981).

It is also possible that some of the D morphologies would have been classified other-

wise with observations of better sensitivity and/or spatial resolution. For instance, much higher resolution CO observations of NGC 1266 presented in Chapter 3 reveal a disturbed nuclear disk and a molecular outflow, both of which are unresolved here. In addition, if only the peak of a spiral structure were detected, and convolved with a beam, it could well be classified as a disc. In fact, as much as half of BIMA SONG spirals (Helfer et al. 2003) would be classified as D if they were located at the average distance of the ATLAS^{3D} sample, with similar noise properties and beam sizes (see Davis et al. 2012, submitted for a full discussion of properly redshifting the BIMA SONG data to match ATLAS^{3D}). However, even assuming that half of the current CO-righ ETGs classified as D are actually spatially unresolved S, the spiral fraction of ATLAS^{3D} would be $30 \pm 7\%$, still much lower than the spiral fraction of BIMA SONG ($62 \pm 10\%$).

While obtaining higher resolution molecular gas maps is the only rigorous way to directly break the S/D degeneracy, we use here the unsharp-masked dust images as proxies. As mentioned in §2.4.1, the molecular gas morphology follows the dust morphology faithfully in the majority of cases. The unsharp-masked images therefore provide the higher spatial resolution and sensitivity required to separate the S and D classifications. The dust comparison indicates that in the majority of cases (with the possible exceptions of NGC 3619, NGC 3626 and NGC 3665), and contrary to LTGs, a disc morphology without distinct spiral arms is indeed the most common morphology for the molecular gas in ETGs.

Summary of the gas morphologies

Table 2.5 lists the total number of ATLAS^{3D} ETGs within each CO morphological class. Overall, it thus appears that the CO in ETGs is most likely to be in a settled configuration, either in regular discs (comprising 50% of the galaxies) or ring, bar+ring and spiral configurations (comprising another 30% of the sample). This means that the majority (80%) of ETGs have a dynamically settled molecular gas configuration. The dynamically unsettled (M and X) systems comprise the remaining 20%, and just over half of those are only mildly disrupted. Of course, the CO structures observed here are rather compact spatially, with an average extent of only 1 kpc (Davis et al. 2012, submitted), and correspondingly small dynamical timescales ($10^7 - 10^8$ yrs). The CO distributions are thus expected to relax and reach equilibrium rapidly.

Figure 2.5 shows the $u - r$ vs. M_r color-magnitude diagram (CMD) of the CARMA ATLAS^{3D} sample, from SDSS and INT data. There is no clear separation of the morphological groups as a function of color, although some trends do appear. The brightest objects ($M_r < -21$) tend to be classified as D galaxies, with the exception of NGC 4753, which was discussed in §2.4.2. The CO discs in these massive galaxies are also generally well-resolved, limiting the chance that these objects are poorly resolved rings or spirals. It also appears that although B+R galaxies can be found throughout the CMD, galaxies classified as R only seem to cluster on the red sequence, perhaps indicating a later

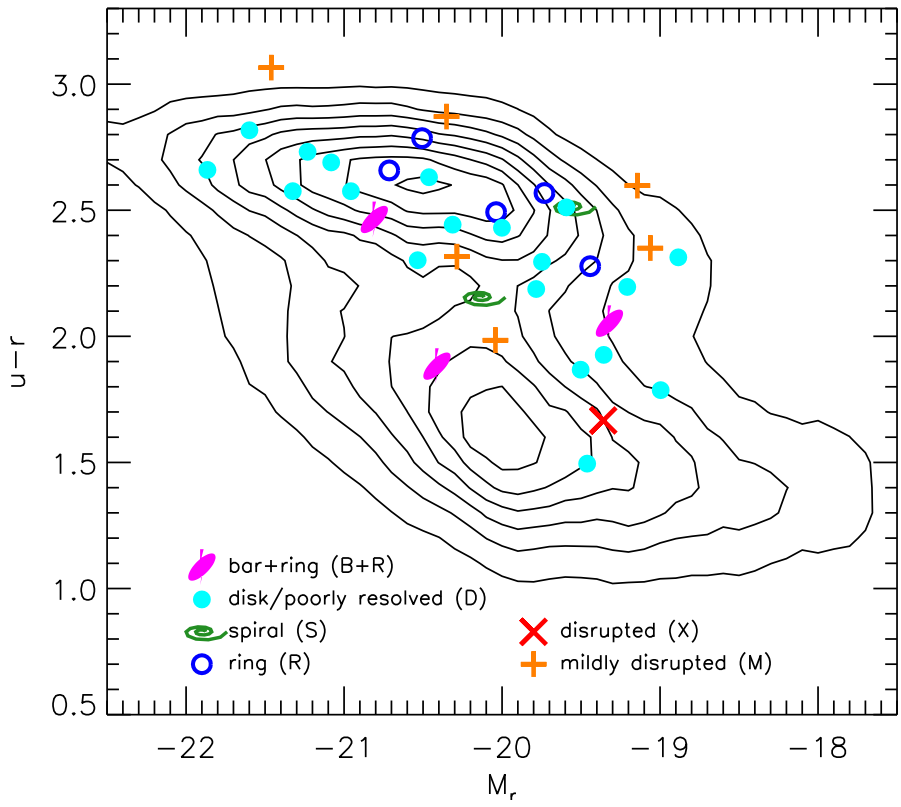

Figure 2.5 Color-magnitude diagram of the CO-imaged ATLAS^{3D} galaxies, sorted based on their CO morphological classifications. The contours (black) are from the SDSS Data Release 7 (DR7), and represent all galaxies with redshift $z > 0.08$. Data for the ATLAS^{3D} ETGs are either from the SDSS DR7 u, r and M_r catalog products or the INT (NGC 524, NGC 3489 and NGC 7465; Scott et al. 2012, in prep). Colour information is unavailable for NGC 1222 and NGC 1266 due to poor u-band photometry, for PGC 058114 because of the presence of a bright star less than a degree from the galaxy, and for NGC 4710 due to erroneous SDSS photometry.

evolutionary stage.

2.4.3 Mass of externally acquired molecular gas in ETGs

Davis et al. (2011b) discusses the origins of the molecular gas in ETGs, and identifies galaxies that likely have externally acquired gas. Using the criteria set forth in Davis et al. (2011b), that the kinematic major axis of the ionized gas must be misaligned with the kinematic major axis of the stars by at least 30°, at least thirteen CARMA ATLAS^{3D} galaxies are identified as having externally acquired gas under these criteria, including IC 719, NGC 1266, NGC 2685, NGC 2768, NGC 2685, NGC 3032, NGC 3626, NGC 4694, NGC 5173, NGC 7465, PGC 029321, PGC 058114 and UGC 09519. NGC 3619 is also classified as M in this work, exhibiting an unsettled CO morphology, but the origin of the CO is difficult to determine, with a kinematic misalignment angle of only $24 \pm 3°$, right at the boundary of being classified as external (Davis et al. 2011b), and it contains a kinematically-misaligned H I disc (Serra et al. 2012). Although it is possible that the CO is indeed from an external origin, there is no conclusive measurement to classify it as such, and NGC 3619 will thus not count as having external CO. NGC 4150 is included as being external in origin, as studies show that its gas-phase metallicity is sub-solar, and thus is very likely from the accretion of a gas-rich companion in a minor merger (Crockett et al. 2011). NGC 4753 is classified as M in this work, and Steiman-Cameron, Kormendy & Durisen (1992) make a compelling argument that the molecular disc is unsettled, and must come from an external source. For this reason, we include NGC 4753 in the category of gas acquired externally. The disrupted stellar and gas kinematics of NGC 1222 (CO class X), which is currently undergoing a strong three-way interaction (Beck, Turner & Kloosterman 2007), suggest that the molecular gas is likely to be of external origin. Including these three additions, 15 (38%) of the 40 gas-rich CARMA ETGs contain external gas, in good agreement with the fraction of externally acquired gas estimated in Paper X (36%).

The fact that the majority of unsettled gas configurations are identified as having an external origin is unsurprising, as a parcel of gas falling into a galaxy takes time to virialise, which is not the case for internal gas (stellar mass loss). The rest of the galaxies with external gas have disc configurations (IC 719, NGC 3032, NGC 3626, PGC 029321 and PGC 058114), represented at about the same rate as in the sample as a whole. NGC 2768 and NGC 2685 are both known polar rings/discs, and are discussed in detail in Crocker et al. (2008) and Schinnerer & Scoville (2002), respectively.

We use the H_2 masses from CARMA, where available, and find that the total molecular gas mass in the 15 sources with external CO is 8.26×10^9 $M_\odot$, or 44% of the total molecular gas mass in our sample of 40 CO-rich galaxies with interferometric maps. There is reasonable agreement between the external number (38%) and mass (44%) fractions. Galaxies that were originally detected in molecular gas (Young et al. 2011) but were not mapped interferometrically have a higher rate of ionised gas kinematically-aligned with

the stars, compared to those actually mapped here (i.e. more massive CO; see Davis et al. 2011b). This likely means that the un-imaged CO-detected ETGs contribute negligibly ($> 6\%$) to the total external molecular gas mass. Assuming reasonable gas depletion timescales and star formation histories (allowing us to adopt the mean current-to-initial correction factor calculated by Kaviraj et al. (2012) for ETGs with prominent dust lanes), we can infer the amount of molecular gas each galaxy acquired before star formation activity consumed some of the molecular gas. The total amount of molecular gas originally acquired externally within the ATLAS^{3D} sample is then approximately 2.48×10^{10} $M_{\odot}$. At the minor merger rate calculated by Lotz et al. (2008), this would mean approximately 8.3×10^{8} $M_{\odot}$ per minor merger.

2.5 Conclusions

We have presented millimeter-wave data products of the CARMA ATLAS^{3D} survey of galaxies, an imaging survey of the CO J = 1–0 emission of 30 nearby CO-rich ETGs, part of the ATLAS^{3D} survey. The main conclusions drawn from these data are:

1. The CARMA ATLAS^{3D} survey is the largest CO imaging survey of ETGs to date, and provides the most detailed view of the nature of molecular gas in ETGs.

2. The molecular gas found in ETGs appears to be co-spatial with the dust, though the dust appears to be more extended, likely because we are unable to trace regions with small molecular gas surface densities.

3. The molecular gas present in ETGs comes in a variety of morphologies: 50% is in inclined gas discs or is poorly resolved (D), 5% show spiral arms or spiral structure (S), 15% is in resolved rings (R), 10% is in bar+ring systems (B+R), 12.5% is in mildly disrupted objects (M) and 7.5% is in strongly disrupted objects (X).

4. The CO morphology does not show a strong correlation with the $u-r$ color of the galaxy, although there appear to be weak trends. For example, the most massive galaxies in this sample tend to have D morphologies, and R morphologies tend to lie on the red sequence whereas B+R morphologies tend to also be present in the blue cloud.

5. We currently observe a total of 8.26×10^{9} $M_{\odot}$ of molecular gas that is likely of external origin in our galaxies. Using the correction factor derived in Kaviraj et al. (2012), we estimate that the total externally acquired molecular gas in those galaxies was $\approx 2.48 \times 10^{10}$ $M_{\odot}$.

Chapter 3

The Unusual Case of NGC 1266

An earlier version of this chapter was previously published as ApJ 735:88–100[1].

Abstract

We report the discovery of a powerful molecular wind from the nucleus of the non-interacting S0 field galaxy NGC 1266. The single-dish CO profile exhibits emission to $\pm$400 km s^{-1} and requires a nested Gaussian fit to be properly described. Interferometric observations reveal a massive, centrally–concentrated molecular component with a mass of 1.1×10^9 M$_\odot$ and a molecular outflow with a molecular mass of $\approx 2.4 \times 10^7$ M$_\odot$. The molecular gas close to the systemic velocity consists of a rotating, compact nucleus with a mass of about 4.1×10^8 M$_\odot$ within a radius of $\approx$ 60 pc. The compact molecular nucleus has a surface density of $\approx 2.7 \times 10^4$ M$_\odot$ pc^{-2}, more than two orders of magnitude larger than that of giant molecular clouds in the disk of the Milky Way, and appears to sit on the Kennicutt-Schmidt relation despite its extreme kinematics and energetic activity. We interpret the nucleus as a disk that confines the outflowing wind. A mass outflow rate of at least $\approx$ 13 M$_\odot$ yr^{-1} leads to a depletion timescale of $\lesssim$ 85 Myr. The star formation in the system is insufficient to drive the outflow, and thus it is likely driven by the active galactic nucleus (AGN) in the system. The concentration of the majority of the molecular gas in the central 100 pc requires an extraordinary loss of angular momentum, but no obvious companion or interacting galaxy is present to enable the transfer. NGC 1266 is the only known outflowing molecular system that does not show any evidence of having undergone a recent interaction.

3.1 Introduction

Early-type galaxies (ETGs) are generally thought to be poor in atomic and molecular gas (Lees et al. 1991), but their disk galaxy progenitors are generally gas-rich (Kauffmann et al. 2003). How these galaxies transform themselves from gas-rich to gas-poor systems is tied to a host of issues in galaxy evolution, including the migration of galaxies from the blue cloud to the red sequence (Faber et al. 2007), merger-driven starbursts and quasar activity (Hopkins et al. 2005), feedback from star formation and central supermassive black holes on the interstellar medium (ISM) (Di Matteo et al. 2005) and radio mode activity (Croton et al. 2006).

The ATLAS^{3D} project aims to address these issues through a complete volume-limited multi-wavelength survey of ETGs within 42 Mpc, spanning a variety of environments and two orders of magnitude in mass (Cappellari et al. 2011). In particular, 259 of the 260 sample galaxies have been searched for CO with the Institut de Radioastronomie Millimétrique (IRAM) 30m telescope (Young et al. 2011). The Combined Array for Research in Millimeter Astronomy (CARMA) interferometer is now mapping the brightest two thirds of the detections in the J=1–0 transition of CO.

Here we report on the S0 field galaxy NGC 1266, the brightest of the CO detections in the ATLAS^{3D} sample. The redshift distance to NGC 1266 is taken from ATLAS^{3D}, 29.9 Mpc, for which $1'' = 145$ pc. The single-dish line profile requires a double Gaussian fit, with broad wings that exceed NGC 1266's escape velocity. The interferometric CO observations suggest that NGC 1266 possesses an extraordinarily dense, centrally compact molecular nucleus with a powerful outflow. In §4.2, we describe the molecular line observations using the IRAM 30m single-dish, CARMA and Submillimeter Array (SMA) telescopes. We show in §3 the two-component structure of the molecular gas – a massive central compact nucleus, and a more extended outflow that appears to be escaping the galaxy. We also derive the basic physical properties of the molecular gas. In §4, we compare NGC 1266 to other galaxies and discuss the remarkable properties of its molecular gas. We summarize our main conclusions in §5.

3.2 Observations

3.2.1 The IRAM 30m Single-dish

NGC 1266 was observed as part of a flux-limited CO(1–0) and CO(2–1) survey of all ATLAS^{3D} galaxies carried out at the IRAM 30m telescope (Young et al. 2011). The data consist of a single pointing at the galaxy center, covering a velocity width of 1300 km s^{-1} with a spectral resolution of 2.6 km s^{-1} at CO(1–0), centered on the systemic velocity of 2155 km s^{-1} as listed in the LEDA catalog (based on absorption lines; Paturel et al. 2003), with a beamsize of $21.6''$ in the CO(1–0) line. The CO(2–1) covered velocity width of 1300 km s^{-1} with a spectral resolution of 5.2 km s^{-1}, with a beamsize of $12''$. A

Figure 3.1 The Institut de Radioastronomie Millimétrique 30m telescope sitting atop Pico Veleta. Credit: Max-Planck-Institut für Radioastronomie.

zeroth order baseline was subtracted, using line-free channels to estimate the continuum contribution to the flux. NGC 1266 has a peak main beam brightness temperature $T_{\rm mb}$ of 250 mK for CO(1–0) and 630 mK for CO(2–1) (Young et al. 2011), or 1.2 Jy for CO(1–0) and 3.5 Jy for CO(2–1) using a conversion factor of 4.73 Jy K^{-1}, standard for the IRAM 30m.

3.2.2 CARMA

NGC 1266 was observed in CO(1–0) with CARMA between 2008 March and 2009 June in three different configurations: D-array (5″ resolution at CO(1–0) with `robust = 0` weighting), B-array (0.7″), and A-array (0.3″). The primary beam had a diameter of 2′ at CO(1–0), covering the full extent of the optical emission. Due to limited correlator bandwidth, a velocity extent of only 420 km s^{-1} at 2.5 km s^{-1} resolution was available for the CO(1–0) line at the time of the observations, enough to adequately measure the properties of the center of the line, but not of the wings. D-array observations of the bright calibrator 0423−013 were taken in order to correct the slope across the bandpass, followed by alternating integrations on the source and a gain calibrator (0339-107), used to correct atmospheric phase fluctuations. The CARMA A and B arrays utilize the

Figure 3.2 The Combined Array for Research in Millimeter Astronomy, sitting at Cedar Flat, CA in the White Mountains. Credit: Katherine Alatalo

Paired Antenna Calibration System (PACS; see Pérez et al. 2010), in which the 3.5 m dishes of the Sunyaev-Zel'dovich Array (SZA) are paired with CARMA antennas forming the longest baselines to correct for atmospheric phase fluctuations. The SZA antennas continually observed a bright quasar (in our case 0339−017) located 5.9° from the source, which was also used to calibrate the gains. The flux calibrator was 0423−013. At 29.9 Mpc, the highest angular resolution (0.3″) corresponds to 44 pc. The data were reduced in the standard manner, using the Multichannel Image Reconstruction, Image Analysis, and Display (`MIRIAD`) software package (Sault et al. 1995).

3.2.3 The SMA

SMA observations were also obtained between 2008 September and 2009 March in two different configurations: compact (4″ resolution at CO(2–1) with `robust = 0` weighting) and extended (2″). The molecular species observed were CO(2–1) and ^{13}CO(2–1) in the 230 GHz band, and CO(3–2) and HCO$^+$(4–3) in the 345 GHz band. The primary beam had a diameter of 45″ at CO(2–1) and 30″ at CO(3–2), which includes all emission captured by the single dish. NGC 1266 was imaged with a bandwidth of 2600 km s^{-1} and a spectral resolution of 2.5 km s^{-1} at CO(2–1), centered on the systemic velocity, and a bandwidth of 1700 km s^{-1} and a spectral resolution of 0.7 km s^{-1} at CO(3–2), also centered on the systemic velocity. We used J0423−013 and J0238+166 as gain calibrators. The bandpass calibrators were 3C454.3 and 3C273, and the flux was calibrated with Titan and Ganymede. The zeroth order continuum emission of 40 mJy and 13 mJy at CO(3–2) and CO(2–1), respectively, was estimated using line-free channels and subtracted from the datacubes. These continuum levels are consistent with being due to the Rayleigh-Jeans tail of dust continuum. The data were reduced using the `MIR` package, and analyzed using `MIRIAD`.

3.2.4 The EVLA

NGC 1266 was observed with the Expanded Very Large Array (EVLA)[2] in the D configuration on 2010 March 20 and 28, giving a total of 264 minutes on source with a correlator setup with 256 channels, each of 31.25 kHz width, centered on H I at the systemic velocity of the galaxy. The gain calibrator was J0323+0534 and the flux and bandpass calibrator was J0137+3309. Standard observing and data reduction techniques were used, performed in the Astronomical Image Processing System (`AIPS`) package. Observations were made at a fixed sky frequency, and the changing topocentric velocity correction between the two observing dates amounts to 0.4 channels; the `AIPS` task CVEL was used to shift one of the datasets before combining them. The data were Hanning smoothed in velocity, which helps to mitigate the effects of interference at 1408 MHz. The final, continuum-subtracted image cube was made with robust weighting (robust parameter = 0), has a beam size $66.9'' \times 43.0''$, and covers the velocity range 1321 to 3014 km s^{-1} at a velocity resolution of 13.4 km s^{-1}. The rms noise level is 0.8 mJy beam^{-1} per channel. There is no H I emission evident anywhere within the primary beam ($31'$ FWHM), but prominent H I absorption against the central continuum source in NGC 1266 is observed.

Archival 1.4 and 5 GHz continuum data obtained at the Very Large Array (VLA) are available for NGC 1266 at resolutions of $1''$ and $0.4''$, respectively. These data for

[2]as of January, 2012, the Enhanced Very Large Array has been renamed the Jansky VLA

Figure 3.3 The Submillimeter Array, located at 13,400ft atop Mauna Kea. There are 8x6m dishes that are used primarily in the submillimeter bands. Credit: Katherine Alatalo

project AB660 were originally taken in December 1992 in the VLA A configuration under the standard 2×50 MHz bands with left and right circular polarizations. Time on source in each frequency was 380 seconds. 3C84 was used as an absolute flux calibrator and B0336–019 was the gain calibrator (Baan & Klöckner 2006). The data were reduced in the standard manner using the `AIPS` package.

3.3 Molecular Line Profile

Figure 3.5 presents the integrated spectra of the ^{12}CO data used in this paper, showing good agreement between the CO(1–0) and CO(2–1) fluxes recovered from the single-dish and the interferometers. Also of note is that the CO(3–2) line profile from the SMA has the same shape as the CO(2–1), including wing emission. The CARMA observations recover $\approx 120\%$ of the single-dish flux, and the SMA observations $\approx 130\%$. Errors in the single-dish baselines and the intrinsic flux variations of the mm-calibrators can account for the discrepancy. Therefore, it appears that both CARMA and the SMA recover all of the single-dish flux.

With its narrow single-peaked central velocity component (hereafter CVC) and high-velocity wings, the integrated profile shape is more akin to those observed in protostellar

Figure 3.4 The Jansky Very Large Array, located in Plains of San Agustin fifty miles west of Socorro, New Mexico.. There are 27×25m dishes and have receivers that observe within the centimeter regime. Credit: Katherine Alatalo

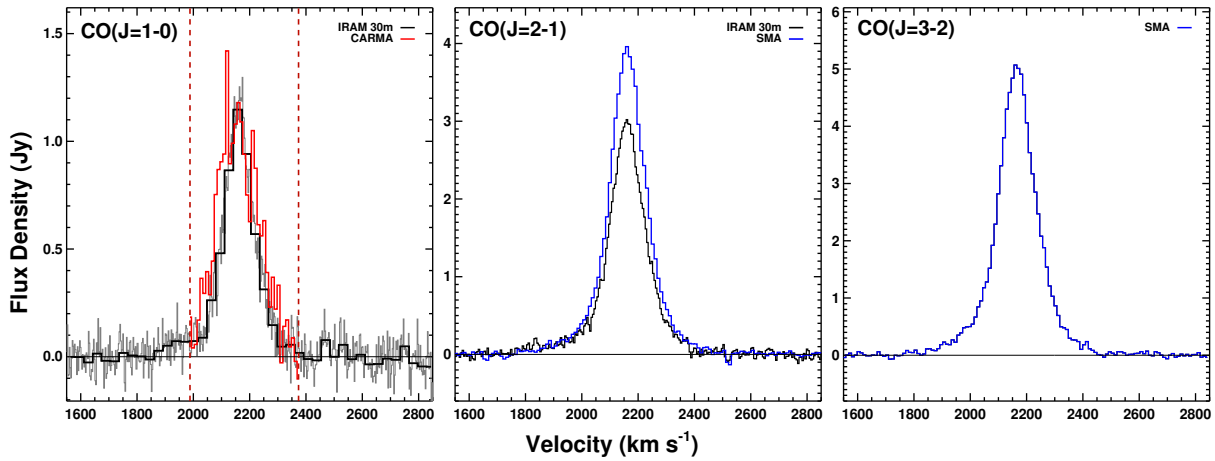

Figure 3.5 **(Left:)** CO(1–0) integrated fluxes from the IRAM 30m (black and gray) and CARMA A, B & D-arrays (red). The total CARMA A, B & D velocity coverage at CO(1–0) is 390 km s^{-1}, compared to 1300 km s^{-1} for the IRAM 30m. The total velocity widths of both observations are present. Dashed red lines indicate the CARMA bandwidth. **(Middle:)** CO(2–1) fluxes from the IRAM 30m (black) and the combined SMA compact (C) and extended (EX) configurations (blue). **(Right:)** CO(3–2) flux from the combined SMA C and EX configurations. CARMA recovers 20% more flux than the single-dish, and the SMA 30%, within single-dish baseline and flux calibration uncertainties.

outflows (e.g. Bally & Lada 1983) than those of typical external galaxies, where a double-horned profile is usually seen.

Fig. 3.3 shows the fits and residuals of the single and nested Gaussians. Table 1 gives a summary of the fitted Gaussian parameters. We find that the broad wing and CVC, which we identify respectively with the broad and narrow Gaussian of the nested Gaussian fits, encompass respectively 34% and 66% of the CO(2–1) single-dish integrated flux, which has the best signal-to-noise ratio. When comparing the line to the escape velocity radial profile measured in the plane of the galaxy (see Figure 3.7), we find that at least 2.5% of the wing emission is from velocities exceeding the innermost local escape velocity (calculated at 2″) of $v_{\rm esc} \approx 340$ km s^{-1}. The true percentage may be higher, depending on the geometry of the high velocity gas. If the molecular gas is located either out of the plane of the galaxy or at larger radii, the local potential (and thus $v_{\rm esc}$) would be much reduced. The $v_{\rm esc}$ profile was calculated using Jeans Anisotropic Multi-Gaussian Expansion (MGE) modeling (JAM; §3.5), to extract the true potential of the galaxy by modeling the observed stellar kinematics (Scott et al. 2009; 2012, submitted).

Table 3.1 Fitted Gaussian parameters for the CO(1–0), CO(2–1) and CO(3–2) lines

	CVC	**broad wing**
CO(1–0)		
$v_{\rm sys}$ =	2162 ± 1.4 km s^{-1}	2142 ± 20 km s^{-1}
FWHM =	114 ± 3.9 km s^{-1}	353 ± 17 km s^{-1}
$T_{\rm mb}$(peak) =	0.21 ± 0.006 K	0.03 ± 0.005 K
$\rm I_{CO}$ =	25.5 ± 1.1 K km s^{-1}	9.6 ± 1.8 K km s^{-1}
CO(2–1)		
$v_{\rm sys}$ =	2161 ± 0.5 km s^{-1}	2151 ± 4.4 km s^{-1}
FWHM =	128 ± 1.9 km s^{-1}	353 ± 17 km s^{-1}
$T_{\rm mb}$(peak) =	0.53 ± 0.01 K	0.10 ± 0.01 K
$\rm I_{CO}$ =	71.1 ± 1.6 K km s^{-1}	36.7 ± 3.8 K km s^{-1}
CO(3–2)		
$v_{\rm sys}$ =	2166 ± 0.4 km s^{-1}	2162 ± 3.7 km s^{-1}
FWHM =	134 ± 1.3 km s^{-1}	353 ± 17 km s^{-1}
$F_{\rm peak}$ =	4.15 ± 0.03 Jy	0.82 ± 0.03 Jy
$\rm S_{CO}$ =	589 ± 7.5 Jy km s^{-1}	306 ± 18 Jy km s^{-1}

Note: $\rm I_{CO}$ is the integrated CO line intensity from the IRAM 30m, similarly for $\rm S_{CO}$ and the SMA. The broad wing component accounts for 27% and 34% of the total flux for CO(1–0) and CO(2–1), respectively. The broad wing component of CO(3–2) also contributes 34% of the total flux. The 7% difference in the broad wing contribution between the transitions is attributed to the uncertainties in the fits to the line profiles. We will adopt 34% as the more likely value, due to the better signal-to-noise ratios at CO(2–1) and CO(3–2). CO(3–2) data were only obtained with an interferometer, thus the natural unit of this line Jy. To convert the CO(3–2) fluxes to Kelvin, we first divide by 9 (the ratio of the CO(3–2) and CO(1–0) frequencies squared), then multiply by the K per Jy conversion factor of the adopted beam of 4.73 Jy K^{-1}. The errors listed are the formal uncertainties of the fits. The value and uncertainty of the FWHM of the broad wing component for all transitions are adopted from the fit to the CO(2–1) line.

3.4 Molecular Gas Mass

Using the CO (1–0) single-dish flux quoted in Young et al. (2011), a column density of molecular hydrogen $\rm N(H_2) = X_{CO} \int T_{mb}\ dv$, where the conversion factor $X_{\rm CO} = 2 \times 10^{20}$ cm^{-2} (K km s^{-1})$^{-1}$ (Dame et al. 2001), a beamsize of 21.6″, and a beam area of 529 sq.arcsec (which includes a beamshape correction of 1/ln(2); Baars 2007), the total mass of the molecular gas would be 1.7×10^9 $\rm M_\odot$, including a correction factor of 1.36 to account for He. However, the wing emission is optically thin (see §3.6.1) and contributes little to the total mass. Considering only the CVC, the molecular gas mass is 1.1×10^9

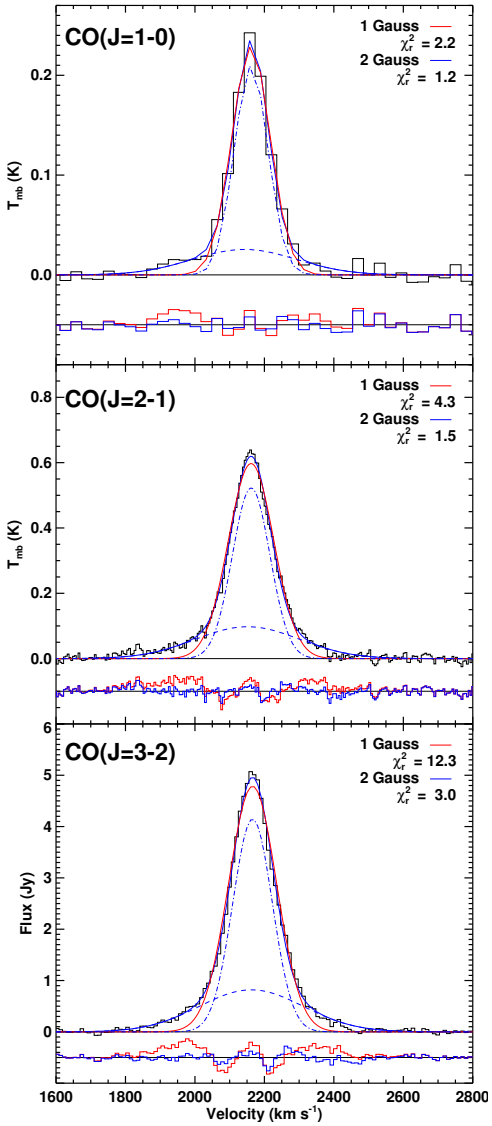

Figure 3.6 CO(1–0) (top), CO(2–1) (middle) and CO(3–2) (bottom) integrated profiles of NGC 1266 from the IRAM 30m and SMA (CO(3–2) only). We also show a comparison between a one Gaussian fit the the data (red) and a two-Gaussian fit (blue) consisting of a narrow (blue dot-dashed line) and a broad (blue dashed line) component. Residuals are plotted below the fits and show that a two-Gaussian fit is a much better match to the data. The width of the broad component is fixed to 353 km s^{-1}, initially constrained using the fit the to the CO(2–1) line. The goodness of fit improves significantly with the addition of the broad component, illustrated both in the measured χ^2 as well as in the residuals.

$M_\odot$, including He.

Draine et al. (2007) derive a total dust mass of 1.02×10^7 $M_\odot$ in NGC 1266 (rescaled to our distance of 29.9 Mpc), using *Spitzer* Infrared Nearby Galaxy Survey (SINGS) data. Since a significant H I reservoir is not observed in NGC 1266 (see below), we may assume that all of the measured dust is associated with the molecular gas. Adopting a gas-to-dust mass ratio of 100 (Savage & Mathis 1979), the dust mass implies a molecular gas mass of 1.0×10^9 $M_\odot$. The derived dust mass is thus in good agreement with the mass derived from the CO measurements and a standard $X_{\rm CO}$ conversion factor.

3.5 Core of the NGC 1266 emission

Figure 3.8 shows the full spatial extent of the CARMA CO(1–0) integrated emission (Δv = 390 km s^{-1}), overlaid on an R-band image of the galaxy from SINGS, illustrating that the vast majority of the molecular gas is restricted to the innermost region of NGC 1266. The righthand panel of the figure shows that the molecular gas is not well described by a single spatial component, but instead as both a diffuse, relatively extended component, which we will call the "envelope," and a highly concentrated nuclear structure, which we will call the "nucleus".

In order to separate the nucleus from the envelope in the CARMA map, we take a slice across the integrated intensity map at a position angle of 145°, to trace the elongation of the narrow component. We then fit two Gaussians to the nucleus and the envelope, respectively. Figure 3.9 illustrates the radial cut as well as the the nuclear Gaussian component, which has a characteristic FWHM of 1.05″. We use FWHM/2 to define a characteristic deconvolved radius $R_{\rm nuc}$ of $\approx$ 60 pc (after accounting for the CARMA beam). Using this, the peak intensity of the profile in Fig. 3.9 (24.3 Jy beam^{-1} km s^{-1}), the pixel size of 0.08″ pix^{-1}, and $X_{\rm CO} = 2 \times 10^{20}$ cm^{-2} (K km s^{-1})$^{-1}$, we derive a molecular gas mass for the nucleus of $M_{\rm nuc,H_2+He} = 4.1 \times 10^8$ M$_\odot$, including He. As the spatial distribution of the broad wing emission in the central region of the CARMA CO(1–0) integrated image is unknown, we do not subtract a potential wing contribution from this nucleus molecular gas mass. If we assume that the rest of the mass in the CVC comes from the envelope, we deduce that $M_{\rm env} \approx 7.0 \times 10^8$ M$_\odot$, including He.

Figure 3.10 is a map of the first moment of the CO(1–0) emission, and shows a clear velocity gradient across the nucleus. Figure 3.11 is the position-velocity (PV) diagram at a position angle of 90° (i.e., roughly along the kinematic major axis), suggestive of a rotating disk with a velocity gradient of 1.8 km s^{-1} pc^{-1}. Rotation can be traced on the PV diagram to a radius of 54 pc, consistent with the radius of the nucleus derived above. At $R_{\rm nuc} \approx 60$ pc, we derive a maximum projected rotation velocity of the nucleus of $v_{\rm rot} \approx$110 km s^{-1}. The corresponding enclosed dynamical mass, assuming circular rotation and spherical symmetry ($M_{\rm dyn,nuc} = R_{\rm nuc} v_{\rm rot}^2 / \sin^2 i_{\rm nuc} G$, where $i_{\rm nuc}$ is the inclination of the nuclear disk and G is the gravitational constant), is uncertain because of the unknown inclination, but the formal lower limit ($i_{\rm nuc} = 90°$) is 1.5×10^8 M$_\odot$. A rough inclination estimate based on the axial ratio of the CO(1–0) integrated intensity map shown in Figure 3.8 and the assumption of a thin disk yields $i_{\rm nuc} \approx 34°$, and thus an enclosed dynamical mass $M_{\rm dyn,nuc} \approx 4.9 \times 10^8$ M$_\odot$. The dynamical mass calculated using the rotation of the nucleus is therefore consistent with the ^{12}CO-derived molecular gas mass of the nucleus, when taking into account a correction associated with the inclination. The stellar contribution to the nucleus mass is discussed later.

An independent estimate of the mass of molecular gas in the core was obtained via dynamical modeling of the stellar kinematics. For this we constructed a MGE model (Emsellem, Monnet & Bacon 1994) of the stellar mass distribution of NGC 1266 from our

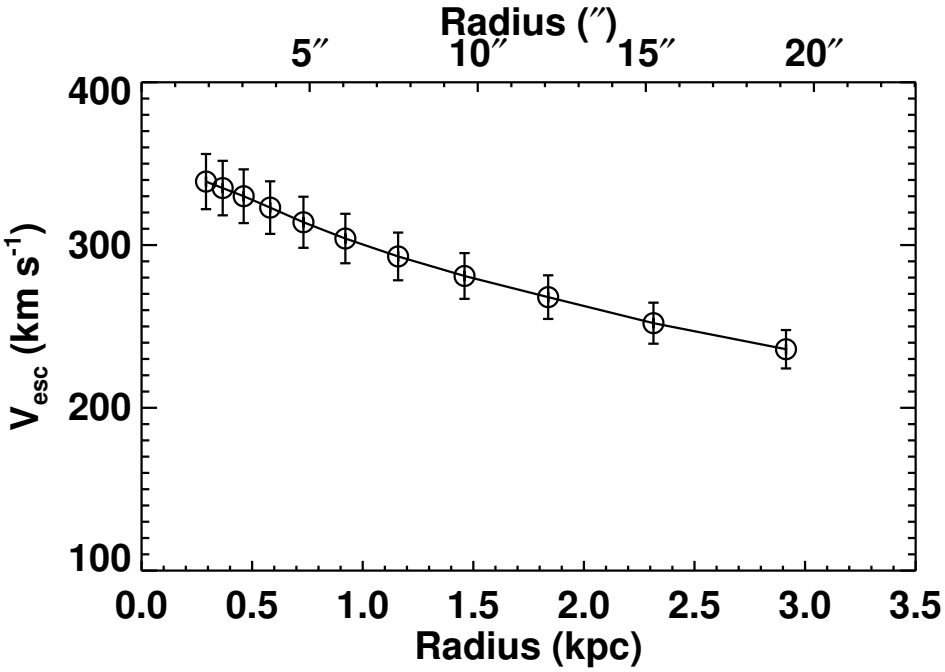

Figure 3.7 The radial escape velocity profile of NGC 1266. The escape velocity was derived using Jeans Anisotropic Multi-Gaussian Expansion modeling (JAM) of the stellar kinematics (Scott et al. 2009, 2012, in prep).

own R-band Isaac Newton Telescope (INT) photometry (Scott et al. 2012, submitted) and the software of Cappellari (2002). We used this MGE model to build an axisymmetric dynamical model of the stellar kinematics based on the Jeans Anisotropic MGE (JAM) formalism (Cappellari 2008). The global anisotropy, inclination and mass-to-light ratio (M/L) of the galaxy were fitted to the large-scale ATLAS^{3D} `SAURON` stellar kinematics (Cappellari et al. 2012) and will be discussed elsewhere. In this particular case the JAM model also explicitly includes as an extra free parameter: the mass of the molecular gas in the core, modeled as a dark Gaussian with a width of 1.2″. The JAM modeling does not include direct evidence of the stellar component in the nucleus of NGC 1266, and is based on interpolation. The mass of molecular gas that best fits the `SAURON` stellar kinematics in the center is $M_{\rm gas} \approx 8 \times 10^8$ M$_\odot$, with a factor ≈ 3 uncertainty dominated by systematic effects. This value is an order of magnitude larger than the mass in stars within 100 pc of the center, $M_{\star,100{\rm pc}} \approx 5 \times 10^7$ $M_\odot$, as determined from an analogous MGE mass model without the molecular core. This result is thus consistent with the mass in the center of NGC 1266 being dominated by molecular gas.

One final consistency check on the molecular gas mass can be performed using the ^{13}CO(1–0) single-dish profile obtained as part of the dense gas census of ATLAS^{3D}

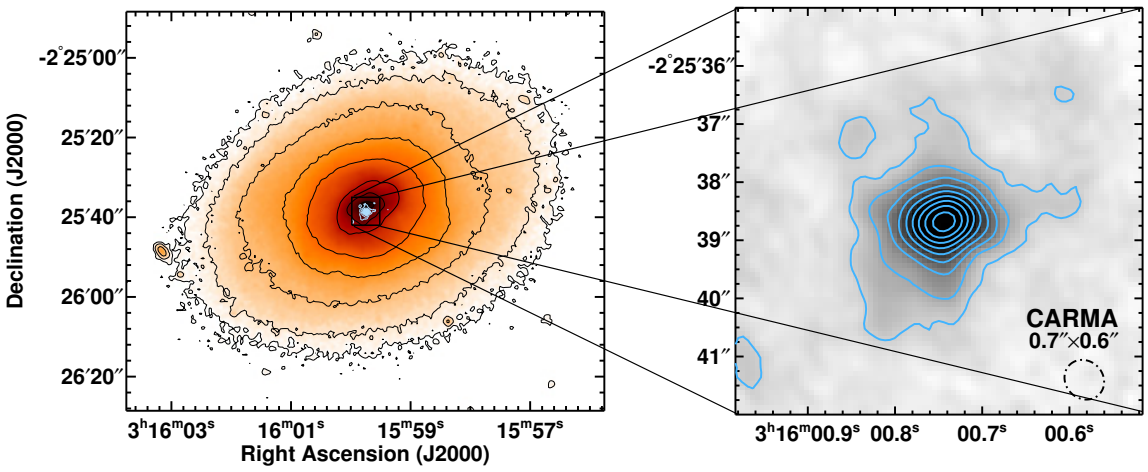

Figure 3.8 **(Left)** Contours of the integrated CO(1–0) molecular gas detected by CARMA (blue), overlaid with the isophotes (black) and grayscale of an R-band image from the Cerro Tololo Inter-american Observatory (CTIO) 1.4m telescope (SINGS). **(Right)** A zoomed-in version of the CO(1–0) integrated intensity map. The synthesized beam ($0.7'' \times 0.6''$) is plotted in the lower right corner. The CARMA CO(1–0) integrated intensity map was created by summing the full velocity width of the CARMA cube, including the A, B and D arrays. Robust = 0 weighting was used in order to reveal low surface brightness, more diffuse structures at the expense of resolving the most compact components. Contour levels are 3, 6, 9, 12, 15, 18, 21, 24 and 27 Jy beam^{-1} km s^{-1} (rms = 1.0 Jy beam^{-1} km s^{-1}).

galaxies (Crocker et al. 2012), shown in Fig. 3.12. The total ^{13}CO(1–0) line intensity is 0.98 K km s^{-1} within the 22.4″beam of the IRAM 30m telescope. We must first correct $I(^{13}\mathrm{CO})$ to reflect a more realistic size for the emitting region for which we adopt a radius of $\approx 1''$. The correction corresponds to the ratio of the two solid angles subtended: $\Omega_{\mathrm{beam}}/\pi R^2$, in this case 567 arcsec^2/3.14 arcsec^2. The resulting corrected $I(^{13}\mathrm{CO})$ is 177 K km s^{-1}. Using the ^{13}CO to A_V conversion from Lada et al. (1994), $I(^{13}\mathrm{CO})/(\mathrm{K\ km\ s^{-1}}) = 1.88 + 0.72\ \mathrm{mag}^{-1}\ A_V$ results in an extinction $A_V \approx 243$ mag. Converting A_V to N(H$_2$) using $N(\mathrm{H_2})/A_V = 9 \times 10^{20}$ cm^{-2} mag^{-1} from Schultz & Wiemer (1975) and Bohlin, Savage & Drake (1978), and then converting N(H$_2$) to a molecular gas mass, yields $M_{\mathrm{nuc}} \approx 3.2 \times 10^8$ M$_\odot$, corrected for He. Therefore the above ^{13}CO–derived mass is in reasonable agreement with the ^{12}CO-derived molecular gas mass of 4.1×10^8 M$_\odot$.

With a molecular gas mass of 4.1×10^8 M$_\odot$ (including He), assuming a circular disk, the mean molecular hydrogen surface density in the nucleus is $\Sigma_{\mathrm{H_2}} \approx 2.7 \times 10^4$ M$_\odot$ pc^{-2}

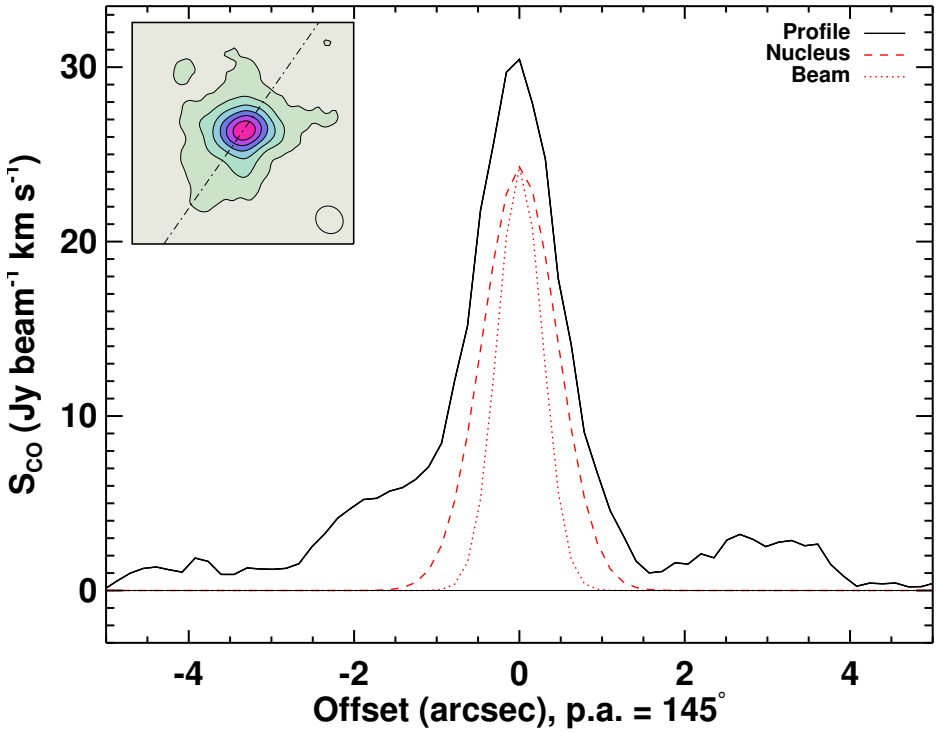

Figure 3.9 Slice of the CO(1–0) integrated intensity map from CARMA at a 145° position angle (see inset). The radial profile requires two Gaussians for a good fit, an "envelope" and a "nuclear" component. The nuclear component (red dashed line) has a peak intensity of 24.3 Jy beam^{-1} km s^{-1} and a FWHM of 1.05″, (0.82″ after correcting for convolution effects from the beam). The radial profile of the beam is also shown (red dotted line), to illustrate that the nucleus is spatially resolved. The envelope is approximately 4.5″, or ≈ 650 pc edge to edge.

(corresponding to a mean column density $N(H_2) \approx 1.7 \times 10^{24}$ cm^{-2}) and the mean volume density of H_2 is at least 6.9×10^3 cm^{-3} (lower limit assuming spherical symmetry). Given that tracers with higher critical densities, such as ^{13}CO, CS, HCO$^+$ and HCN, are robustly detected in the nucleus (Alatalo et al. 2012, in prep), the molecular gas is likely to be clumpy.

The dynamical mass, JAM mass and ^{13}CO-derived mass agree quite well with the ^{12}CO(1–0)-derived molecular gas mass of the nucleus, indicating that using the standard Milky Way conversion factor $X_{CO} = 2 \times 10^{20}$ cm^{-2} (K km s^{-1})$^{-1}$ is appropriate to determine the mass of the molecular material in the center of NGC 1266. The JAM modeling also indicates that the stellar contribution to the mass of the region with molecular gas is negligible.

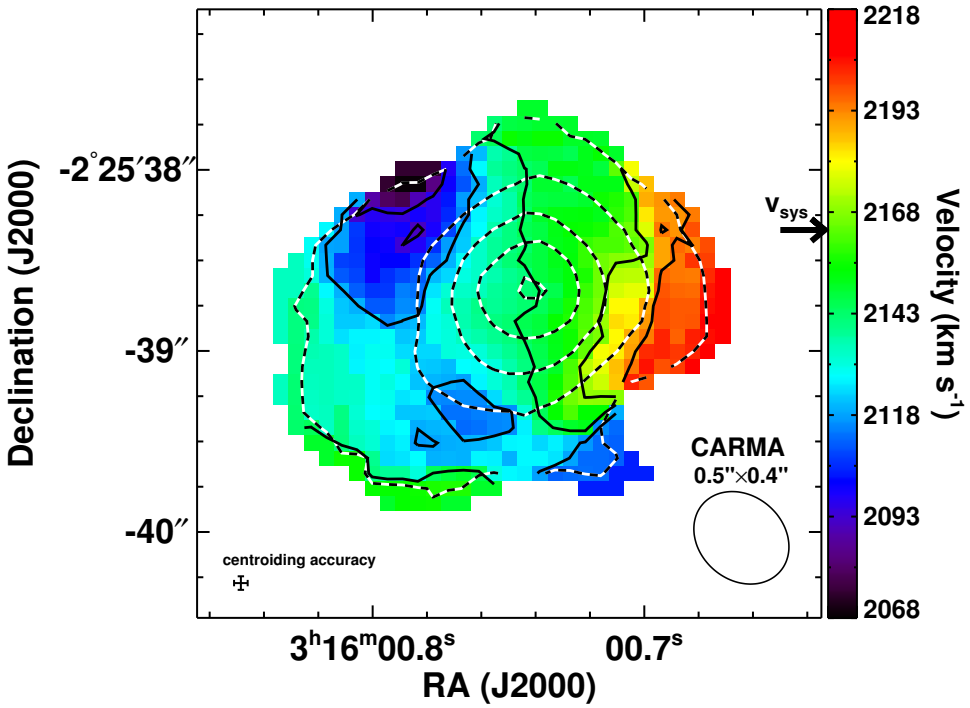

Figure 3.10 CO(1–0) mean velocity map from CARMA overlaid with contours from the corresponding integrated intensity map (black and white). A velocity gradient is clearly seen across the nucleus, interpreted as a thick rotating disk (see text). These velocity moments were constructed from the CARMA A and B array data only (synthesized beam $0.5'' \times 0.4''$), to extract structures at the smallest spatial scales at the expense of the extended, diffuse emission. The velocity contours are spaced at 25 km s^{-1}, or 2069, 2094, 2119, 2144, 2169, and 2194 km s^{-1}. The systemic velocity of 2160 km s^{-1} is denoted with an arrow. The centroiding accuracy is derived using the FWHM$_{\rm beam}$/2 SNR (Taylor, Carilli & Perley 1999), where SNR is the signal-to-noise ratio and is at least 3 per channel, yielding an accuracy of at least $0.08''$.

3.6 The Outflow of NGC 1266

3.6.1 Wings of the Emission

We use the CO(2–1) SMA data to resolve the spatial extent of the high velocity wings of the molecular gas, because of the limited velocity coverage of the correlator when the CARMA data were taken. This hybrid data were used in order to overcome the resolution impairment of the SMA and the velocity impairment of CARMA, to fully illustrate the nature of the molecular gas in NGC 1266. In order to minimize contamination from the nucleus, we made a map of the emission over the velocity ranges v=1590–1890 km s^{-1}

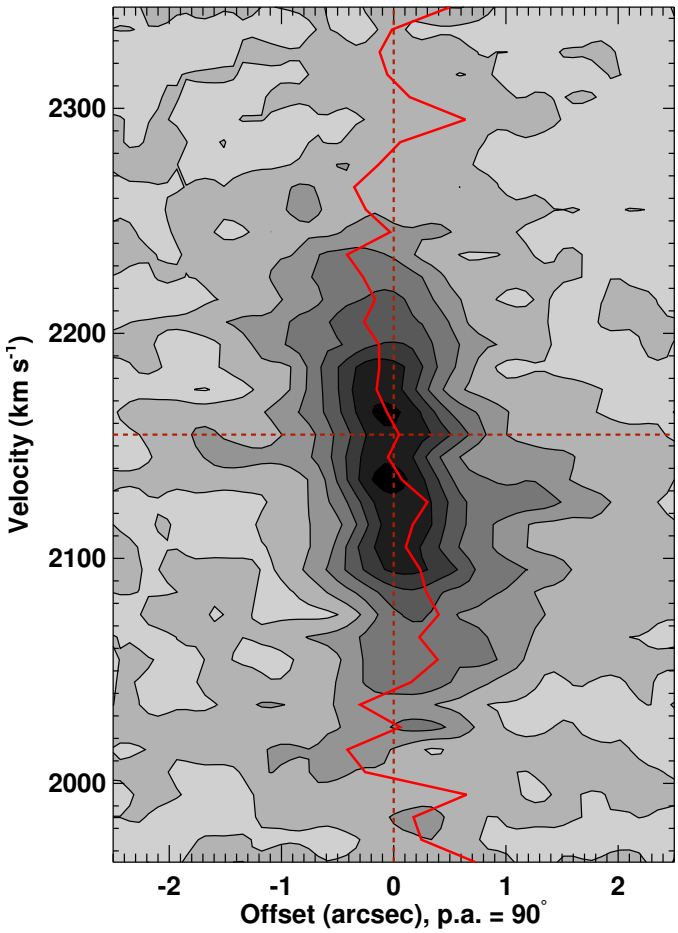

Figure 3.11 Position-velocity diagram of NGC 1266 for our CO(1–0) A and B array CARMA data, taken at position angle of 90°. The observed lack of a turnover is indicative of the gas not reaching the flat part of the rotation curve. The data are consistent with rotation with a gradient of 1.8 km s^{-1} pc^{-1} in the inner parts. The red line is a trace of the peak at each velocity. The dark red dashed lines indicate $v_{\rm sys}$ and the center.

and v=2350–2650 km s^{-1}, eliminating the central 460 km s^{-1}. Figure 3.13 shows the velocity ranges of the CVC and the wings of the line used for mapping. The offsets from $v_{\rm sys}$ were chosen to achieve equal signal-to-noise ratios of 6 for the peaks of the red- and blue-shifted images in Figure 3.14, which shows that the wings are considerably more extended spatially than the nucleus. If we model the outflow as a bi-spherical structure, similar to what is observed in M82 (Walter, Weiss & Scoville 2002), and represent the red- and blueshifted lobes by two tangent spheres whose point of contact is the nucleus, the distance the molecular gas has traveled from the center is equal to the diameter of the lobes. We measure the width of the blueshifted and redshifted lobes to be $\approx 3.4''$and $4.2''$, respectively. Taking the average of the lobe extents and correcting for convolution

with the 2″ SMA beam, gives us a characteristic extent of ≈ 3.2″, or 460 pc. The red- and blue-shifted wings are also spatially offset from one another. The position centroids of the lobes are separated by ≈ 2.3″, thus each is offset by about 170 pc from the galaxy center. The large spatial extent of the wing emission rules out an interpretation whereby the high gas velocities are the result of gas having fallen into the central potential well of the galaxy. We thus conclude that the source of the high velocity wing emission is a kpc–scale molecular outflow, with $R_{\rm outflow} \approx 460$ pc.

Further evidence that the wings represent an outflow is that the axis connecting the lobes is intersected by the CVC and is not aligned with the kinematic major-axis of the nuclear gas disk. This suggests that the broad wing emission is composed of gas that is being expelled, and is not an extension of the nuclear material. If we estimate the inclination of the outflow (with respect to the plane of the sky) using the average offset of the centroids with respect to the nucleus (2.3″) divided by the average extent of the lobes (3.2″) calculated above, we obtain an inclination angle of roughly 20°.

The mass of outflowing gas is somewhat uncertain because the wings are unambiguously detected only in ^{12}CO (Fig. 3.5), requiring that the density, optical depth and temperature of the outflow be determined from the excitation of the three lowest CO rotational transitions. We use the beam-normalized (to the single-dish CO(1–0) beam of 21.6″) intensities of the wing emission from the CO(1–0) and (2–1) IRAM 30m single-dish spectra and the CO(3–2) SMA spectrum (see Table 1). The beam-corrected values are 11.93 K km s^{-1} for CO(1–0), 9.16 K km s^{-1} for CO(2–1) and 7.16 K km s^{-1} for CO(3–2).

We use the `RADEX` large velocity gradient (LVG) software (van der Tak et al. 2007) to determine volume densities and column densities in the wind. With `RADEX`, assuming a line width $v_{\rm fwhm} = 353$ km s^{-1}, we find that the conditions required to reproduce the beam-corrected flux ratios above are an H_2 density $n(H_2) \approx 10^3$ cm^{-3}, a kinetic temperature $T_{\rm kin} \approx 100$ K, and a CO column density $N({\rm CO}) \approx 1.0 \times 10^{16}$ cm^{-2}. The N(CO) was also constrained using on the optically thin estimate of Knapp & Jura (1976) assuming subthermally excited CO, and the result is consistent with that from `RADEX`. Assuming a CO/H_2 abundance ratio of 10^{-4}, the derived N(CO) and our adopted beamsize of 21.6″imply a molecular outflow mass of 2.4×10^7 M$_\odot$, including He. It is however possible that the outflowing molecular mass is higher. The optically thin approximation (i.e. that we are seeing all CO molecules) provides us with a lower limit to the total outflowing molecular mass. If the state of the molecular gas in the outflow of NGC 1266 is more akin to gas in either ULIRGs or giant molecular clouds (GMCs) in the Milky Way, where a conversion factor ($X_{\rm CO}$) is used, the total outflowing mass could be a factor of ≈ 10 – 20 higher.

3.6.2 Additional Data

While no H I emission is detected in NGC 1266, H I appears in absorption against the 1.4 GHz continuum source. The H I observations have thus far only been taken at

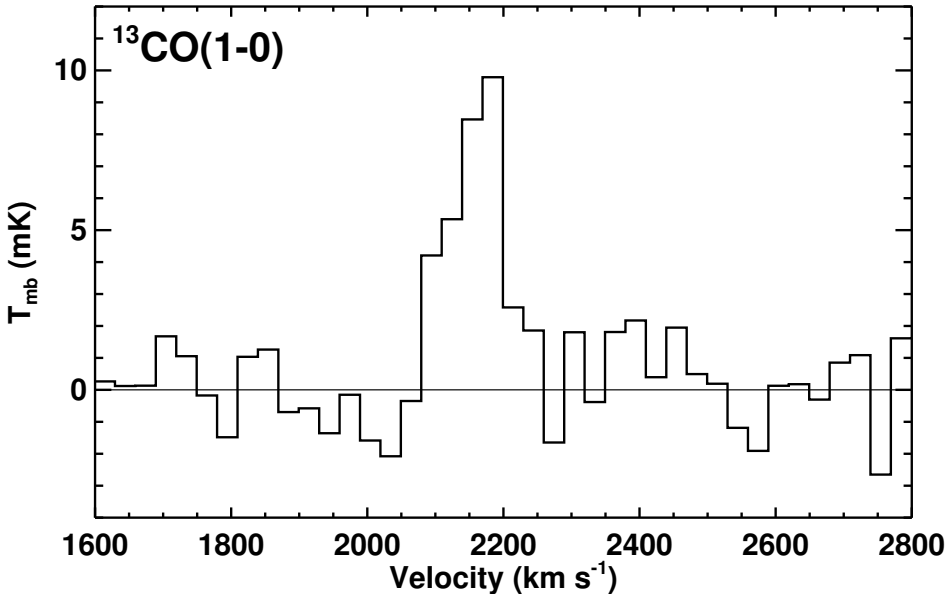

Figure 3.12 ^{13}CO(1-0) spectrum taken with the IRAM 30m telescope, as part of a larger census of dense gas in ATLAS^{3D} ETGs (Crocker et al. 2012). The beam at this frequency has a 22″ half-power beam width (HPBW) and the channels shown are 30 km s^{-1}.

low resolution, so are presently unresolved. The top panel of Figure 3.15 shows the H I absorption profile, which exhibits a broad blueshifted velocity component, and the fitted Gaussians describing the absorption profile. The bottom panel of Figure 3.15 shows a good correspondence between the blueshifted absorption feature in the H I and the high-velocity wing of the CO(2–1) emission line profile. This identifies the blueshifted molecular gas as moving out (as opposed to infalling from behind), and implies that the outflow in NGC 1266 has multiple phases.

Calculating the column density from the absorption feature, assuming $T_{\rm spin} = 100$ K, reveals that the H I column in front of the continuum source is $N_{\rm H} = 2.1 \times 10^{21}$ cm^{-2}, with the outflowing component contributing 8.9×10^{20} cm^{-2} and the systemic component contributing 1.2×10^{21} cm^{-2}. If we assume that the H I and CO are co-spatial ($R_{\rm HI} = R_{\rm outflow} = 460$ pc), and that the total mass of outflowing H I is twice what we calculate (since we are only able to detect the blueshifted lobe), we derive the total H I mass in the outflow to be 4.8×10^6 M$_\odot$ per lobe, totaling 9.5×10^6 M$_\odot$. If we include the H I contribution, the total neutral gas mass (H I + H_2 + He) of the outflow is thus 3.3×10^7 M$_\odot$.

The molecular gas (as traced by CO) and atomic gas are likely not the only constituents of the mass in the outflow. By not accounting for other states of the gas, we are underestimating the true outflow mass. For example, Roussel et al. (2007) detect a large reservoir of warm (T > 100 K) H_2 in NGC 1266 using *Spitzer*, with a total mass of

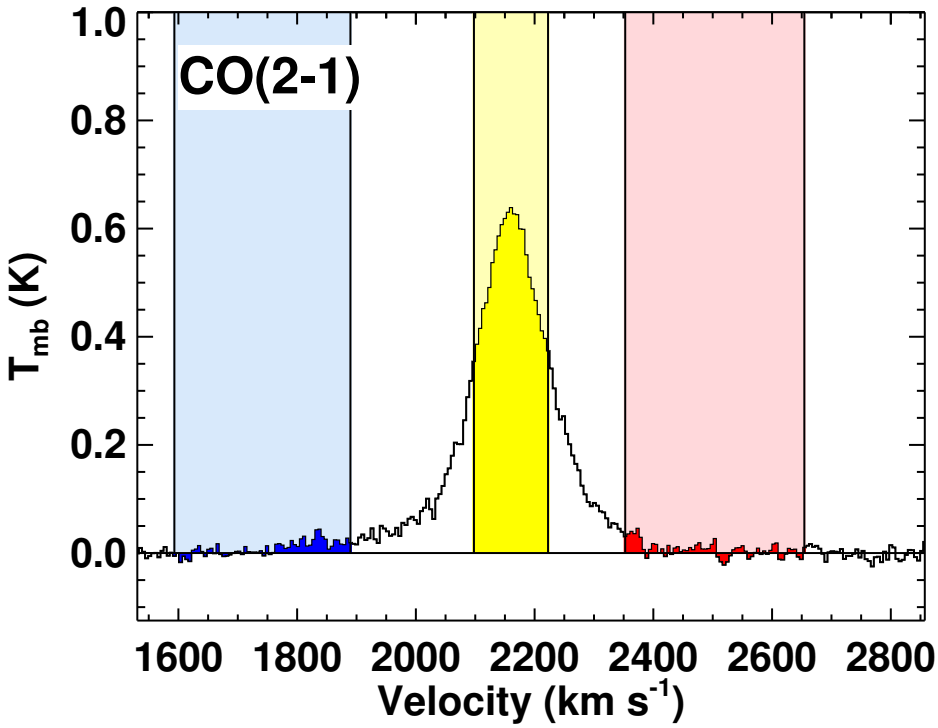

Figure 3.13 CO(2–1) spectrum from the IRAM 30m telescope, indicating the velocity ranges that were summed together in order to gauge the larger scale nature of the outflows.

$M_{\rm H_2,warm} \approx 1.3\times10^7$ M$_\odot$. It is very likely that this mass of warm H_2 belongs to the outflow rather than the nuclear disk. The total warm H_2 luminosity is $L_{\rm H_2,warm} \approx 1\times10^{41}$ erg s^{-1}. For the nuclear region to sustain this luminosity of warm H_2 would require an AGN with a bolometric luminosity of $\gtrsim 2\times10^{44}$ erg s^{-1}, assuming first that $L_{X,\rm AGN} \gtrsim 100 L_{\rm H_2,warm}$, Ogle et al. 2010; and $L_{\rm bol,AGN} \gtrsim 16 L_X$, Ho 2008), a factor of three larger than $L_{\rm FIR}$ (7×10^{43} erg s^{-1}; Gil de Paz et al. 2007). If this warm H_2 is indeed part of the outflow, our estimate of the total mass of the outflow should increase by 40%. Adding in the contribution of the ionized and hot gas would increase the mass of the outflow further, thus we consider our estimate of 3.3×10^7 M$_\odot$ to be a conservative lower limit.

Combined with the molecular emission and H I absorption data, X-ray, Hα, and radio continuum data further elucidate the nature of the outflow. Figure 3.16 shows a comparison of the Hα narrow-band image from the SINGS survey (Kennicutt et al. 2003), a 1.4 GHz radio continuum map (Baan & Klöckner 2006), and the unsmoothed X-ray map from the *Chandra* X-ray Telescope Advanced CCD Imaging Spectrometer (ACIS) on the same spatial scale (Alatalo et al. 2012, in prep). A spectral fit to the *Chandra* data co-added over the extent of the emission shows that the X-ray emission is dominated

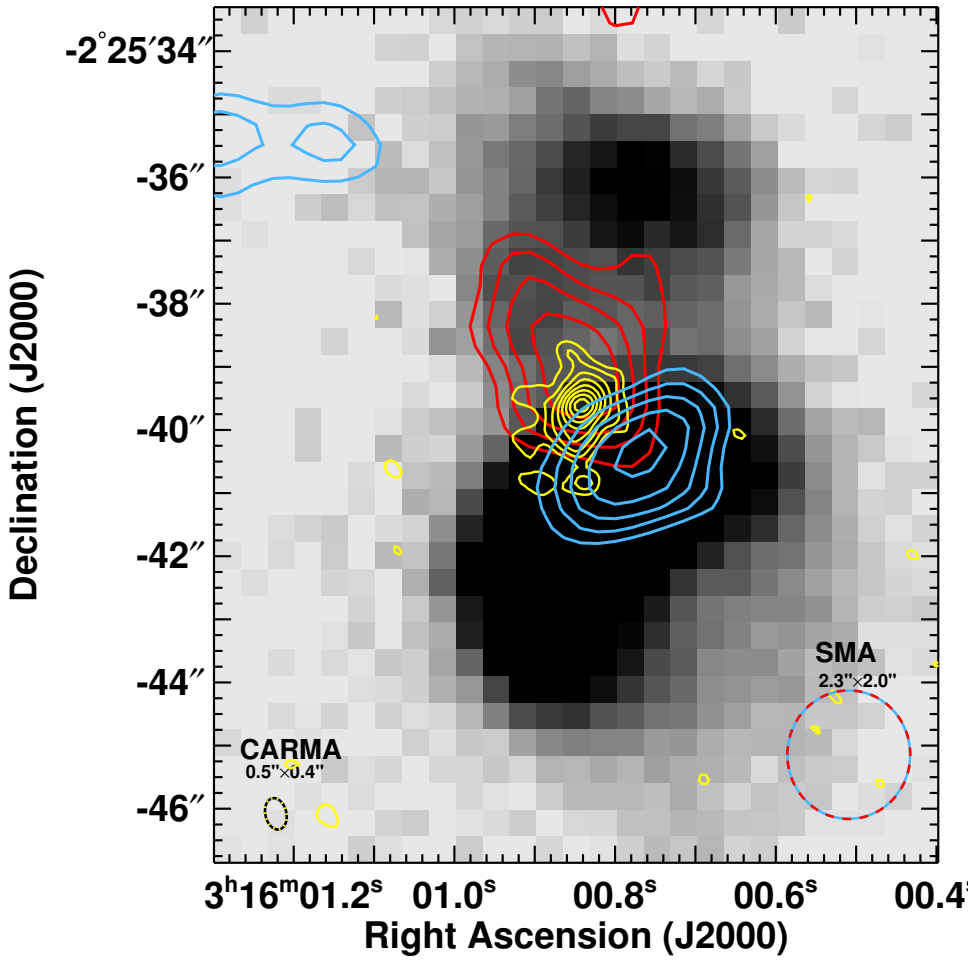

Figure 3.14 CO core and wings in NGC 1266, overlaid on a greyscale Hα narrow-band image from SINGS. Superimposed contours are from the CARMA CO(1–0) integrated intensity map (yellow) and the SMA CO(2–1) redshifted (red) and blueshifted (blue) wings. Contours are 3, 4, 5 and 6 Jy beam^{-1} km s^{-1} for the red and blue components (rms = 1 Jy beam^{-1} km s^{-1}) and 6.4, 8.6, 10.8, 13.0, 15.2 and 17.4 Jy beam^{-1} km s^{-1} for the yellow component (rms = 1.1 Jy beam^{-1} km s^{-1}). The yellow component respresents the CVC, showing that the majority of the gas at $v_{\rm sys}$ sits in the nucleus.

by thermal bremsstrahlung. The 1.4 GHz continuum shows both a centrally peaked, unresolved core (possibly from a radio jet), as well as two more diffuse spurs running from the southeast to the northwest. The lobed structure first apparent in the molecular gas (Fig. 3.14) is seen in all these tracers. In fact, the X-rays and the 1.4 GHz spurs, which do not suffer significantly from extinction, show an asymmetry between the foreground and background lobes, relative to the CO at $v_{\rm sys}$. This likely means that the relative faintness of the Hα flux from the redshifted lobe as compared to the blueshifted lobe is not primarily due to extinction. The spatial relationship between the molecular gas and the X-ray, 1.4 GHz and Hα emitting material supports this picture. The Hα, radio spurs, and X-rays likely are emitted from the interface where the outflowing material collides with the interstellar medium (ISM) of NGC 1266. This interpretation is supported by the thermal bremsstrahlung emission in the *Chandra* spectrum, although the radio spur emission could also possibly come from a radio jet.

The geometry of the CO outflow can be explained using two possible scenarios. Firstly, it could be due to a molecular outflow launched deep in the nucleus of the galaxy, confined azimuthally by the massive molecular disk. Secondly, it could directly originate from the molecular disk, and be entrained by hot winds launched by the AGN, surviving only because of the extreme density of the molecular disk. In either of these scenarios, at least some of the molecular material escapes from the galaxy still intact, and will energize the intergalactic medium (IGM). This is especially true if the outflow continues to accelerate from its launch point.

Table 3.2 NGC1266 Characteristic Properties

$M_{\rm nucleus}$	4.1×10^8 M$_\odot$
$R_{\rm nucleus}$	60 pc
$M_{\rm CVC}$	1.1×10^9 M$_\odot$
$< \Sigma({\rm H_2})_{\rm nucleus} >$	2.7×10^4 M$_\odot$ pc^{-2}
$< N({\rm H_2})_{\rm nucleus} >$	1.7×10^{24} cm^{-2}
$< n({\rm H_2})_{\rm nucleus} >$	6.9×10^3 cm^{-3}
$M_{\rm H\ I+H_2,outflow}$	3.3×10^7 M$_\odot$
$M_{\rm H_2,outflow}$	2.4×10^7 M$_\odot$
$R_{\rm outflow}$	450 pc
$v_{\rm outflow}$	177 km s^{-1}
$\tau_{\rm dyn}$	2.6 Myr
$\dot{M}$	13 M$_\odot$ yr^{-1}
KE$_{\rm outflow}$	1.0×10^{55} ergs
$L_{\rm outflow}$	1.3×10^{41} erg s^{-1}
$\tau_{\rm dep}$	85 Myr

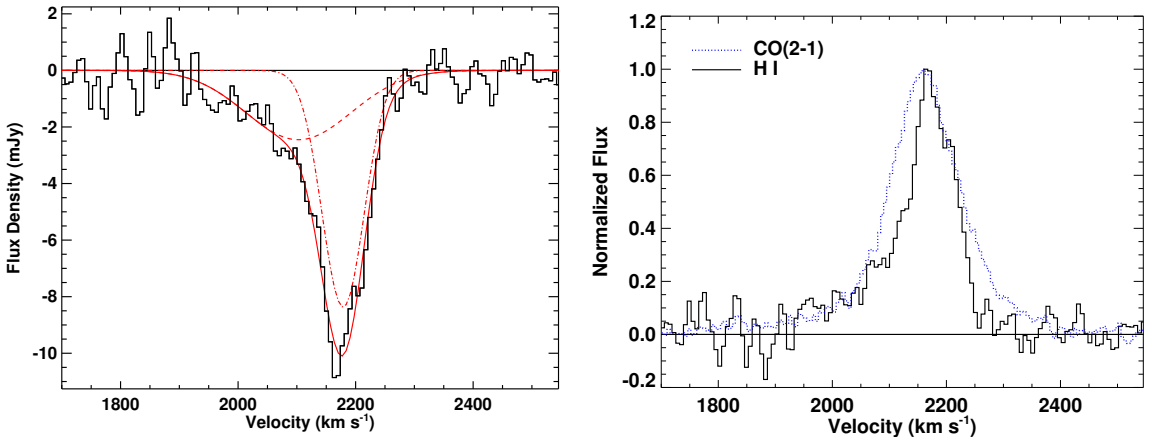

Figure 3.15 **(Top:)** Continuum-subtracted H I profile in the central pixel of the unresolved map observed with the EVLA D-array (black). The continuum level for the source is 113 mJy. The blueshifted wing is evident in the absorption profile, reaching $\gtrsim 200$ km s^{-1} before dropping into the noise. Overlaid (red) is a two-Gaussian fit to the absorption profile, including a blueshifted high-velocity contribution (dashed) and a deeper absorption contribution near $v_{\rm sys}$ (dot-dashed). **(Bottom:)** A direct comparison between the H I absorption profile (black) and the CO(2–1) emission spectrum from the IRAM 30m telescope (blue dotted). The CO emission and H I absorption profiles trace each other well at high blueshifted velocities, and the marked absence of redshifted H I absorption is confirmation that NGC 1266 harbors an H I outflow.

3.6.3 Derived Properties

A summary of the derived properties of NGC 1266 is presented in Table 3.2. The mean molecular hydrogen surface density of the nucleus is 2.7×10^4 M$_\odot$ pc^{-2}, corresponding to a mean column density $N(\rm H_2) \approx 1.7 \times 10^{24}$ cm^{-2}, two orders of magnitude higher than the surface density of individual GMCs in the Milky Way, and comparable to what is seen in some of the most luminous starburst galaxies (Kennicutt 1998).

For an outflow with a mass of 3.3×10^7 M$_\odot$ and an outflow velocity of half the full width-half maximum ($v_{\rm fwhm}$) of the broad wing component (177 km s^{-1}), the kinetic energy associated with the outflow is 1.0×10^{55} ergs, equivalent to the total kinetic energy expelled from 10^4 supernova explosions. The dynamical time, $\tau_{\rm dyn}$, for the outflow to reach its maximum radius of 460 pc at this velocity is only 2.6 Myr. If the edge of the CO emission in the lobes is produced from only the highest velocity gas, the relevant timescale is even shorter, $\tau_{\rm dyn} \sim 1$ Myr.

From the total kinetic energy and $\tau_{\rm dyn}$, the mechanical luminosity of the outflow $L_{\rm outflow} = 1.3 \times 10^{41}$ erg s^{-1}. The mass outflow rate is $\dot{M} = M_{\rm outflow}/\tau_{\rm dyn} = 13$ M$_\odot$ yr^{-1}. At this rate, if the source of the gas in the outflow is the nuclear molecular disk, the nucleus of NGC 1266 will be completely depleted in $\tau_{\rm dep} = 32$ Myr, or 85 Myr for all of

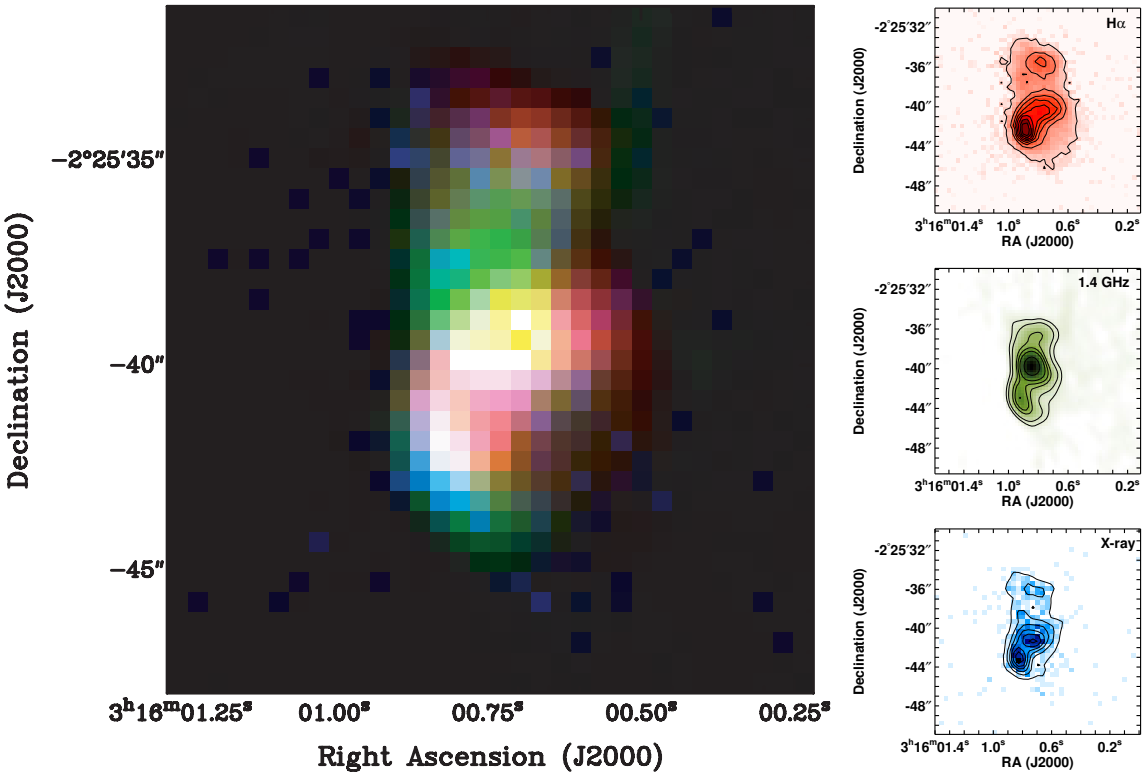

Figure 3.16 **(Left:)** A RGB image of the Hα (red), radio continuum (green), and *Chandra* X-ray (blue) emission. A spatial correlation is clearly seen in the area of the blueshifted CO outflow, revealing that these features are co-spatial. We conclude that the Hα, the spurs in the radio continuum image, and some of the X-ray emission originate from the outflowing material, although the 1.4 GHz continuum emission could also be coming from a radio jet. **(Top right:)** Hα image from the SINGS survey. **(Middle right:)** VLA A-array 1.4 GHz continuum emission (Baan & Klöckner 2006). The unresolved peak in the emission is assumed to be from an AGN, and the lobe extending southeast to northwest is assumed to trace the interface between the outflowing material and the galaxy ISM. **(Bottom right:)** Un-smoothed *Chandra* X-ray image (Alatalo et al. 2011, in prep). The majority of the X-ray photons from NGC 1266 can be fit with a thermal bremsstrahlung spectrum with an excess of hard X-rays. All images are at the same spatial scale.

the gas in the center (nucleus + envelope), both very short timescales.

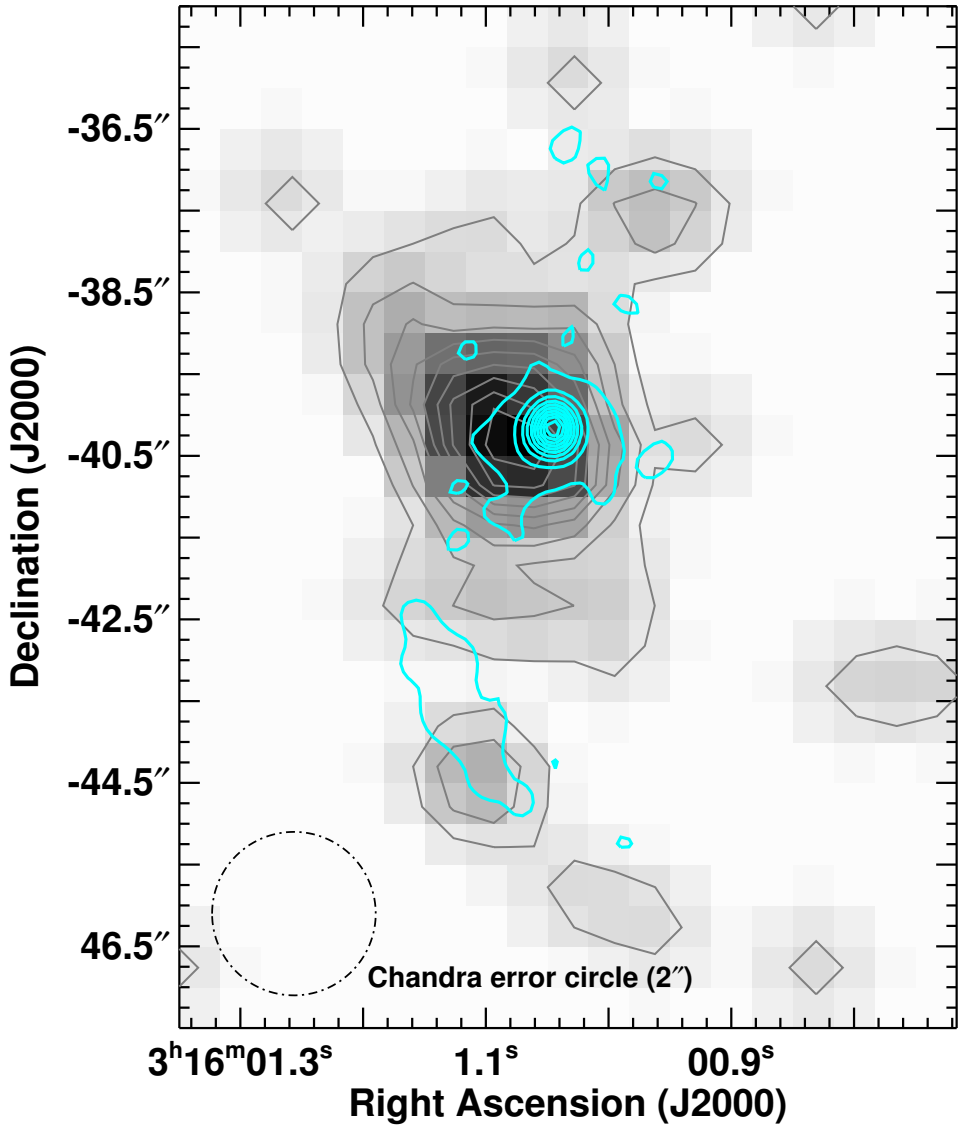

Figure 3.17 *Chandra* smoothed hard X-ray image truncated to only include 4–8 keV photons (greyscale and black contours), overlaid with the 5 GHz radio continuum emission (cyan contours; Baan & Klöckner 2006). The radio core and hard X-rays from *Chandra* are co-spatial within the expected positional accuracy of the *Chandra* data in the hard X-ray band (2″), convincingly identifying NGC 1266 as harboring an AGN.

3.7 NGC 1266 in context

3.7.1 How unique is NGC 1266?

NGC 1266 is unusual in several respects. There is a large reservoir of molecular gas concentrated within the central 100 pc. The concentration of H_2 in the nucleus implies

that the gas must have lost nearly all of its angular momentum. Although such high central concentrations of H_2 are observed in interacting galaxies, NGC 1266 is an isolated galaxy with no sign of interaction or merger.

Is the outflow in NGC 1266 a common evolutionary stage through which most ETGs pass, or is NGC 1266 a pathological phenomenon? The short gas depletion time of ≈ 85 Myr is reasonably consistent with finding only one such case so far in the 60 ATLAS^{3D} CO detections (Young et al. 2011). The expectation would be to find 3, assuming that the typical molecular gas depletion time due to star formation in ETGs is the same as the 2 Gyr found in late-type galaxies (Leroy et al. 2008; Bigiel et al. 2008). However, the sheer strength of the CO line in NGC 1266 certainly aided the outflow detection, and it is likely that, given the lower signal-to-noise ratios present in the rest of the sample, the low surface brightness features at high velocities would generally be lost in the noise.

Optically, NGC 1266 does not stand out within the ATLAS^{3D} sample. It is a fast rotator with regular stellar kinematics (Krajnović et al. 2011), and is of normal metallicity. Its absolute magnitude, $M_K = -22.9$, corresponds to a stellar mass just below the median of the sample. On the other hand, its radio flux at 1.4 GHz places NGC 1266 in the top 10% of radio emitters within the sample, although this emission could be explained by the FIR-radio SF correlation based on the amount of molecular gas detected in the source (Murgia et al. 2005). Among the ~ 100 known ETGs with detected molecular gas (Wiklind, Combes & Henkel 1995; Welch & Sage 2003; Sage, Welch & Young 2007; Combes, Young & Bureau 2007; Young et al. 2011), ≈ 20 have been previously mapped interferometrically (see Crocker et al. 2011, and references therein). Compared to those, the molecular gas in NGC 1266 stands out both in terms of its compactness and its large mass. The star-forming ETGs seem to exhibit only a narrow range of mean molecular gas surface densities, 10–500 $M_\odot$ pc^{-2}, similar to the range of Milky Way values. The surface density of the nucleus of NGC 1266 ($\approx 2.7 \times 10^4$ $M_\odot$ pc^{-2}) is two orders of magnitude larger than this.

NGC 1266 should perhaps be compared to radio galaxies, 1/4 - 1/3 of which have been shown to contain significant reservoirs of molecular gas (Evans et al. 2005; Ogle et al. 2010). The H I absorption profile seen in NGC 1266 is akin to that in the handful of known radio galaxies with outflowing H I IC 5063, 3C 305 (Morganti et al. 1998; Oosterloo et al. 2000; Morganti et al. 2005a,b), 4C 12.50 (Morganti et al. 2004) and 3C 293 (Morganti et al. 2003; Emonts et al. 2005), with mass outflow rates ~ 50 $M_\odot$ yr^{-1} at high ($\gtrsim 1000$ km s^{-1}) velocities. The H I in each of these galaxies is detected in absorption against a radio source, and covers hundreds of parsecs to kiloparsecs. While the outflowing H I mass in NGC 1266 is orders of magnitude lower than in these galaxies, it is possible that both types of systems share a common origin. However, although the luminosity and structure of the H I absorption do mirror those in radio galaxies, the samples described by Evans et al. (2005) and Ogle et al. (2010) and the outflowing systems all show signs of interactions, companions and tidal features, which are all markedly absent from NGC 1266.

3.8 Star Formation in NGC 1266

Given the high surface density of the molecular gas, NGC 1266 ought to be forming stars. Based on the Kennicutt-Schmidt (K-S) relation (Kennicutt 1998), $\Sigma_{H_2} \approx 2.7 \times 10^4$ $M_\odot$ pc^{-2}, and a radius of 60 pc, the expected star formation rate (SFR) of the nucleus alone is 3.1 $M_\odot$ yr^{-1}, adjusted for a Kroupa initial mass function (IMF). In order to understand the star formation efficiency of the gas, we use multiple tracers to place constraints on the SFR, including the total far-infrared luminosity ($L_{\rm FIR}$), the 24μm emission, and the 8μm emission from polycyclic aromatic hydrocarbons (PAHs). Those three tracers are systematically affected by the presence of an AGN, but in different ways, so we use all three to define a range of possible SFRs. Both the 24μm emission and $L_{\rm FIR}$ suffer from contamination by a buried AGN, and will thus systematically overestimate the SFR. PAH molecules are destroyed by the harsh ionization fields associated with strong AGN, and will thus possibly underestimate the true SFR (Voit 1992).

If we assume that all of the far-infrared (FIR) luminosity (7×10^{43} erg s^{-1}; Gil de Paz et al. 2007; Combes, Young & Bureau 2007) is from star formation (an upper limit since the nucleus of NGC 1266 contains an AGN), we calculate a global obscured SFR_{FIR} of 2.2 $M_\odot$ yr^{-1} using Kennicutt (1998), re-calibrated for a Kroupa IMF. The unobscured SFR from the measured far ultraviolet (FUV) contributes negligibly to the overall SFR ($SFR_{FUV} = 0.003$ $M_\odot$ yr^{-1}; Gil de Paz et al. 2007; Leroy et al. 2008). We also calculate the SFR using the 24μm and PAH emission, measured by *Spitzer* as part of the SINGs survey (Kennicutt et al. 2003). The SFR is related to the 24μm luminosity (L_{24}) following Calzetti et al. (2007): SFR_{24} / ($M_\odot$ yr^{-1}) $= 1.27 \times 10^{-38} (L_{24}/\text{erg s}^{-1})^{0.885}$. For NGC 1266, $L_{24} = 1.06 \times 10^{43}$ erg s^{-1} once adjusted to our adopted distance (Temi, Brighenti & Mathews 2009), so the associated $SFR_{24} \approx 1.5$ $M_\odot$ yr^{-1} (the stellar continuum contribution to the 24μm emission is $<<$ 1%), within 33% of the SFR_{FIR} derived from the FIR emission. To measure the SFR from the PAH emission, we use the mid-IR fluxes from Falcón-Barroso et al. (2012, in prep). We subtract off the stellar contribution from the 8.0μm flux by scaling the 3.6μm image; the scale factor of the 3.6μm image can range from 0.22 to 0.29 (Calzetti et al. 2007), with elliptical galaxies having typical values of 0.26 (Wu et al. 2005; Shapiro et al. 2010). From the corrected PAH emission, we measure $SFR_{PAH} \approx 0.57$ $M_\odot$ yr^{-1} (Falcón-Barroso et al. 2012, in prep) a factor of 4 lower than the SFR_{FIR} derived using the FIR emission.

Comparing the SFR predicted from the molecular gas via the K-S relation to the SFRs derived from the 8μm, 24μm and FIR emission, we find that the predicted SFR is a factor of 1.4 to 5 times larger than the measured SFR, depending on which SFR tracer is used. However, NGC 1266 is well within the scatter of the K-S relation (Leroy et al. 2008), as well as the range of SFRs observed in the SAURON and ATLAS^{3D} sample galaxies (Shapiro et al. 2010; Falcón-Barroso et al. 2012, in prep).

The star formation-driven wind model of Murray et al. (2005) requires that the star formation rate be equal to or greater than the mass outflow rate for radiation-driven

outflows, which we refer to as the Murray criterion. Our calculations for NGC 1266 show that even if we consider the higher SFR estimate (SFR ≈ 2 $M_\odot$ yr^{-1}), our lower limit on the mass outflow rate ($\dot{M} \approx 13$ $M_\odot$ yr^{-1}) still exceeds it by a factor of at least a few. This will only increase with more accurate accounting of the the total mass of the outflow. Therefore, the NGC 1266 molecular outflow does not fulfill the Murray criterion, and momentum coupling (i.e. radiation-driving) and star formation are unlikely to be the drivers of the outflow.

3.8.1 Comparison to other outflowing systems

NGC 1266 is classified as a low-ionization nuclear emission-line region (LINER) (Moustakas & Kennicutt 2006). The 1.4 and 5 GHz radio continuum images reveal a prominent and unresolved point source in the nucleus (e.g. Figs 3.16 and 3.17). *Chandra* observations reveal hard X-ray emission centered on the radio point source, consistent with an obscured AGN (see Figure 3.17). Given the overwhelming evidence for the presence of an AGN in NGC 1266, and that star formation is much less intense than in the few other galaxies exhibiting molecular outflows (see §3.7.1), an AGN-driven outflow seems a reasonable possibility.

To investigate whether the AGN is any more capable, we use the relationship between the 1.4 GHz luminosity and total jet power from Bîrzan et al. (2008): $\log(P_{\rm jet}/10^{42}$ erg s$^{-1}) = 0.35\log(P_{1.4\rm GHz}/10^{24}$ W Hz$^{-1}) + 1.85$. The total radio flux at 1.4 GHz is 9.3×10^{20} W Hz^{-1}, resulting in a total jet power of 6.1×10^{42} erg s^{-1}. Comparing this to the $L_{\rm mech}$ of the outflow of 1.3×10^{41} erg s^{-1}, a coupling of $\sim 2\%$ is required to drive the outflow with the AGN, a rather modest value. Therefore, the AGN does indeed generate sufficient energy to power the outflow through the mechanical work of the radio jet.

There is a small sample of galaxies that have been shown to exhibit molecular outflows: M82, Arp 220, Mrk 231 and M51. Arp 220 is a starbursting major merger and has a molecular gas surface density of 6×10^4 $M_\odot$ pc^{-2} (Mauersberger et al. 1996), similar to that of the molecular nucleus of NGC 1266. Sakamoto et al. (2009) detected an outflow that they estimate has a mass of 5×10^7 $M_\odot$ and a mass outflow rate of 100 $M_\odot$ yr^{-1}, with an outflow velocity of ~ 100 km s^{-1}. These numbers, though uncertain, are also comparable to what is observed in NGC 1266. However, the star formation rate in Arp 220 is $\gtrsim 200$ $M_\odot$ yr^{-1} (Soifer et al. 1987), almost two orders of magnitude greater than in NGC 1266, providing a ready source of energy for the outflow and meaning that the Murray criterion is met.

M82 has $\approx 3 \times 10^8$ $M_\odot$ of molecular gas entrained in an outflow with velocities up to ≈ 230 km s^{-1} (Walter, Weiss & Scoville 2002). It is unclear whether this is sufficient for any gas to escape the galaxy. The mass outflow rate is ≈ 30 $M_\odot$ yr^{-1}, comparable to that estimated for the wind in NGC 1266, and roughly equivalent to the global SFR of M82 (Kennicutt 1998), thus satisfying the Murray criterion. The outflows can thus be driven out via radiation pressure.

Matsushita, Muller & Lim (2007) have shown recently that M51 has entrained molecular gas in an outflow close to the AGN, with a total molecular mass of 6×10^5 $M_\odot$, two orders of magnitude less than the mass estimate for the NGC 1266 outflow. The derived mass outflow rate of M51 is ≈ 4 $M_\odot$ yr^{-1}. While this outflow rate is equivalent to the total SFR, the star formation in M51 is known to be distributed throughout the disk (Calzetti et al. 2005), and thus is likely unable to effectively drive much of the nuclear molecular gas out. The AGN luminosity of 2×10^{42} erg s^{-1} (Terashima & Wilson 2001) is also too low to sustain the molecular outflow via photon-driving. Therefore, M51 appears to be a scaled down version of the outflow we observe in NGC 1266, requiring a similar mechanism, such as mechanical work done by a radio jet, to drive out the gas.

Mrk 231, a nearby advanced major merger, shows a molecular outflow similar to that of NGC 1266 (Feruglio et al. 2010). The Mrk 231 CO(1–0) spectrum exhibits a similar profile to that seen in NGC 1266, with broad wings requiring a nested Gaussian fit. This similarity seems to confirm that neither NGC 1266 nor Mrk 231 is a unique case, and AGN feedback may be an efficient means of removing the molecular gas close to the AGN. Feruglio et al. (2010) claim that Mrk 231 has a mass outflow rate of ≈ 700 $M_\odot$ yr^{-1} (assuming a density profile of r^{-2}), exceeding its star formation rate of 200 $M_\odot$ yr^{-1}and thus requiring AGN feedback to be powered. If the CO in the outflow is optically thick, as assumed by Feruglio et al. (2010), then the mass outflow rate in Mrk 231 is indeed too high for a star formation-driven wind. On the other hand, if the correct L(CO)-to-M(H_2) mass conversion for both the NGC 1266 and Mrk 231 outflows is the optically thin conversion (as assumed for NGC 1266), then $M(H_2)$ for the Mrk 231 outflow is a factor of ≈ 5 lower, leading to a mass outflow rate of ~ 100 $M_\odot$ yr^{-1}. This is sustainable using the Murray criterion, and is similar to Arp 220. Therefore the case for the molecular outflow in Mrk 231 requiring AGN feedback is uncertain. To obtain a robust estimate of the outflowing mass of Mrk 231, the opacity of the outflowing component must be determined. The correct choice of $X_{\rm CO}$ in each of these cases is essential, as the mass outflow rates can vary by a factor of 10 depending on the conversion that is adopted by the authors. Particularly in cases where the choice of a large $X_{\rm CO}$ is able to create an outflow rate unsustainable by star formation, caution is necessary.

New stacked CO(1–0) observations of local ultra-luminous infrared galaxies (ULIRGs) by Chung et al. (2011) also show clear evidence that high-velocity broad emission at up to 1000 km s^{-1} from the systemic velocity is a common feature in these systems. In particular, the authors find that only the starburst–dominated ULIRGs exhibit broad wings, while AGN–dominated ULIRGS (identified by their optical spectra) do not. These results are thus clear evidence that in most observed molecular outflows, photon-coupling with the star formation is the principle driver. It is also important to note that the Chung et al. (2011) results are based on populations. If an individual galaxy in the AGN regime had an outflow, it is possible that the signal could be averaged out with the many Sy I galaxies that do not have active molecular outflows. For this reason, it is difficult to use the Chung et al. (2011) results to directly interpret NGC 1266.

While the aforementioned galaxies all exhibit molecular outflows, M51 is the only other bonafide case of a non-photon-driven molecular outflow. However, it has almost two orders of magnitude less molecular gas being driven out than NGC 1266. Mrk 231 might well be an equivalent system, but the mechanisms capable of driving the gas out depend on the CO luminosity–to–H_2 mass conversion in the outflow. The most acute contrast between NGC 1266 and the other molecular outflow sources is its lack of interaction. All other galaxies are undergoing interactions; major mergers in the case of Arp 220, Mrk 231 and some of the (Chung et al. 2011) ULIRGs. NGC 1266 shows no evidence of having undergone an interaction at any time in the recent past, with unperturbed stellar kinematics, no companion, and a lack of H I emission internal or external to the galaxy. This means that while we can point to an interaction as the triggering mechanism in the other known molecular outflows, the striking absence of such a perturbing event makes NGC 1266 even more remarkable.

3.9 Summary and Conclusions

We report the detection of a massive centrally-concentrated molecular component ($M_{\rm CVC} = 1.1 \times 10^9$ M$_\odot$) and a powerful molecular outflow ($M_{\rm H_2,outflow} = 2.4 \times 10^7$ M$_\odot$) in the field S0 galaxy NGC 1266. The maximum velocity of the wind exceeds the escape velocity so that at least some gas will escape the galaxy to energize the IGM, and the total neutral gas mass outflow rate $\dot{M} \approx 13$ M$_\odot$ yr^{-1}. The star formation rate in NGC 1266 appears to be incapable of driving this outflow; the AGN appears to be the main driving mechanism, as for H I outflows observed in radio galaxies. It is however unclear how the gas lost its angular momentum to fall so completely into the nucleus.

The central molecular gas contains a rapidly rotating nuclear disk of ≈ 60 pc radius enshrouded in a diffuse molecular envelope, and the molecular outflow emerges normal to the disk plane. Although the molecular nucleus is compact and very near the AGN, multiple estimates of the star formation rate point to a low star formation efficiency, but the uncertainties in these SFRs place NGC 1266 within the scatter of the K-S relation (assuming that $L_{\rm FIR}$ is not dominated by the AGN).

If the gas in the nucleus is the source of the molecular outflow, the gas depletion timescale is 85 Myr, short enough for all ETGs to go through such a phase while remaining consistent with having found only one such case among the 260 ETGs in the ATLAS^{3D} sample. NGC 1266 is the brightest detection, however, so there might be more outflows in the sample, undetected so far because of lower S/N ratios.

While molecular outflows have been identified in a handful of galaxies, NGC 1266 is the only one that shows no evidence of having undergone an interaction, leaving the mechanism to transport the molecular gas into the center unknown.

3.10 Addendum

In the previous sections, we described the sections originally published in Alatalo et al. (2011). At the publication of this work, we had not been able to entirely rule out the possibility that the outflow is driven by photon momentum coupling to the central star formation (Murray et al. 2005). Given the expected optical depth of this system, it is still possible that a compact starburst efficiently forming stars within the molecular gas would be able to power the outflow, as currently the estimated molecular outflow rate is only a factor of 5.9 larger.

Although we use the smallest possible conversion factor between $L(\mathrm{CO})$ and $\mathrm{M}(\mathrm{H_2})$ for a solar metallicity galaxy, it is possible that the mass outflow rate, $\dot{M}$ is still overestimated. If the outflow is more collimated than we assumed, and aimed directly at the line of sight, the timescale for the outflow could be much longer, and therefore the mass outflow rate could be smaller, and therefore fit the Murray et al. (2005) criterion.

It is also possible that the total infrared luminosity, L_{FIR} has been underestimated. If there are multiple peaks in the spectral energy distribution (SED) near 100μm, it is possible that the estimate used, which assumed one peak, underestimated L_{FIR}. To remedy this, proving that the 100μm point lies in the Rayleigh-Jeans tail of the dust emission is essential. We utilize the SED and the addition of the CARMA and SMA continuum points at 115, 230 and 345 GHz, as well as newly published *Herschel* data (Dale et al. 2012). With the addition of the sub-mm data points, Figure 3.18 shows that the dust continuum is singly peaked, and that we are able to trace the Rayleigh-Jeans tail.

It is finally important to note that the choice of spin temperature to determine the mass associated with the H I absorption seen in Figure 3.15 can have a significant effect on the resultant neutral Hydrogen mass. The original choice of 100 K is possibly not reflective of the state of the Hydrogen in the system, as the Roussel et al. (2007) results show that there is hot ($\gtrsim$ 1400 K) $\mathrm{H_2}$ in the system. Assuming that T_{spin} is 1000 K rather than 100 K, the total mass of H I in the outflow becomes 9.5×10^7 $\mathrm{M_\odot}$, a factor of 10 larger than was previously underestimated. This would therefore mean that the total mass of the outflow is above 10^8 $\mathrm{M_\odot}$, a factor of 3 larger than reported in the preceding chapter, and that in the outflow, there is more H I than $\mathrm{H_2}$, if the optically thin L(CO)–to–M($\mathrm{H_2}$) conversion factor is correct.

With these caveats in mind, Chapter 4 sets out to either rule out or confirm photon momentum coupling to the outflow with measurements that are independent of the assumptions made about the molecular gas. In Chapter 4, we use dust obscuration from the Hubble Space telescope to constrain the opening angle of the outflow, which tells us about the collimation and therefore timescale, and use A_V to calculate the molecular gas mass, to constrain X_{CO}, the conversion factor used to determine $\mathrm{M}(\mathrm{H_2})$ from the CO luminosity.

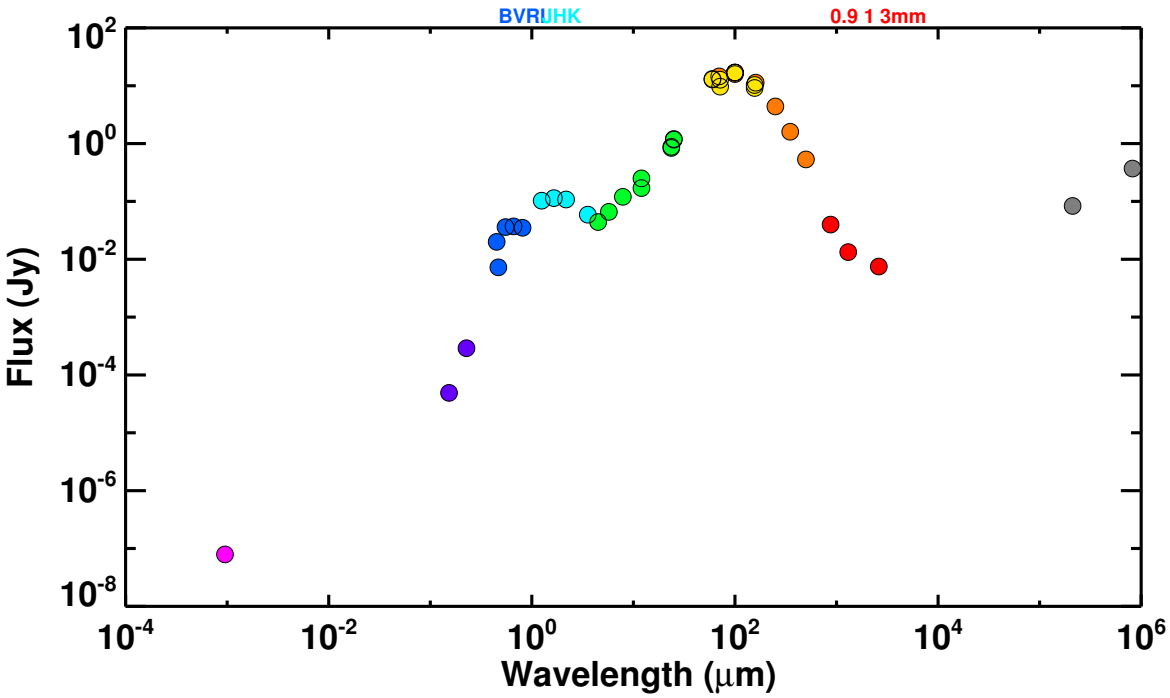

Figure 3.18 The integrated spectral energy distribution (SED) of NGC 1266, from X-ray to the radio wavelengths. The references used to compile this SED are reported from left to right as follows: 0.2–2.0 keV (White, Giommi & Angelini 2000), FUV, NUV, B, V, R, and I (Dale et al. 2007), J, H and K (Jarrett et al. 2003), 3.6, 4.5, 5.8, 8.0, 24, 70 and 160 μm *Spitzer* (Dale et al. 2005), 12, 25, 60 and 100 μm IRAS (Soifer et al. 1989), 70, 100, 160, 250, 350 and 500 μm *Herschel* (Dale et al. 2012), 0.9 and 1mm (Alatalo et al. 2011; Chapter 3), 3mm (Chapter 2), 1.4 GHz (Baan & Klöckner 2006) and 365 MHz (Douglas et al. 1996).

Chapter 4

High Resolution Observations of NGC 1266

Abstract

We present new observations of NGC 1266, a local example of an AGN-driven molecular outflow, from the Very Long Baseline Array (VLBA) and the Hubble Space Telescope (HST). VLBA observations confirm the presence of the AGN, via an unresolved high brightness temperature point source, located directly atop the peak of the molecular gas originally reported in Alatalo et al. (2011) and Chapter 3, and confirming that NGC 1266 contains a Compton-thick AGN. B, V, I, Y, J and H-band photometry from the HST show both a high level of dust obscuration spatially coincident with the vertex of the outflow, as well as faint stellar spiral structure. A dust-derived outflow gas mass 1.65×10^8 $M_\odot$ was calculated from A_V, a factor of 5 larger than was reported reported in Alatalo et al. (2011), leading to a mass outflow rate of 52 $M_\odot$ yr^{-1}, unsustainable energetically by star formation and requiring coupling to the AGN to explain. NGC 1266 appears to fit the K+A criterion (Dressler & Gunn 1986), and should be considered a poststarburst galaxy, despite having ionized gas emission. Davis et al. (2012) have shown that all this gas emission is due to the shock associated with the outflow, indicating that galaxies with shock-like ionized gas diagnostics are an important and overlooked segment of the poststarburst population.

4.1 Introduction

The present-day galaxy population has a bimodal color distribution, with a genuine lack of intermediate-color galaxies (Strateva et al. 2001; Baldry et al. 2004). The lack of galaxies in the "green valley" suggests that galaxies migrate rapidly between the blue

cloud and red sequence, requiring a rapid quenching of star formation (SF). It appears that this cessation of SF requires a more powerful event than can be explained solely from starbursting activity, and thus "AGN feedback" has been invoked to explain the quenching (Springel, Di Matteo & Hernquist 2005; Croton et al. 2006; Hopkins et al. 2005). While circumstantial evidence exists to the presence of AGN feedback (Schawinski et al. 2007), direct evidence is lacking. There are promising candidates of powerful AGN feedback at $z \sim 2$ (Nesvadba et al. 2008), but only limited information can be obtained for such objects. Markarian 231 has also recently been shown to exhibit evidence of AGN feedback (Feruglio et al. 2010; Fischer et al. 2010), and evidence is mounting that many such quasars are also undergoing AGN driven expulsions of their interstellar media (ISMs) (Morganti et al. 2006). But finding a quiescent system undergoing these events has thus far been limited.

Poststarburst galaxies (i.e. K+A and E+A galaxies; Dressler & Gunn 1986; Quintero et al. 2004) contain evidence of having undergone rapid cessation of star formation, with young stellar populations but a lack of current star formation, via tracers such as Hα emission. Poststarburst galaxies are commonly found within the green valley of the color-magnitude distribution of galaxies, and therefore are considered to be a key to how rapid cessation of star formation takes place within galaxies. The poststarburst population has been shown to be bimodal (Cales et al. 2011). The first population comprises of galaxies that show signs of having undergone mergers, through strong isophote disturbances, tidal features and quasar activity. The merger population of poststarburst galaxies have an obvious trigger for the cessation of star formation: the disruption of the molecular gas and star formation from the merger itself.

The second poststarburst population is generally morphologically classified as "late type" galaxies, exhibiting spiral features, and showing far fewer signs of disruption. For this second population of poststarburst galaxies, the triggering mechanism is far less clear. Suggested mechanisms include strangulation (when a gas-rich galaxy falls into a cluster, and subsequently loses its ability to replenish its cold ISM due to the presence of the intracluster medium; Evrard 1991; Fujita 1998; Bekki et al. 2002; Boselli & Gavazzi 2006), harassment (where nearby companions gravitationally interact with the galaxy without completely merging; Icke 1985; Mihos 1995; Bekki 1998; Moore et al. 1996), and morphological quenching (where the molecular gas within a bulge-dominated system is more stable against gravitational collapse and therefore has a lower star formation efficiency; Martig et al. 2009). The first two suggestions require a cluster environment. Despite these suggestions, thus far the triggering mechanism responsible for a nonnegligible fraction of the poststarburst population has remained speculative.

Finding quiescent galaxies that provide direct links between AGN activity and the quenching of SF activity has thus far proved elusive. Poststarburst galaxies represent one of the last stages in a galaxy's migration from star forming to quiescent, but most of these systems are found after they have successfully expelled their starforming material. Therefore, finding a candidate that is still actively expelling its molecular material pro-

vides a snapshot into an important part of a galaxy's journey from star forming, through the green valley, and finally to a quiescent red sequence galaxy.

Here we report on new high resolution observations and detailed analyses of the field galaxy NGC 1266, reported previously as having a powerful AGN-driven molecular outflow (Alatalo et al. 2011 and Chapter 3, hereafter A+11), an ideal local candidate for studies of gas expulsion in poststarburst galaxies. In §4.2, we describe the observations taken in 7 wide bands with the Hubble Space Telescope (HST) as well as with the Very Long Baseline Array (VLBA). In §4.3, we confirm the presence of an active galactic nucleus (AGN) from the radio continuum, and derive a dust mass and the morphology of NGC 1266 from the B, V, I, Y, J and H band photometry from the HST. In §4.4, we discuss how to detect other NGC 1266-like events, and put them in context. In §4.5, we report our conclusions.

4.2 Observations and Data Reduction

4.2.1 The Hubble Space Telescope

Visible and infrared images of NGC 1266 were obtained with the Hubble Advanced Camera for Surveys (ACS) Wide Field Camera and the Wide Field Camera 3 (WFC3) instruments on the HST in December 2011. Table 4.2.1 lists the dataset identification, instrument, channel, filter and exposure time for the HST observations. All images are full frame, and were processed with the standard reduction pipelines `CALACS` for the ACS data and `CALWF3` for the WFC3 data. In addition, destriping was applied to the ACS frames to remove the effect of bias level effects. Cleaned images were coadded, registered and

Figure 4.1 The Hubble Space Telescope. Image Credit: NASA.

scaled to a common pixel scale of 0.13 arcsec/pixel with `MULTIDRIZZLE`. Flux calibration was applied to the resulting drizzled images. The final step was creating the color maps, by combining the visible and infrared images. (Figures 4.3 and 4.4). We note that the UV observations taken with the F225W do not have sufficient signal to noise to be useful, indicating either that dust extinction is high or that the nucleus is not active. Based on the millimeter and IR data, however, the more likely explanation is high extinction.

Table 4.1 Observations of NGC 1266 taken with HST (Program 12525, 3 orbits)

Obs ID	Instrument	Channel	Filter	Exp. Time (seconds)
ibr701a2q	WFC3	UVIS	F225W	875
ibr701a3q	WFC3	UVIS	F225W	875
ibr701a4q	WFC3	UVIS	F225W	875
ibr702c6q	WFC3	IR	F160W	449
ibr702c7q	WFC3	IR	F140W	449
ibr702c9q	WFC3	IR	F110W	399
ibr702cbq	WFC3	IR	F160W	449
ibr702cdq	WFC3	IR	F140W	449
ibr702cfq	WFC3	IR	F110W	399
jbr704f6q	ACS	WFC	F814W	135
jbr704f7q	ACS	WFC	F435W	560
jbr704f9q	ACS	WFC	F555W	339
jbr704fbq	ACS	WFC	F435W	560
jbr704fdq	ACS	WFC	F555W	339

4.2.2 The Very Long Baseline Array

NGC 1266 and calibrators were observed with all 10 antennas of the NRAO[1] Very Long Baseline Array (VLBA) on October 5, 2011 over 8 hours. The observations were centered at a frequency of 1.6245 GHz with a bandwidth of 16 MHz. All VLBA data were correlated using the new DiFX software correlator (Deller et al. 2011) in dual polarization mode. Due to the expected faintness of the target source, we utilized phase referencing with a switching angle of 2°. Two minute-long scans on the phase, rate, and delay calibrator, J0318-0029, preceded and followed 3 minute scans of NCG 1266. The calibrators J0238+1636 and J0312+0133 were also observed as coherence-check sources. Data editing and calibration were performed using the December 31, 2011 release of the Astronomical Image Processing System (`AIPS`) using the standard VLBA procedures.

[1]The National Radio Astronomy Observatory is a facility of the National Science Foundation operated under cooperative agreement by Associated Universities, Inc.

Figure 4.2 The Very Long Baseline Array antenna located in Owens Valley, CA. Image courtesy of NRAO/AUI.

The AIPS task IMAGR was used to form and deconvolve the image of the Stokes I emission of NGC 1266. Visibility data were uniformly weighted in order to minimize artifacts due to residual radio frequency interference. We used the AIPS task JMFIT to fit a single elliptical Gaussian component to the emission to determine its flux density, extent and position. Observational parameters are summarized in Table 1.

4.3 Results

4.3.1 The AGN within NGC 1266

A radio image with contours is shown in Figure 4.5b. The milliarcsecond ($\approx$ 1 pc scale) resolution observations of NGC 1266 reveal slightly resolved emission consistent with the location of the vertex of the dust cone, as well as the peak of the CO emission (Fig. 4.5a), as well as the *Chandra* hard X-ray point source (A+11). The emission is centered at $\alpha_{\rm J2000} = 03^{\rm h}16^{\rm m}00.74216^{\rm s}$ and $\delta_{\rm J2000} = -02^{\circ}25'38.6574''$ with a positional uncertainty of $\sim$ 1 mas, dominated by the positional uncertainty of the phase calibrator.

Table 4.2 VLBA observational parameters of NGC 1266

Frequency	(MHz)	1656[a]
rms noise	(μJy beam^{-1})	42[b]
Beam	**Parameters**	
$\theta_M \times \theta_m$	(mas)	9.75×4.31[c]
P.A.	(deg)	-0.39[d]
Source	**Parameters**	
$\theta_M \times \theta_m$	(mas)	$7.98 \pm 1.46 \times 6.19 \pm 0.96$[e]
P.A.	(deg)	10.39 ± 40.88[f]
$M \times m$	(pc)	$1.16 \pm 0.21 \times 0.89 \pm 0.14$[g]
S	(mJy)	1.38 ± 0.12[h]
$\log(P_{\rm rad})$	(W Hz^{-1})	20.17[i]
$T_{\rm b}$	K	1.5×10^7 [j]

[a] Center frequency.
[b] Average rms noise in image.
[c] Clean beam major × minor axis.
[d] Clean beam position angle.
[e] Angular dimensions (major × minor axis) and error bars from JMFIT in `AIPS`.
[f] Position angle of deconvolved emission from JMFIT in `AIPS`.
[g] Linear dimensions (major × minor axis) of the deconvolved emission assuming a distance of 29.9 Mpc (Cappellari et al. 2011a).
[h] Total integrated flux density and error. The error shown is the sum of the error reported by JMFIT in `AIPS` and the 3% calibration error, added in quadrature.
[i] Log of the radio power assuming a distance of 29.9 Mpc.
[j] Brightness temperature.

Using the standard equation for brightness temperature[2], we calculated $T_{\rm b} = 1.5 \times 10^7$ K for NGC 1266.

Since compact nuclear starbursts are limited to $T_{\rm b} \lesssim 10^5$ K (Condon et al. 1991), the detection of a high brightness temperature radio core beyond this limit is generally considered strong evidence for accretion onto a black hole. The VLBA source in NGC 1266 exceeds this limit by over two dex, thus excluding the possibility of a compact starburst origin.

4.3.2 The dust content of NGC 1266

Placing independent constraints on the mass of the outflowing material is essential to understanding the nature of the molecular outflow that exists in NGC 1266. Calculating

[2] $T_{\rm b} = (S/\Omega_{\rm Beam})\frac{c^2}{2k\nu^2}$; where S is the integrated flux density and $\Omega_{\rm A}$ is the beam solid angle.

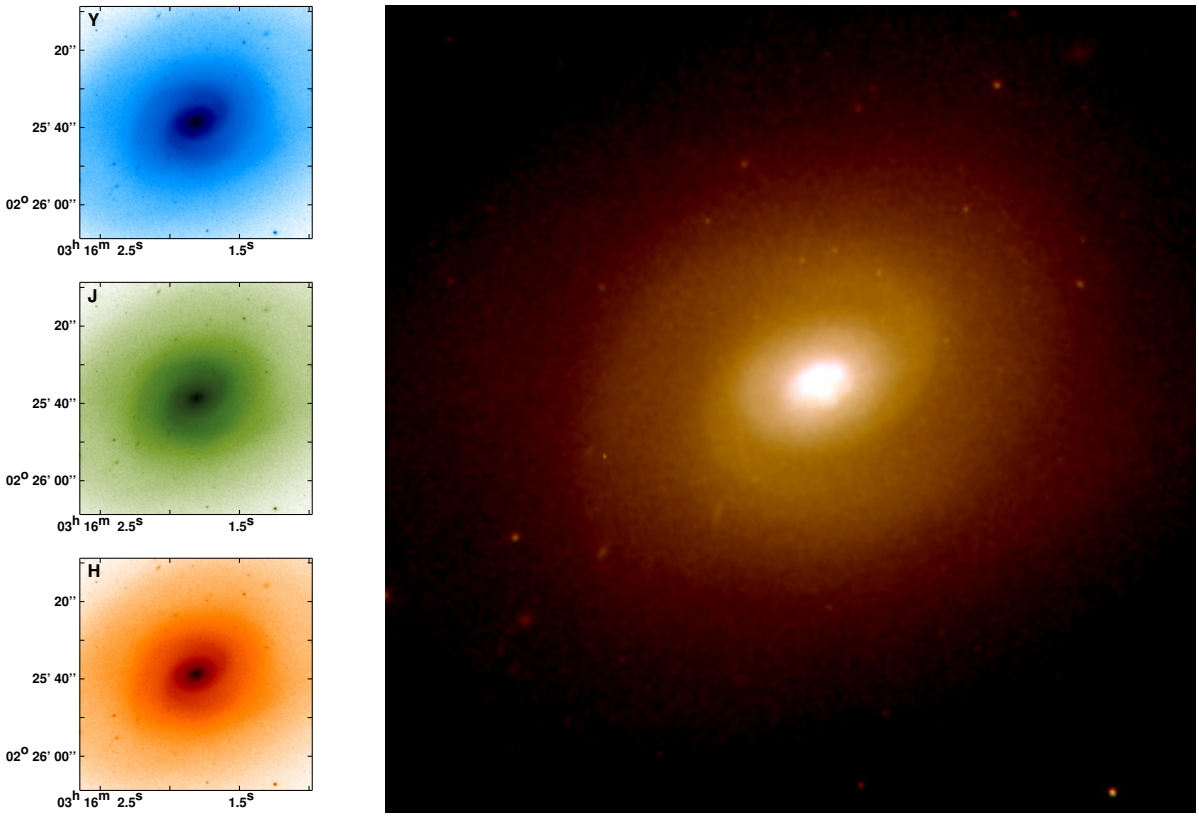

Figure 4.3 **(Left):** The 3-panel figure shows the calibrated emission from HST Widefield Camera 3 (WFC3). The bluescale image corresponds to the Y-band image, the greenscale image corresponds to the J-band image, and the redscale image corresponds to the H-band image. **(Right):** The 3-color image constructed from the Y-, J- and H-bands corresponding to B, G and R respectively. The near-IR bands from HST show that there is an underlying spiral structure in the galaxy, previously un-discovered from ground-based observations. The spiral structure seen here shows that NGC 1266 should be re-classified as an early-type spiral (SA) rather than as a lenticular (S0) galaxy.

the mass of the outflow in NGC 1266 has many uncertainties. When calculating the mass from the CO emission in A+11, the L(CO)–to–H_2 conversion factor is important, and harbors many uncertainties. An optically thin L(CO)–to–H_2 conversion factor assumes that the observer is seeing all CO molecules in a given object. This has the effect of creating the smallest possible conversion to molecular gas mass, assuming solar metallicity to determine the CO abundance (Knapp & Jura 1976). In most GMCs in the Milky Way however, the molecular gas is optically thick, meaning that we are not seeing all CO emission, therefore there is a larger mass of H_2 per emitting CO molecule (Solomon et al. 1987). A+11 used the optically thin L(CO)–to–H_2 conversion when calculating the mass of the molecular gas in the outflow, in order to obtain the lower limit to the molecular

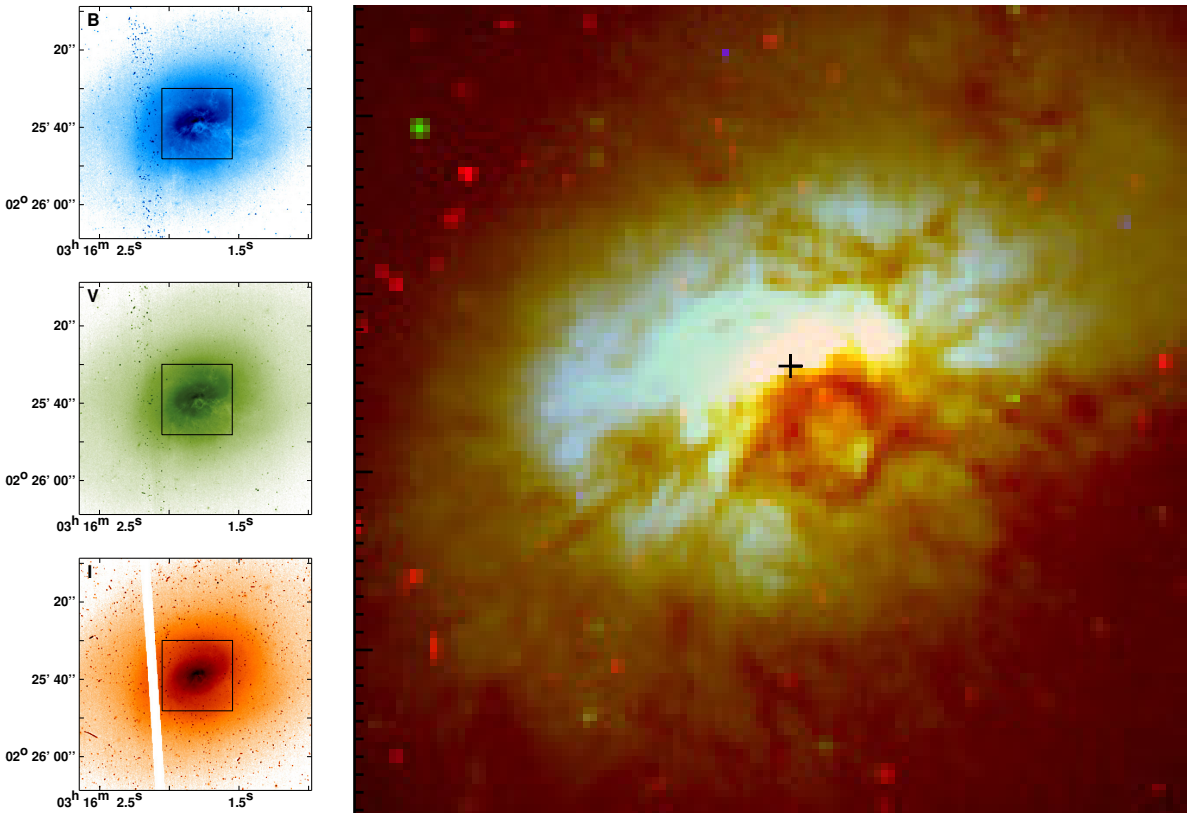

Figure 4.4 **(Left):** The 3-panel figure shows the calibrated emission from HST Advanced Camera for Surveys (ACS). The bluescale image corresponds to the B-band image, the greenscale image corresponds to the V-band image, and the redscale image corresponds to the I-band image. Overlaid on each image is a black box, which represents the size of the 3-color ACS image. **(Right):** The 3-color image constructed from the B-, V- and I-bands corresponding to B, G and R respectively. Overplotted as a black cross is the VLBA position of the AGN. The dust extinction in this image is clearly visible both in the single band images as well as in the 3-color image, where the vertex of the dust appears to be the AGN. It is also apparent that there is an enhancement of flux just to the north-northwest of the AGN point source, possibly reflected light from the AGN region, but it is also possible that the enhancement is from a compact starburst within the dense molecular gas disk.

gas. If the molecular gas in the outflow is not diffuse, then the optically thin assumption is not valid. We are able to use the dust obscuration from the HST as a lever arm to determine the correct conversion factor, and test the optically thin assumption. We will utilize the HST data to calculate the mass of gas from the dust obscuration present in the galaxy via calculating the extinction, A_V.

The 3-color optical ACS image (Figure 4.4) makes it clear that NGC 1266 contains a

large quantity of dust, with extinction features visible even into the reddest bands of J and H. To calculate a lower limit to the A_V measured across NGC 1266, we used the equation: $F_{\rm color,obs} = F_{\rm color,inp} 2.51^{-A_{\rm color}}$ (Rybicki & Lightman 2004), where the color in this case was B, V, I, Y, J and H bands, and $F_{\rm color,inp}$ is the flux of the underlying stellar population. In order to find A_V, we assumed a galactic extinction curve (Cardelli, Clayton & Mathis 1989), a reasonable assumption given that NGC 1266 is normal metallicity (McDermid et al. 2012, in prep). We first constructed color maps of all combinations of the available 6 HST bands, and by taking the logarithm of the calibrated maps, and subtracting them from one another. This created 15 color maps which could be used to fit for A_V. Using the $B - H$ map, which had the strongest extinction features, we created a dust mask, meant to mask out all places with signs of dust, and applied this mask to all 15 color images. For the outer extent of the galaxy, we calculated the radius based on the H-band image, at 2 counts, seen as the black outline in Figure 4.3.2. We calculated the the color of the underlying stellar populations in the map by assuming that the unmasked region contained no extinction. This method results in the reddest possible stellar population,

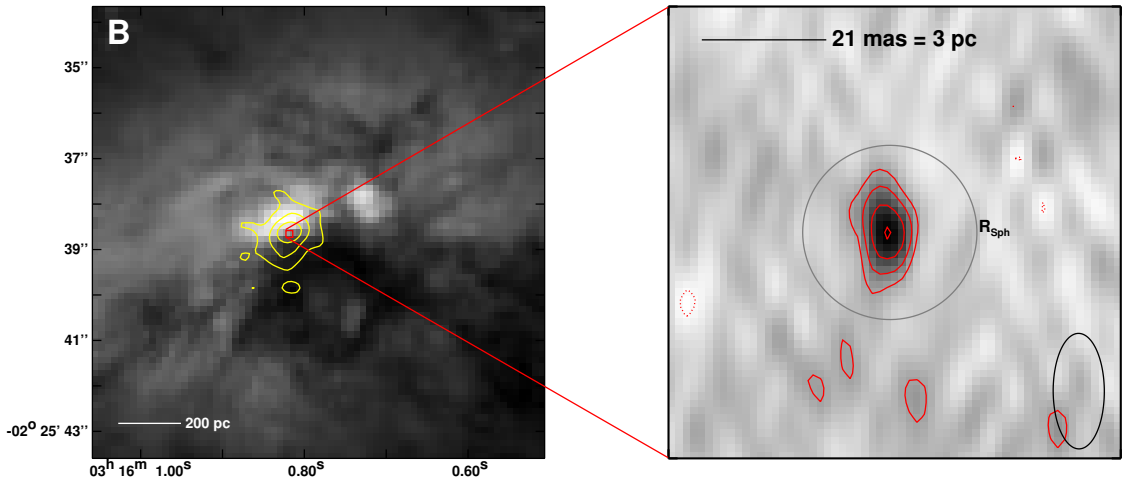

Figure 4.5 **(Left):** A zoomed-in image of the HST B-band in greyscale, plotted to emphasize the enhancement in flux to the north-northwest of the dust cone. Overlaid in yellow contours is the CO(1–0) $v_{\rm sys}$ emission presented in A+11, at levels of [0.25, 0.5, 0.75] of the peak CO emission. Finally a box is presented that shows the relative field-of-view of the VLBA image. **(Right):** NGC 1266 1.65 GHz radio continuum image with contours. The VLBA beam is the black ellipse in the lower right corner and has a major axis diameter of 9.75 mas (1.14 pc). The relative contour levels are [-3, 3, 6, 10, 14] and the unit of the contour level is 42 μJy beam^{-1}. The AGN is detected to 14σ significance, and the VLBA does indeed probe the black hole sphere of influence ($R_{\rm Sph}$), but does not appear to be resolved.

thus maintaining that we are searching for a lower limit to A_V, and the total dust content.

We then calculated the color in each pixel of the masked region, assuming that the color of the stellar population within the masked region was equivalent to the average color in the unmasked region, and solved the equation above for A_V. This resulted in 15 A_V measurements in each pixel of the masked region. We then took the average of these 15 A_V measurements for each pixel to calculate the most accurate A_V. Figure 4.8 shows the extinction map calculated using this method. The map shows that the extent of the extinction is ≈ 3 kpc and that the A_V increases the nearer to the AGN we get. The total gas mass calculated using this method, as well as using the equation $N(\mathrm{H_2})/A_V = 9 \times 10^{20}$ $\mathrm{cm^{-2}\ mag^{-1}}$, from a combination of Schultz & Wiemer (1975) and Bohlin, Savage & Drake (1978) leads to a corresponding total gas mass of 1.65×10^8 $\mathrm{M_\odot}$.

There are many caveats to the mass calculated above. Firstly, it is very likely that A_V in the central regions is underestimated. A+11 use the CO emission as well as dynamical arguments to make the claim that the gas column within the molecular disk is around $N(\mathrm{H_2}) \approx 1.7 \times 10^{24}$ $\mathrm{cm^{-2}}$, which corresponds to $A_V \approx 1900$ mag towards the line of sight of the AGN. In fact, the $J-H$ image shown in Fig. 4.3.2c indicates that toward the AGN, there still appears to be a decrement of light in these near-IR bands, possibly indicating that A_V is larger than can be feasibly measured by extinction, especially toward the center.

In order to calculate the dust mass of the molecular outflow, rather than of the whole molecular complex, we remove the A_V contribution from all pixels that are within the extent of the systemic velocity molecular gas (overlaid in black contours on Fig. 4.8). The dust observed comes only from the blueshifted component of the outflow.

4.3.3 The morphology of NGC 1266

Understanding transition objects such as NGC 1266 requires a holistic accounting of the nature of the galaxy. Determining what secular processes that operate within the galaxy help set constraints on the mechanisms capable of rapidly transitioning NGC 1266 from a starforming galaxy to a quiescent galaxy. Figure 4.3 shows that the galaxy indeed has density fluctuations that appear to be spirals. In order to test if these were indeed spirals, rather than shells, we first did a Multi-gaussian expansion (MGE) fit to the Y, J, and H images (Cappellari 2002), in order to quantify the smoothly varying components of NGC 1266. The MGE models were then subtracted from the original images, creating artifact images (the H-band image, fitted model and artifacts are present in Figure 4.9). The H-band artifact image was then clipped to contain flux values where the spiral features were present. Once the clip was in place, the resultant image was smoothed. The resultant image was then flattened, using the IDL task `GAL_FLAT`, based on the inclination and position angle from the MGE model. Finally, all pixels were transformed from Cartesian (x,y) coordinates to Polar (r, θ) coordinates, in order to fit to the logarithmic spiral equation of $r = a \exp b\theta$, where a and b are free parameters. A mask was again applied,

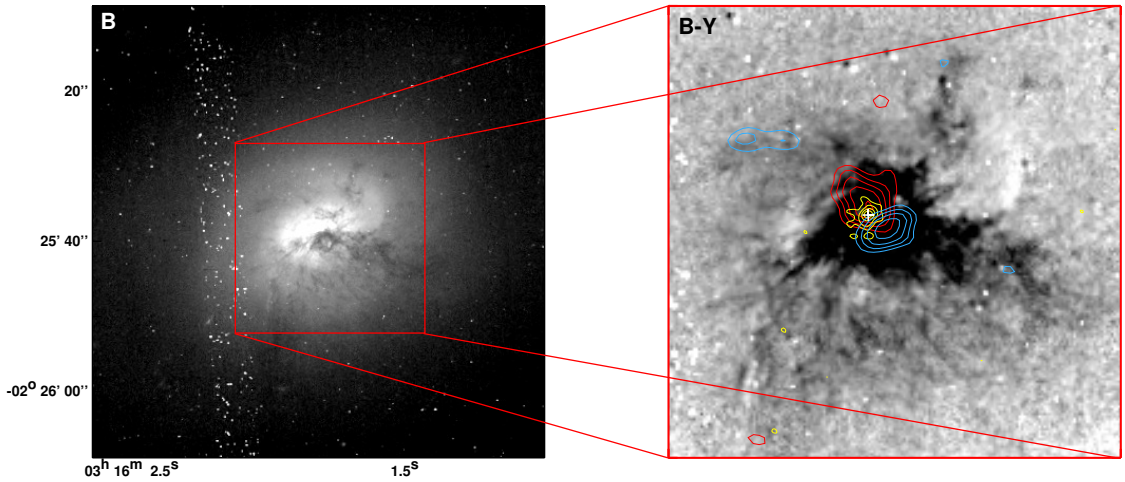

Figure 4.6 **(Left):** The B-band image from HST ACS, which shows the extent of the dust extinction within NGC 1266. **(Right):** A zoomed-in $B-Y$ color image to show the dust features closest to the center. Overlaid is the CO outflowing contours from A+11. The red contours corresponds to the redshifted emission, the blue to blueshifted emission. The yellow contours correspond to the central 130 km s^{-1} gas (i.e. molecular gas close to $v_{\rm sys}$.) Finally, a white cross is placed at the position of the VLBA radio continuum peak. It appears that the blueshifted molecular gas spatially agrees with the dust cone visible, and that the AGN lies directly below the molecular gas.

where all values above the mask were considered real spiral emission (represented by the red contour on Fig. 4.10). The $\ln(r)$ and θ values corresponding to unmasked pixels were then plotted, and linear features were isolated and fit. The logarithmic spiral fit parameters were then re-mapped to Cartesian coordinates and overplotted in Fig. 4.10, clearly overlaying real spiral features. Figure 4.10 shows that the spiral features in the galaxy did indeed follow the logarithmic spiral pattern quite well, and the fluctuations are therefore ruled out from being shells. Therefore, NGC 1266 should no longer be classified as a lenticular galaxy, and instead is clearly an early-type spiral.

In order to attempt to determine a color for the spiral pattern in NGC 1266, a mask was created using the artifact H-band image, which indicated the likely spatial extent of the spirals. Once the spirals were identified, we compared the colors from the three near-IR bands (Y, J, and H band) of the regions that contained spirals and those that did not after applying the dust mask, described in §4.3.2. The colors of the spirals appeared to be exactly the same as the colors of the non-spirals, suggesting that the spirals are a dynamical effect, rather than from stars formed out of gas that was present at previous epochs.

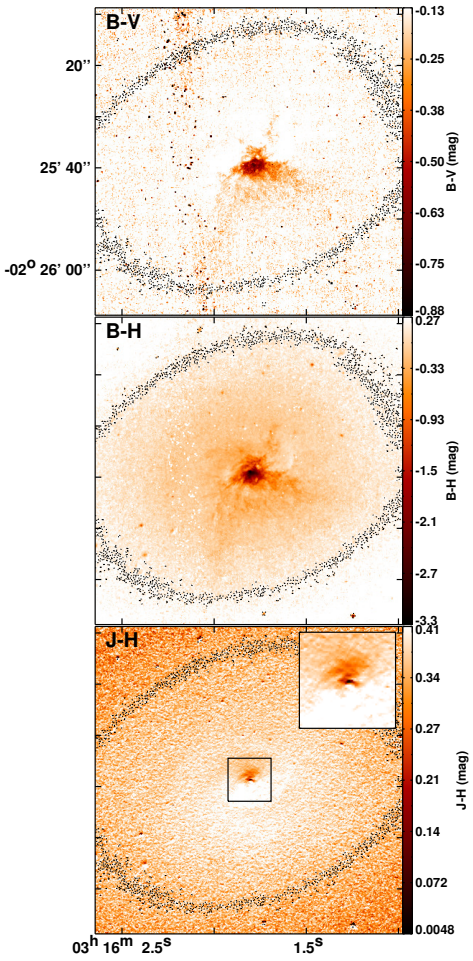

Figure 4.7 Three sample color images of NGC 1266 from HST. **(Top):** $B-V$ colors are shown, tending to be the most commonly displayed. It is clear that both B and V images suffer from a large amount of extinction, especially toward the center, and are likely not the proper choice to gain an understanding of the total extent of the dust. **(Middle):** $B-H$ colors (the bluest and reddest bands available) are shown, indicating the full extent of the dust in NGC 1266. Both the strong extinction in the middle, as well as the total extent of the dust are visible in the image. The dust vertex, which originates at the AGN can be seen extending at least $30''$ out into the galaxy. **(Bottom):** $J-H$ colors are shown to probe the highest levels of extinction. The fact that there is still a significant detriment of color toward the center atop the AGN confirms that there is heavy extinction toward the center (first seen in the molecular gas in A+11.)

4.3.4 The stellar composition of NGC 1266

We use the nuclear and integrated spectra of NGC 1266 originally published in Moustakas & Kennicutt (2006), and illustrated in Figures 4.11, 4.12 and 4.13. First, we masked out the strong emission lines at [O III]λ3727, [O II]λ5007, Hα, [N II]λ6583 and [S II]λ6716 and smoothed each spectrum with a very broad Gaussian filter to derive the continuum shape (red line in Fig. 4.11). We then use Penalized Pixel-Fitting (`PPXF`) IDL procedure (Cappellari & Emsellem 2004) to fit a set of stellar population templates to the integrated (Fig. 4.12a) and the nuclear (Fig. 4.12b). With `PPXF`, we fit a linear combination of stellar templates, in this case, chosen to be solar metallicity that span a range of ages, 0.3, 1.0, 1.6, 2.5, 5.0, 10.0 and 17.8 Gyr. We also masked out Na D absorption that is visible, and a sky-line (λ5577 in the observed frame).

Figure 4.12 shows the results from the `PPXF` stellar population fits. First, it is clear that the Balmer absorption lines (Hβ λ4860, Hγ λ4340, and Hδ λ4100) are strong throughout the spectra, indicating that there is a young stellar population throughout the galaxy.

The Ca H and K lines, located just blue-ward of the 4000Å break, are approximately equally strong in the integrated spectrum (Fig. 4.12a). That the Ca H is stronger in the nuclear spectrum (Fig. 4.12b) is due to a contribution from Hϵ, whose wavelength lies in the same position as Ca H. The fact that the Hϵ contribution to Ca H is quite visible in the nuclear spectrum suggests strong post-starburst activity.

The light fractions of various stellar populations are indicated in the second panel of each spectral fit. The integrated spectra show relatively young stellar populations, with the light being made up of a combination of 1.0 Gyr and 2.5 Gyr stars, with the intermediate age (2.5 Gyr) stars contributing over half the light. In contrast, the nuclear spectrum contains a significant (18%) contribution from a very young (0.3 Gyr) post-starburst "A-star" population. Another 60% of the light comes from the 1 Gyr population, with only a 22% contribution from older stars. From the multi-component stellar population fit, it is clear that NGC 1266 has a young-to-intermediate stellar population throughout, with the strongest young stellar component in its nucleus.

In order to detemine whether NGC 1266 would classically be considered a post-starburst galaxy, we also ran a classical K+A analysis, first described in Dressler & Gunn (1986), and later in Quintero et al. (2004). Instead of allowing `PPXF` to fit multiple stellar

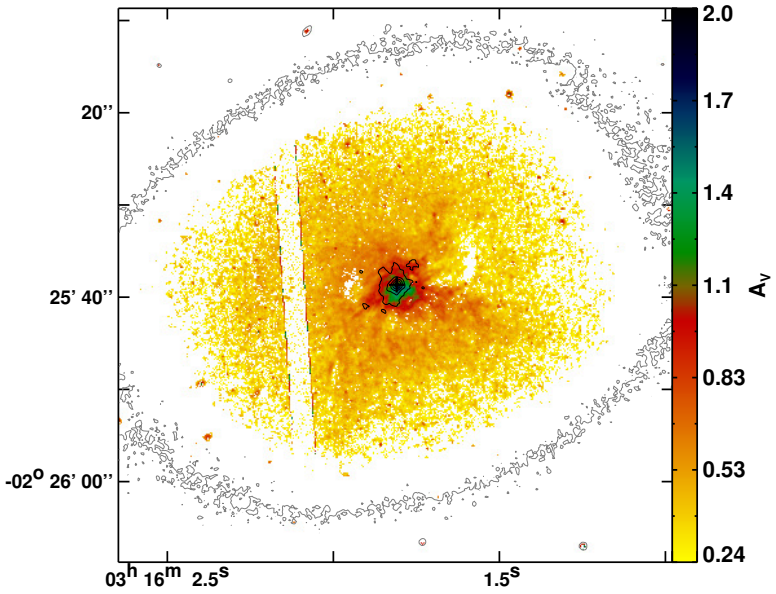

Figure 4.8 The A_V map of NGC 1266. The gray contour represents the "edge" of the galaxy from the H-band image. The black contours represent the central molecular disk, via CO imaging from CARMA (A+11). A_V was calculated by deriving the mean of the 15 combinations of the bands for all pixels with a smaller root mean square than mean.

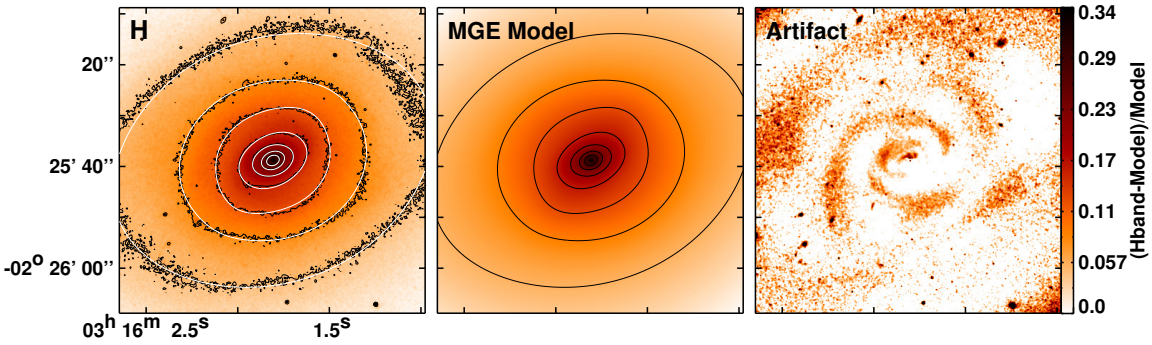

Figure 4.9 **(Left):** The H-band HST image in colorscale and black contours, overlaid with the results of the MGE model-fit (white contours.) **(Middle):** The fitted MGE model derived from fitting the H-band image. **(Right):** The artifacts that remain after the MGE model is subtracted from the H-band data. Overall, the MGE model does a reasonable job fitting much of the underlying stellar features present in the H-band image, but the artifacts clearly show the spiral structure present in NGC 1266, as well as a slight enhangement at the center, in the position of the AGN.

population templates, we restricted the fit to solar metallicity A-star (0.3 Gyr) and K-star (10.0 Gyr) populations only. In this case, using this population restriction, we find that the A-star contribution to the integrated spectrum is 20%. The nucleus is more pronounced, with an A-star contribution of 46%. Following the definition of Quintero et al. (2004), which states that K+A galaxies are defined as galaxies with a A/K ratio of $\gtrsim 0.2$, we find that NGC 1266 fits the absorption classification of being K+A, with ratios of 0.25 and 0.85 for the whole galaxy and nucleus, respectively.

4.4 Discussion

4.4.1 Confirmation of an AGN within NGC 1266

A+11 argued that an AGN was present in NGC 1266, but both the subarcsecond 5 GHz radio continuum point source and the hard X-rays could also be attributed to a compact starburst. The detection of a bright ($T_B > 10^7$ K) VLBA point source, on the other hand, confirms that there is indeed an AGN in NGC 1266. Figures 4.5 and 4.6 show the outflowing CO as well as a cross at the VLBA position for the AGN. It is striking that the source sits directly atop the densest portion of the CO emission. The column located in the line-of-sight of the AGN is approximately an H_2 column of 2.4×10^{24} cm^{-2}, assuming the standard CO-to-H_2 conversion factor (confirmed in A+11 to apply in the case of NGC 1266). It is likely that this column is a lower limit, as NGC 1266 has been strongly detected in many dense gas tracers, including CS (Alatalo et al. 2012, in prep), and the molecular gas in the center is not well-resolved by current instruments. It is

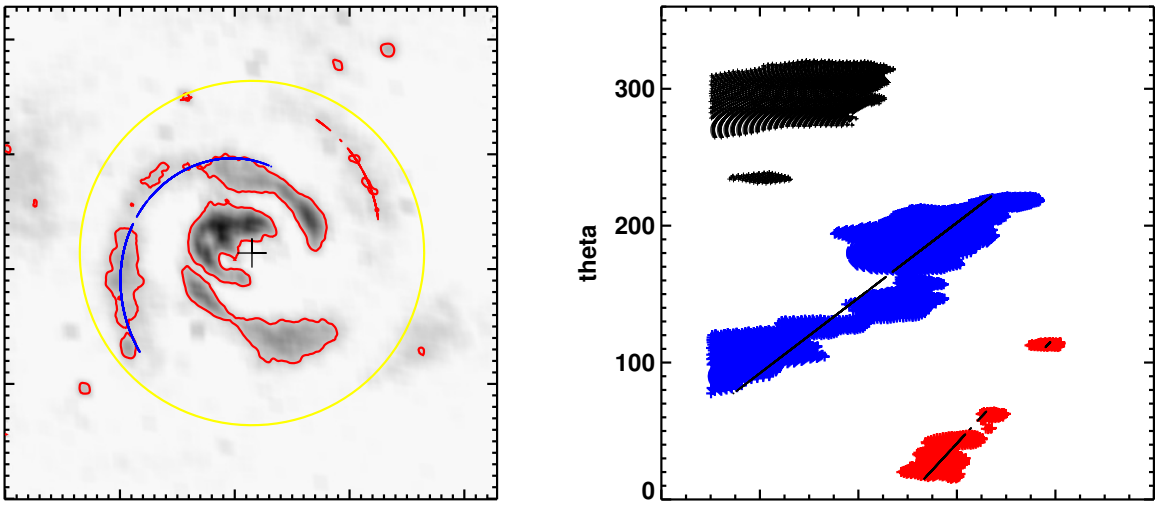

Figure 4.10 **(Left):** The underlying greyscale image is a MGE model-subtracted, flattened, clipped and smoothed H-band image, meant to parametrize the spiral structure seen in the galaxy. The overlaid yellow circle represents the outer radius which was used in the spiral fit. The red contours represent the minimum flux levels in the image that were used in the spiral fit. The cross in the image represents the center found by the MGE fit. The overlaid blue and red lines represent the logarithmic spiral fits to the two spiral arms. The fact that a logarithmic spiral fit is able to well-model the artifacts is clear evidence that the galaxy indeed exhibits spiral structure, rather than shell structure. **(Right):** The spiral pattern is mapped to $\ln(R), \theta$ space, where linear elements are isolated and fit. The blue points are are fit, and the blue line overplotted on the galaxy as well as the red line. The black points are too numerous to allow for a proper fit.

likely that NGC 1266 is a local mildly Compton-thick AGN, having an obscuring column in the line-of-sight of the AGN of $> 10^{24}$ cm^{-2} (Murphy & Yaqoob 2009). If NGC 1266 is indeed Compton-thick, it would explain the dearth of hard X-rays originally detected by *Chandra*, allowing us to conclude that the molecular disk obscures the X-rays originating from the AGN.

Treister et al. (2004) have shown that the ratio of obscured ($N_{\rm H} \geq 10^{22}$ cm^{-2}) to unobscured AGNs is around 4 in the Great Observatories Origins Deep Survey (GOODS) North and South fields, but many of the most Compton thick objects were missed by this survey. As soon as $N_{\rm H}$ increases to $> 10^{24}$ cm^{-2}, Treister et al. (2004) point out that their completeness drops to 30%. This means that the most obscured AGNs are the least likely to be detected.

If NGC 1266 is any sort of model of the behavior of AGNs when such high densities of molecular gas are nearby, it is clear that the most interesting set of AGNs are being missed by most AGN surveys. The VLBA continuum detection of NGC 1266 was essential in

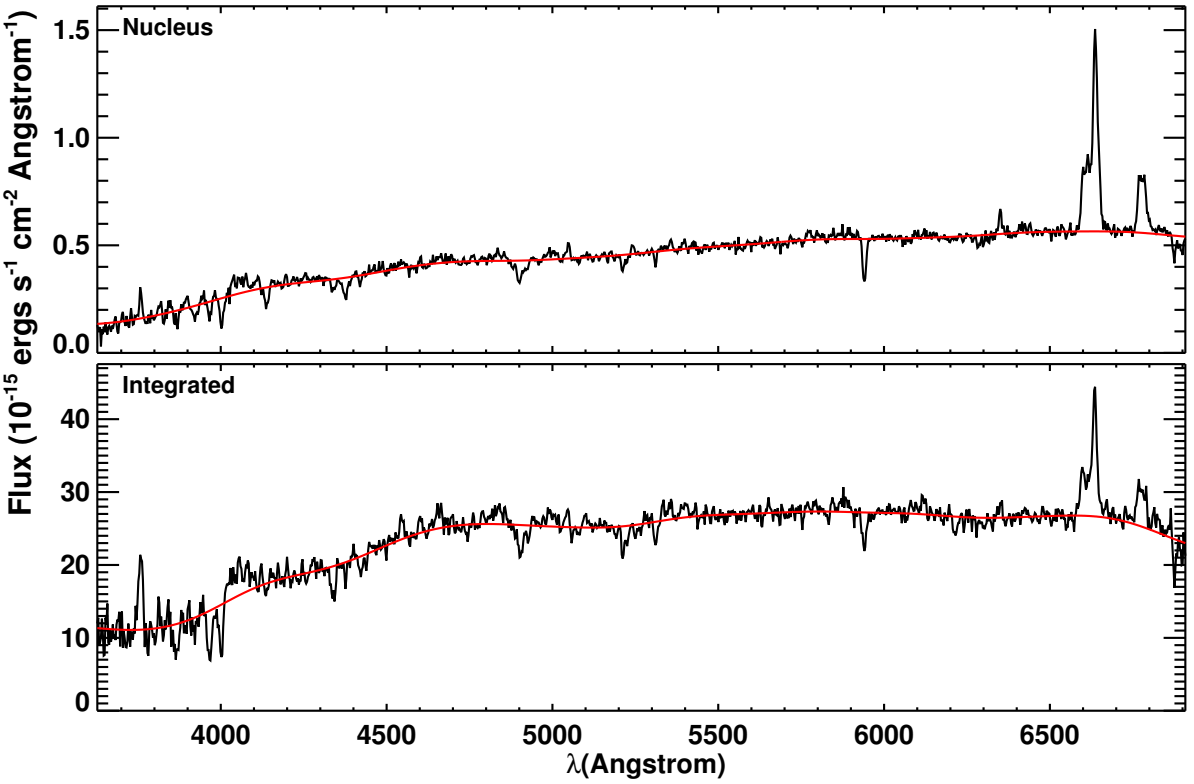

Figure 4.11 The integrated and nuclear spectra of NGC 1266 from Moustakas & Kennicutt (2006) are shown overlaid with a continuum fit. The light for each spectrum is convolved with a wide Gaussian to isolate the continuum light, which represents the stellar continuum within the galaxy.

confirming the presence of the AGN, the suspected driving mechanism for the molecular outflow. We suggest that radio continuum searches play an important role in the detection of the most obscured AGNs. These obscured AGNs are both having an extreme impact on their environment, because of the presence of large quantities of molecular gas proximate to the AGN, and the speed at which NGC 1266-like objects can expel a large amount of starforming material.

4.4.2 The dust properties of NGC 1266

The HST data indicate that the original lower limit to the mass of the outflow 3.3×10^7 $M_\odot$ was indeed a low estimate, and the real outflow mass is at least a factor of 5 larger. The dust visible in Figure 4.8 seems to extend to $\approx$ 3 kpc, larger than A+11 CO extent by a factor of $\approx$ 6, but quite similar to the extent of the ionized gas found by D+12. Therefore, because the extent of the dust involved in the outflow is larger than that originally found in A+11 for the molecular gas, we will use the ionized gas velocities from

Davis et al. (2012, in prep), which measured the line diagnostics, extent, and velocities of many ionized species. D+12 reports that the maximum velocity of ionized species is $\pm$900 km s^{-1}.

We recalculate the properties of the outflowing mass based on the HST A_V estimate and update the values reported in A+11. For an outflow mass of 1.65×10^8 M$_\odot$ and a velocity of 500 km s^{-1} reported in D+12, to represent the velocity seen in the NaD absorption feature, the kinetic energy associated with the outflow is 8.3×10^{56} ergs, equivalent to 10^6 supernovae. In order for supernovae to sustain this outflow, one supernova would have to explode at least every 3 years, a value that requires a sustained star formation rate of $\approx$ 30 M$_\odot$ yr^{-1} over the past Myr, a factor of 10 higher than the star formation upper limit of 3.2 M$_\odot$ yr^{-1} from A+11.

The dynamical time, $\tau_{\rm dyn}$, for the outflow to reach the radius of 3 kpc at the maximum ionized gas velocity of 900 km s^{-1} is 3.2 Myr (very close to the 2.6 Myr calculated using the molecular gas alone; A+11). From the total kinetic energy and $\tau_{\rm dyn}$, the mechanical luminosity $L_{\rm mech} = 8.2 \times 10^{42}$ erg s^{-1}, of order the jet energy 6.1×10^{42} erg s^{-1} found based on the 1.4 GHz - jet power relation found in Bîrzan et al. (2008). Because of the 1/2 dex uncertainty in the Bîrzan et al. (2008) relation, it is entirely possible that the jet energy in NGC 1266 is larger, and therefore is capable of driving the mass-loaded outflow. The mass outflow rate $M_{\rm outflow}/\tau_{\rm dyn}$, originally calculated to be 13 M$_\odot$ yr^{-1} by A+11, is recalculated to be 52 M$_\odot$ yr^{-1}. This is a factor of 15 larger than the maximum SFR of NGC 1266. The total gas depletion time, $\tau_{\rm dep}$, is reduced from 85 Myr to 21 Myr.

The updated outflow mass, calculated using A_V derived from the HST, paints a more powerful picture of the outflow phenomenon in NGC 1266. Clearly, the initial choice of $X_{\rm CO}$ to be optically thin does not correctly represent the nature of the outflowing gas. It is unsurprising that the mass outflow rate has increased, given that the calculated mass of the molecular gas was a lower limit, but the new value is able to completely rule out star formation as the main driving factor. Whereas 13 M$_\odot$ yr^{-1} was possibly sufficiently low that the Murray et al. (2005) criterion, that $\dot{M}_{\rm SFR} \sim \dot{M}_{\rm outflow}$, was satisfied, the updated mass outflow rate, of 52 M$_\odot$ yr^{-1} is over an order of magnitude higher than the upper limit to the SFR. More importantly, the timescale for NGC 1266 to expel all of its gas drops from 85 Myr to 21 Myr if the mass outflow rate remains constant. This means such objects are rare, so finding a single event within the ATLAS$^{\rm 3D}$ sample therefore is unsurprising.

4.4.3 Should NGC 1266 be classified as a poststarburst galaxy?

In §4.3.4, we argued that the stellar population of NGC 1266 is poststarburst, with a large amount of young stars contributing to the light in the galaxy, especially within the nucleus, but the K+A classification requires both a young stellar population as well as a cessation of current star formation. NGC 1266 has an A/K star ratio that satisfies the poststarburst conditions, but it would be rejected from the sample of poststarburst

galaxies, since it has strong Hα emission. This Hα emission would immediately reject NGC 1266 from a poststarburst classification, even if the mechanism responsible for the emission had nothing to do with star formation.

In the case of NGC 1266, the Hα emission is not due to H II regions from star formation. D+12 obtained 3-dimensional Integral Field Unit (IFU) spectra from both the SAURON instrument on the William Herschel Telescope (WHT) and the GMOS-IFU on the Gemini North telescope. With those observations, D+12 detected Hα, Hβ, [O III], [O II], [N II], and [S II] emission. Both spatial maps and line ratios presented in D+12 clearly indicated that the mechanism responsible for the emission from all of these ionized species was a shock emanating from the outflow, meaning that the majority of Hα emission seen in NGC 1266 is completely decoupled from star formation. NGC 1266 therefore fits the criterion for being a poststarburst quite well, with both evidence of a young stellar population as well as a lack of indicators of current star formation.

The fact that NGC 1266 is a poststarburst is fairly unsurprising, given the rapid expulsion of molecular gas from the center, and the lack of signs that the galaxy will be replenishing those stores. What this does bring to light is the possibility that classic searches for poststarburst galaxies are missing the most exciting specimens: those that are actively expelling their molecular gas, a short timescale event If NGC 1266 is any indication, systematic searches for poststarburst galaxies should not a priori reject all galaxies with strong Hα emission, but rather look at the line ratios of various ionized gas emission lines, and search for indications that the emission is due to shocks.

Given a the typical timescale where a poststarburst galaxy is detectable as such ($\sim$ 1 Gyr; Quintero et al. 2004), 3% of the poststarburst population would be undergoing a NGC 1266-like molecular gas expulsion (assuming a $\sim$ 30 Myr timescale for this event), and a significant fraction of these actively expelling poststarburst objects would be rejected due to the presence shock-originated Hα emission. Because the event that NGC 1266 is exhibiting is such an important factor in a galaxy's transition between star-forming, poststarburst, and quiescent, it is essential that we modify poststarburst search routines to include these objects.

The spiral structure seen in NGC 1266 indicates that it has not had a tumultuous event in at least many dynamical times. MEGACAM high sensitivity, wide-field imaging also seems to confirm this to be the case (Fig. 4.14; Duc et al., 2012, in prep), exhibiting little evidence of even a mild interaction. Cales et al. (2011) studied poststarburst quasars, and found that they seemed to be bimodal, with populations that were either merger remnants or non-interacting. The cause of the cessation of star formation in the former is clear, with the merger being the likely culprit. In the non-interacting galaxies, the cause is less clear. NGC 1266 fits into the non-interacting poststarburst population and is still in the stage of expelling its gas. Therefore the possibility that there is still evidence pointing to the culprit that caused the cessation of its star formation exists. Identifying this culprit in NGC 1266 could therefore shed light on the non-interacting poststarburst population, and possibly provide the key to how star formation abruptly ceases without

an obvious trigger. Future modeling work on NGC 1266 will focus on simulations designed to create an NGC 1266-like object, searching for triggering mechanisms that could leave so few dynamical signs in a galaxy, but still abruptly expel all starforming material.

4.5 Summary and Conclusions

We report new observations of NGC 1266, a local example of mass-loaded, AGN-driven molecular feedback. The VLBA observations presented here were able to confirm the presence of an AGN in the system, with a brightness temperature (a proxy for specific intensity) of $T_b \approx 10^7$ K at 1.6 GHz, far too high to be explained by a compact starforming disk. The position of the AGN is also coincident with the peak of the molecular gas, indicating that NGC 1266 is a Compton-thick AGN. It is therefore clear that detection of AGNs located in objects similar to NGC 1266 will depend on high resolution radio continuum measurements.

B, V, I, Y, J and H-band photometry from the ACS and WFC3 on the HST are also presented. The B, V and I bands indicate that there is a large amount of obscuring dust present in NGC 1266, spatially coincident with the molecular gas in the outflow, and likely belonging to the outflow. The Y, J and H bands show that NGC 1266, once considered an S0, is in fact an early-type spiral. A dust-derived outflow gas mass was calculated from A_V to be 1.65×10^8 $M_\odot$, a factor of 5 higher than was reported in A+11, leading to a mass outflow rate of 52 $M_\odot$ yr^{-1}, unsustainable energetically by star formation and requiring coupling to the AGN to explain.

A closer analysis of the absorption features of NGC 1266 indicate that there is a non-negligible fraction of young stars within the galaxy, with A/K fraction ranging from 0.25 to 0.85. Utilizing results from D+12, we are able to conclude that ionized gas emission features are dominated by shock emission, rather than tracers of star formation. Therefore NGC 1266 appears to fit the K+A criterion, and should be considered a poststarburst galaxy. NGC 1266-like poststarbursts are likely rejected by standard post-starburst searches due to the presence of ionized gas emission, therefore it is imperative to expand the search to include galaxies with line ratios representative of shocks.

The lack of dynamical disturbance or interaction within NGC 1266 indicates that it has become a poststarburst in a non-violent manner, and thereforeprovides an excellent local test laboratory to study scenarios in which molecular gas is completely expelled from the galaxy, while very little dynamical evidence is left behind. Future work will focus on studying scenarios that trigger such events, and finding evidence for other galaxies similar to NGC 1266.

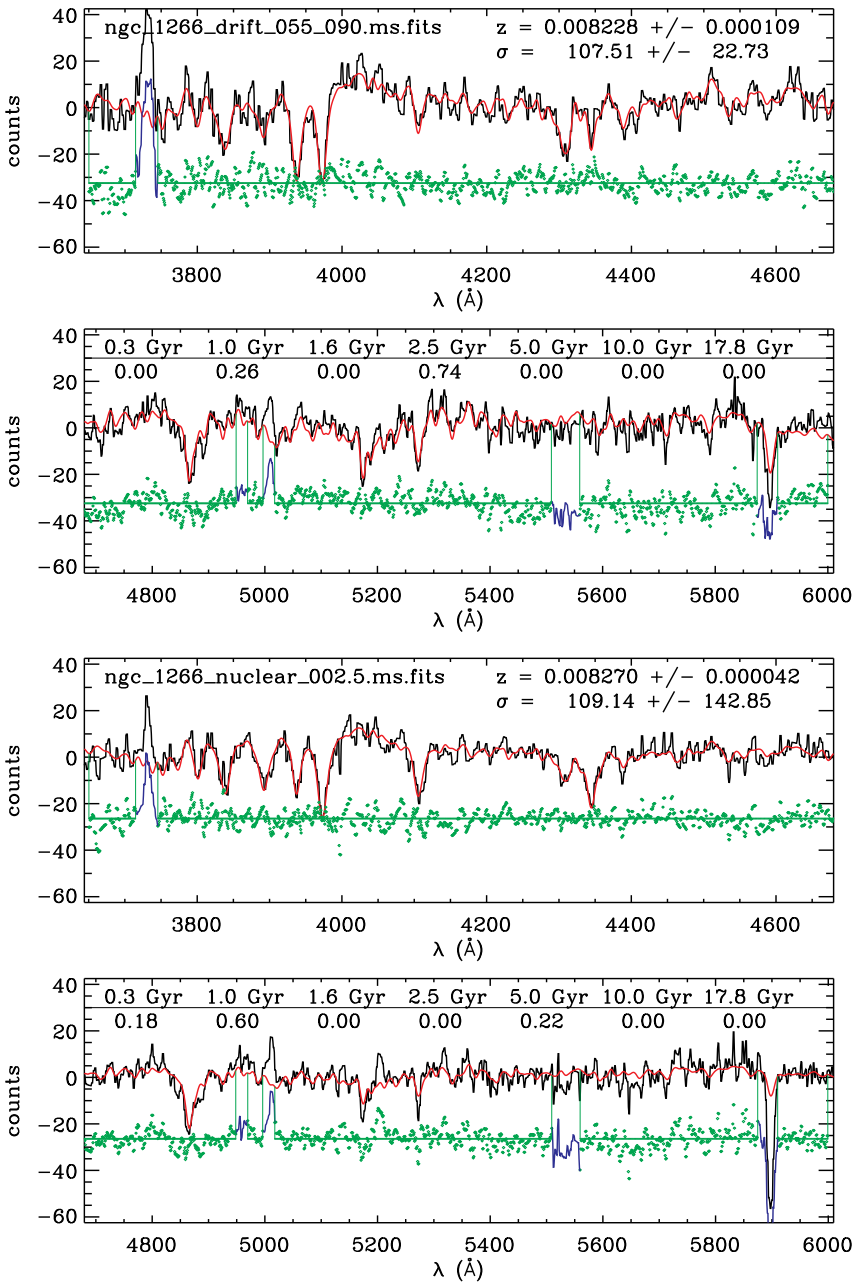

Figure 4.12 The top two panels represent the whole range of the integrated spectra, with the black line representing the continuum subtracted data. The red overlaid line is the stellar population fit created by PPXF, with the strong emission lines (from the shock; D+12) masked out. The underlying green line are the residuals. The relative percentages of different stellar populations are shown in the second of the top panels, showing the results of the model. The bottom two panels represent the nuclear spectra.

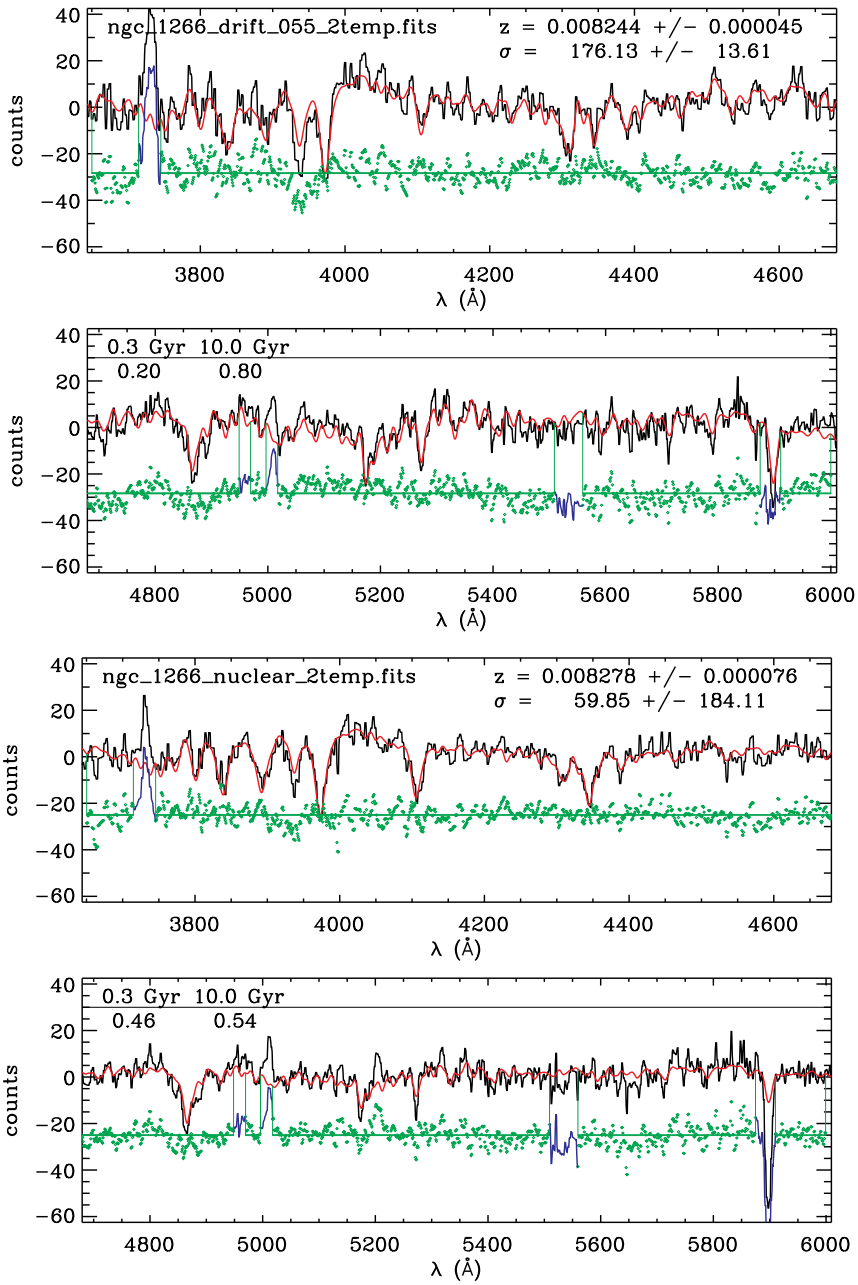

Figure 4.13 The top two panels represent the whole range of the integrated spectra, with the black line representing the continuum subtracted data. The red overlaid line is the stellar population fit created by PPXF, with the strong emission lines (from the shock; D+12) masked out, and only two possible stellar populations: A-stars (0.3 Gyr) and K-stars (10.0 Gyr). The underlying green line are the residuals. The relative percentages of different stellar populations are shown in the second of the top panels, showing the results of the model. The bottom two panels represent the nuclear spectra.

Figure 4.14 g and r wide-field imaging of NGC 1266 taken with the MEGACAM instrument on the Canada-France-Hawaii Telescope on Mauna Kea (Duc et al. 2012, in prep). NGC 1266 is the large early-type galaxy in the field, with its spiral structure visible. The spiral galaxy seen nearby has been shown to be in projection (J. Silverman, private communication). There are possibly faint tidal streams seen near the galaxy, but larger scale imaging indicates that they are also possibly a part of a large galactic cirrus complex that is seen in the region.

Chapter 5

Conclusions and Future Work

5.1 The CARMA ATLAS^{3D} Survey

We have presented the millimeter-wave data products of the CARMA ATLAS^{3D} survey of galaxies, an imaging survey of CO(J=1–0) emission of 30 nearly CO-rich early-type galaxies (ETGs). The CARMA ATLAS^{3D} survey is the largest CO imaging survey of ETGs to date, and provides the most detailed view of the nature of molecular gas in ETGs. The molecular gas found in ETGs appears to be co-spatial with the dust, though the dust appears to be more extended, likely because we are unable to trace regions with small molecular gas surface densities. The molecular gas present in ETCs comes in a variety of morphologies: 50% in inclined gas disks or are poorly resolved, 5% show spiral arms or spiral structure, 15% are in resolved rings, 10% are within bar+ring systems, 12.5% are in mildly disrupted objects, and 7.5% are in strongly disrupted objects. The CO morphology does not show strong correlation with the $u-r$ color of the galaxy, although there appear to be weak trends. For example, the most massive galaxies in the sample tend to have disk morphologies, and ring morphologies tend to lie on the red sequence whereas bar+ring morphologies tend to be present in the blue cloud. We currently observe a total of 8.26×10^9 $M_\odot$ of molecular gas that is likely of external origin for all of our galaxies. Using the correction factor derived in Kaviraj et al. (2012), we estimate that the total externally acquired molecular gas in those galaxies was $\approx 2.48 \times 10^{10}$ $M_\odot$.

5.2 The Unusual Case of NGC 1266

We report the detection of a massive centrally-concentrated molecular component ($M_{\rm CVC} = 1.1 \times 10^9$ $M_\odot$) and a powerful molecular outflow ($M_{\rm H_2,outflow} = 2.4 \times 10^7$ $M_\odot$) in the field galaxy NGC 1266. The maximum velocity of the wind exceeds the escape velocity so that at least some gas will escape the galaxy to energize the IGM, and the total neutral gas mass outflow rate $\dot{M} \approx 13$ $M_\odot$ yr^{-1}. The 3.1 $M_\odot$ yr^{-1} star formation

rate in NGC 1266 appears to be incapable of driving this outflow; the AGN appears to be the main driving mechanism, as for H I outflows observed in radio galaxies. It is however unclear how the gas lost its angular momentum to fall so completely into the nucleus.

The 1.1×10^9 central molecular gas contains a rapidly rotating nuclear disk of ≈ 60 pc radius enshrouded in a diffuse molecular envelope, and the molecular outflow emerges normal to the disk plane. Although the molecular nucleus is compact and very near the AGN, multiple estimates of the star formation rate point to a low star formation efficiency, but the uncertainties in these SFRs place NGC 1266 within the scatter of the K-S relation (assuming that L_{FIR} is not dominated by the AGN).

If the gas in the nucleus is the source of the molecular outflow, then the gas depletion timescale is 85 Myr, short enough for all ETGs to go through such a phase while remaining consistent with having found only one such case among the 260 ETGs in the ATLAS^{3D} sample. NGC 1266 is one of the brightest detections, however, so there might be more outflows in the sample, undetected so far because of lower S/N ratios.

While molecular outflows have been identified in a handful of galaxies, NGC 1266 is the only one that shows no evidence of having undergone an interaction. The mechanism responsible for transporting the molecular gas into the center remains unknown.

5.3 High resolution imaging of NGC 1266 with HST and the VLBA

We report new observations of NGC 1266, a local example of mass-loaded, AGN-driven molecular feedback. The VLBA observations presented here were able to confirm the presence of an AGN in the system, with a brightness temperature (a proxy for specific intensity) of $T_b \approx 10^7$ K at 1.6 GHz, far too high to be explained by a compact starforming disk. The position of the AGN is also coincident with the peak of the molecular gas, indicating that NGC 1266 is a Compton-thick AGN. It is therefore clear that detection of AGNs located in objects similar to NGC 1266 will depend on high resolution radio continuum measurements.

We also present B, V, I, Y, J and H-band photometry from the ACS and WFC3 on the HST. The B, V and I bands indicate that there is a large amount of obscuring dust present in NGC 1266, spatially coincident with the molecular gas in the outflow, and likely belonging to the outflow. The Y, J and H bands show that NGC 1266, once considered an S0, is in fact an early-type spiral. We derive an outflow gas mass from A_V, of 1.65×10^8 $M_\odot$, a factor of 5 higher than was reported in Alatalo et al. (2011) and Chapter 3, leading to a mass outflow rate of 52 $M_\odot$ yr^{-1}, unsustainable energetically by star formation and requiring coupling to the AGN to explain.

A closer analysis of the optical absorption features of NGC 1266 indicate that there is a non-negligible fraction of young stars within the galaxy, with A/K fraction ranging from 0.25 to 0.85. Utilizing results from D+12, we are able to conclude that ionized gas

emission features are dominated by shock emission, rather than by tracers of star formation. Therefore NGC 1266 appears to fit the K+A criterion, and should be considered a poststarburst galaxy. NGC 1266-like poststarbursts are likely rejected by standard poststarburst searches due to the presence of ionized gas emission, therefore it is imperative to expand the search to include galaxies with line ratios representative of shocks.

The lack of dynamical disturbance or interaction within NGC 1266 indicates that it has become a poststarburst in a non-violent manner, and therefore provides an excellent local test laboratory to study scenarios in which molecular gas is completely expelled from the galaxy, while very little dynamical evidence is left behind. Future work will focus on studying scenarios that trigger such events, and finding evidence for other galaxies similar to NGC 1266.

5.4 Future Work and Directions with Upcoming Telescopes

With the onset of the Atacama Large Millimeter Array (ALMA) era, the study of molecular gas across the universe has become accessible. With the unprecedented sensitivity of an instrument like ALMA, we are able to expand the study of molecular gas in ETGs from the most nearby examples in the relatively small Virgo Cluster into much denser environments, such as the Coma Cluster. This will allow us to test whether the kinematic alignment seen in Virgo, but not in the field, is a fundamental property of the molecular gas in cluster members. Using ALMA, we will be able to probe deeper, to lower molecular gas surface densities, to see whether the 23% detection rate of ETGs is a sensitivity effect, or something intrinsic to the galaxies.

The James Webb Space Telescope (JWST) also promises to add to the field of molecular gas in quiescent galaxies, by providing high sensitivity, high resolution imaging of star formation tracers such as the polycyclic aromatic hydrocarbons (PAHs), allowing for a pixel-by-pixel comparison to the molecular gas. ALMA, in conjunction with the JWST will expand the range of environments that we are able to study star formation in ETGs.

In the search for more NGC 1266-like objects, ALMA will prove invaluable. It appears that molecular outflows are a common feature, but that most instruments were not, until recently, capable of detecting the low lying, high velocity emission. The faint, high velocity features require an instrument to have sufficient sensitivity to detect faint features, wide bandwidths to encompass the entirety of the line, and sufficiently reliable calibrations to deal with the 10:1 dynamic ranges observed between the peak CO intensity and the CO outflow intensity (Feruglio et al. 2010; Alatalo et al. 2011). ALMA is the optimal instrument for the continuing search for outflowing systems. It provides sufficient bandwidth ($\gtrsim$ 2000 km s^{-1} at 230 GHz), and sensitivity to search for faint high velocity features in ULIRGs, Seyfert galaxies, and starbursting systems. ALMA also includes the capability for high fidelity imaging. The extent of the outflow in NGC 1266 allowed for

a robust derivation of the mass outflow rate and molecular gas exhaustion time. Imaging high velocity CO features ienables us to create a census of the mass, mass outflow rate, and timescales of quenching systems in the local universe.

Both the Nuclear Spectroscopic Telescope Array (NuSTAR) and the JWST will also have an impact in the search for more NGC 1266-like objects. NuSTAR probes the energy range 6–79 keV, higher than *Chandra*. Since hard X-rays are less susceptible to absorption, this means that NuSTAR is an ideal telescope for Compton thick objects, such as NGC 1266. The JWST on the other hand will provide high resolution imaging of outflowing objects at $z \sim 2$, where the peak star formation occurred in the Universe. This means that NuSTAR is able to detect the AGNs buried in molecular gas, and the JWST is able to image these objects. Between ALMA, NuSTAR and the JWST, we will be able to detect, image, and study the kinematics of objects that are actively expelling their molecular gas and transitioning to the red sequence across a Hubble time.

The era of ALMA promises to be an upswell in the area of molecular gas in ETGs, both mapping the present molecular gas in quiescent hosts, as well as detecting transition objects that are currently expelling all of their starforming material, and are on their way to being completely quenched. NuSTAR promises to revolutionize the field of Compton thick AGNs, where molecular gas is the most likely to be influenced directly by the action of the supermassive black hole. The JWST will revolutionize both the fields of molecular gas in quiescent galaxies and transition galaxies with its high resolution and sensitivity, able to map these populations over a Hubble time and study their evolution.

Bibliography

Alatalo, K. et al., 2011, ApJ, 735, 88
Athanassoula, E., Bureau, M., 1999, ApJ, 522, 699
Baan, W. A. & Klöckner, H. R. 2006, A&A, 449, 559
Baars, Jacob W. M. (2007). *The Paraboloidal Reflector Antenna in Radio Astronomy and Communication:* (First Edition), Springer, ISBN 978-0-387-69733-8
Baldry, I. K. et al., 2004, ApJ, 600, 681
Bally, J. & Lada, C. J. 1983, ApJ, 265, 824
Beck, S. C., Turner, J. L., Kloosterman, J., 2007, AJ, 134, 1237
Bekki, K. 1998, ApJ, 502, L133
Bekki, K., Couch, W. J., & Shioya, Y. 2002, ApJ, 577, 651
Bell,E. F., et al., 2004, ApJ, 608, 752
Bigiel, F., et al. 2008, AJ, 136, 2846
Bîrzan, L., et al. 2008, ApJ, 686, 859
Bohlin, R. C., Savage, B. D., & Drake, J. F. 1978, ApJ, 224, 132
Böhringer, H. et al., 1994, Nature, 368, 828
Bois, M., et al. 2011, MNRAS, 416, 1654
Boselli, A., & Gavazzi, G. 2006, PASP, 118, 517
Bournaud, F., Combes, F., 2002, A&A, 392, 83
Bower, R. G., Lucey, J. J., Ellis, R. S., 1991, MNRAS, 254, 601
Buta, R., Combes, F., 1996, FCPh, 17, 95
Bundy, K., et al. 2010, ApJ, 719,1969
Cales, S. L., et al., 2011, ApJ, 741, 106
Calzetti, D., et al. 2005, ApJ, 633, 871
Calzetti, D., et al. 2007, ApJ, 666, 870
Cappellari, M. 2002, MNRAS, 333, 400
Cappellari, M., & Emsellem, E., 2004, PASP, 116, 138
Cappellari, M. 2008, MNRAS, 390, 71
Cappellari, M. et al., 2011a, MNRAS, 413, 813
Cappellari, M. et al., 2011b, MNRAS, 416, 1680
Cappellari, M., et al. 2012, Nature, 484, 485
Cardelli, J. A., Clayton, G. C., & Mathis, J. S. 1989, ApJ, 345,245
Cayatte, V., van Gorkom, J. H., Balkowski, C., Kotanyi, C., 1990, AJ, 100, 604

Cecil, G. et al., 2001, ApJ, 555, 338
Chung, A., et al. 2011, ApJ, 732, L15
Ciotti, L., D'Ercole, A., Pellegrini, S., Renzini, A., 1991, ApJ, 376, 380
Condon, J. J., Huang, Z.-P., Yin, Q. F., & Thuan, T. X., 1991, ApJ, 378, 65
Combes, F., Young, L. M., & Bureau, M. 2007, MNRAS, 377, 1795
Crocker, A. C., Bureau, M., Young, L. M., Combes, F., 2008, MNRAS, 368, 1811
Crocker, A. C. et al., 2009, MNRAS, 393, 1255
Crocker, A. F., et al., 2011, MNRAS, 410, 1197
Crocker, A. C. et al., 2012, MNRAS, 421, 1298
Crockett, R. M. et al., 2011, ApJ, 727, 115
Croton, D. J., et al. 2006, MNRAS, 365, 11
Dale, D. A., et al. 2005, ApJ, 633, 857
Dale, D. A., et al. 2007, ApJ, 655, 863
Dale, D. A., et al. 2012, ApJ, 725, 95
Dame, T. M., Hartmann, D., & Thaddeus, P. 2001, ApJ, 547, 792
Davis, T. A. et al., 2011a, MNRAS, 414, 968
Davis, T. A. et al., 2011b, MNRAS, 417, 882
Davis,T. A. et al. 2012, MNRASaccepted (arXiv:1207.5799)
Deller, A. T., et al., 2011, PASP, 123, 275
Di Matteo, T., Springel, V., & Hernquist, L. 2005, Nature, 433, 604
Douglas, J. N., et al. 1996, AJ, 111, 1945
Downes, D., & Solomon, P. M. 1998, ApJ, 507, 615
Draine, B. T., et al. 2007, ApJ, 663, 866
Dressler, A., & Gunn, J. E., 1986, ApJ, 270, 7
Duc, P.-A., Braine, J., Lisenfeld, U., Brinks, E., Boquien, M., 2007, A&A, 475, 187
Duc, P.-A. et al., 2011, MNRAS, 417, 863
Emonts, B. H. C., et al. 2005, MNRAS, 362, 931
Emsellem, E., Monnet, G. & Bacon, R. 1994, A&A, 285, 723
Emsellem, E., et al. 2004, MNRAS, 352, 721
Emsellem, E., et al., 2011, MNRAS, 414, 888
Evans, A. S., et al. 2005, ApJS, 159, 197
Evrard, A. E. 1991, MNRAS, 248, 8
Faber, S. M., Gallagher, J. S., 1976, ApJ, 204, 365
Faber, S. M., et al. 2007,ApJ, 665, 265
Feruglio, C., et al. 2010, A&A, 518, L155
Fischer, J., et al. 2010, A&A, 518, L41
Fujita, Y. 1998, ApJ, 509, 587
Gao, Y., & Solomon, P. M. 2004, ApJS, 152, 63
Gebhardt, K. et al., 2000, ApJ, 529, 16
Gil de Paz, A., et al. 2007, ApJS, 173, 185
Giovanelli, R. et al., 2005, AJ, 130, 2598

Harker, J. J., Schiavon, R. P., Weiner, B. J. Faber, S. M., 2006, ApJ, 647, L103
Hawarden, T. G. et al., 1981, MNRAS, 196, 747
Helfer, T. T., et al. 2003, ApJS, 145, 249
Ho, L. C. 2008, ARA&A, 46, 475
Hopkins, P. F., et al. 2005, ApJ, 630, 705
Hubble, E., 1926, ApJ, 64, 321
Icke, V. 1985, A&A, 144, 115
Jarrett, T. H., Chester, T., Cutri, R., Schneider, S. E. & Huchra, J. P. 2003, AJ, 125,525
Jeong, H. et al., 2009, MNRAS, 398, 2028
J ozsa, G. I. G., et al. 2009, A&A, 500, L33
Jura, M., 1986, ApJ, 306, 483
Kauffmann, G., et al. 2003, MNRAS, 341, 33
Kaviraj, S., et al. 2012, MNRAS, 423, 49
Kennicutt, R. C., Jr. 1998, ApJ, 498, 541
Kennicutt, R. C., Jr., et al. 2003, PASP, 115, 928
Khochfar, S., et al. 2011, MNRAS, 417, 845
Knapp, G. R. & Jura, M. 1976, ApJ, 209, 782
Knapp, G. R., Turner, E. L., Cunniffe, P. E., 1985, AJ, 90, 3
Knapp, G. R., Guhathukarta, P., Kim, D.-W., Jura, M., 1989, ApJS, 70, 329
Krajnović, D. et al., 2011, MNRAS, 414, 2923
Kuntschner, H., et al., 2006, MNRAS, 369, 497
Lablanche, P.-Y., et al. 2012, MNRAS, 424, 1495
Lada, C. J., Lada, E. A., Clemens, D. P., & Bally, J. 1994, ApJ, 429, 694
Lauer, T. R. et al. 2005,AJ, 129, 2138
Lees, J. F., Knapp, G. R., Rupen, M. P., & Phillips, T. G. 1991, ApJ, 379, 177
Leroy, A. K., et al. 2008, AJ, 136, 2782
Li, J. J., Seaquist, E. R., 1994, AJ, 107, 1953
Lintott, C. J., et al., 2009, MNRAS, 399, 129
Lotz, J. M. et al. 2008, ApJ, 672, 177
Lotz J. M. et al. 2011, ApJ, 742, L103
Martig, M., Bournaud, F., Teyssier, R., Dekel, A., 2009, ApJ, 707, 250
Masters, K. L., et al. 2010, MNRAS, 405, 783
Matsushita, S., Muller, S., & Lim, J. 2007, A&A, 468, L49
Mauersberger, R., et al. 1996, A&A, 305, 421
Mei, S. et al. 2007, ApJ, 655, 144
Mihos, J. C. 1995, ApJ, 438, L75
Moore, B., Katz, N., Lake, G., Dressler, A., & Oemler, A. 1996, Nature, 379, 613
Morganti, R., Oosterloo, T., & Tsvetanov, Z. 1998, AJ, 115, 915
Morganti, R., et al. 2003, ApJ, 593, L69
Morganti, R., et al. 2004, A&A, 424, 119
Morganti, R., et al. 2005, A&A, 439, 521

Morganti, R., Tadhunter, C. N., & Oosterloo, T. A. 2005, A&A, 444, L9
Morganti, R. et al., 2006, MNRAS, 371, 157
Moustakas, J. & Kennicutt, R. C. 2006, ApJS, 164, 81
Murgia, M. et al. 2005, A&A, 437, 389
Murphy, K. D., & Yaqoob, T. 2009, MNRAS, 397, 1549
Murray, N., Quataert, E., & Thompson, T. A. 2005, ApJ, 618, 569
Nesvadba, N. P. H., et al. et al., 2008, A&A, 491, 407
Nesvadba, N. P. H., et al. et al., 2011, MNRAS, 415, 2359
Ogle, P., et al. 2010, ApJ, 724, 1193
Oosterloo, T. A., et al. 2000, AJ, 119, 2085
Oosterloo, T. et al., 2010, MNRAS, 409, 500
Paturel, G., et al. 2003, A&A, 412, 45
Pérez, L. M., et al. 2010, ApJ, 724, 493
Quintero, A. D., et al., 2004, ApJ, 602, 190
Rampadarath, H., et al., 2010, A&A, 517, L8
Roussel, H., et al. 2007, ApJ, 669, 959
Rybicki, George B., & Lightman, Alan P. (2004). *Radiative Processes in Astrophysics:* (Second Edition), Wiley-VCH, ISBN 978-0-471-82759-7
Sage, L. J., Wrobel, J. M., 1989, ApJ, 344, 204
Sage, L. J., Galletta, G., 1993, ApJ, 419, 544
Sage, L. J., Welch, G. A., 2006, ApJ, 644, 850
Sage, L. J., Welch, G. A., & Young, L. M. 2007, ApJ, 657, 232
Sakamoto, K., et al. 2009, ApJ, 700, L104
Sarzi, M., et al., 2006, MNRAS, 366, 1151
Sault, R. J., Teuben, P. J., & Wright, M. C. H. 1995, in ASP Conf. Ser. 77, Astronomical Data Analysis Software and Systems IV (San Francisco: ASP), 433
Savage, B. D., & Mathis, J. S. 1979, ARA&A, 17, 73
Schawinski, K., et al., 2007, MNRAS, 382, 1415
Schawinski, K., et al., 2010, ApJ, 724, 30
Schinnerer, E., Scoville, N., 2002, ApJ, 577, 103
Schultz, G. V., & Wiemer, W. 1975, A&A, 43, 133
Schuster, K. F., et al. 2007, A&A, 461, 143
Scott, N., et al. 2009, MNRAS, 398, 1835
Serra, P., et al. 2012, MNRAS, 422, 1835
Shapiro, K. L., et al. 2010, MNRAS, 402, 2140
Sheth, K. et al. 2002, AJ, 124, 2581
Skibba, R. A., et al. 2012, ApJ, 738, 89
Soifer, B. T., et al. 1987, ApJ, 320, 238
Soifer, B. T., Boehmer, L., Neugebauer, G. & Sanders, D. B. 1989, AJ, 98, 766
Solomon, P. M., Rivolo, A. R., Barrett, J., & Yahil, A. 1987, ApJ, 319, 730
Solomon, P. M., Downes, D., Radford, S. J. E. & Barrett, J. W. 1997, ApJ, 478, 144

Springel, V., Di Matteo, T., Hernquist, L., 2005, MNRAS, 361, 776
Strateva,I., et al., 2001, AJ, 122, 1861
Steiman-Cameron, T. Y., Kormendy, J., Durisen, R. H., 1992, AJ, 104, 4
Taylor,G. B., Carilli, C. L., & Perley, R. A. (1999) *Synthesis Imaging in Radio Astronomy II*: (First Edition), ASP Conference Series, ISBN 978-1-58381-516-8
Temi, P., Brighenti, F., & Mathews, W. G. 2009, ApJ, 707, 890
Terashima, Y., & Wilson, A. S. 2001, ApJ, 560, 139
Tonry, J. L. et al. 2001, ApJ, 546, 681
Toomre, A., Toomre, J., 1972, ApJ, 178, 623
Toomre, A. 1981, in The Structure and Evolution of Normal Galaxies, ed. S. M. Fall & D. Lynden-Bell (Cambridge : Cambridge Univ. Press), 111
Tran, H. D. et al., 2001, AJ, 191, 2928
Treister, E., et al., 2004, ApJ, 616, 123
Tremonti, C. A., Moustakas, J., & Diamond-Stanic, A. M., 2007, ApJ, 663, L77
Trump, J. R., et al. 2006, ApJS, 165, 1
van der Tak, F. F. S., Black, J. H., Schöier, F. L., Jansen, D. J., & van Dishoeck, E. F. 2007, A&A, 468, 627
Visvanathan, N., Sandage, A., 1977, ApJ, 216, 214
Veilleux, S., Cecil, G., Bland-Hawthorn, J. & Shopbell, P. L. 2002, Rev. Mexicana Astron. Astrofis., 13, 222
Voit, G. M., 1992, MNRAS, 258,841
Walter, F., Weiss, A., & Scoville, N. 2002, ApJ. 580, L21
Wei, L. H., Vogel, S. N., Kannappan, S. J., Baker, A. J., Stark, D. V., Laine, S., 2010, ApJ, 725, 62
Wei, L. H., Kannappan, S. J., Vogel, S. N., Baker, A. J., 2010, ApJ, 708, 841
Welch, G. A., & Sage, L. J. 2003, ApJ, 584, 260
Welch, G. A., Sage, L. J., Young, L. M., 2010, ApJ, 735, 100
White, N. E., Giommi, P. & Angelini, L. 2000, *The WGACAT version of ROSAT sources*, VizieR Online Data Catalog, 9031
Wiklind, T., Combes, F., & Henkel, C. 1995, A&A, 297, 643
Wrobel, J. M., Kenney, J. D. P., 1992, ApJ, 399, 94
Wrobel, J. M., & Ho, L. C., 2006, ApJ, 646, 95
Wu, H., et al. 2005, ApJ, 632, L79
Yan,R., et al., 2006, ApJ, 648, 281
Young, L. M., 2002, AJ, 124, 788
Young, L. M., 2005, ApJ, 258, 271
Young, L. M., Bureau, M., Cappellari, M., 2008, ApJ, 676, 317
Young, L. M., Bendo, G. J., Lucero, D. M., 2009, AJ, 137, 3053
Young, L. M. et al., 2011, MNRAS, 414, 940

Appendix A

CARMA data for the ATLAS3D galaxies

A.1 CO CARMA data of ATLAS^{3D} galaxies

For each galaxy of the CARMA ATLAS^{3D} sample, we provide six figures:

Top Left: r-band image (grayscale) either from SDSS or from the INT; overlaid with black contours. The CO integrated intensity (moment0) map is also overlaid (cyan contours corresponding to 20, 40, 60, 80 and 100% of the peak). The cyan-black box corresponds to the size of the individual moment maps directly to the right of the image.

Top Right: Comparison of the single-dish IRAM 30m CO(1–0) integrated flux (black) and the CARMA integrated flux (red). The total integrated CARMA flux is obtained by summing all flux above a threshold (see §2.3.3). The grey dashed vertical lines indicate the total spectral range of CARMA. Both heliocentric velocities and velocities with respect to systemic are indicated.

Middle Left: CO(1–0) integrated intensity (moment0) map (colorscale), overlaid with black and grey contours (at equal increments of 20% of the peak). The colour table on the right provides the integrated flux scale. The dot-dashed gray circle corresponds to the 21.6″ primary beam of the IRAM 30m telescope. The CARMA synthesized beam is shown in the bottom-right corner (black ellipse).

Middle Center: CO(1–0) mean velocity (moment1) map (colorscale and black contours at 20 km s^{-1} intervals unless otherwise stated). The colour table on the right provides the velocity scale with respect to the systemic velocity (taken from Paper I and indicated in the top-left corner of the panel). The dot-dashed gray circle corresponds to the 21.6″ primary beam of the IRAM 30m telescope. The CARMA synthesized beam is shown in

the bottom-right corner (black ellipse).

Middle Right: CO(1–0) position-velocity diagram (PVD) taken over a synthesized beam width (5 pixels) slice at the position angle indicated in the top-right corner inset and at the bottom of the panel (see §2.3.3). Velocities are heliocentric. The synthesized beam taken in the PV slice direction is indicated in the bottom-right corner. Contours are spaced by 1σ starting at 3σ (unless otherwise stated), where σ is the rms noise in an individual channel multiplied by $\sqrt{5}$, to account the summation over the synthesized beam width.

Bottom: CO(1–0) channel maps. The panels for velocity channels with flux are color-coded based on their velocity with respect to systemic. The mean velocity offset is listed in the top-left corner of each panel. The cross indicates a fixed reference position in all panels. Contours are spaced by 1σ beginning at $\pm 2\sigma$ (unless otherwise stated), where 1σ is the rms noise in an individual channel. Grey contours are negative. The CARMA synthesized beam is shown in the lower-right corner of the first panel (black ellipse).

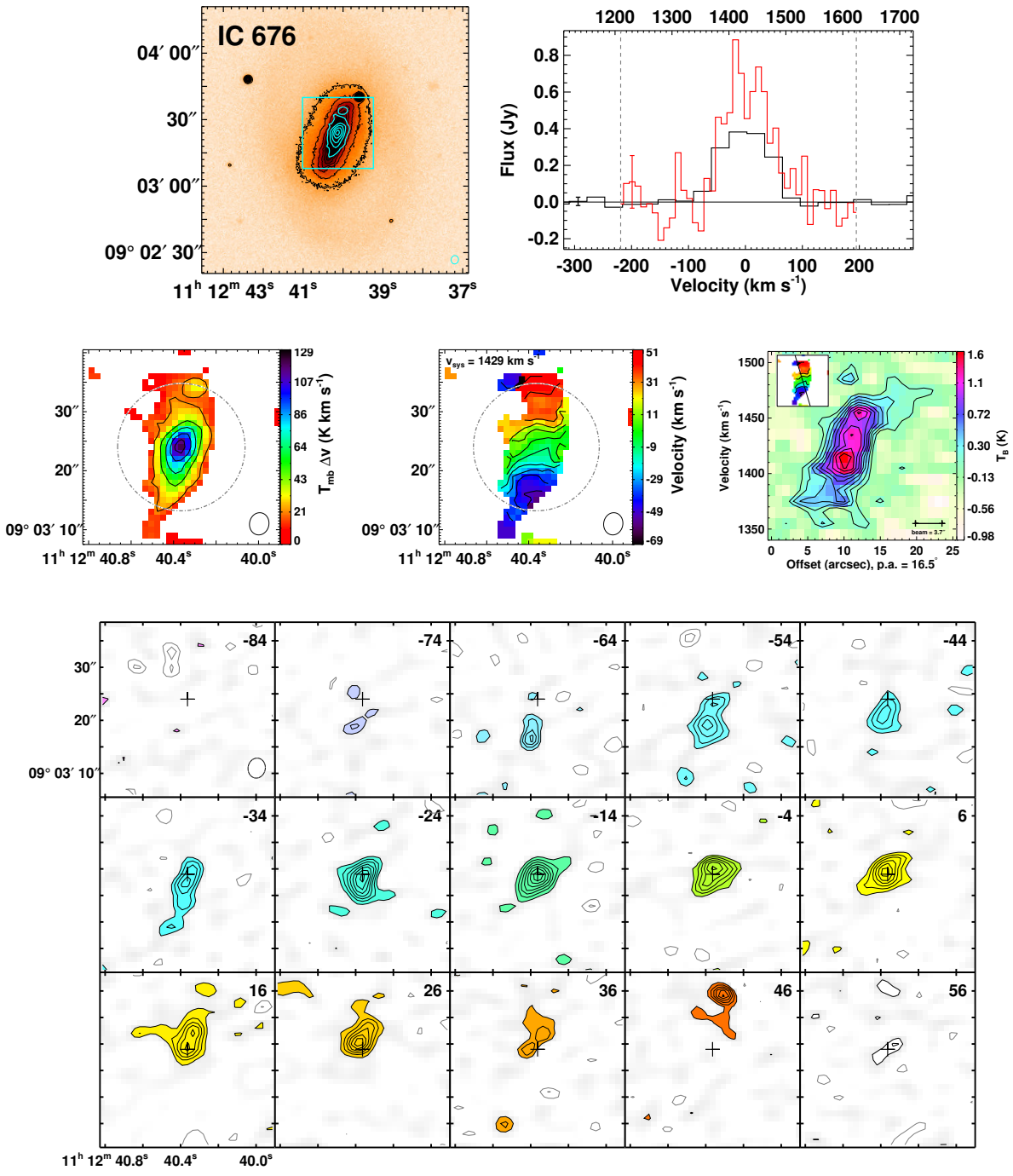

Figure A.1 **IC 676** is a field regular rotator (M_K = -22.27) with a bar and ring stellar morphology. It has a dust filament. The moment0 peak is 17 Jy beam^{-1} km s^{-1}. The moment1 contours are placed at 10km s^{-1} intervals and the PVD contours are placed at 1.5σ intervals.

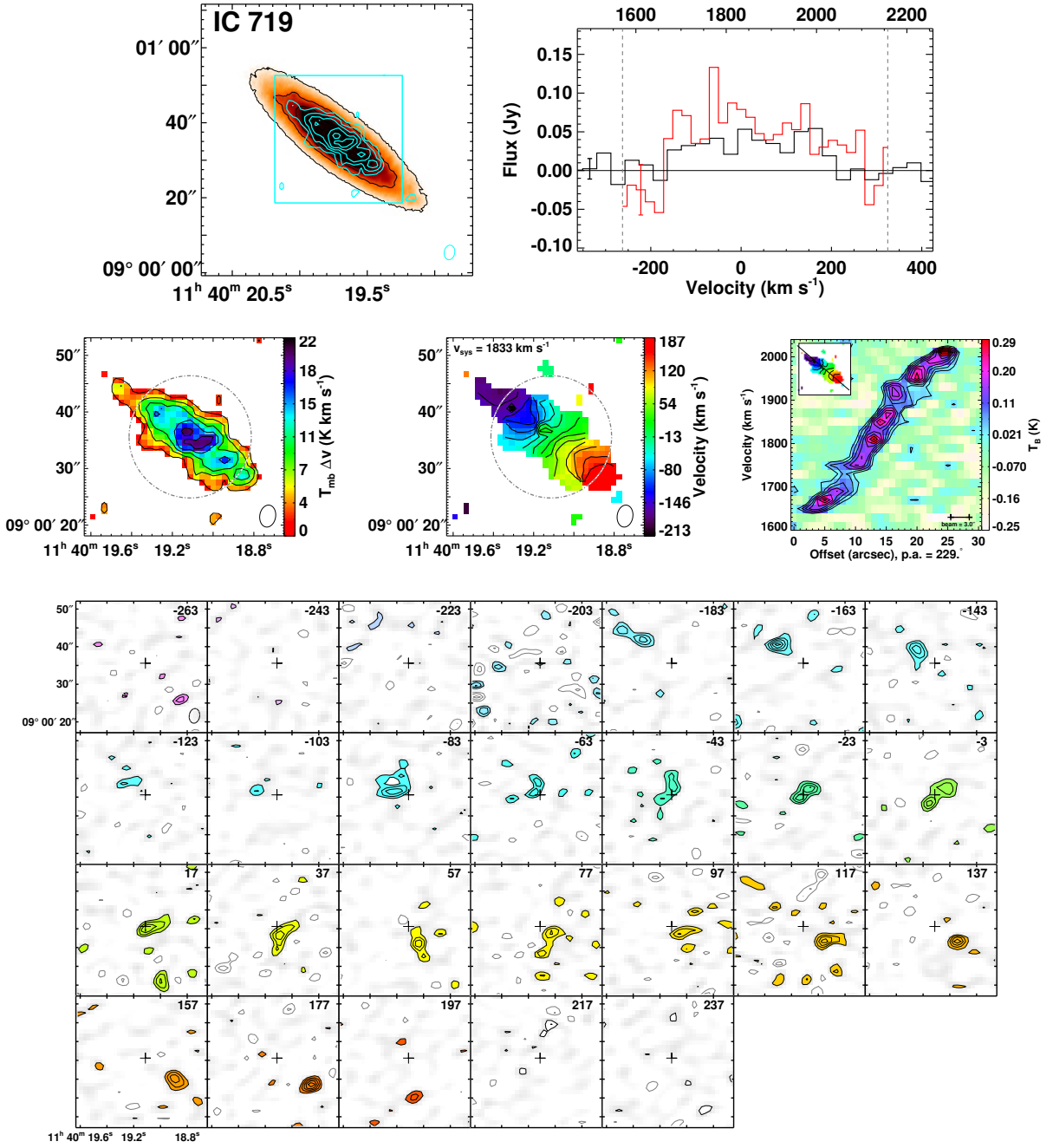

Figure A.2 **IC 719** is a field 2σ non-regular rotator (M_K = -22.70) with normal stellar morphology. It contains a dusty disc. The 2σ peak is the signature of two counter-rotating stellar discs with opposite angular momenta. The molecular gas is co-rotating with a kinematically decoupled core, and counter-rotating with respect to the dominant stellar component. The moment0 peak is 2.6 Jy beam^{-1} km s^{-1}. The moment1 contours are placed at 25km s^{-1} intervals.

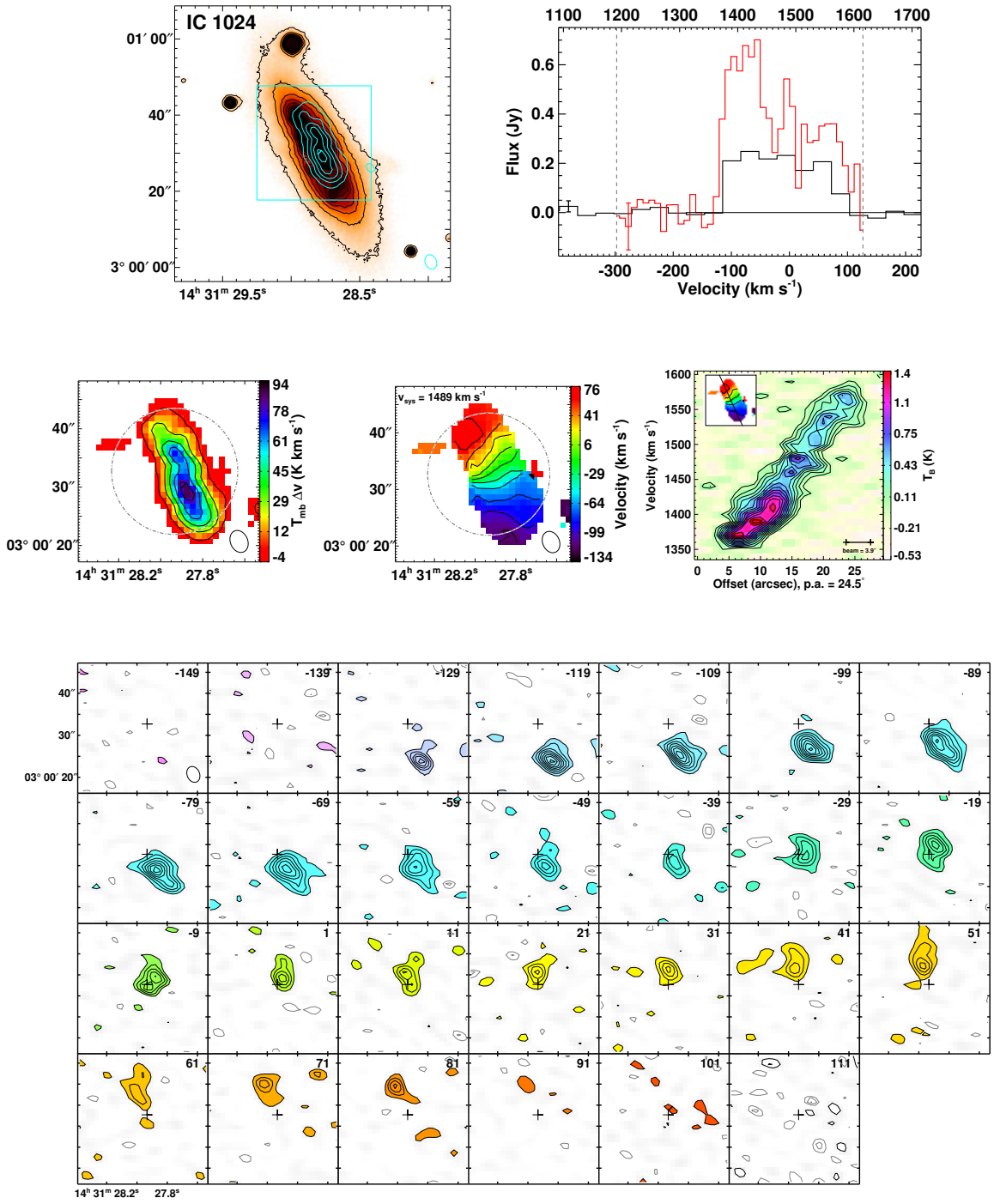

Figure A.3 **IC 1024** is a field regular rotator (M_K = -21.85) with stellar morphology that shows interaction features as well as a dust filament. The moment0 peak is 14 Jy beam^{-1} km s^{-1}. The channel map and PVD contours are placed at 1.5σ intervals.

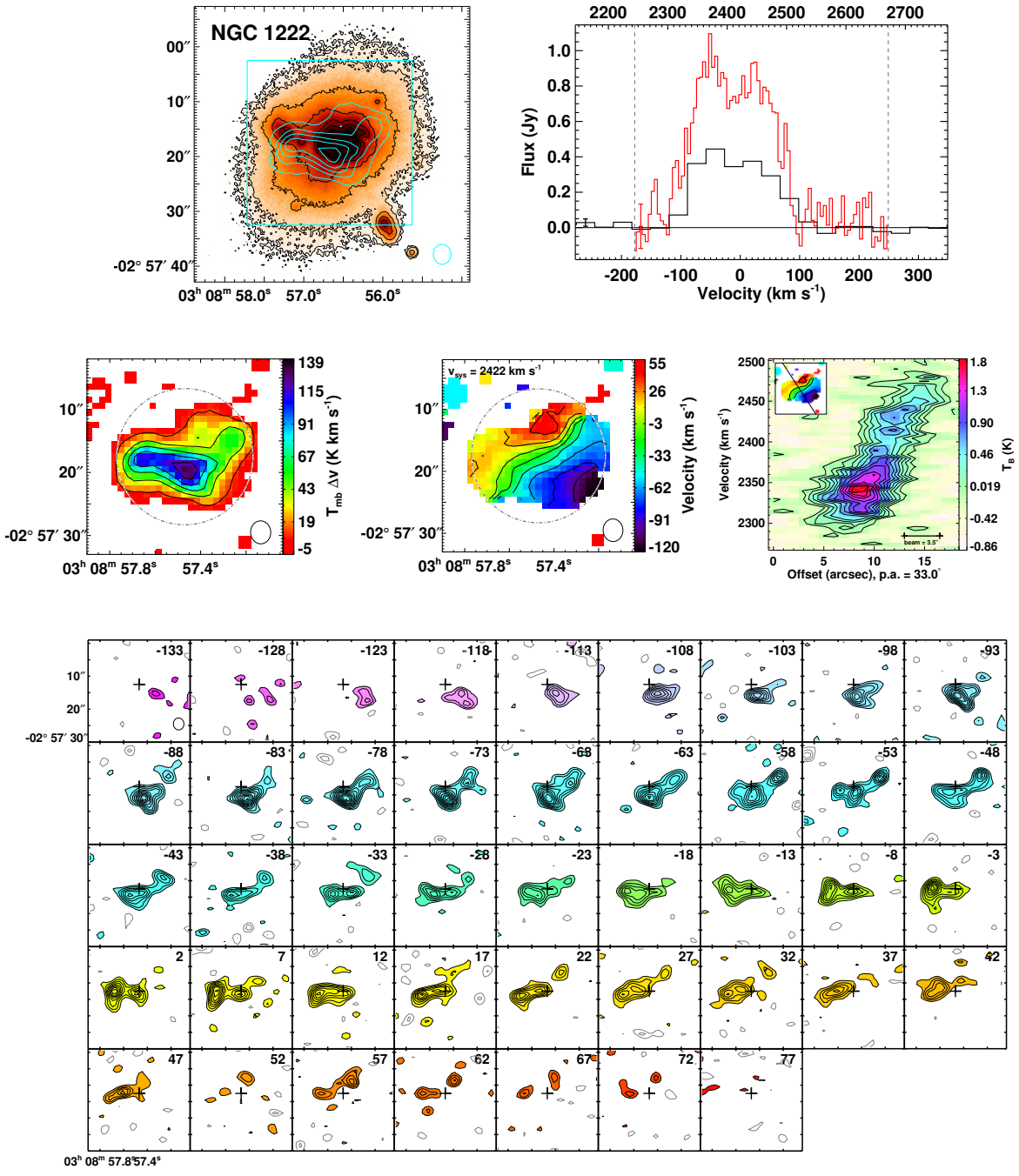

Figure A.4 **NGC 1222** is a field non-regular rotator (M_K = -22.71) with stellar morphology that shows interaction features as well as dust filaments. It is a well-known interaction, and cross-identified as Markarian 603 (Beck, Turner & Kloosterman 2007). The moment0 peak is 18 Jy beam^{-1} km s^{-1}. The PVD contours are placed at 1.5σ intervals.

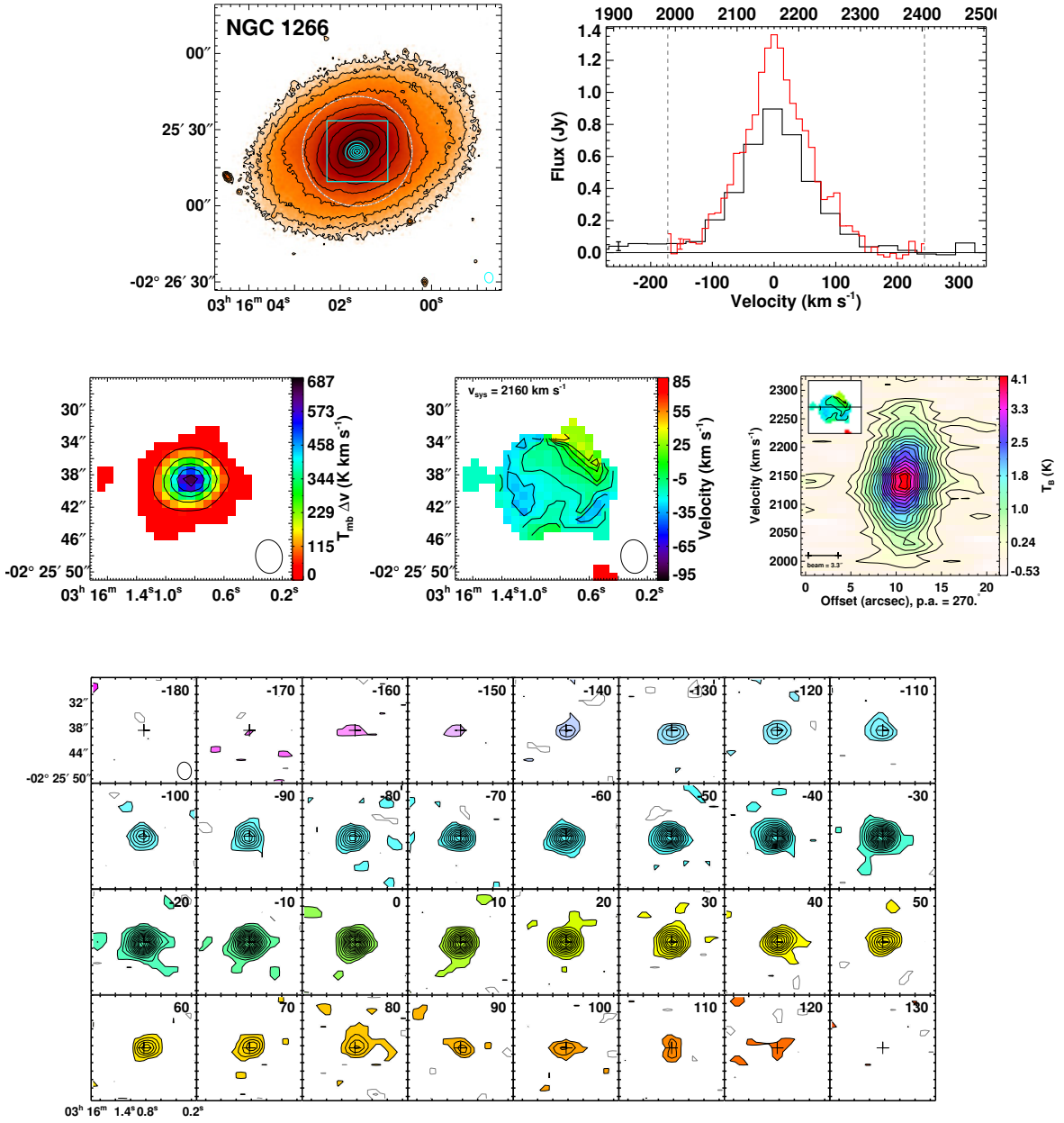

Figure A.5 **NGC 1266** is a field regular rotator (M_K = -22.93) with normal stellar morphology. It is also observed to have a dust filament. Not only was it the brightest detection in the sample, but it had the largest linewidths observed. It was initially unresolved in CARMA D-array, thus was observed in the much higher resolution arrays. NGC 1266 hosts a massive molecular outflow that appears to be driven by an AGN. Further details can be found in Alatalo et al. 2011. The moment0 peak is 100 Jy beam^{-1}. The moment1 contours are placed at 10km s^{-1} intervals. The channel map contours are placed at 2σ intervals and the PVD contours are placed at 3σ intervals.

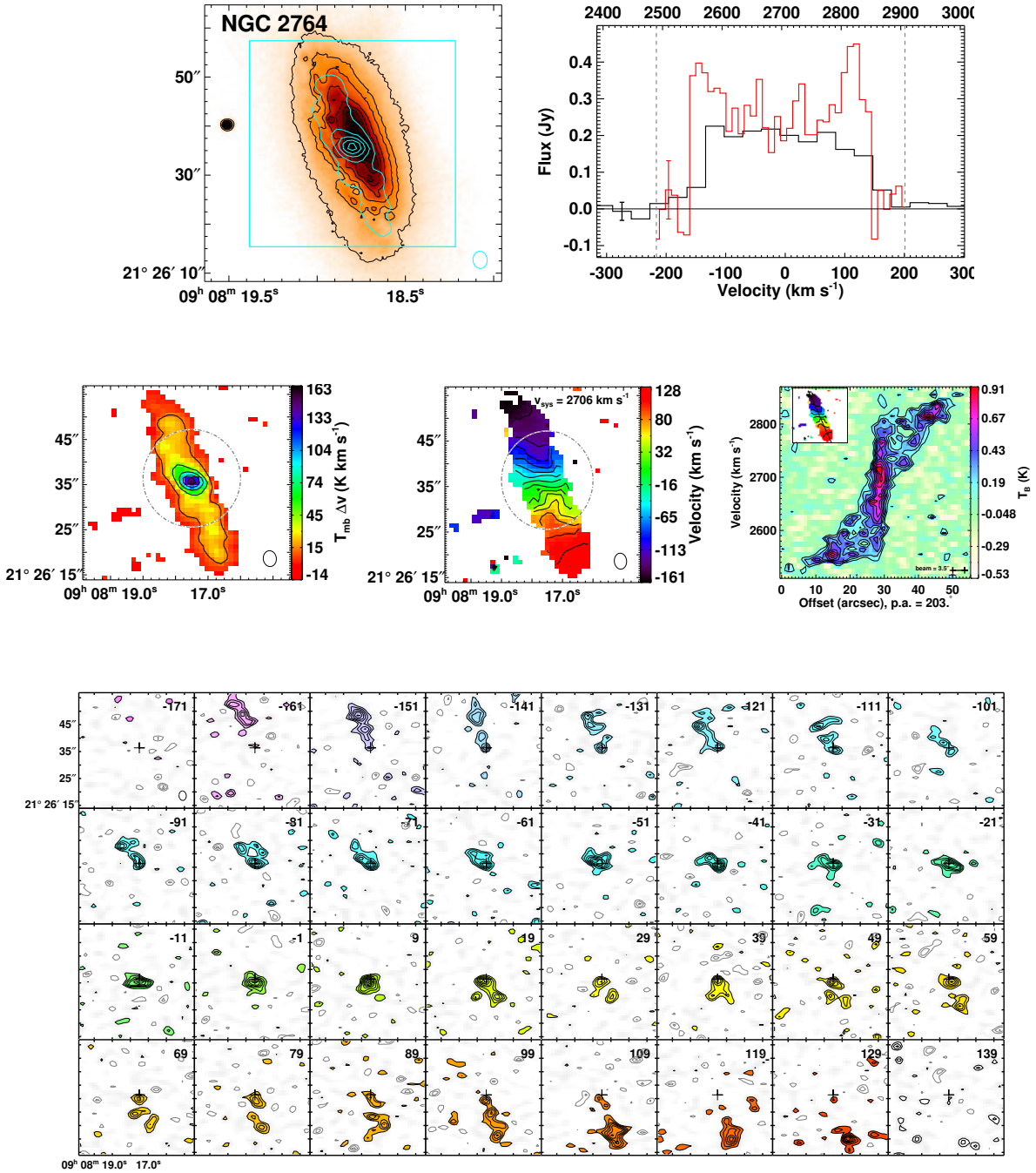

Figure A.6 **NGC 2764** is a field regular rotator (M_K = -23.19) with stellar morphology that indicates interaction. It is also observed to contain a blue nucleus and dust filaments. The moment0 peak is 18 Jy beam^{-1} km s^{-1}. The PVD contours are placed at 1.5σ intervals.

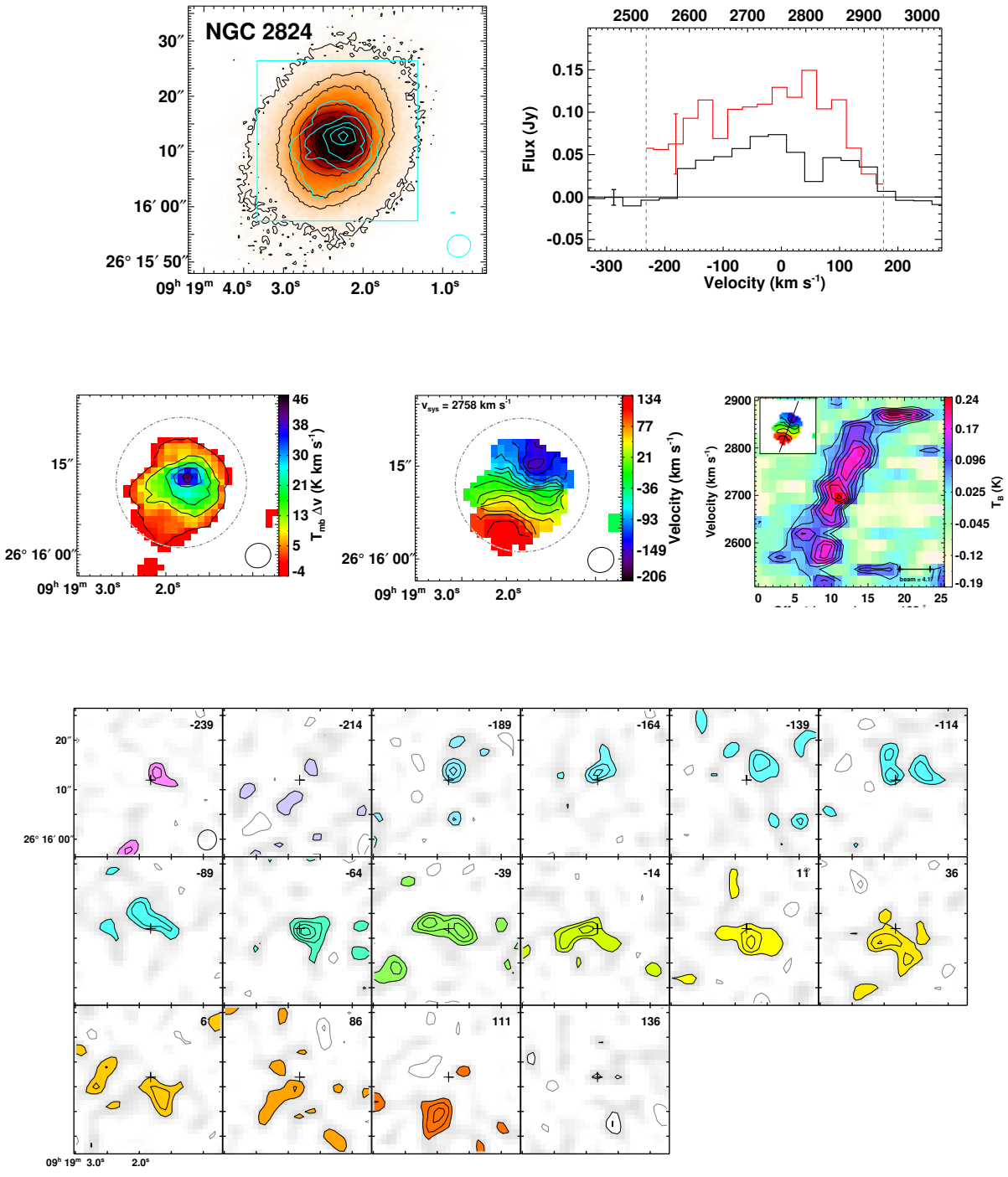

Figure A.7 **NGC 2824** is a field regular rotator (M_K = -22.93) with a ring stellar morphology. It contains a dust disc. The moment0 peak is 8.6 Jy beam^{-1} km s^{-1}.

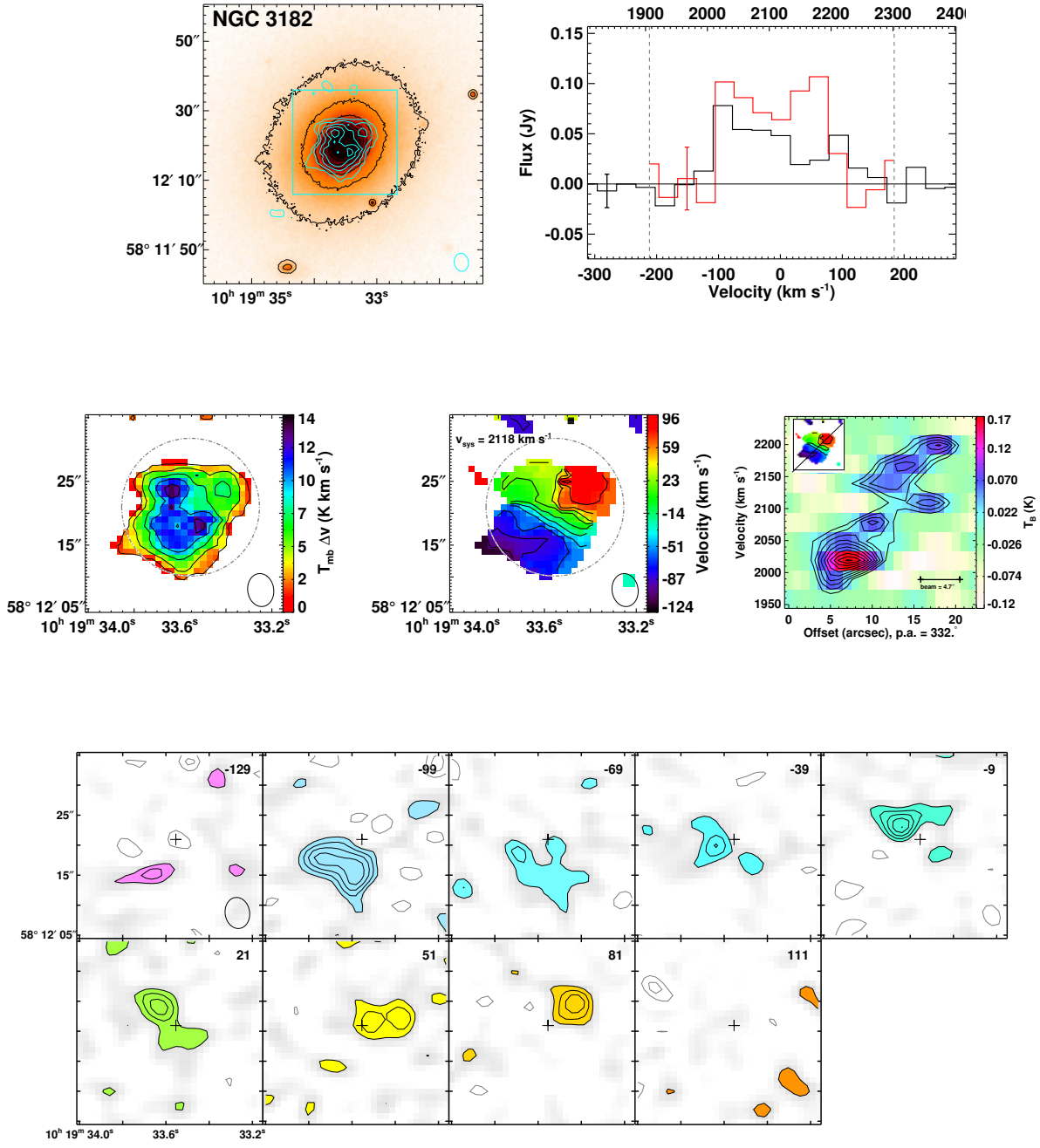

Figure A.8 **NGC 3182** is a field regular rotator (M_K = -23.19) with normal stellar morphology and contains a dust bar and ring. It is one of the faintest detections within the sample, thus it is likely much of the CO emission in this system is below the noise in the channel maps. The moment0 peak is 3.3 Jy beam^{-1} km s^{-1}.

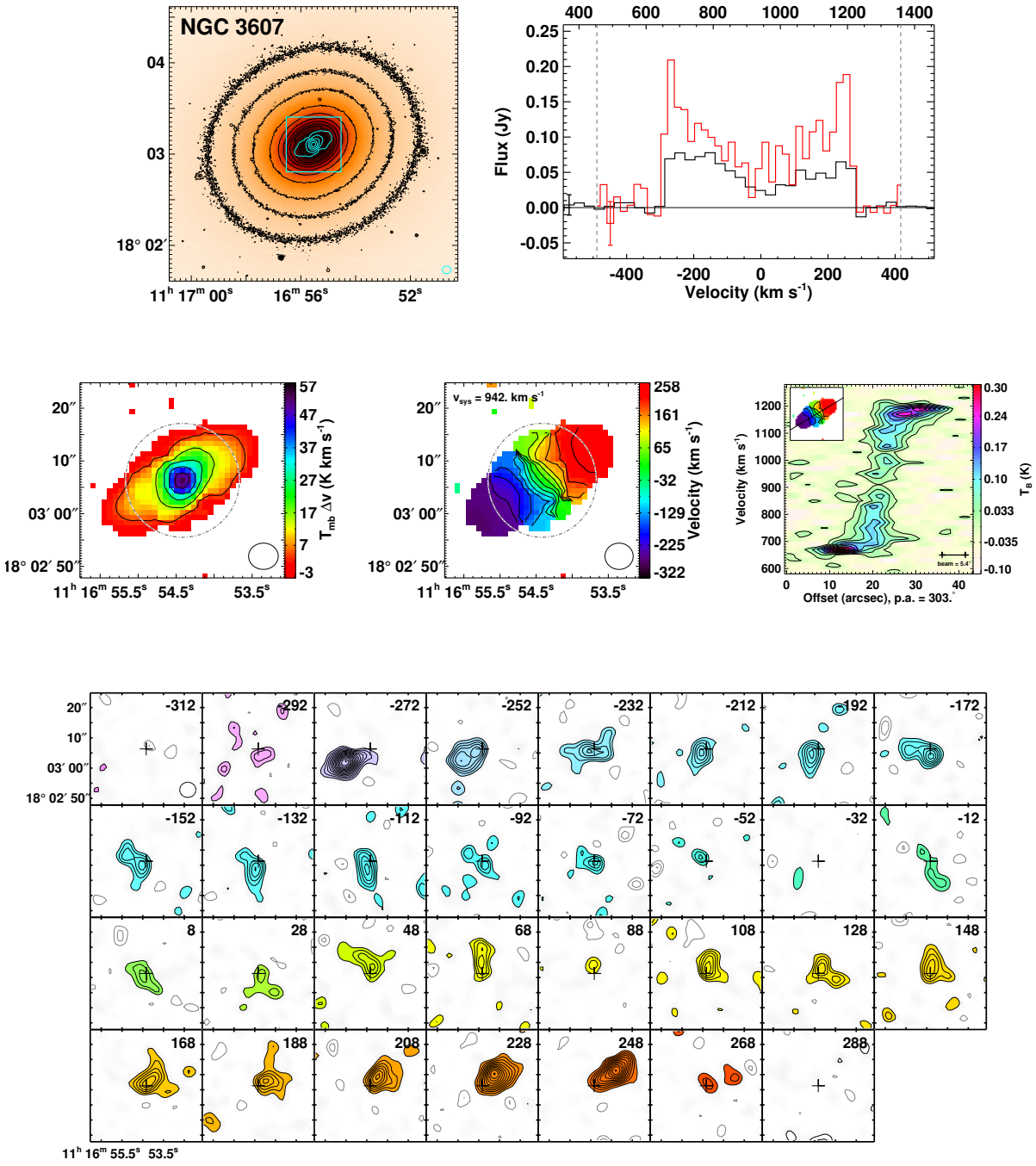

Figure A.9 **NGC 3607** is a field regular rotator (M_K = -24.74) with normal stellar morphology. It contains a dust disc. The moment0 peak is 17 Jy beam^{-1} km s^{-1}. The moment1 contours are placed at 40km s^{-1} intervals and the PVD contours are placed at 3σ intervals.

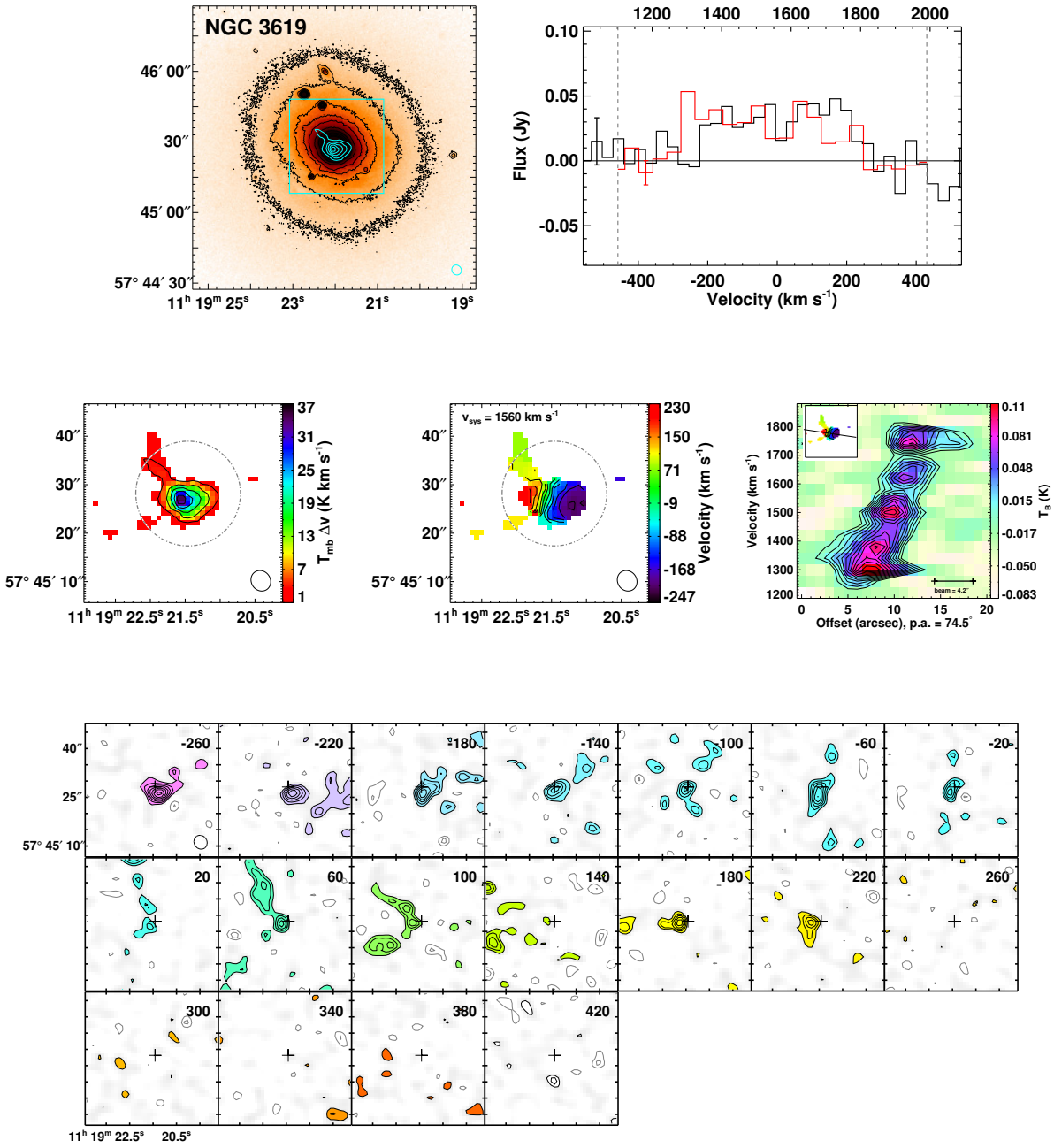

Figure A.10 **NGC 3619** is a field regular rotator (M_K = -23.57) with a shell stellar morphology. It contains dust filaments, bars and rings. It is very likely that CARMA has resolved out what is possibly an extended gas disc. Observations that are sensitive to larger size scales is required to confirm this. The moment0 peak is 6.9 Jy beam^{-1} km s^{-1}. The moment1 contours are placed at 40km s^{-1} intervals.

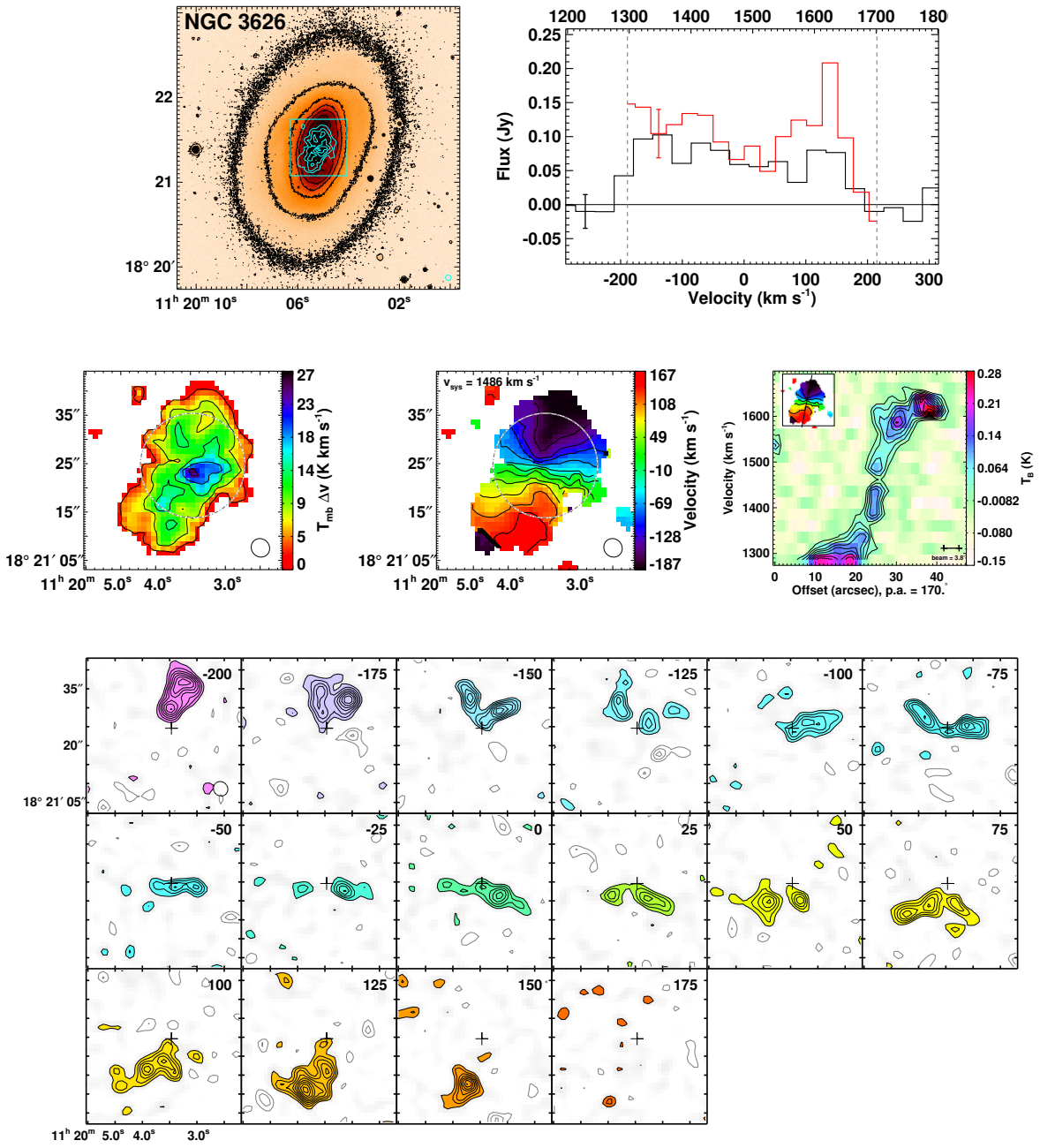

Figure A.11 **NGC 3626** is a group regular rotator (M_K = -23.30) that includes a double maximum velocity feature, with ring stellar morphology. It contains a dust disc. Unfortunately the central velocity of the observations were offset from $v_{\rm sys}$, and due to its large linewidth, a small amount of the blueshifted spectrum was not within the 420 km s^{-1} CARMA window. The moment0 peak is 4.3 Jy beam^{-1} km s^{-1}. The moment1 contours are placed at 30km s^{-1} intervals and PVD contours are placed at 1.5σ intervals.

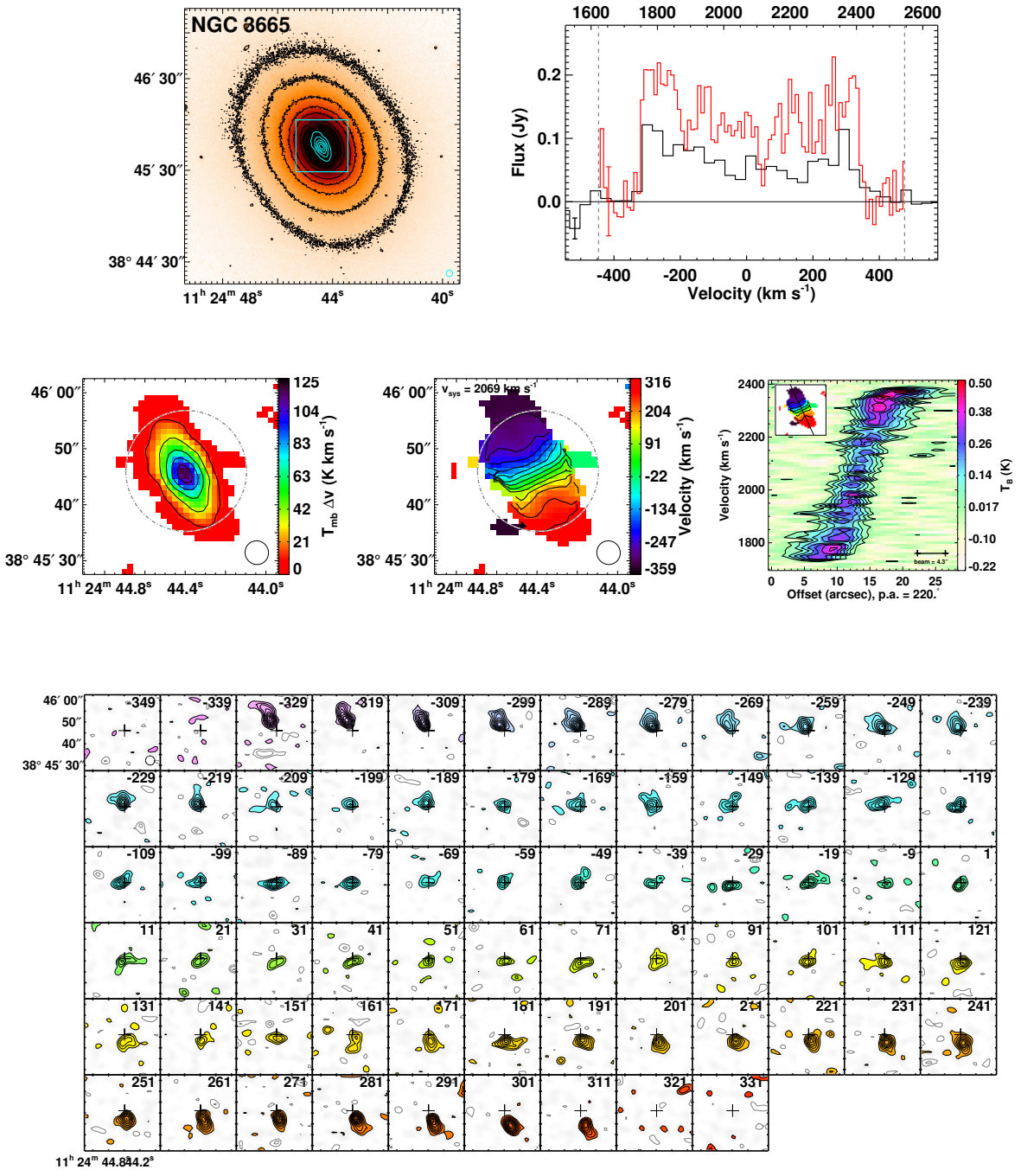

Figure A.12 **NGC 3665** is a group regular rotator (M_K = -24.92) with normal stellar morphology. It contains a dust disc. The moment0 peak is 24 Jy beam^{-1} km s^{-1}. The moment1 contours are placed at 50 km s^{-1} intervals and the PVD contours are placed at 2σ intervals.

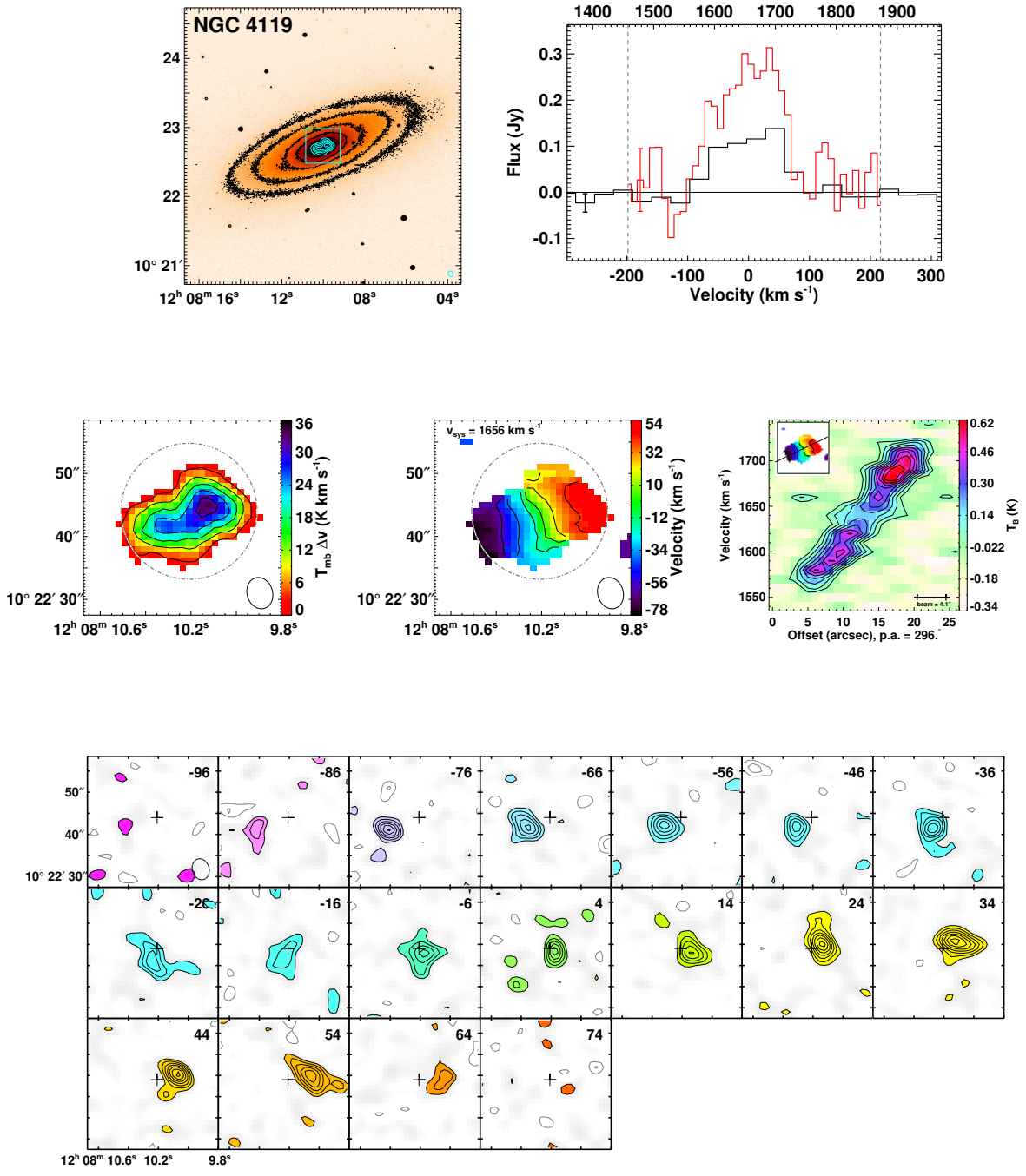

Figure A.13 **NGC 4119** is a Virgo regular rotator (M_K = -22.60) with normal stellar morphology. It contains a dust disc. The moment0 peak is 8.1 Jy beam^{-1} km s^{-1}. The PVD contours are placed at 1.5σ intervals.

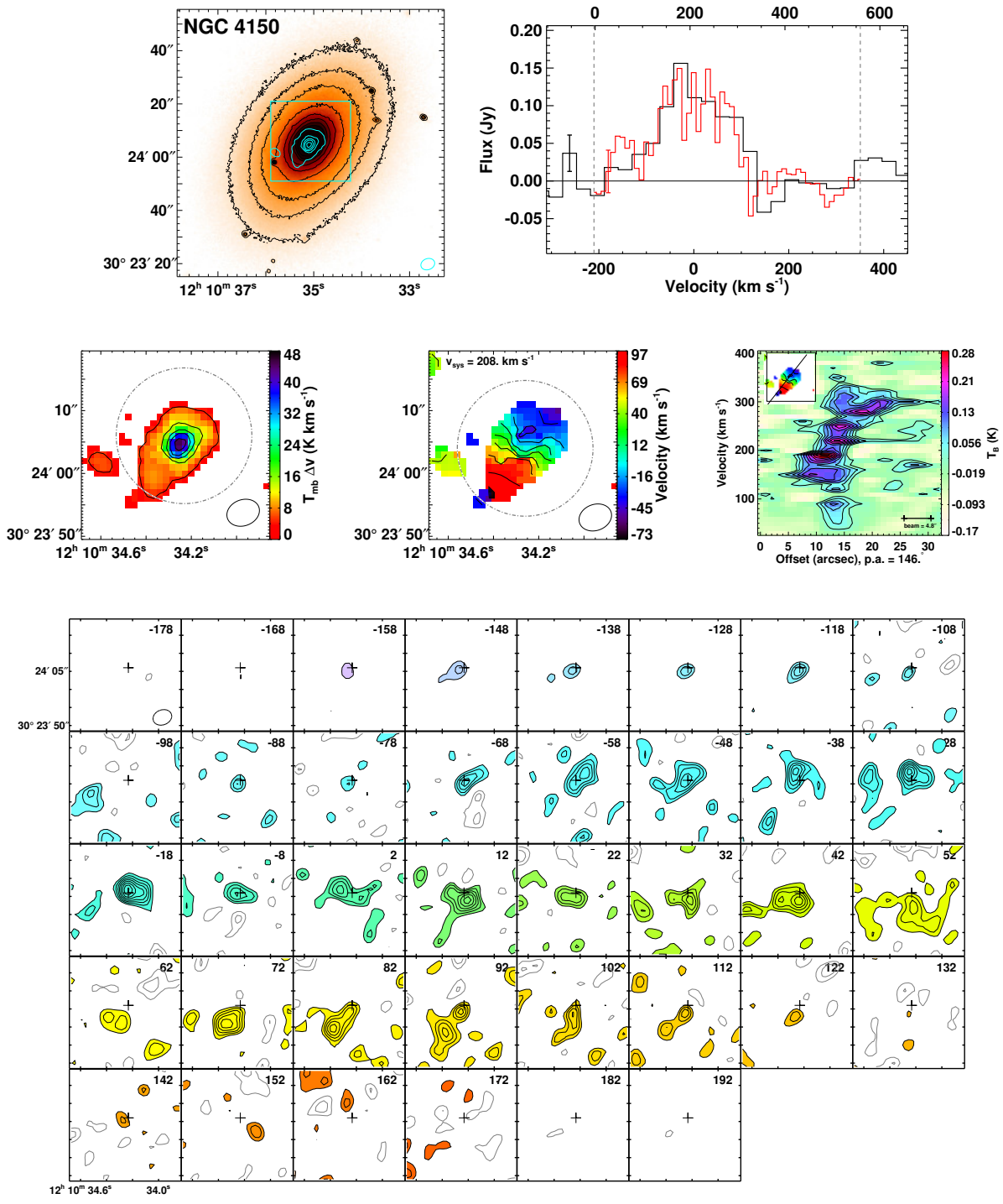

Figure A.14 **NGC 4150** is a Virgo regular rotator (M_K = -21.65) with normal stellar morphology. The moment0 peak is 9.9 Jy beam^{-1} km s^{-1}. The PVD contours are placed at 1.5σ intervals.

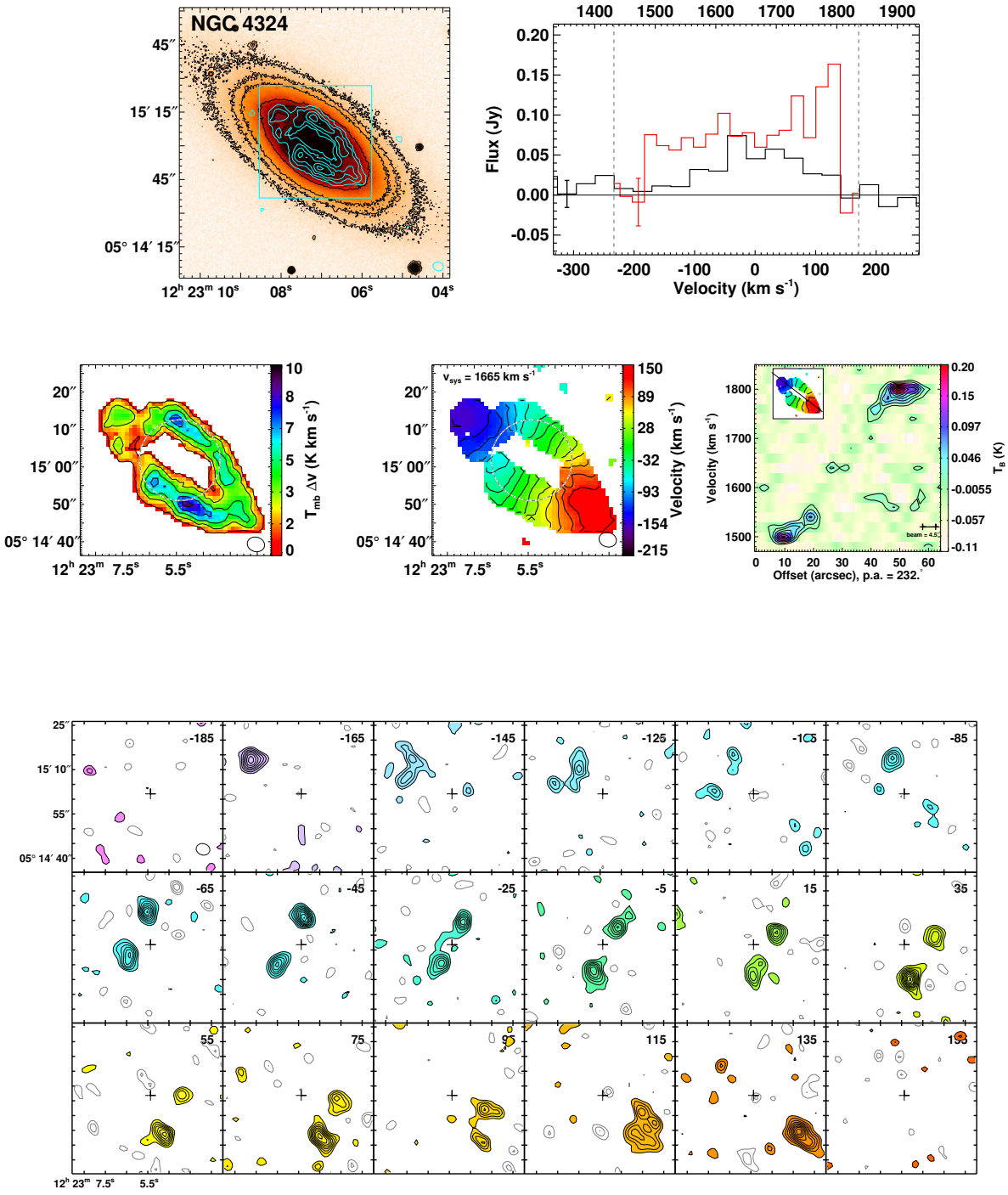

Figure A.15 **NGC 4324** is a field regular rotator (M_K = -21.61) that includes two velocity maxima. It contains a ring stellar morphology, as well as a dust disc, bar, and ring. The moment0 peak is 2.0 Jy beam^{-1} km s^{-1}. The PVD contours are placed at 2σ intervals.

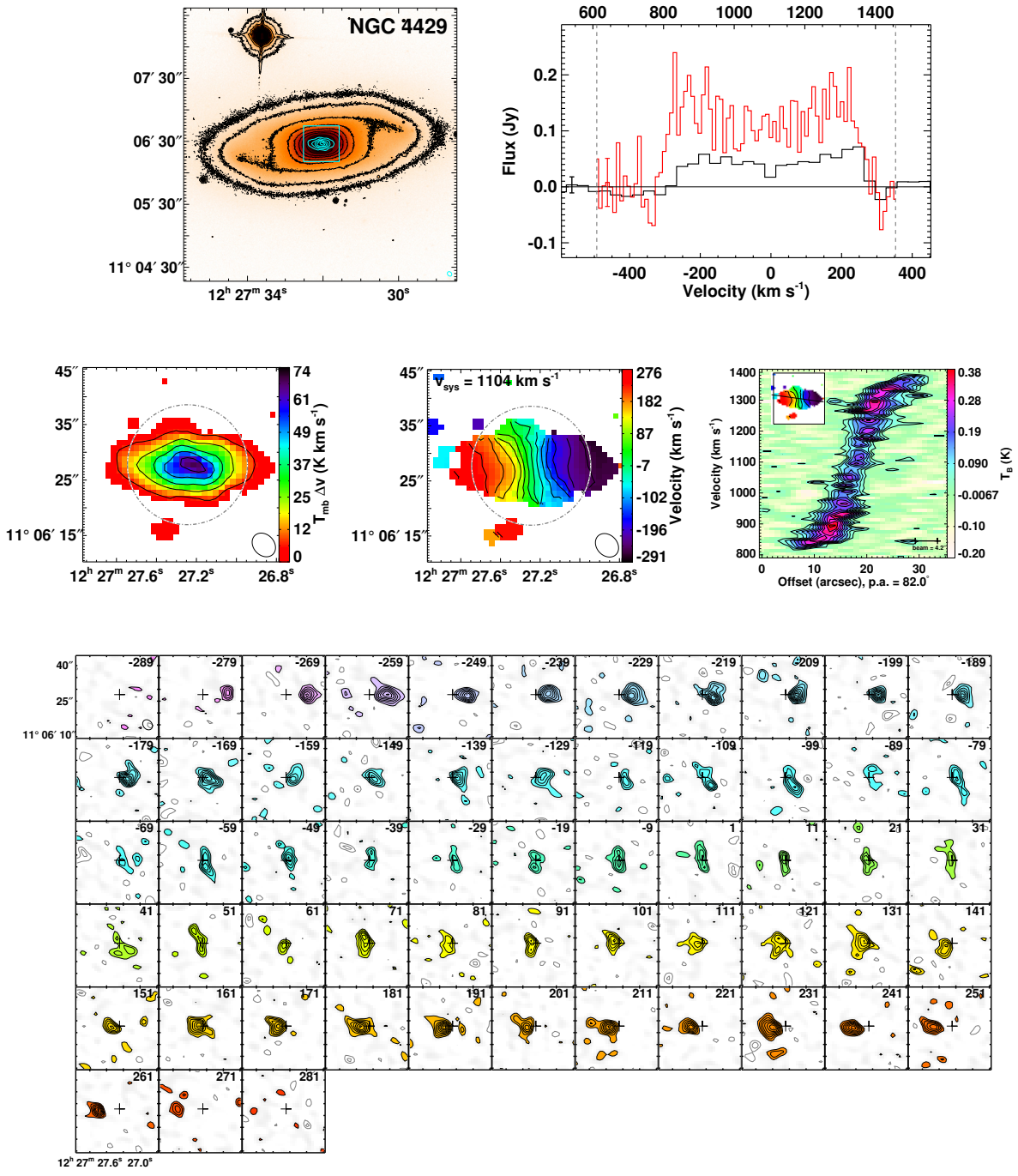

Figure A.16 **NGC 4429** is a Virgo regular rotator (M_K = -24.32) that includes two velocity maxima, with a bar and ring stellar morphology. It contains a dust disc. The moment0 peak is 14 Jy beam^{-1} km s^{-1}. The moment1 contours are at 40 km s^{-1} intervals and the PVD contours are placed at 1.5σ intervals.

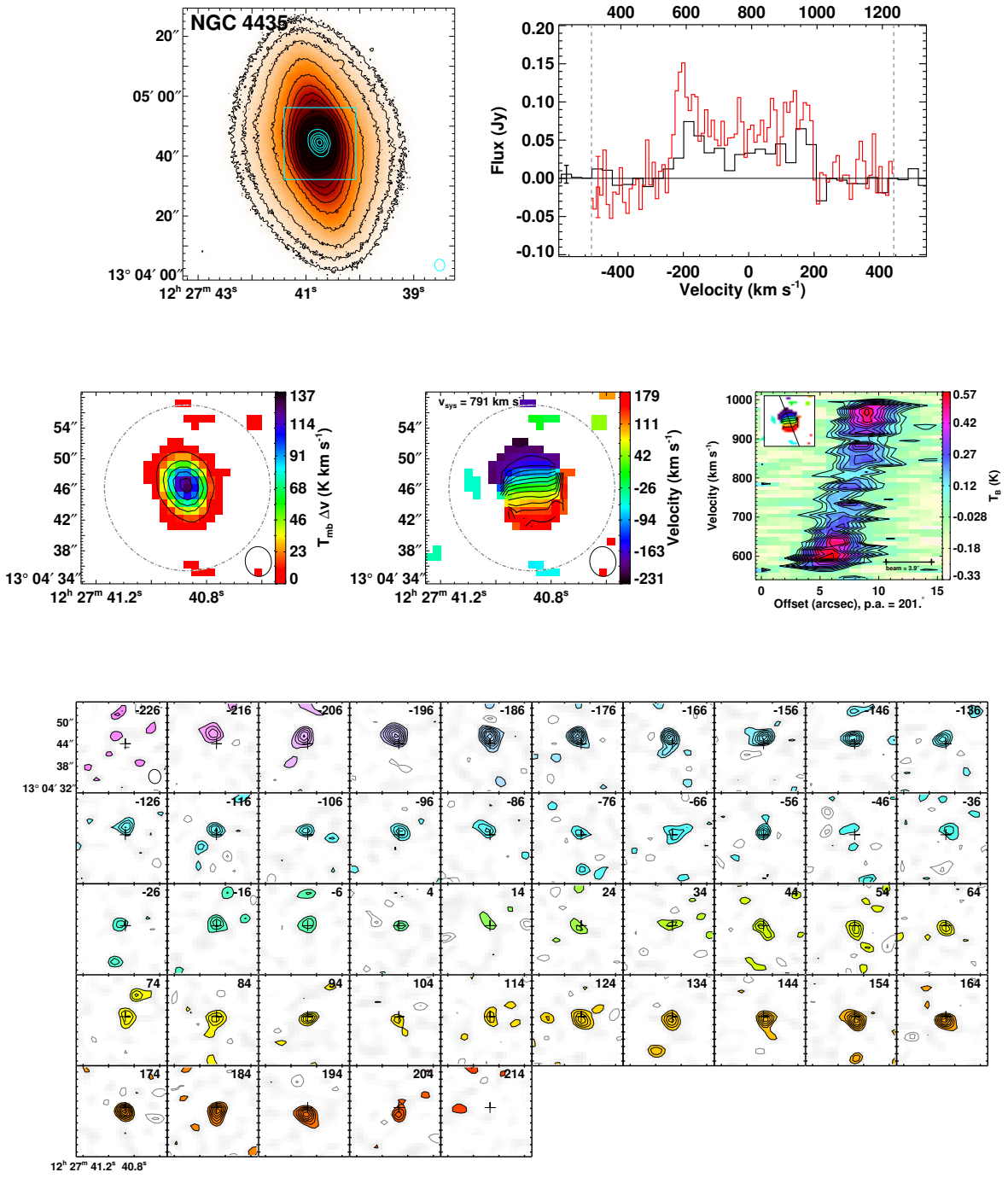

Figure A.17 **NGC 4435** is a Virgo regular rotator (M_K = -23.82) that includes two velocity maxima, with a normal stellar morphology. It contains a dust disc. The moment0 peak is 20 Jy beam^{-1} km s^{-1}. The moment1 contours are at 30 km s^{-1} intervals.

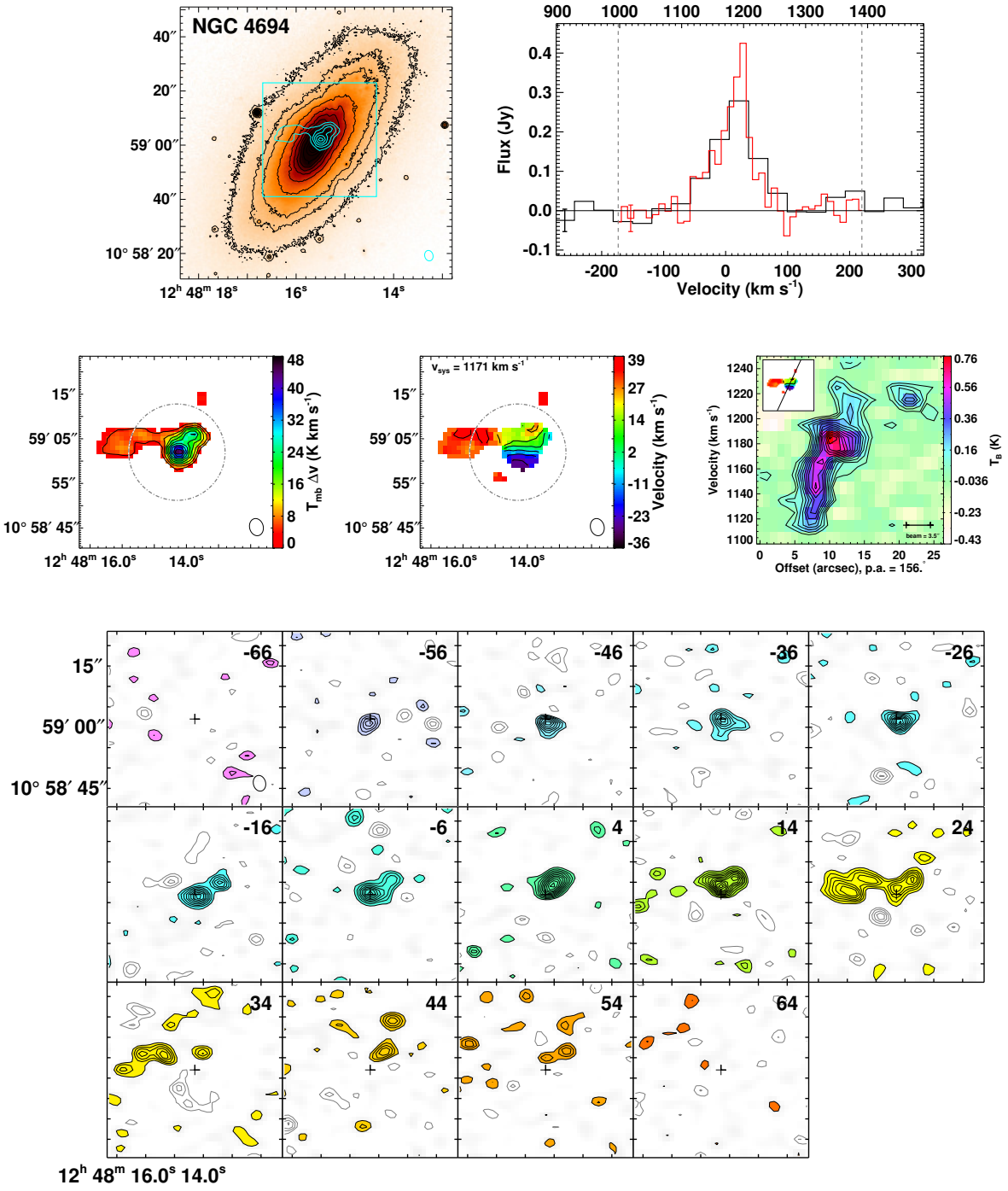

Figure A.18 **NGC 4694** is a Virgo regular rotator (M_K = -22.15) with normal stellar morphology. It appears to be on its first approach into Virgo. It contains a dust filaments and bars. The moment0 peak is 6.0 Jy beam^{-1} km s^{-1}. The moment1 contours are placed at 10km s^{-1} intervals and the PVD contours are placed at 1.5σ intervals.

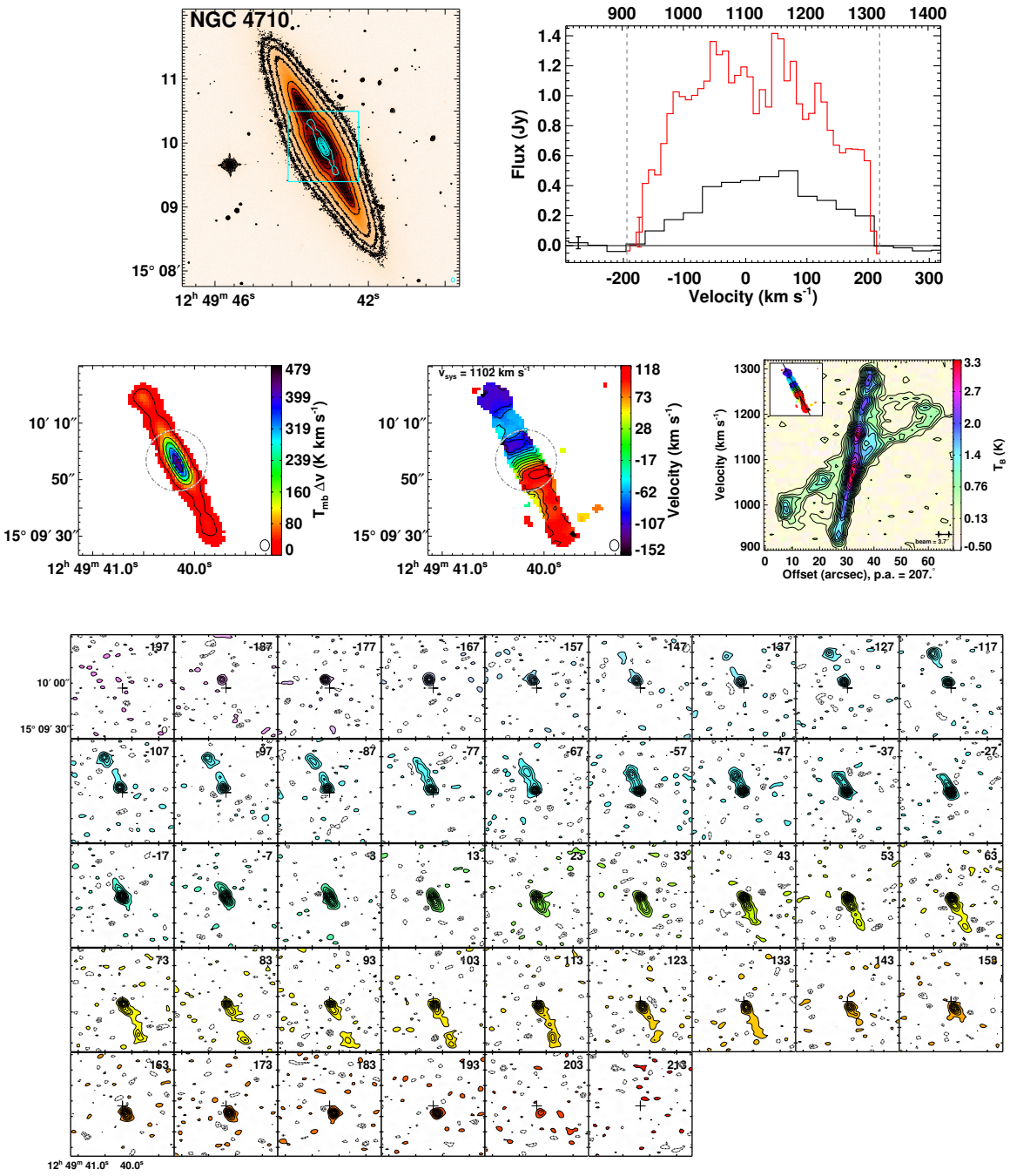

Figure A.19 **NGC 4710** is a Virgo regular rotator (M_K = -23.52) with normal stellar morphology. It appears to be on the outskirts of Virgo and is likely to be on its first approach. It contains a dust disc, and is one of the nearest to edge-on systems in the sample. The moment0 peak is 62 Jy beam^{-1} km s^{-1}. Channel map and PVD contours are placed at 3σ intervals.

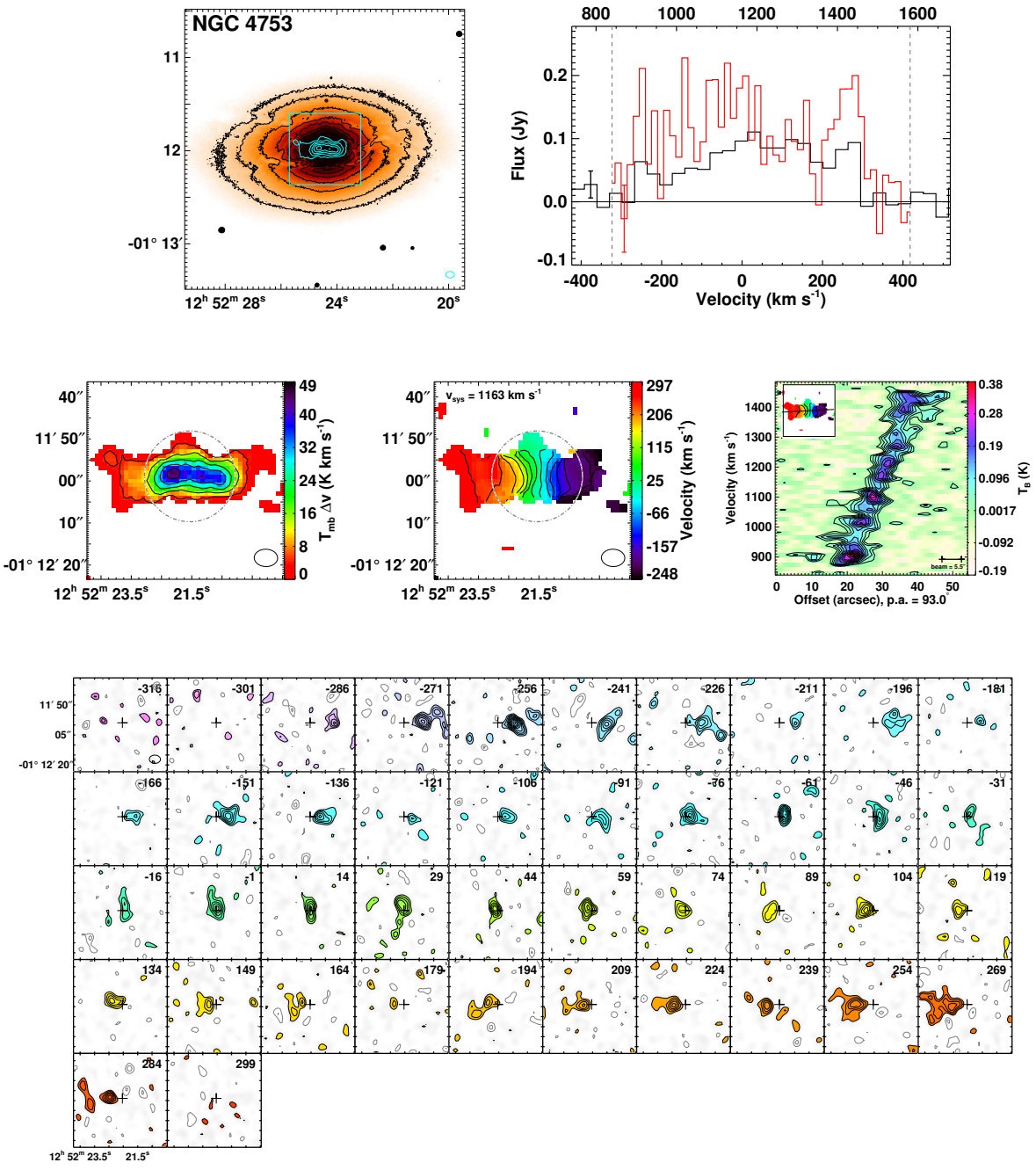

Figure A.20 **NGC 4753** is a field regular rotator (M_K = -25.09) that includes two velocity maxima, with stellar morphology consistent with interaction. It contains a dust filament. It is also the most massive galaxy in the CARMA ATLAS^{3D} survey. The moment0 peak is 12 Jy beam^{-1} km s^{-1}. Moment1 contours are placed at 40km s^{-1} intervals and PVD contours are placed at 1.5σ intervals.

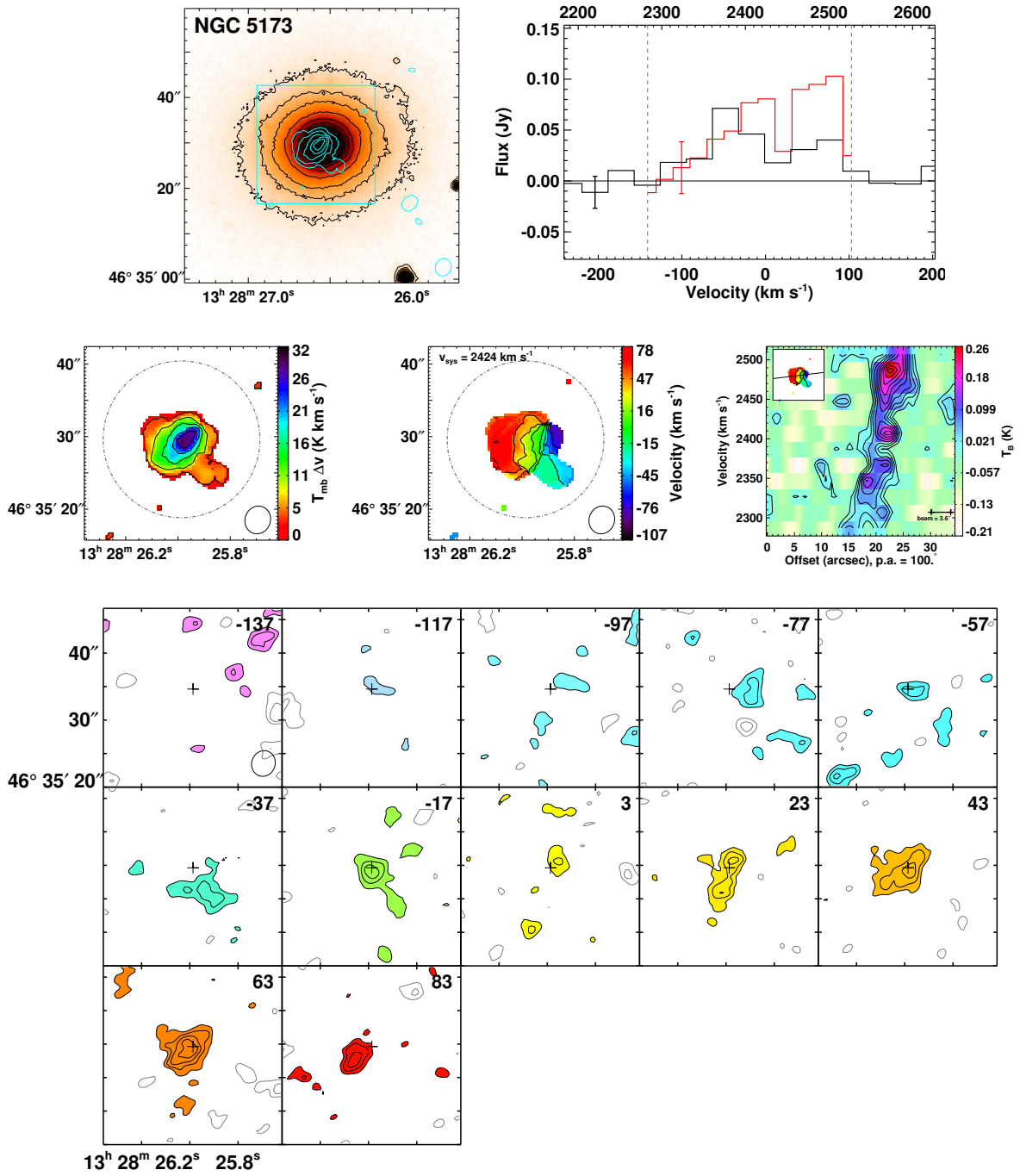

Figure A.21 **NGC 5173** is a group regular rotator (M_K = -22.88) with normal stellar morphology. It contains a dust bar. NGC 5173 was observed in CARMA D- and C- arrays, and the data were shared between this survey, and the work of Wei et al. 2010b, and thus uses the smaller pixel size of 0.4″, to reflect the superior resolution of the observations. The moment0 peak is 4.6 Jy beam^{-1} km s^{-1}. PVD contours are placed at 1.5σ intervals.

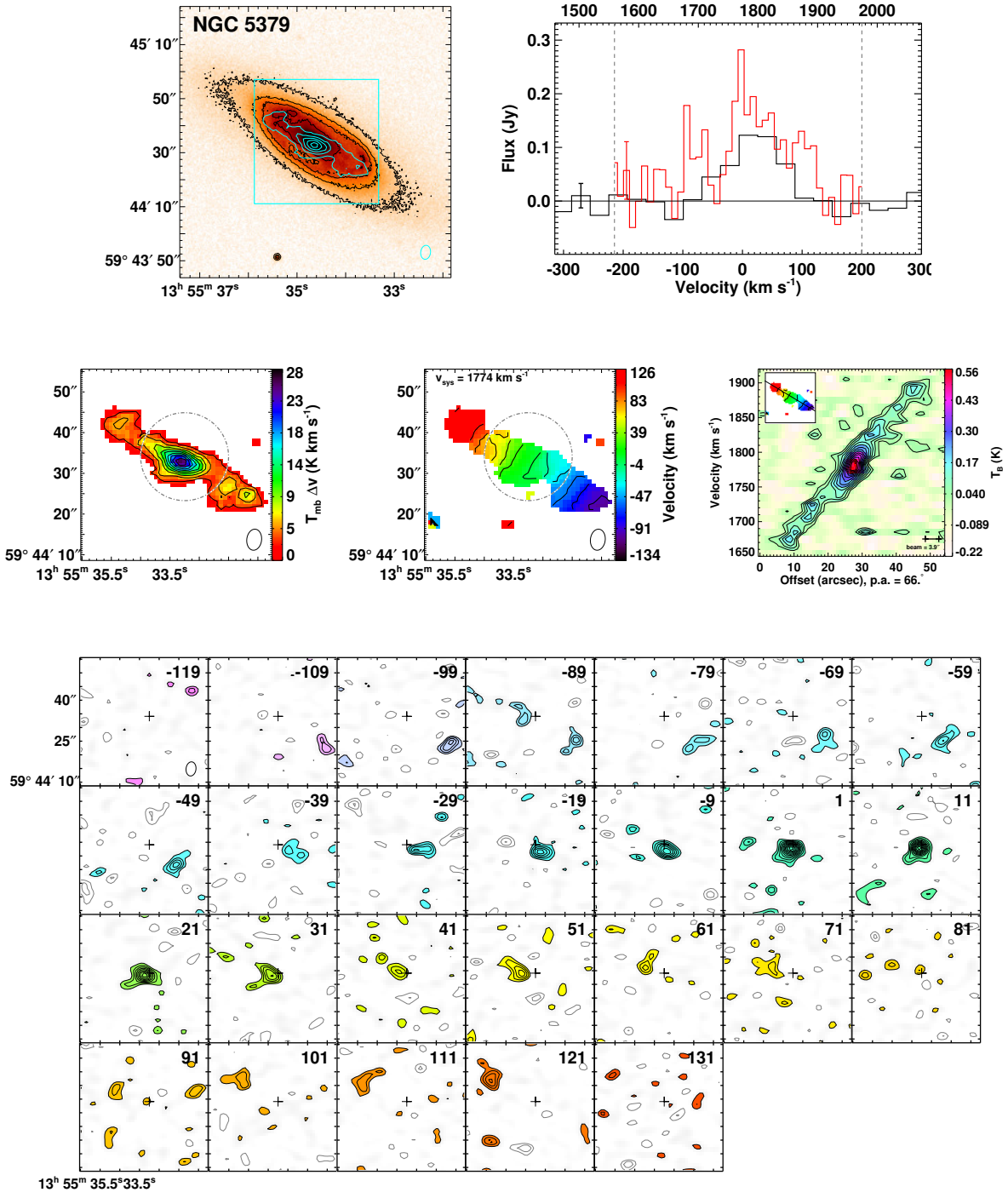

Figure A.22 **NGC 5379** is a group regular rotator (M_K = -22.08) with ring stellar morphology. It contains a dust bar, ring, and filaments. The moment0 peak is 5.7 Jy beam^{-1} km s^{-1}. PVD contours are placed at 1.5σ intervals.

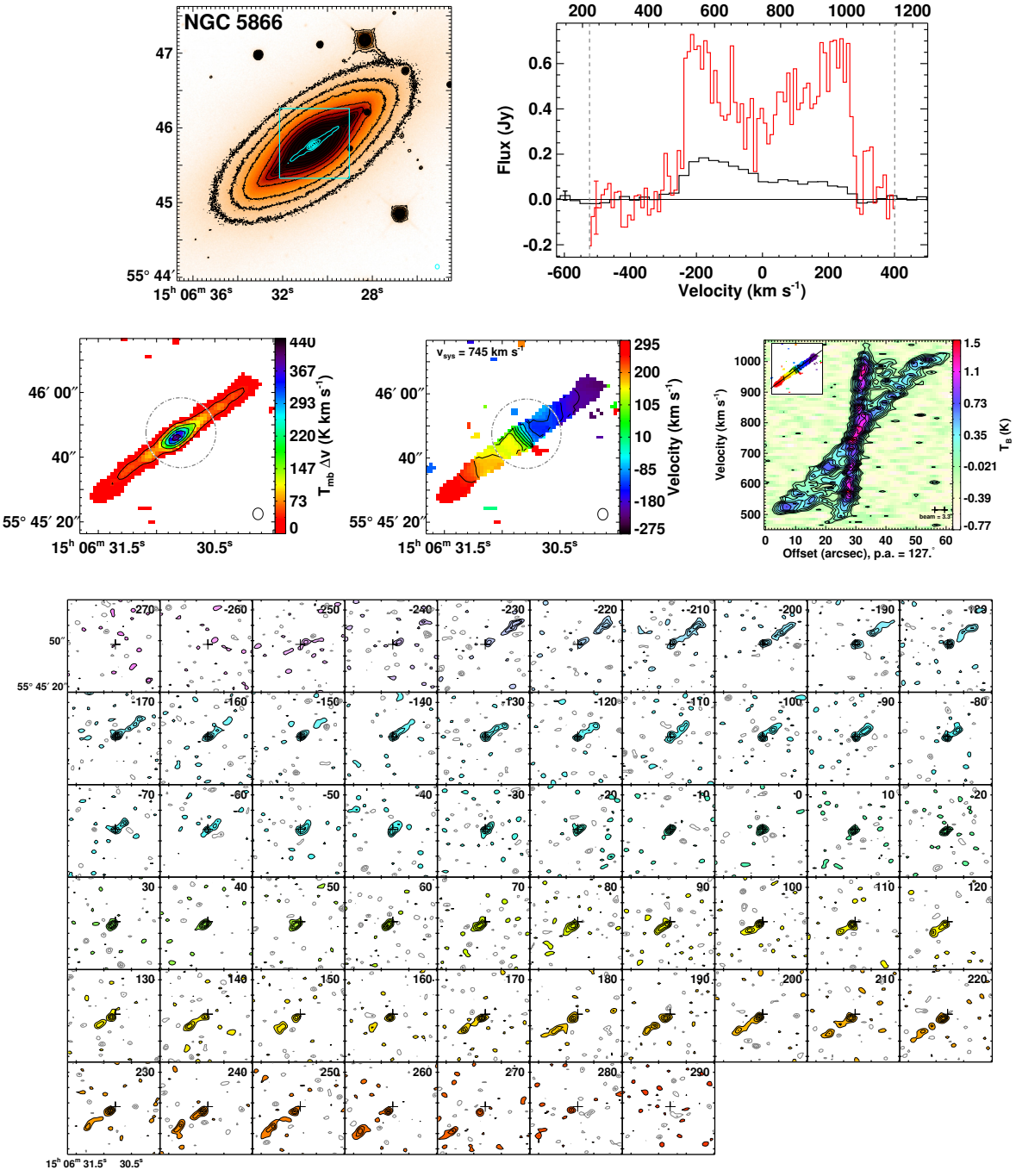

Figure A.23 **NGC 5866** is a field regular rotator (M_K = -24.00) with normal stellar morphology. It contains a dust disc. The molecular gas also strongly suggests that this galaxy contains a bar. The moment0 peak is 54 Jy beam^{-1} km s^{-1}. Moment1 contours are placed at 40km s^{-1} intervals. Channel map contours are placed at 2σ intervals and PVD contours are placed at 2σ intervals.

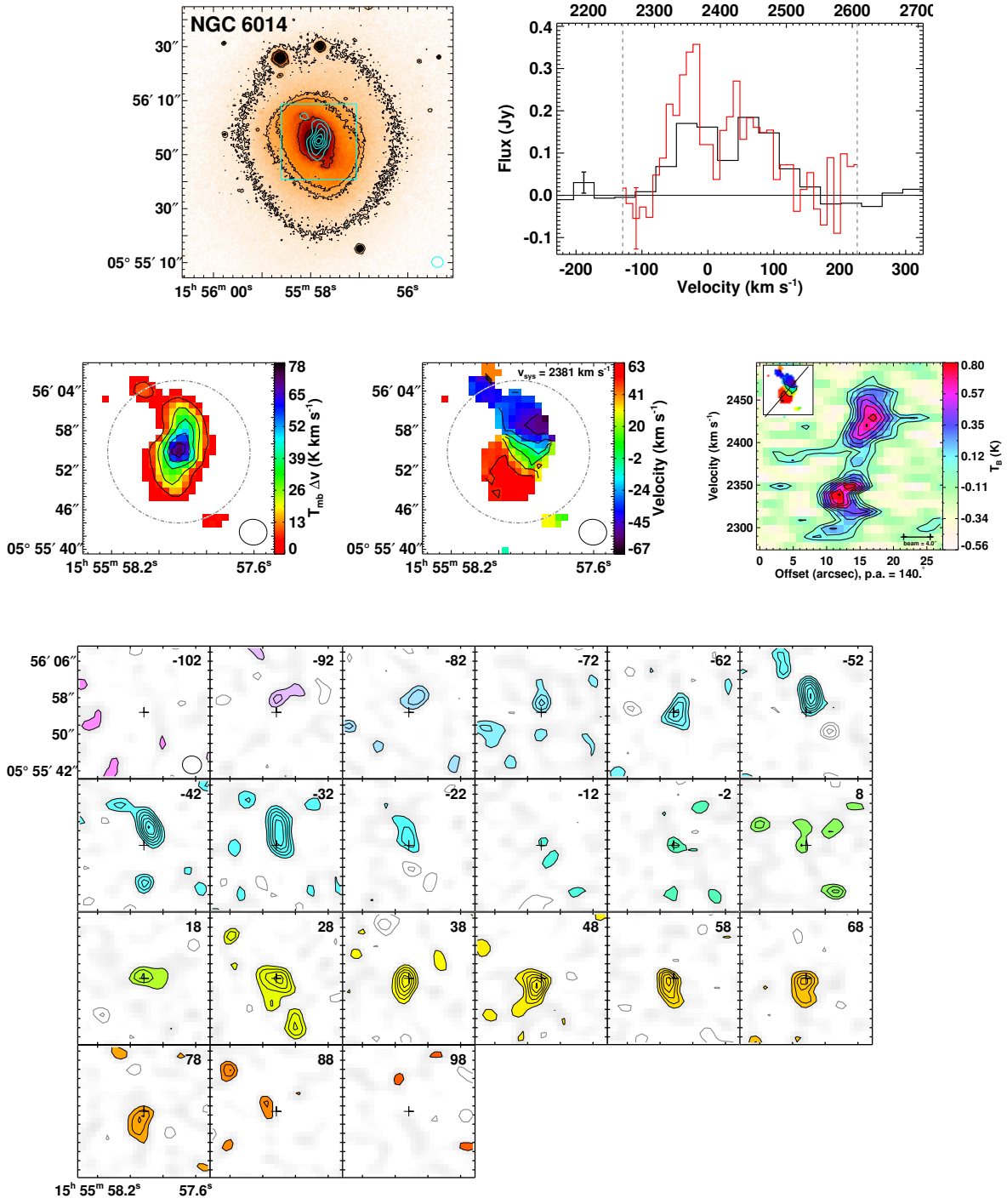

Figure A.24 **NGC 6014** is a field regular rotator (M_K = -22.99) with normal stellar morphology. It contains a dust bar, ring and filaments. The moment0 peak is 14 Jy beam^{-1} km s^{-1}. PVD contours are placed at 1.5σ intervals.

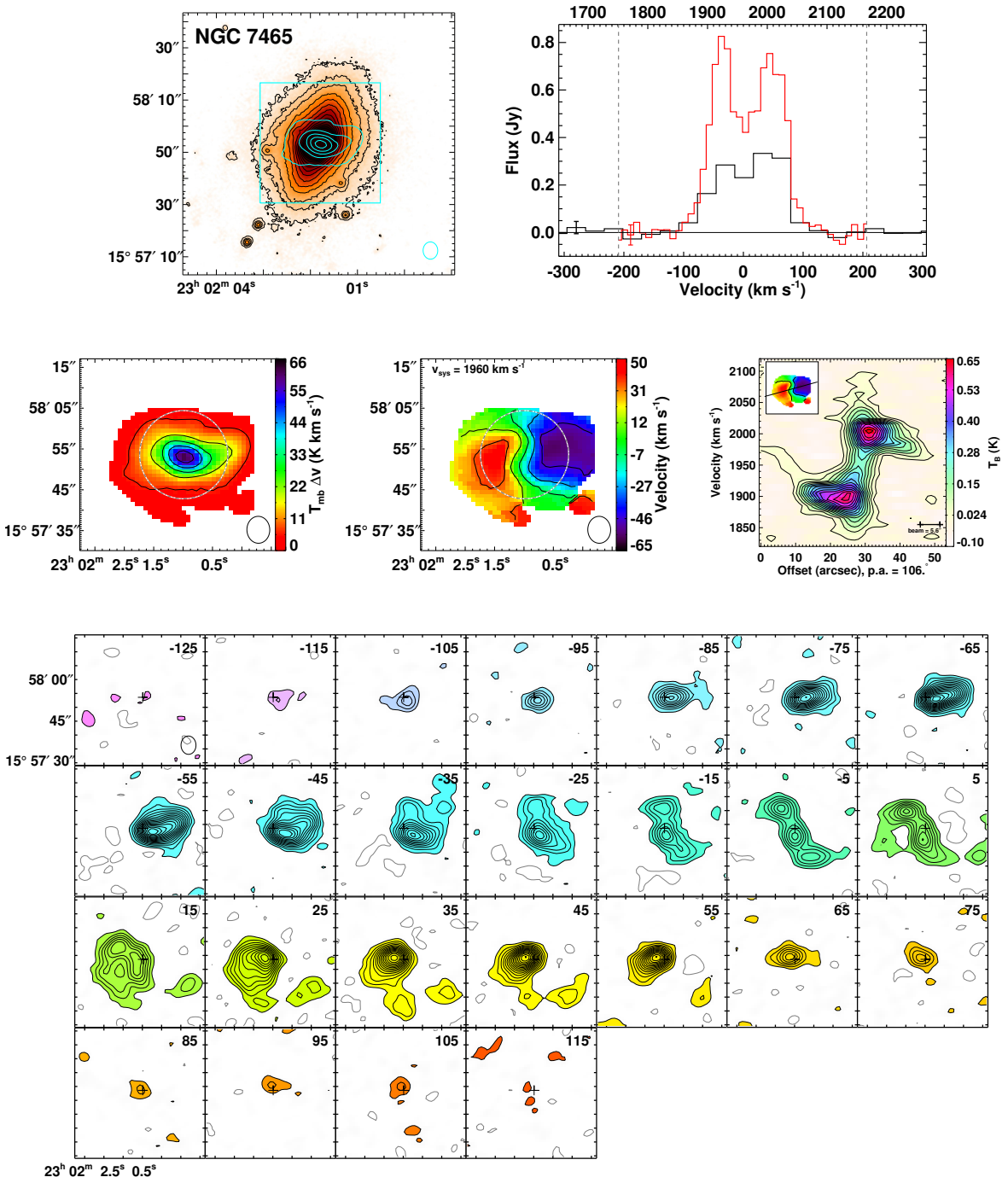

Figure A.25 **NGC 7465** is a field non-regular rotator (M_K = -22.82) with a kinematically-decoupled core (KDC) with stellar morphology indicative of interaction. It contains dust filaments. The moment0 peak is 26 Jy beam^{-1} km s^{-1}. Channel map contours are placed at 2σ intervals and PVD contours are placed at 4σ intervals.

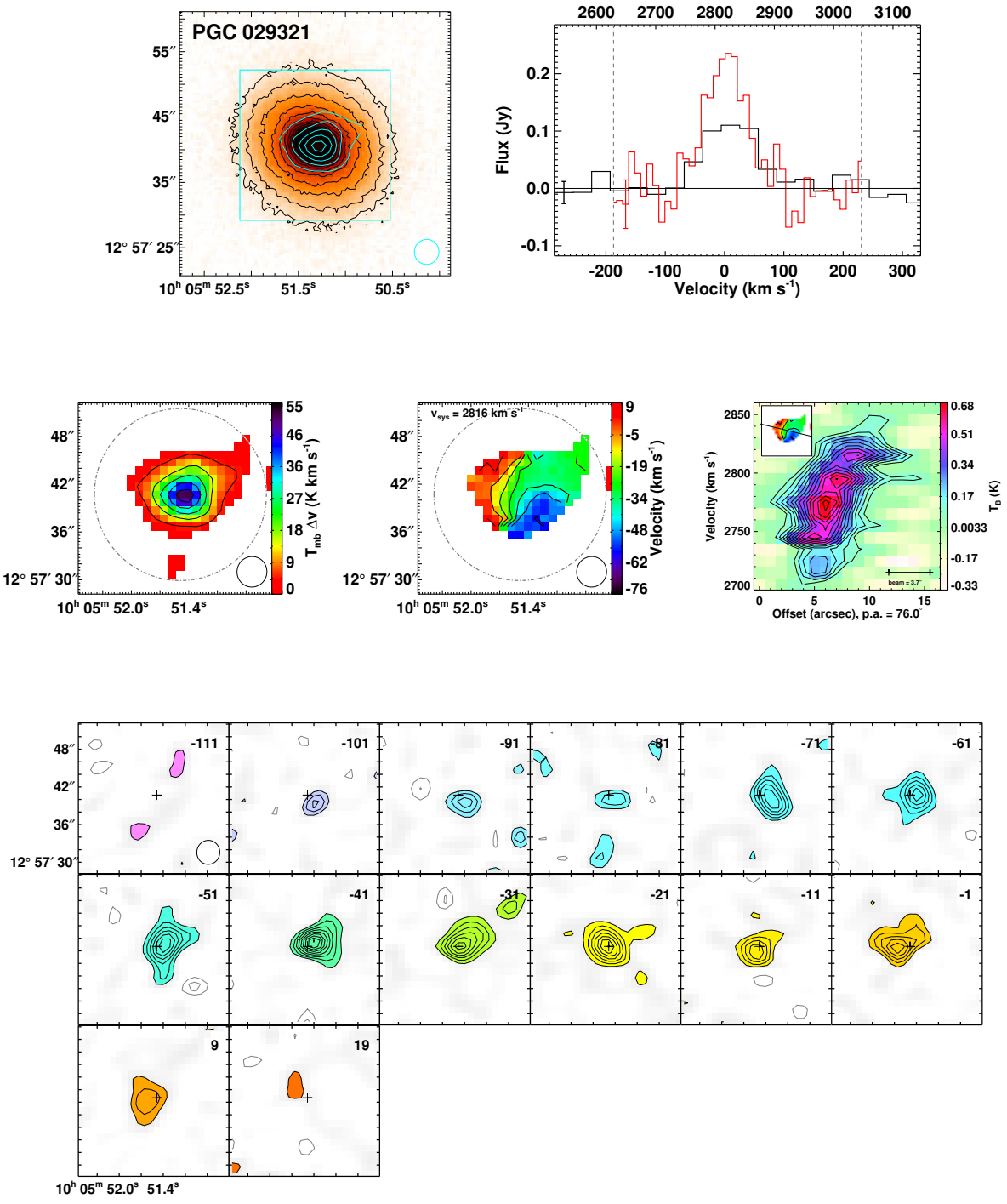

Figure A.26 **PGC 029321** is a field regular rotator (M_K = -21.66) with normal stellar morphology. It contains dust filaments. The moment0 peak is 8.5 Jy beam^{-1} km s^{-1}.

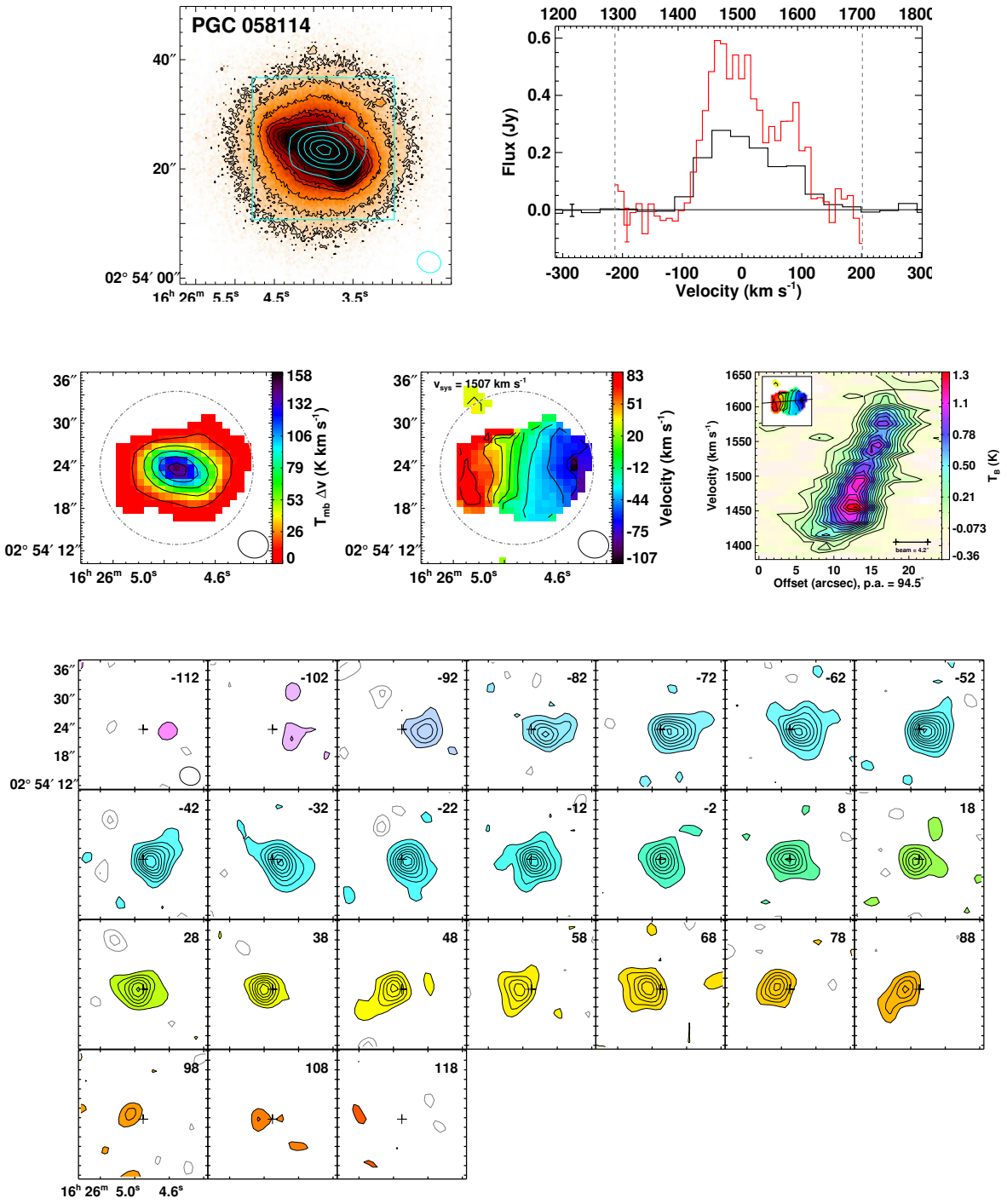

Figure A.27 **PGC 058114** is a field galaxy (M_K = -21.57) with unknown kinematic structure or morphology. The moment0 peak is 28 Jy beam^{-1} km s^{-1}. Channel map and PVD contours are placed at 2σ intervals.

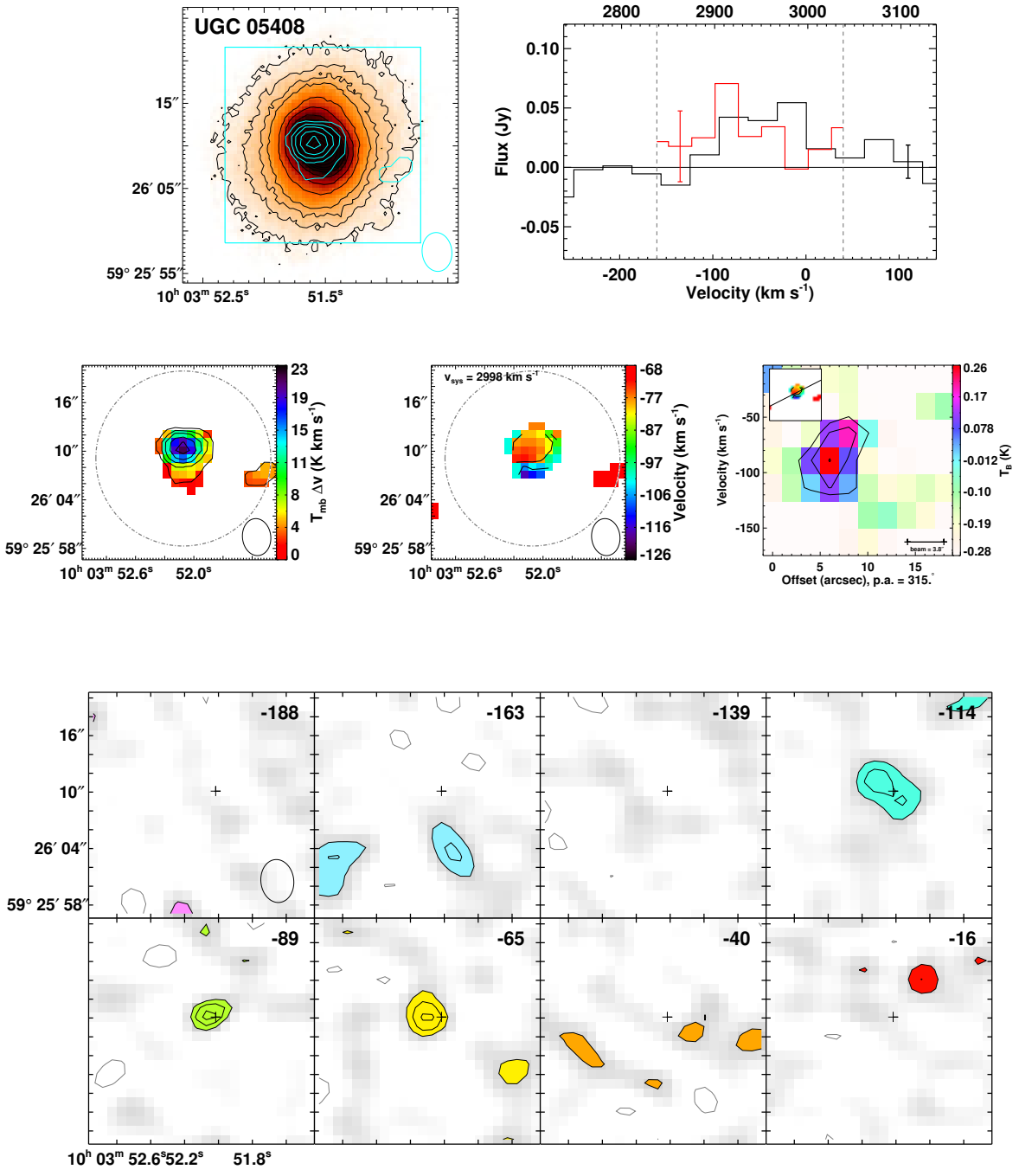

Figure A.28 **UGC 05408** is a field regular rotator (M_K = -22.03) with a bar stellar morphology. It contains a dust bar and filaments. At a distance 45.8 Mpc, it is the most distant detection in the CARMA ATLAS^{3D} survey. The moment0 peak is 3.5 Jy beam^{-1} km s^{-1}.

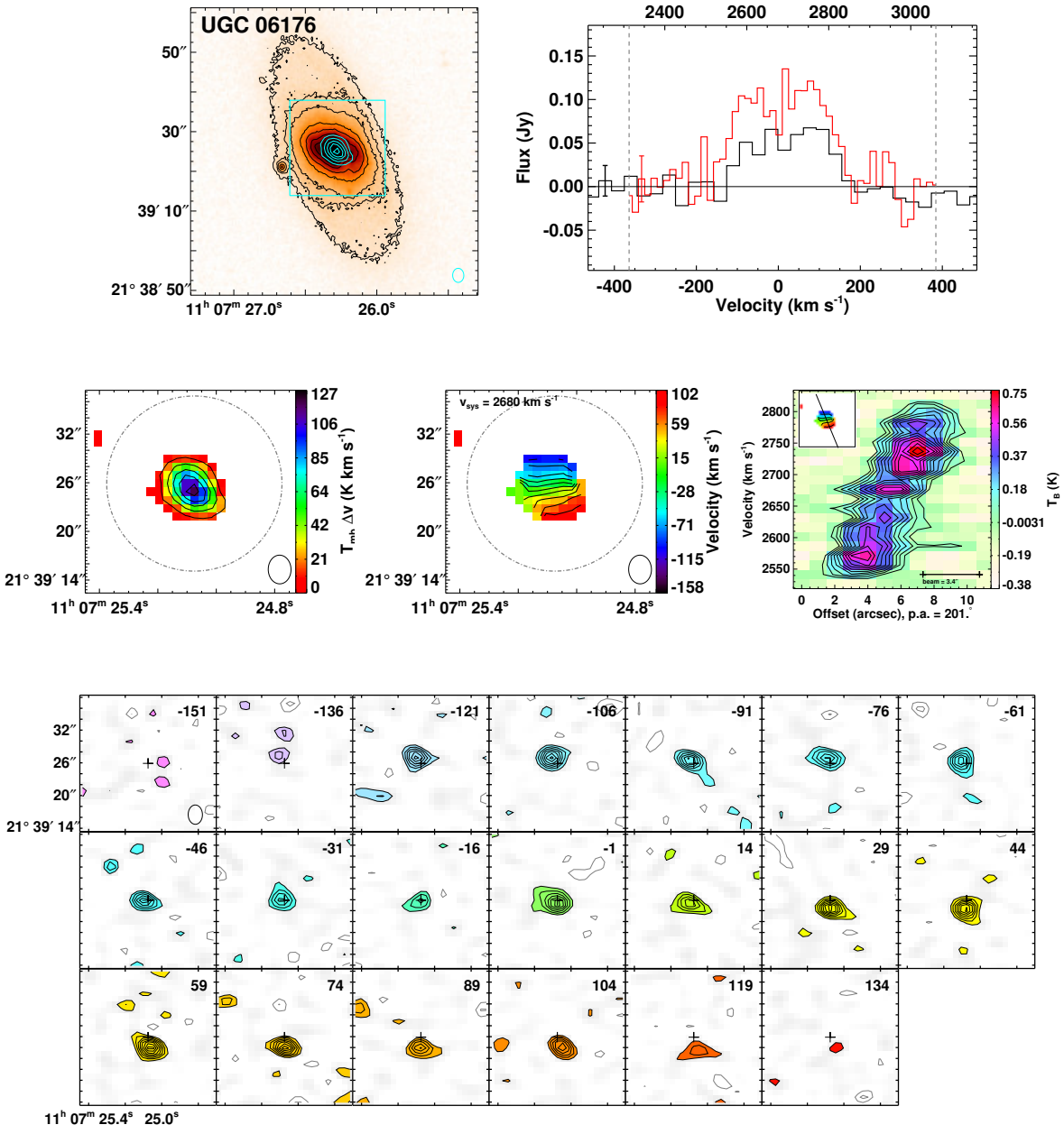

Figure A.29 **UGC 06176** is a field regular rotator (M_K = -22.66) with bar and ring stellar morphology. It contains a dust bar, ring, and filaments. The moment0 peak is 14 Jy beam^{-1} km s^{-1}.

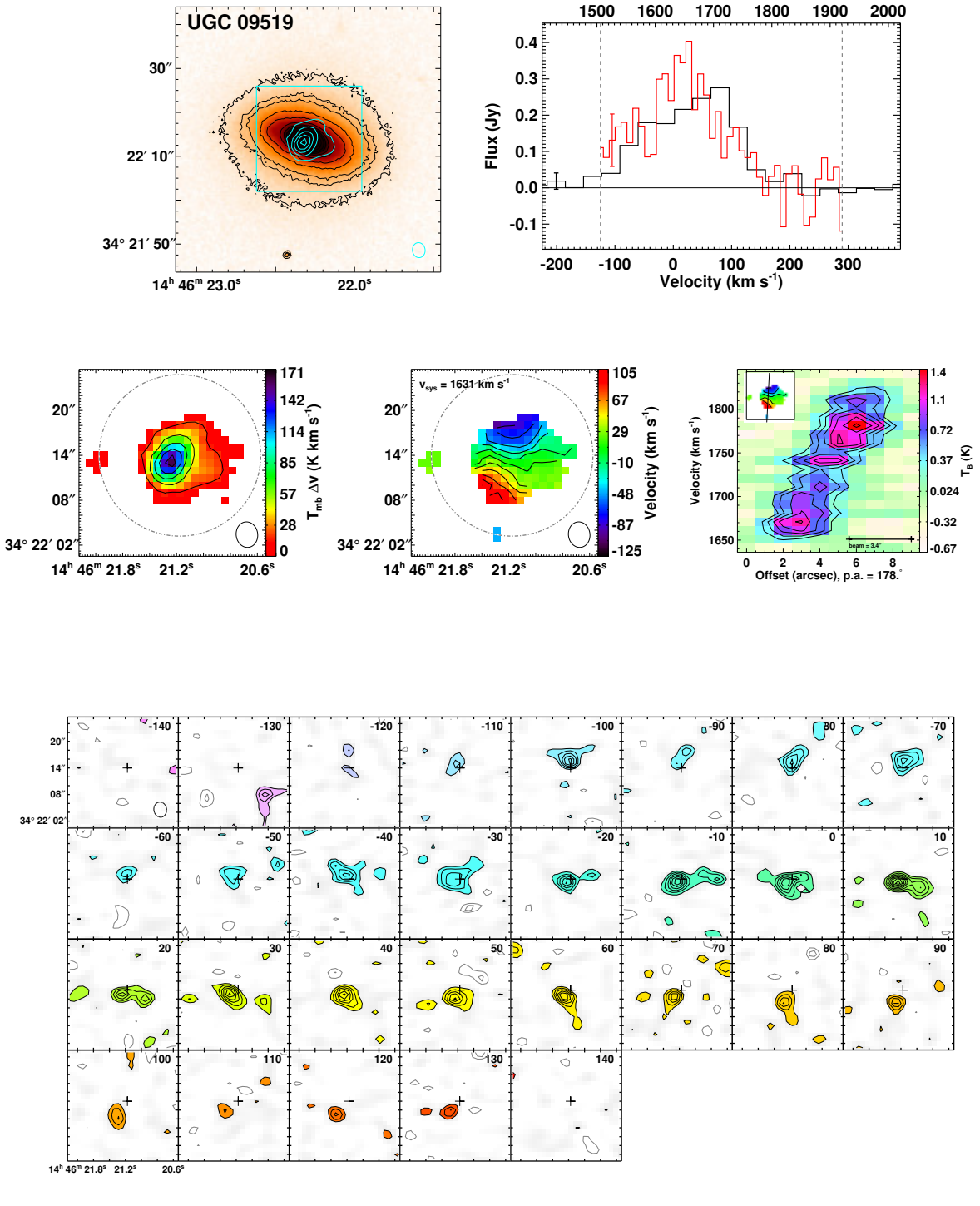

Figure A.30 **UGC 09519** is a field regular rotator (M_K = -21.98) with normal stellar morphology. It contains dust filaments. The moment0 peak is 18 Jy beam^{-1} km s^{-1}.

A.2 Interferometric CO data from the literature

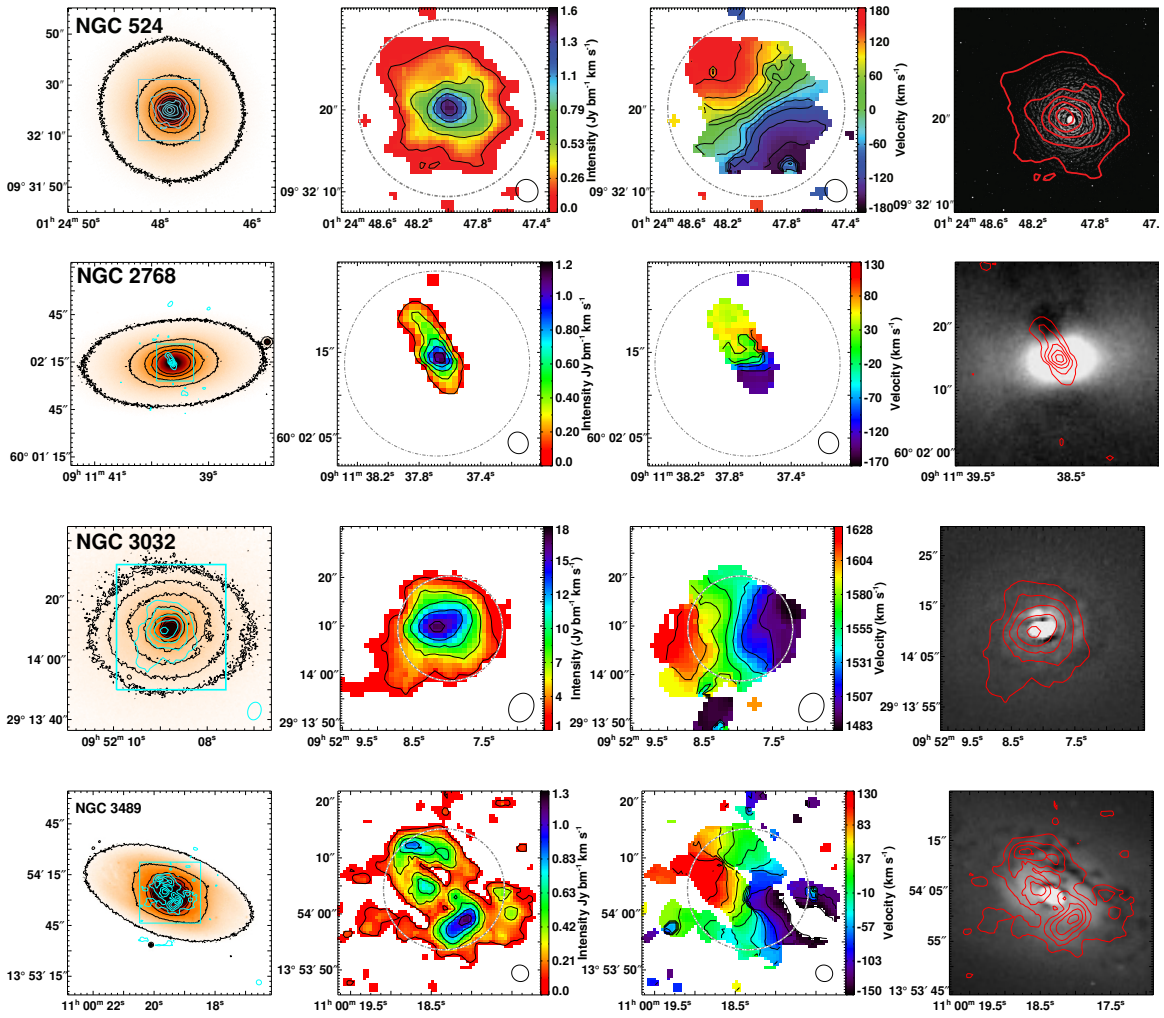

Figure A.31 Interferometric CO(1–0) data from ATLAS^{3D} in the literature. From top-to-bottom, NGC 524 (Crocker et al. 2011), NGC 2768 (Crocker et al. 2008), NGC 3032 (Young, Bureau & Cappellari 2008), NGC 3489 (Crocker et al. 2011), NGC 4459 (Young, Bureau & Cappellari 2008), NGC 4476 (Young 2002), NGC 4477 (Crocker et al. 2011), NGC 4526 (Young, Bureau & Cappellari 2008) and NGC 4550 (Crocker et al. 2009). For each galaxy, from left-to-right, the panels show the r-band image overlaid with the CO(1–0) integrated intensity (moment0) contours (cyan), the color-scale of the moment0 overlaid with the contours and the IRAM 30m telescope beam (gray), the color-scale mean velocity (moment1) map overlaid with isovelocity contours, and the g-band unsharp-masked image overlaid with the CO(1–0) moment0 contours (red). For comparisons to unsharp-masked HST data for these galaxies, please see the papers cited above.

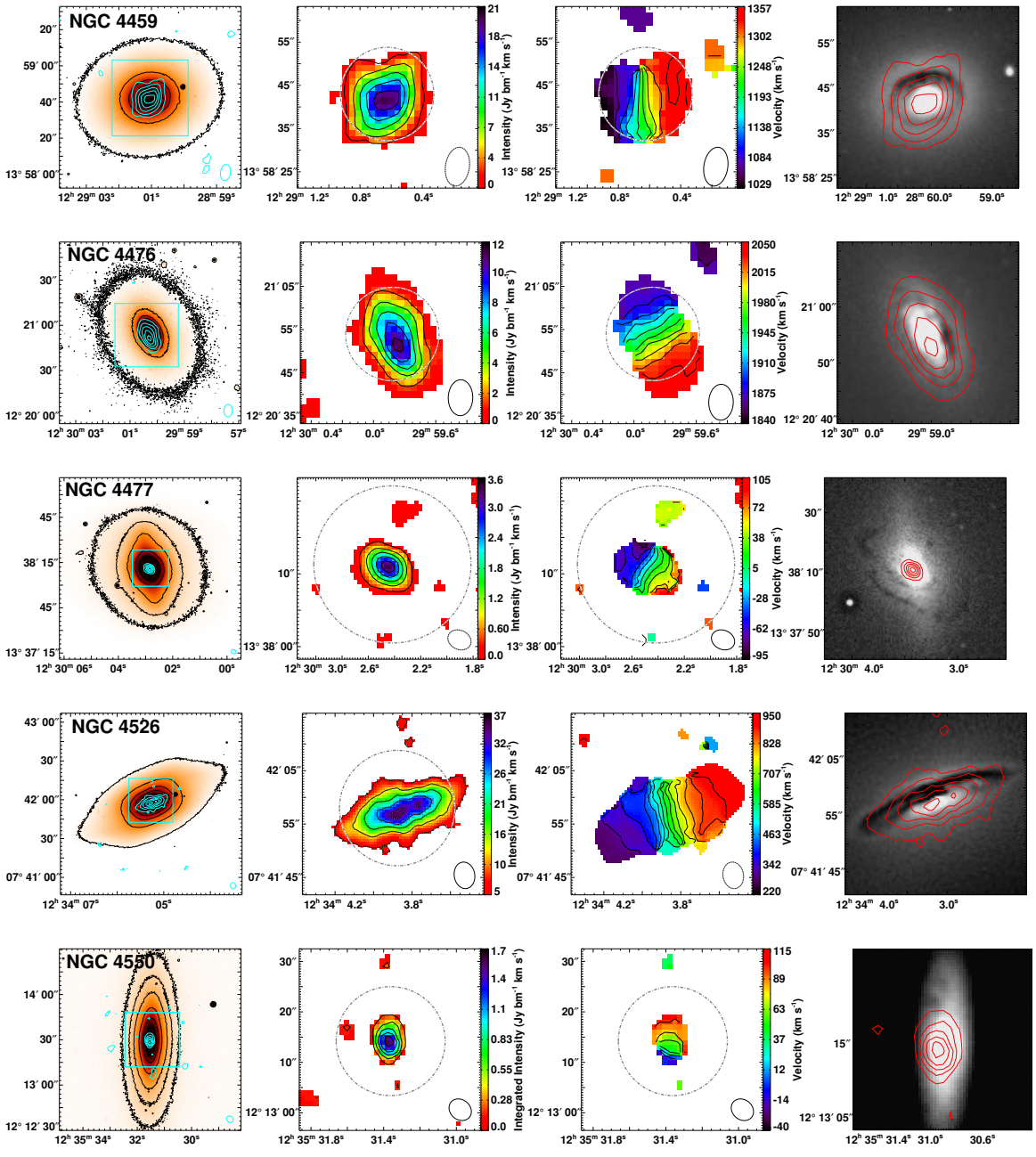

Figure A.32 Continued...

A.3 Galaxies observed with CARMA not in the ATLAS^{3D} survey

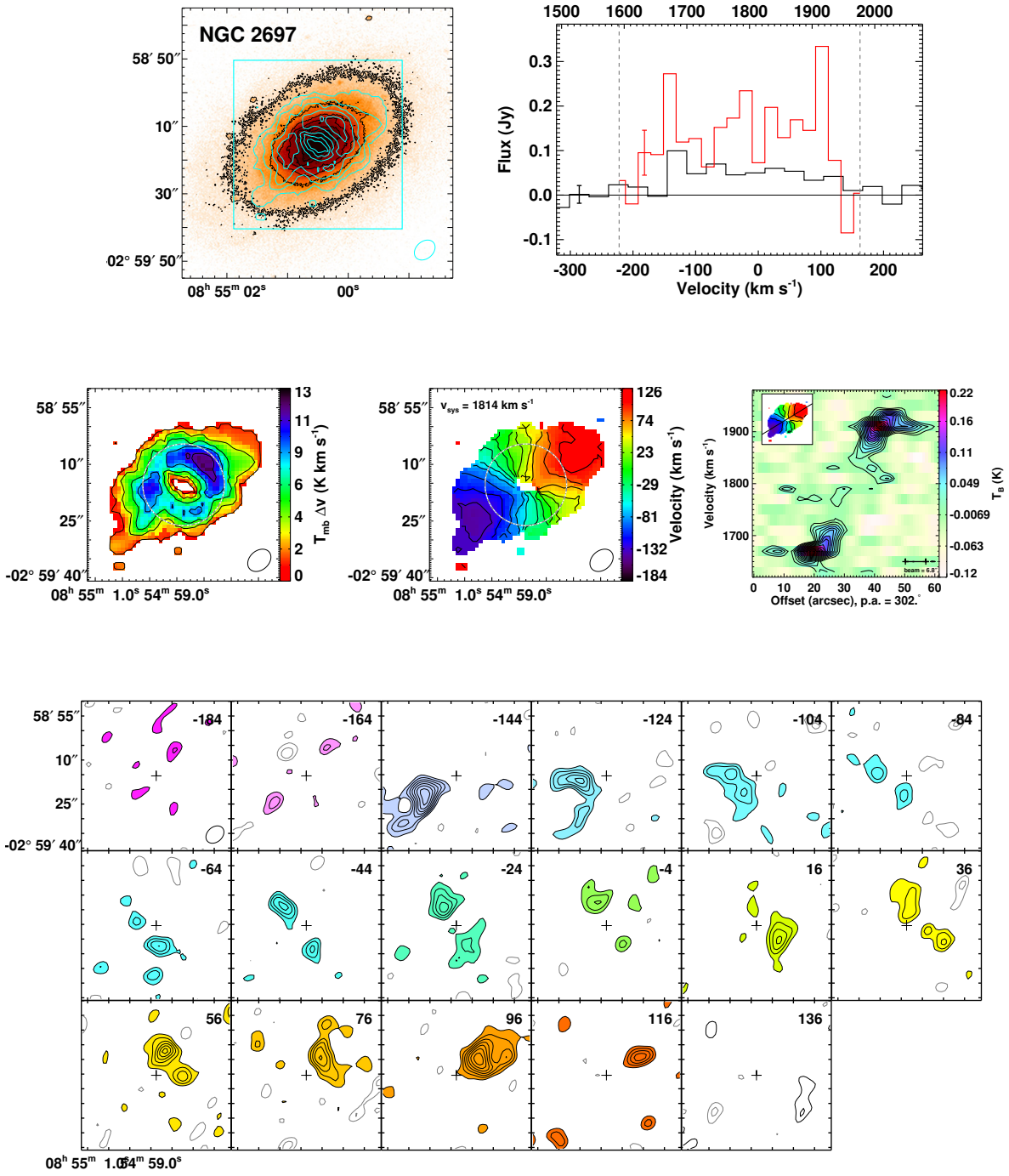

Figure A.33 **NGC 2697** (M_K = -22.19) was removed from the sample as being misclassified and containing spiral structure in the stellar isophotes. The moment0 peak is 4.1 Jy beam^{-1} km s^{-1}.

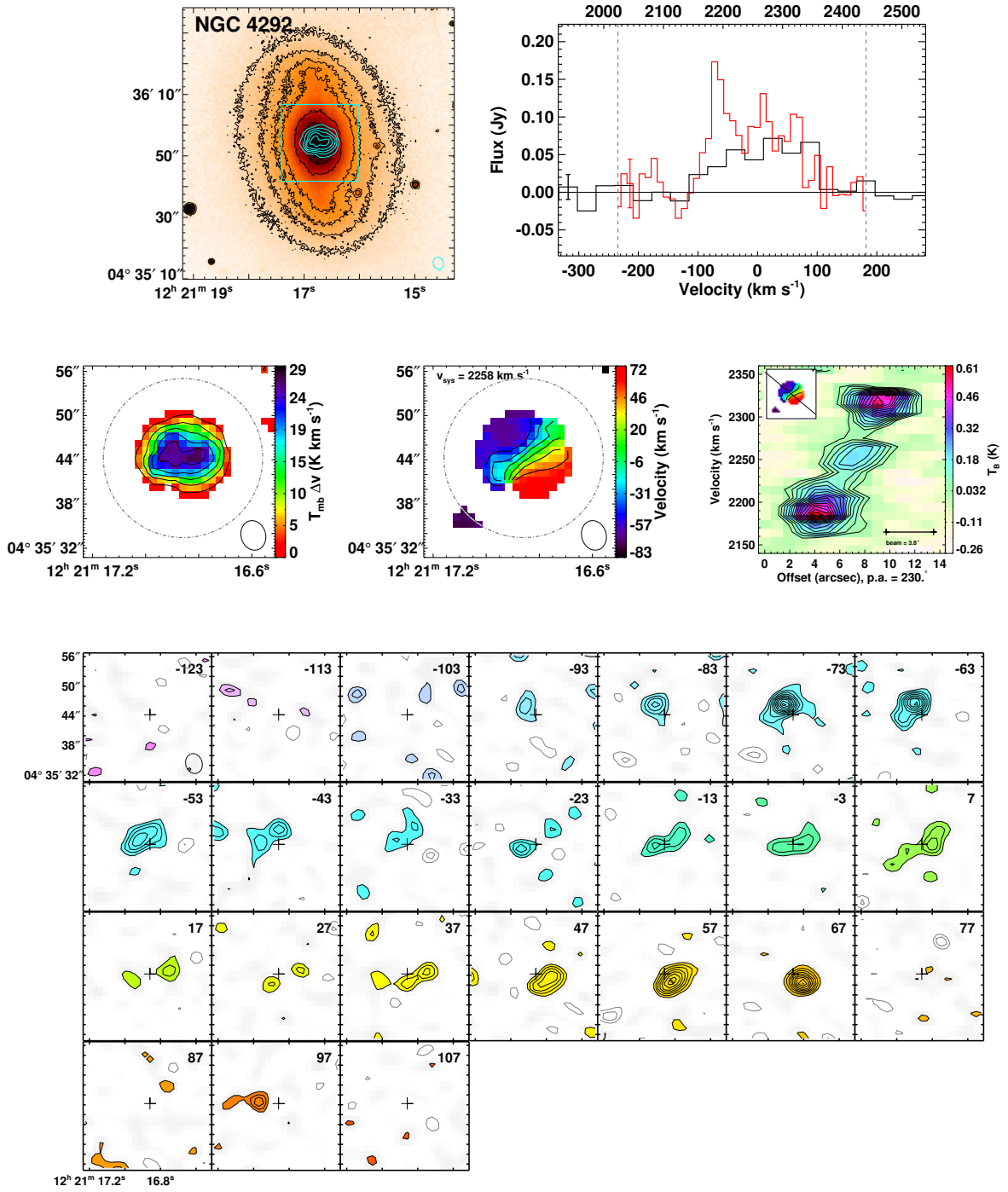

Figure A.34 **NGC 4292** is a Virgo cluster galaxy (M_K = -23.2). It was removed from the ATLAS^{3D} sample based on its not being observed with SAURON, and thus lacks stellar kinematic data. The moment0 peak is 4.3 Jy beam^{-1} km s^{-1}.